

https://dspace.org/

Development and Characterisation of Antibacterial Titanium-Copper based Alloys for Additive Manufacturing for Biomedical Applications

Phala, Ngwakoana Succes

2025

University of the Witwatersrand, Johannesburg

https://hdl.handle.net/10539/49855

Phala, Ngwakoana Succes. (2025). Development and Characterisation of Antibacterial Titanium-Copper based Alloys for Additive Manufacturing for Biomedical Applications. [Master's dissertation, University of the Witwatersrand, Johannesburg]. WIReDSpace. https://hdl.handle.net/10539/49855

Downloaded from a DSpace repository. https://dspace.org/



UNIVERSITY OF THE
WITWATERSRAND,
JOHANNESBURG

Development and Characterisation of Antibacterial Titanium-Copper based Alloys for Additive Manufacturing for Biomedical Applications

MSc Dissertation

Prepared by

Phala Ngwakoana Succes

Student number

820850

Submitted to

School of Chemical and Metallurgical Engineering, Faculty of Engineering and the Built Environment, University of the Witwatersrand, Johannesburg, South Africa

Supervisors:

Prof. L.A. Cornish and Prof. C. Polese

Declaration

I Ngwakoana Phala declare that this dissertation is my own, unaided work. It is being submitted for the Degree of Master of Science in Engineering in the University of the Witwatersrand, Johannesburg. It has not been submitted before for any degree or examination in any other University.



Signature

28 February 2025

Date

Abstract

The development of biomedical implants for dental implants aims to address limitations in strength, biocompatibility and infection prevention. This study investigated the fabrication and optimisation of Ti-6Ta-1.5Zr-0.2Ru-5Cu (mass%) alloy using Laser Powder Bed Fusion (LPBF), focusing on its hardness, microstructural, corrosion and antibacterial properties. The alloy replaces toxic aluminium and vanadium with non-toxic elements while maintaining the same phase proportions and mechanical properties. Ruthenium was added to enhance corrosion resistance and copper was added for its antibacterial properties.

Powder atomisation was done using the ultrasound rePowder system to ensure suitability for LPBF. The process parameters were optimised by printing single tracks and assessing their morphology. Subsequently, square samples were printed using the best parameters. The manufactured samples were characterised and compared with as-cast alloys for their microstructure, hardness, corrosion resistance and antibacterial properties.

Microstructures were finer for LPBF than as-cast alloys, contributing to enhanced antibacterial properties. However, samples fabricated by both techniques showed similar hardness. Corrosion tests in phosphate-buffered saline (PBS) solution showed good corrosion resistance attributed to the stabilisation of the passive oxide layer, with a corrosion rate below 0.13 mm/year for both techniques. These findings demonstrated the potential of Ti-6Ta-1.5Zr-0.2Ru-5Cu (mass%) alloy as a promising biomedical implant for dental applications.

Dedication

Firstly, I would like to dedicate this work to my God without whom all this would not have been possible.

I would like to dedicate this work to my late Grandmother Maria Phala, Sebutse wa Senamela le Napogadi. for always seeing the potential in me and my siblings and your encouragement helped us reach our potential. Looking back at us, you will be proud. Robala ka kgotso Sebutse.

Lastly, my Daughter Thakgalelo (Hunadi) Phala to look at this and be encouraged whenever she doubts herself.

Acknowledgements

Sir Isaac Newton once said, "If I have seen further, it is by standing on the shoulders of giants." Reflecting on my journey over the past three years, I am deeply grateful for Prof. Lesley Cornish's immense impact on my professional and personal growth. Her unwavering support has been invaluable, and I also extend my heartfelt thanks to Prof. Claudia Polese for being an essential part of this incredible team. Together, they have imparted invaluable lessons, from constructive criticism to encouraging messages that have shaped my values. I truly appreciate the knowledge and experience I have gained under their supervision, which will guide me as I move forward in my career.

I would like to express my heartfelt gratitude to Mr Nthape Mphasha and Dr Kiyaasha Dyal Ukabhai for their constant availability and willingness to address my questions, no matter how trivial. Your encouragement to share my ideas and your guidance have been invaluable. Additionally, I thank Prof. Michael Bodunrin and Dr Desmond Klenam for their unwavering support and reassurance throughout this journey. I truly appreciate everything you have done for me.

I would like to extend my heartfelt appreciation to Mintek for their invaluable assistance with mixing and binding my powder and for corrosion testing. I also thank the team at AMAZEMET, especially Tomasz Choma, Jakub Cifti, and Lukasz Zrodowski, for their support in conducting powder atomisation tests and producing LPBF and as-cast samples of my alloys. Your expertise and collaboration have been instrumental to my work, and I am truly grateful for your contributions. Uppsala University for assisting with anti-bacterial testing, special thanks go to Prof. Caroline Öhman Mägi. For her warm welcome during our stay and her financial support for making this trip possible.

I would like to express my sincere gratitude to Mrs Marina Labuschagne for her invaluable administrative support. Your dedication and commitment have been instrumental, and I truly appreciate your reliability throughout this journey. Thank you!

I would like to express my heartfelt appreciation to the NRF (National Research Foundation), CPAM (Collaborative Programme in Additive manufacturing), and the DSI-NRF Centre of Excellence in Strong Materials (CoE-SM) for their financial support for this project. I am

especially grateful to my supervisors for organising the funding that has made this journey smoother and contributed to my success. I also thank Prof. L.A. Cornish for the opportunity to visit Sweden for antibacterial testing. Lastly, I appreciate my supervisors for enabling my attendance at the MSSA conferences in 2022 and 2024, and the RAPDASA conferences in 2023 and 2024, which provided invaluable networking opportunities.

I would like to express my heartfelt gratitude to the staff of the School of Chemical and Metallurgical Engineering at the University of the Witwatersrand for providing a conducive workplace, essential equipment, and access to well-equipped laboratories, all of which have been crucial to my success. I especially acknowledge Letta Ntuli and Collen Makola.

I would like to extend my heartfelt thanks to my friends for their support and love throughout this journey. Special thanks to Nompumelelo, Kgolane, Itumeleng, Merrily, Jason, Matome, Boitumelo, John, Milka, Tebatso Phala (Mr Mike) and the Wits Alumni Relations staff.

I am deeply grateful to my siblings, Rodney, Bauba, Malope, Phemelo and Matladi, for their unwavering love and support. Your constant encouragement has been a source of strength and inspiration, and I truly appreciate all you have done for me.

To my supportive partner, Marvin Ngele, I am deeply grateful for your unwavering support, patience and encouragement during tough times. Your belief in me has made all the difference, and I truly appreciate everything you do.

I want to acknowledge my wonderful daughter (Thakgalelo), whose laughter and curiosity have been a constant source of inspiration. Your presence has brought joy and meaning to my life, and I thank you for being my little cheerleader. I hope to inspire you as much as you inspire me every day.

I cannot fully convey my gratitude to my unwavering pillars of strength, my parents, Malope wa Repo le Sebutse and Hunadi wa Phaahla le Boledi. Words fall short when I try to express just how thankful I am to you both. Your love and support have made this journey possible, allowing me to pursue my dreams while selflessly caring for my child. Despite not fully understanding the path I chose, you encouraged me to follow my aspirations. Your belief in me has been a guiding light, and I am eternally grateful for everything you have done.

Table of Contents

Declaration ..... **ii**

Abstract ..... **iii**

Dedication ..... **iv**

Acknowledgements ..... **v**

Table of Contents ..... **vii**

List of Figures ..... **x**

List of Tables ..... **xv**

Nomenclature ..... **xvii**

Chapter 1. Introduction **1**

1.1 Background 1

1.2 Research questions 3

1.3 Research aim and objectives 4

1.4 Scope of the dissertation 4

Chapter 2. Literature review **5**

2.1 Titanium alloys 5

2.1.1 Development of Ti-6Al-4V alloys 7

2.1.2 Titanium alloy in dental applications 12

2.1.3 Corrosion behaviour of titanium alloys 17

2.1.4 Microstructure, mechanical and biocompatibility of titanium implants 20

2.1.5 Titanium alloys with copper in biomedical applications 26

2.2 Additive Manufacturing 32

2.2.1 Additive manufacturing Methods 32

2.2.2 Feedstock preparation 38

2.2.3 Laser powder bed fusion 44

2.2.3.1 Properties of LPBF 44
2.2.3.2 Optimisation of printing parameters of LPBF 47
2.2.4 Additive Manufacturing in Biomedical Applications 52
2.3 Literature review summary and the design of this project 53
Chapter 3. Experimental Procedure 56
3.1 Powder manufacturing and characterisation 56
3.1.1 Powder Manufacturing 56
3.1.2 Power Characterisation 57
3.2 Single tracks 57
3.2.1 Printing of the Single Tracks 57
3.3 LPBF-manufactured and as-cast samples: manufacturing and characterisation 59
3.3.1 As-cast manufactured sample 59
3.3.2 Printing of LPBF-manufactured samples 59
3.3.3 Density calculations 60
3.3.4 Microstructural analysis and phase identification of LPBF and as-cast samples 61
3.3.5 Hardness testing 62
3.3.6 Anti-bacterial testing 62
3.3.7 Corrosion testing 64
Chapter 4. Results 66
4.1 Powder Characterisation 66
4.2 Characterisation of single tracks 75
4.3 Characterisation of LPBF-manufactured cuboids and as-cast samples 80
4.3.1 Density testing 80
4.3.2 Microstructural and XRD analysis 80
4.3.3 Hardness testing 84
4.3.4 Anti-bacterial testing 86

4.3.5 Corrosion test results 89

Chapter 5. Discussion 94

5.1 Powder characterisation 94

5.2 Single tracks 95

5.3 Comparison between LPBF and as-cast manufactured alloy samples 97

5.3.1 Density 97

5.3.2 Microstructures and chemical compositions of the manufactured alloys 98

5.3.3 Hardness 102

5.3.4 Anti-bacterial resistance 104

5.3.5 Corrosion resistance 105

Chapter 6. Conclusions and Recommendation 110

6.1 Conclusion 110

6.2 Recommendation for future work 111

References 112

Appendices 134

Appendix 1: List of Publications from the MSc 134

Appendix 2: Sample preparation 135

Appendix 3: XRD DATA 137

Appendix 4: Copies of publications from the MSc 143

List of Figures

Figure 2.1. Unit cells and allotropic transformation of pure titanium (Veiga et al., 2003). 5
Figure 2.2. Effects of alloying elements on titanium phase diagrams (Leyens and Peters, 2003). 7
Figure 2.3. Influence of thermomechanical processing on the formation of different microstructures in α+β titanium alloys (Geeth et al., 2009). 8
Figure 2.4. Development of a Widmanstätten microstructure in α+β Ti-6Al-4V alloy (Donachie, 2000). 9
Figure 2.5. Examples of biomedical implants: (a) cranial prosthesis, (b) surgical guide, (c) scapula prosthesis, (d) knee prosthesis, (e) dental implants, (f) interbody fusion cage, (g) acetabular cup and (h) hip prosthesis (Ni et al., 2019). 12
Figure 2.6. Dental implant (Xin et al., 2022). 13
Figure 2.7. Implant thread pattern types (Moulyashree and Mahantesha, 2023). 16
Figure 2.8. Factors that affect osseointegration (Gaviria et al., 2014). 17
Figure 2.9. Schematic diagram of biochemical mechanisms involved in the corrosion-related interaction between titanium surface (with the oxide layer) and tissue in dental implants (Nagay et al., 2022). 18
Figure 2.10. SEM-BSE image showing parameters of the lamellar microstructure that was analysed using stereological methods: D = primary β grain size, d = size of the colony of parallel α lamellae, t = thickness of α lamellae (Sieniawski et al., 2013). 25
Figure 2.11. SEM-BSE image showing Widmanstätten microstructure of Ti-6Al-4V alloy cooled from the β-phase field at 9°C/s (Sieniawski et al., 2013). 25
Figure 2.12. SEM-BSE images of Ti-6Al-4V cooled from the β phase field: (a) α growing as lamellae into β grains and (b) colonies of lamellae oriented at different angles (Leyens and Peters, 2003). 26
Figure 2.13. XRD patterns of: (a) Ti powder, (b) Ti–Cu mixed powder and (c) Ti–Cu sample (Zhang et al., 2013). 27
Figure 2.14. Schematic diagram of potential antibacterial activity of Cu^{2+} from Ti-Cu alloy (Liu et al., 2016). 28
Figure 2.15. SEM-SE micrographs (a, b, c, d) and DAPI images (e, f, g, h) of *S. mutans* and *P. gingivalis* on Ti and Ti-5Cu alloy surface after 24-hour co-culture showing damaged cells (white

arrows) on the Ti-Cu alloy, while cells on the Ti surface had normal morphology (red arrows) (Liu et al., 2016). 29
Figure 2.16. Corrosion results of Ti–Cu alloys with different Cu contents: (a) OCP and (b) Tafel curves (Liu et al., 2014a). 31
Figure 2.17. SEM-BSE images as-cast Ti-6Ta-1.5Zr-0.2Ru-5Cu (mass%) (Spotose, 2023), (a) low magnification showing (αTi) needles (dark), (βTi) matrix (medium) and (b) high magnification Ti_2Cu (white arrow). 32
Figure 2.18. Schematic diagrams for additive manufacturing: (a) powder bed fusion (PBF) and (b) directed energy deposition (DED) (Liu et al., 2022). 33
Figure 2.19. Time-temperature-transformation (T-T-T) curves for Ti-6Al-4V: open squares = 0.05 mass% O, circles = 0.1 mass% O, crosses = 0.2 mass% O, solid line from empirical data, showing oxygen content reduced M_s (Yan and Yu., 2015). 35
Figure 2.20. SEM-BSE images of Ti-6Al-4V fabricated using laser metal deposition (LMD) and electron beam melting (EBM) in three layers: (a-c) LMD (bottom, middle, top) and (d-f) EBM (bottom, middle, top), showing basketweave morphology (red ellipses) and colony morphology (yellow ellipses). The acicular phase shown (white arrow) in the bottom layer of the LMD sample. (Rashid et al., 2022). 36
Figure 2.21. SEM-BSE micrograph of LMD showing shear band formation (Rashid et al., 2022). 37
Figure 2.22. Schematic diagram showing powder atomisation (Yadroitsev et al., 2021). 39
Figure 2.23. SEM-SE images of: (**a**) <50 µm particle size ultrasonically atomised powder and (**b**) gas-atomised powder (Żrodowski et al., 2021). 42
Figure 2.24. Process diagram and experimental set-up: (**a**) material feedstock and (**b**) (1) Au-based alloy earrings, (2) AMZ4 (Heraeus GmbH) Zr-based metallic glass, (3) slabs of Ni–Mn–Ga magnetocaloric alloy, (4) forged equiatomic Fe–Cr–Mn–Ni high entropy alloy, (5) AISI 304 steel as a M10 bolt, (6) Grade 2 titanium porous implant (Żrodowski et al., 2021). 43
Figure 2.25. Process flow diagram for creating parts with LPBF, including designing in CAD, setting up the LPBF machine and laser-material interaction process (Yadroitsev et al., 2021). 45
Figure 2.26. Main parameters affecting the quality of LPBF components (Yadroitsev et al., 2021). 46

Figure 2.27. SEM-SE image of single-track showing adhered partially melted powder particles and solidification ripples (Simson and Subbu, 2022). 49
Figure 2.28. SEM-SE images showing the effect of laser power and scanning speed on single-track surface topography at constant LED (Simson and Subbu, 2022). 50
Figure 2.29. SEM-BSE images of single-track surface morphologies at varying scanning speeds (V) and laser powers (P), with white circles showing balling (Yueling et al., 2018). 51
Figure 2.30. SEM-SE images of top views of single tracks on the substrate for 80°C and 900°C preheating at 0.12 m/s scanning speed, with white arrows indicating satellites (Yadroitsev et al., 2013). 51
Figure 2.31. AM manufactured Ti-6Al-4V femur (Zadpoor and Malda, 2017). 53

Figure 3. 1. Photograph of the Ti-6Al-4V substrate disc with eight LPBF squares supporting five horizontal single tracks each, showing directions of argon gas flow, melting and recoating. . 59
Figure 4.1. SEM-BSE images of blended elemental powders of Ti, Ta, Zr, Ru and Cu before atomisation: (a) lower and (b) higher magnification: Ta (light contrast) and Ti (dark). 66

Figure 4.2. X-ray maps of the blended powder of Ti, Ta, Zr, Ru and Cu before atomisation. .. 67
Figure 4.3. SEM-SE images of Ti-6Ta-1.5Zr-0.2Ru-5Cu (mass%) powder after atomisation: (a) lower and (b) higher magnification showing large spherical particles and an irregular particle (shown by the yellow arrow). 68
Figure 4.4. X-ray maps of the atomised Ti-6Ta-1.5Zr-0.2Ru-5Cu (mass%) powder. 69
Figure 4.5. X-ray maps of cross-sections of three Ti-6Ta-1.5Zr-0.2Ru-5Cu (mass%) atomised powder particles. 70
Figure 4.6. SEM-BSE images of cross-sections of Ti-6Ta-1.5Zr-0.2Ru-5Cu (mass%) powder, yellow arrows show internal porosity, and blue arrow shows an irregular particle. 71
Figure 4.7. SEM-BSE image indicating the areas of the EDX analyses on cross-sectioned atomised powder particles. 71
Figure 4.8. X-ray line scans of a cross-section of a single spherical powder particle. 72
Figure 4.9. X-ray line scans of a cross-section of an agglomerated powder particle. 72
Figure 4.10. X-ray line scans of a cross-section of irregular and spherical powder particles. . 73
Figure 4.11. Particle size distribution of blended elemental powders of Ti, Ta, Zr, Ru and Cu before atomisation. 73

Figure 4.12. Particle size distribution of Ti-6Ta-1.5Zr-0.2Ru-5Cu (mass%) powder after atomisation. 74
Figure 4.13. SEM-BSE image showing an agglomeration of particles.....74
Figure 4.14. XRD pattern for blended elemental powder before atomisation. 75
Figure 4.15. XRD pattern for Ti-6Ta-1.5Zr-0.2Ru-5Cu (mass%) powder after atomisation. 76
Figure 4.16. SEM-BSE images showing morphology of the single tracks at 157.5 W laser power, 0.15 mm beam diameter and scanning speeds of: (a) 600 mm/s, (b) 800 mm/s, (c) 1000 mm/s and (d) 1200 mm/s. White ellipse indicates balling.....77
Figure 4.17. SEM-BSE images showing the morphology of single tracks at 315 W laser power, 0.08 mm beam diameter and scanning speeds of: (a) 600 mm/s, (b) 800 mm/s, (c) 1000 mm/s and (d) 1200 mm/s.....78
Figure 4.18. SEM-BSE images showing the morphology of the single tracks at 280 W laser power and 1200 mm/s scanning speed for beam diameter: (a) 0.15 mm, (b) 0.22 mm, (c) 0.29 mm and (d) 0.3 mm. 79
Figure 4.19. XRD pattern of the best single track of Ti-6Ta-1.5Zr-0.2Ru-5Cu (mass%).....79
Figure 4.20. SEM-SE image showing porosity within the LPBF sample. 81
Figure 4.21. SEM-BSE image showing the side of the LPBF sample: yellow arrow indicates a pore, blue arrows show unmelted powder particles and the light region is probably unmelted tantalum. 81
Figure 4.22. SEM-BSE images of as-cast Ti-6Ta-1.5Zr-0.2Ru-5Cu (mass%): (a) lower magnification: (βTi) (light) grains with (αTi) (dark) precipitated on grain boundaries and within and (b) higher magnification. Black arrow indicates Ti_2Cu precipitates. 82
Figure 4.23. SEM-BSE images of Ti-6Ta-1.5Zr-0.2Ru-5Cu (mass%) LPBF horizontal cross-section: (a) low magnification showing equiaxed (αTi) along (βTi) grain boundaries and within the grains and (b) high magnification, (βTi) (light contrast) and (αTi) (dark contrast); the black arrow indicates Ti_2Cu precipitates (very light contrast). 82
Figure 4.24. SEM-BSE images of LPBF Ti-6Ta-1.5Zr-0.2Ru-5Cu (mass%) vertical cross-section: (a) low magnification showing (αTi) along (βTi) grains and (b) high magnification, (βTi) (light) and (αTi) (dark). White arrow indicates build direction. 83
Figure 4.25. XRD patterns of LPBF-manufactured and as-cast Ti-6Ta-1.5Zr-0.2Ru-5Cu (mass%). 84
Figure 4.26. Hardness profile for LPBF and as-cast samples measured from the edge.....85

Figure 4.27. Photographs of: (a) as-cast sample and (b) LPBF-manufactured sample showing indentations inside the white ellipses. 85
Figure 4.28. Hardness values from random indentations across the samples. 86
Figure 4.29. Photographs of bacteria count tests after 24 hours: (a) LPBF, (b) as-cast, and (c) Ti-6Al-4V samples, all conducted with three iterative 10-fold dilutions from the second test. 86
Figure 4.30. Photographs of bacteria count tests after 24 hours: (a) LPBF, (b) As-cast and (c) Ti-6Al-4V samples, all conducted with two iterative 10-fold dilutions from the second test. 87
Figure 4.31. Number of colonies counted on each sample in the third 10-fold dilution test (there were no colony counts for copper sample). 87
Figure 4.32. Colony-forming unit (CFU) counts of each sample bacteria after 24 hours (there were no colony counts for copper sample). 88
Figure 4.33. OCP profiles of the Ti-6Ta-1.5Zr-0.2Ru-5Cu (mass%) alloys in phosphate-buffered saline solution. 89
Figure 4.34. Potentiodynamic polarisation curves of Ti-6Ta-1.5Zr-0.2Ru-5Cu (mass%) alloys in phosphate-buffered saline solution, black arrow shows broader passive region in LPBF. 90
Figure 4.35. SEM-SE images of as-cast Ti-6Ta-1.5Zr-0.2Ru-5Cu (mass%) after corrosion tests: (a) lower magnification and (b) higher magnification: Yellow arrow indicates pore from casting and blue arrow indicates a precipitate from PBS solution. 91
Figure 4.36. SEM-SE images of LPBF Ti-6Ta-1.5Zr-0.2Ru-5Cu (mass%) after corrosion tests: (a) low magnification showing scattered corrosion products on the surface (dark contrast) and (b) high magnification showing unmelted powder particles (orange arrows) and a pore (white arrow). 92

Figure 5.1. IPF maps and TEM images of LPBF-produced Ti-xCu alloys (x = 2, 5, 8 wt%), showing finer α′ martensite and increased Ti_2Cu precipitation with higher Cu content (Liu et al., 2024) 99
Figure 5.2. Phase proportion diagram of Ti-6Ta-1.5Zr-0.2Ru-5Cu (mass%) (Spotose, 2023).101

List of Tables

Table 2.1. Phase stabilising alloying elements (Chandrasekaran and Xia, 2005). 6
Table 2.2. Heat treatments for α+β titanium alloys (Donachie, 2000). 10
Table 2.3. Ti-6Al-4V for biomedical applications and its properties (Balazic et al., 2007). 11
Table 2.4. Effect of alloying elements on titanium alloys' microstructure and electrochemical properties (Nagay et al., 2022), where Rp = polarisation resistance, i_{corr} = corrosion current density, E_{corr} = corrosion potential and E_{pit} = pitting potential. 19
Table 2.5. Titanium alloys for dental applications and their mechanical properties (Niinomi, 2003; Li et al., 2014). 22
Table 2.6. Mechanical properties of the Ti-6Al-2Mo-2Cr alloy (Sieniawski et al., 2013). 24
Table 2.7. Parameters of fusion-based additive manufacturing techniques (Liu et al., 2022). 34
Table 2.8. Summary of Powder Bed fusion methods for biomedical applications (Ni et al., 2019). 40
Table 2.9. Characteristics of powder atomisation medium for LPBF (Anderson et al., 2018). 41

Table 3.1. Powder specifications. 56
Table 3.2. Printing parameter ranges for the single tracks. 57
Table 3.3. Parameters for printing single tracks. 58
Table 3.4. LPBF process parameters for cuboid samples. 60
Table 3.5. Grinding and polishing steps for Ti-6Ta-1.5Zr-0.2Ru-5Cu (mass%) alloys. 61
Table 4.1. EDX results for atomised Ti-6Ta-1.5Zr-0.2Ru-5Cu (mass%) powder. 67

Table 4.2. Targeted composition and EDX results for area scans of cross-sections of atomised Ti-6Ta-1.5Zr-0.2Ru-5Cu (mass%) powder particles. 68
Table 4.3. Average particle size distributions of blended powder and after atomisation. 75
Table 4.4. EDX results of best single track and the spherical particle on the track. 77
Table 4.5. EDX results of dark spots on Ti-6Ta-1.5Zr-0.2Ru-5Cu (mass%) best single track. ... 78
Table 4.6. Densities of the LPBF-manufactured samples. 80
Table 4.7. Areal EDX results of LPBF, as-cast and as-cast (Spotose,2023) samples of Ti-6Ta-1.5Zr-0.2Ru-5Cu (mass%). 83
Table 4.8. EDX results of as-cast light and dark phases of Ti-6Ta-1.5Zr-0.2Ru-5Cu (mass%) ... 83
Table 4.9. Comparison of average colony-forming unit (CFU) counts for different samples. ... 88

Table 4.10. Polarisation results of the Ti-6Ta-1.5Zr-0.2Ru-5Cu (mass%) alloy. 91
Table 4.11. EDX results of as-cast and LPBF Ti-6Ta-1.5Zr-0.2Ru-5Cu (mass%) after corrosion tests. 93

Nomenclature

AM	Additive manufacturing
BCC/bcc	body-centred cubic
BSE	Backscattered electrons
CP-Ti	Commercially pure titanium
EBM	Electron beam melting
E_{corr}	Corrosion potential
EDX	Energy dispersive X-ray spectroscopy
E_{pit}	Pitting potential
HCP/hcp	hexagonally-close packed
I_{corr}	Corrosion current density
LBM	Laser beam melting
LED	Linear energy density
LPBF	Laser powder bed fusion
OCP	Open circuit potential
PBS	Phosphate buffered saline (solution)
PED	Planar energy density
ROS	Reactive oxygen species
Rp	Polarisation resistance
SCE	Saturated calomel electrode
SE	Secondary electrons
SEM	Scanning electron microscopy/microscope
WE	Working electrode
XRD	X-Ray diffraction

Chapter 1. Introduction

1.1 Background

Titanium alloys are used in biomedical applications, including dental uses, due to their high strength, low Young's modulus which is fairly close to the human bone (10 - 30 GPa), excellent corrosion resistance and biocompatibility (i.e., the ability of a material to perform with an appropriate host response in a specific situation) (Leyens and Peters, 2003; Williams, 2008). The Ti-6Al-4V alloy and commercially pure titanium (CP-Ti) have been used in aerospace for engine components because they are lightweight, have high strength and good corrosion resistance (Inagaki et al., 2014). Both these materials started to replace stainless steels and cobalt-based alloys in many biomedical applications since the 1970s (Mantovani, 2000) and are considered compatible due to their excellent combination of tensile and fatigue properties and biocompatibility (Xu et al., 2019).

In dental implants, commercially pure titanium (CPTi) is used (Froes, 2018; Gubbi and Wojtisek, 2018). Also, (α+β)-alloys, including (1) Ti-6Al-4V, (2) Ti-6Al-4V ELI (with extremely low interstitial elements) and (3) Ti-6Al-7Nb, are commonly used in biomedical applications due to their higher strength than CP titanium (Li et al., 2014). However, there are some concerns about Ti-6Al-4V as Al has been associated with Alzheimer's disease and phosphorus deficiency in the blood and bone (Leyens and Peter 2003; Niinomi et al., 2012). Furthermore, V has been reported as being cytotoxic and shows carcinogenic properties (Niinomi et al., 2012; Challa et al., 2013). Additionally, CP-Ti has insufficient strength for load-bearing implants (Soro et al., 2019).

In 2011, ~15% of the world's population was reported to have a disability (WHO, 2011). Developing countries suffer the most; South Africa being a good example (Word Bank, 2021). According to the United Nations 2030 Sustainable Development Agenda (United Nations, 2015), disability cannot be a reason for denying access to development programming and human rights. Therefore, many people who live with a disability need biomedical devices or implants to live a quality and healthy life.

The annual number of hip fractures in South Africa is estimated to increase from ~11,000 in 2020 to ~26,400 by 2050 (Pubmed, 2022). To alleviate this situation, fixing and reconstructing

are required, resulting in high demands for good biomedical materials with complex shapes. These shapes are complicated to manufacture using conventional methods. However, with additive manufacturing (AM or 3D printing), complex shapes for metallic implants can be printed (Ryan et al., 2021). Additive manufacturing enables the manufacture of highly customised medical implants with complex designs, tailored to individual patients for improved treatment outcomes (DebRoy et al., 2018). Implanting 3D-printed Ti-alloys has significantly reduced operation, hospitalisation times and overall medical costs (Ni et al., 2019).

Using Ti-6Al-4V as the (α+β) alloy reference, Stenland et al. (2015) replaced Al and V with non-toxic zirconium and tantalum for stabilising α and β phases. Tantalum was chosen to replace V as a β-stabiliser and Zr as a solution-hardening element and to help form a protective passive film to give good corrosion resistance. By adding copper, which has antibacterial properties (Hong and Koo, 2005; Zhang et al., 2013), the Ti-Cu alloys also had antimicrobial properties (Zhang et al., 2013; Liu et al., 2014). Liu et al. (2014) stated that the copper content must be at least 5 mass% to obtain stable antibacterial properties and balanced mechanical properties. The Ti-6Ta-1.5Zr-0.2Ru-5Cu (mass%) alloy was identified as a new potential (α+β) titanium alloy for dental applications (Spotose, 2023). Ruthenium was added to Ti alloys enhance corrosion resistance without changing the microstructure and it is non-toxic to living tissues (Schutz, 1996; Allardyce and Dyson, 2011).

Additive manufacturing includes different technologies and for this work, the laser powder-based fusion (LPBF) method was selected because it can manufacture almost all metal alloys and has a low direct cost (Ni et al., 2019). The LPBF method requires spherical powder with a size range of 15 - 45 µm for optimal flowability and spreadability (Yadroitsev et al., 2021). However, AMAZEMET suggested a broader range of 10 - 100 µm (Żrodowski et al., 2021). The rePowder ultrasound atomisation system (AMAZEMET) was used to atomise the powder in small batches (Żrodowski et al., 2021) under common laboratory conditions and generated high-purity spherical powders.

To achieve the desired properties, high quality and defect-free components are targeted. Optimisation of the LPBF parameters is therefore necessary (Carrozza et al., 2021). Thus, it is important to understand the relationship between the processing parameters, geometry and the resulting microstructures (Svetlizky et al., 2021). Preliminary methods that are mostly

used are expensive and require more material and energy, as aviation standards state that the first 2.5 mm of the part from the base plate should be discarded as the process has not reached thermal stability (Blakey-Milner et al., 2021). However, a more recent single-track approach is cost-effective, requiring less material and energy to preliminarily evaluate how different LPBF process parameters influence the shape, dimensions, and microstructure of the printed material (Gonnabattula et al., 2024). Single tracks might ~~i~~ndicate weldability to the base plate and the interaction with the base plate limits their ability to provide insights into the final properties of the components. However, the single tracks can also assist in identifying a suitable process window to build complex 3D shapes.

1.2 Research questions

1.2.1 Can the Ti-6Ta-1.5Zr-0.2Ru-5Cu (mass%) alloy be effectively fabricated using LPBF and what are the optimal conditions for achieving desirable properties for dental applications?

The production of Ti powders for alloying is difficult because of their high melting points and reactivity. To assess the suitability of Ti powders for LPBF, it is important to atomise the powder and characterise it to ensure it meets the required properties. Ti-6Ta-1.5Zr-0.2Ru-5Cu (mass%) was printed as single tracks to determine the best printing parameters.

1.2.2 How do the mechanical properties and corrosion resistance of the Ti-6Ta-1.5Zr-0.2Ru-5Cu (mass%) alloy fabricated using LPBF compared to those of as-cast alloys?

Due to its finer microstructure, the mechanical properties and corrosion resistance of the Ti-6Ta-1.5Zr-0.2Ru-5Cu (mass%) alloy fabricated by LPBF could be similar or even superior to those of the as-cast alloy.

1.2.3 What is the effect of ruthenium on its corrosion resistance?

The addition of ruthenium enhances corrosion resistance by promoting the formation of a stable and protective oxide layer without changing the alloy's microstructure (Liu et al., 2014a). As ruthenium is expensive, it can only be added in small amounts, so its effectiveness needs to be tested.

1.2.4 **What is the effect of copper (Cu) addition on the antibacterial properties of the Ti-6Ta-1.5Zr-0.2Ru-5Cu (mass%) alloy?**

Copper is known for its antibacterial properties. Investigating how its presence in this alloy

affects anti-bacterial properties, particularly for dental applications, will be important in evaluating its clinical potential.

1.3 Research aim and objectives

The research aimed to assess whether the Ti-6Ta-1.5Zr-0.2Ru-5Cu (mass%) alloy could be shaped by 3D printing, using suitable powders. The employed techniques involved printing single tracks under different conditions and assessing the tracks. Thereafter, samples were printed using the best printing parameters.

Objectives

- To produce Ti-6Ta-1.5Zr-0.2Ru-5Cu (mass%) powders suitable for laser powder bed fusion (LPBF), optimise the laser power and scan speed processing parameters for printing, and build cuboids with these parameters.
- To evaluate the microstructures and properties of the manufactured of Ti-6Ta-1.5Zr-0.2Ru-5Cu (mass%) cuboids and compare with those of the as-cast alloy.
- To study the corrosion behaviour of the additively manufactured Ti-6Ta-1.5Zr-0.2Ru-5Cu (mass%) cuboids in phosphate-buffered saline solution and compare with the as-cast alloy.
- To assess the antibacterial properties of the additively manufactured Ti-6Ta-1.5Zr-0.2Ru-5Cu (mass%) cuboids and compare them with the as-cast alloy.

1.4 Scope of the dissertation

This work focused on the characterisation of Ti-6Ta-1.5Zr-0.2Ru-5Cu (mass%) alloy for additive manufacturing using the laser powder bed fusion (LPBF) technique. The research included powder preparation, atomisation, printing and characterising of the single tracks and LPBF sample fabrication, followed by evaluating the resulting material's microstructure, hardness, antibacterial and corrosion properties. A comparison of the LPBF-manufactured samples with as-cast alloys was done to determine the effect of processing techniques on the alloy’s properties.

Chapter 2. Literature review

2.1 Titanium alloys

Titanium is the fourth most abundant metal element in the Earth's crust (Joshi, 2006). According to Leyens and Peters (2003), it has a density of 4.51 g/cm^3, an electrical conductivity of 4.20×10^{-7} Ωm and a thermal conductivity of 14.99 W/m. Pure titanium is hexagonally close-packed (hcp) at low temperatures and is known as α-titanium (αTi). Above 885°C, it is body-centred cubic (bcc), known as β-titanium (βTi). **Figure 2.1** shows pure titanium's unit cells and its allotropic transformation (Veiga et al., 2012). Only three easy slip systems exist in the hcp structure, compared to 48 in bcc (which are active at different temperatures) (Chandrasekaran and Xia, 2005). This difference in slip systems affects the material's plastic deformation and workability (Leyens and Peters, 2003).

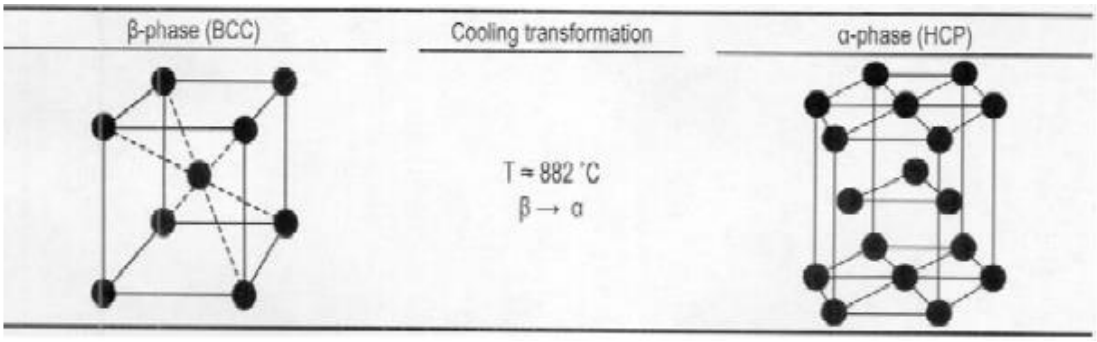

Figure 2.1. Unit cells and allotropic transformation of pure titanium (Veiga et al., 2003).

Titanium and its alloys have gained a preference over 316L stainless steel and cobalt-based alloys as first choice materials in biomedical applications due to their superior biocompatibility (Oldani and Dominguez, 2012). The mechanical properties of titanium alloys are changed by the addition of alloying elements, which modify their microstructures (Leyens and Peters, 2003) and thus properties. Alloying elements are classified into α-, neutral, or β-stabilisers, depending on their effect on the α/β transformation temperature (Lütjering, Williams and Gysler, 2000). Thus, α-stabilising elements like Al expand the α-phase region, while β-stabilising elements like Mo reduce the α/β transformation temperature, allowing the

β-phase to form at lower temperatures (Leyens and Peters, 2003). Chandrasekaran and Xia (2005) list the effects of various alloying elements on the α and β phases in **Table 2.1**. Although Zr is classified as neutral, it also acts as an α-stabilising element (Welsch et al., 1993).

Table 2.1. Phase stabilising alloying elements (Chandrasekaran and Xia, 2005).

α-stabilising	**Neutral**	**β-stabilising**	
		β isomorphous	**β eutectoid**
Al	Sn	Mo	Fe
O	Zr	V	Mn
N		W	Co
C		Ta	Ni
Ga		Nb	Cu
			Si
			H
			W
			Cr

Titanium alloys are categorised into three types: α, α+β and β depending on their microstructure and predominant phases (Leyens and Peters, 2003; Lütjering, Williams and Gysler, 2009). Alpha alloys mainly contain α-stabilising and neutral elements, while near-α alloys have small additions of β-stabilisers. The α+β alloys, which include both types of stabilisers, are often used as commercial alloys (Leyens and Peters, 2003). The stabilisation effects of these elements are quantitatively represented by the molybdenum equivalency (Mo eq) for β-stabilisers and the aluminium equivalency (Al eq) for α-stabilisers (Veiga et al, 2012). The effect of these alloying elements on titanium phase diagrams is shown in **Figure 2.2** (Leyens and Peters, 2003).

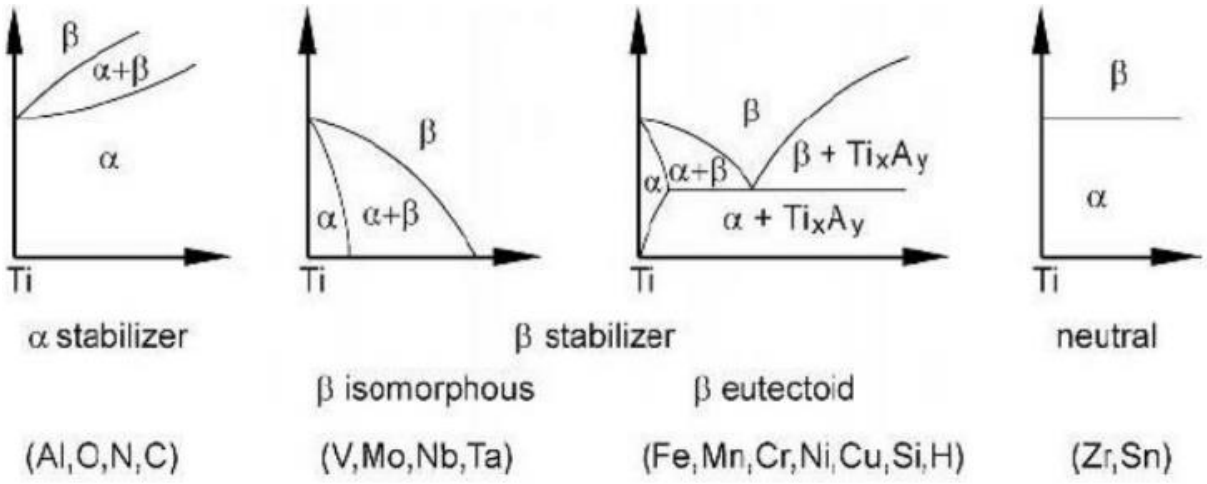

Figure 2.2. Effects of alloying elements on titanium phase diagrams (Leyens and Peters, 2003).

In conventional titanium alloys, the β transus temperature plays an important role in the evolution of microstructure and it defines heat treatment and processing schedules (Geeth et al., 2009). **Figure 2.3** shows different microstructures that resulted from different processing conditions (Geeth et al., 2009). When these alloys are heat treated above the β transus, they develop an acicular or lamellar structure, commonly referred to as a beta-treated structure and when treated below the β transus (within the α+β phase) they consist of equiaxed α+β phases (Niinomi, 2003; Geeth et al., 2009). The volume fraction of the equiaxed α+β varies, depending on alloy composition, heat treatment temperatures and cooling rate. For fast cooling rates, the β transforms into martensite or α laths, with some retained β remaining (Niinomi, 2003; Geeth et al., 2009). In metastable β alloys, quenching from the β region retains the β, while ageing at lower temperatures results in fine α precipitates, enhancing the strength (Geeth et al., 2009).

2.1.1 Development of Ti-6Al-4V alloys

The Ti-6Al-4V alloys have microstructures that consist of α and β phases, which vary depending on temperature and cooling rates (Donachie, 2000). The alloy shown in **Figure 2.4** shows the development of the Widmanstätten microstructure by slow cooling from above the β transus temperature.

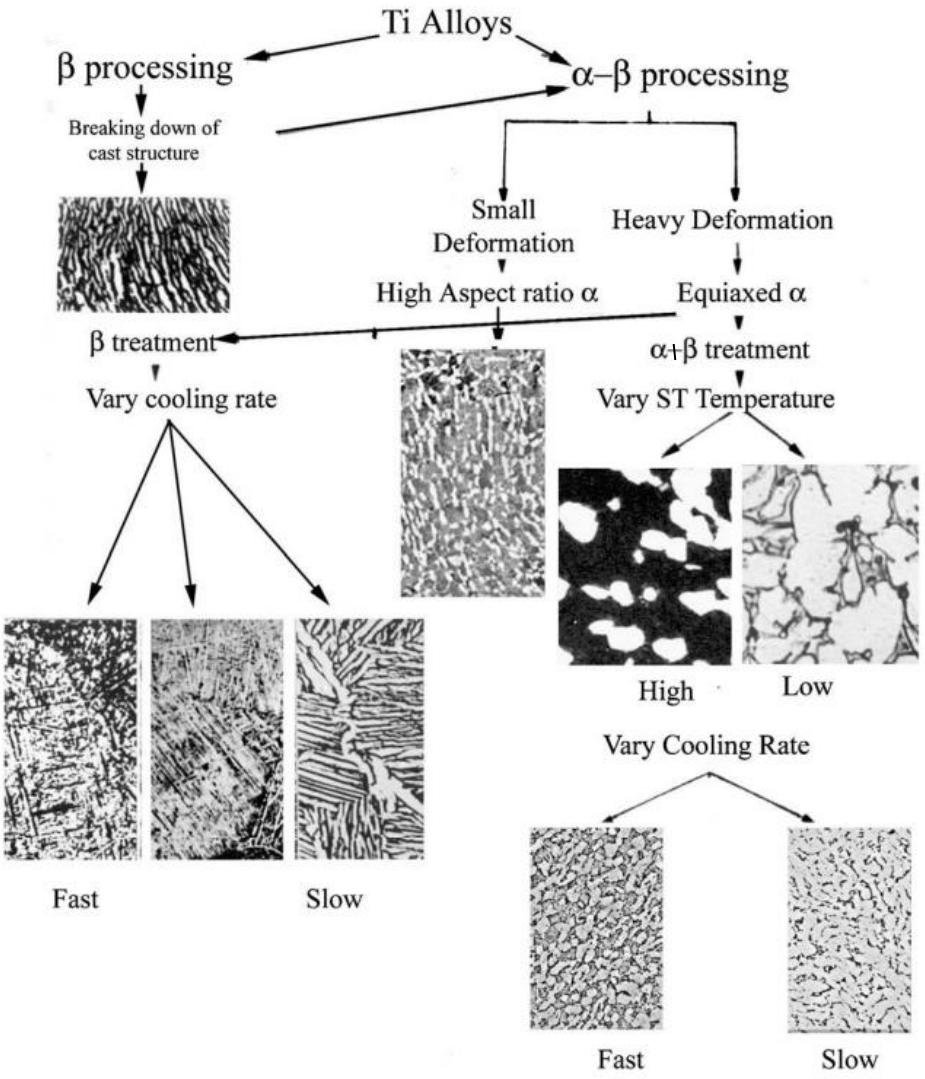

Figure 2.3. Influence of thermomechanical processing on the formation of different microstructures in α+β titanium alloys (Geeth et al., 2009).

In Ti-6Al-4V, the microstructure varies depending on the cooling rate from β, which changes the mechanical properties (Leyens and Peters, 2003). Coarser α lamellae form during slow cooling due to the gradual transformation from the β, while rapid quenching results in finer acicular (needle-like) α. When cooled rapidly from above the martensite start temperature (M_s) through the α+β field, β undergoes a martensitic transformation, forming α'-martensite, a fine, hard microstructure. At lower temperatures, the β volume fraction decreases and any remaining β does not transform to martensite once the martensitic finish temperature (M_f) is reached.

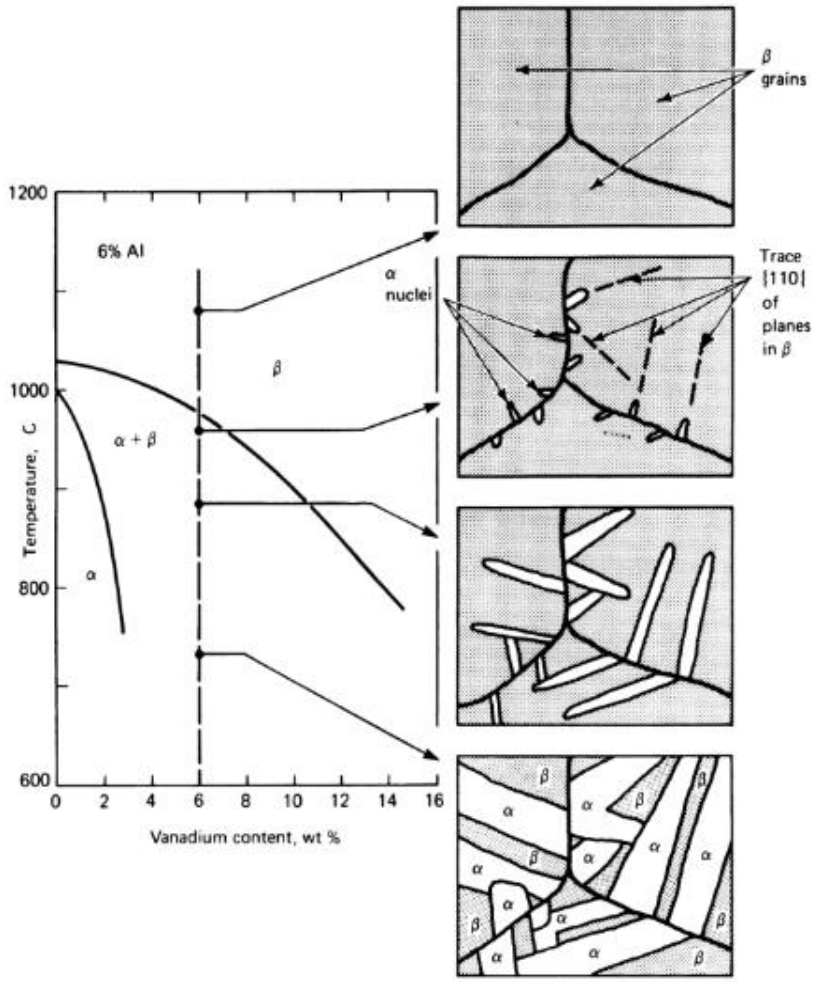

Figure 2.4. Development of a Widmanstätten microstructure in α+β Ti-6Al-4V alloy (Donachie, 2000).

In the annealed condition, Ti-6Al-4V approaches a near-equilibrium microstructure, which consists of 5–10 vol.% retained β within a primary α matrix at room temperature (Leyens and Peters, 2003). The exact phase distribution depends on the annealing temperature and cooling rate: slower cooling promotes a coarser α morphology, whereas faster cooling produces finer α grains (Poondla et al., 2009; Luan et al., 2017). In contrast, as-cast Ti-6Al-4V contains only 2–7 vol.% β, with a coarse lamellar microstructure of α and retained β (Luen et al., 2014). Key microstructural features, such as prior β grain size, β phase volume fraction and α colony size, affect the mechanical properties, including strength, ductility and fatigue resistance (Leyens and Peter, 2003). Grain boundaries can act as barriers to dislocation motion, thereby increasing strength, but they may also be sites for crack initiation, potentially reducing fatigue resistance.

Different applications of Ti-6Al-4V (and other titanium alloys) require specific mechanical properties, which are achieved by tailoring the microstructures by post-manufacturing heat treatments. These treatments modify the microstructure by controlling the transformation of β phase, which directly affects the mechanical performance of the alloys (Welsch et al., 1993; Lütjering et al., 2000). For example, a fine equiaxed microstructure is ideal for high cyclic loads, making it well-suited for biomedical implants such as joint replacements and dental devices. **Table 2.2** summarises the heat treatment processes used to optimise these properties.

Table 2.2. Heat treatments for α+β titanium alloys (Donachie, 2000).

Heat treatment designation	**Heat treatment cycle**	**Microstructure**
Duplex anneal	Solution treatment at 50–75°C (90–135°F) below T_β(a), air cool and age for 2–8 h at 540–675°C (1000–1250°F)	Primary α, with Widmanstätten α+β regions
Solution treatment and age	Solution treatment at ~40°C (70°F) below T_β, water quench and age for 2–8 h at 535–675°C (995–1250°F)	Primary α, with tempered α′ or a α+β mixture
Beta anneal	Solution treatment at ~15°C (30°F) above T_β, air cool and stabilise at 650–760°C (1200–1400°F) for 2 h	Widmanstätten α+β colony microstructure
Beta quench	Solution treatment at ~15°C (30°F) above T_β, water quench and temper at 650–760°C (1200–1400°F) for 2 hours	Tempered α′
Recrystallisation anneal	925°C (1700°F) for 4 hours, cool at 50°C/h (90°F/h) to 760°C (1400°F), air cool	Equiaxed α with β at grain boundary triple points
Mill anneal	A+β hot work plus anneal at 705°C (1300°F) for 30 min to several hours and air cool	Incompletely recrystallised α with a small volume fraction of small β particles

Heat treatments, including annealing, solution treating, ageing and beta annealing, determine the resulting microstructure and mechanical properties (Poondla et al., 2009). For example, annealing produces a microstructure consisting of α phase and Widmanstätten α+β regions (Welsch et al., 1993; Leyens and Peters, 2003). In contrast, solution treating and ageing result in a mixture of α and tempered α′ or β+α phases, improving toughness and ductility (Lütjering

et al., 2000; Poondla et al., 2009). Additionally, beta annealing yields a Widmanstätten colony microstructure, which is beneficial for applications that require strength and wear resistance (Leyens and Peters, 2003; Donachie, 2000).

Commercially pure titanium and titanium alloys, particularly Ti-6Al-4V, have been used in biomedical applications since the early 1970s due to their excellent properties (**Table 2.3**) (Veiga et al, 2012). Implants (**Figure 2.5**) are used to replace lost functions due to trauma or illness (Bose et al., 2012; Ni et al., 2019). Titanium alloys, particularly Ti-6Al-4V, were the first modern materials implemented for dental implants and are still used today (Gaviria et al., 2014). Other metals used include zirconium and gold (Searson et al., 2019), which may strengthen the implant, although they can have poor bone-to-implant contact (Searson et al., 2019). The titanium oxide layer on implant surfaces is critical to prevent corrosion (Delgado-Ruiz and Romanos, 2018).

Table 2.3. Ti-6Al-4V for biomedical applications and its properties (Balazic et al., 2007).

Alloy	**Properties**
Titanium alloy (Ti-6Al-4V) and pure titanium	Reduced elastic modulus
	Excellent biocompatibility
	High strength to weight ratio
	Enhanced corrosion resistance than conventional stainless steel and Co-Cr alloys
	Good osseointegration

The development of titanium alloys for biomedical applications aimed to improve biocompatibility and corrosion resistance, providing an alternative to other materials like 316L stainless steel and cobalt-chromium (Co-Cr) alloys. Commercially pure titanium (CP-Ti) emerged as a better option since it has no toxic elements like nickel, cobalt and chromium which are present in stainless steel and Co-Cr alloys (Bannon and Mild, 1983). However, the mechanical properties of CP-Ti, such as strength, are limited for high-load applications like hard tissue replacements (Oliveira et al., 1998). To address this, α+β titanium alloys, particularly Ti-6Al-4V, replaced CP-Ti in such applications, offering enhanced strength and

fatigue resistance (Zwicker et al., 1980). However, Ti-6Al-4V alloy contains cytotoxic elements, such as Al and V, which can pose serious health risks when released into the body (Li et al., 2014).

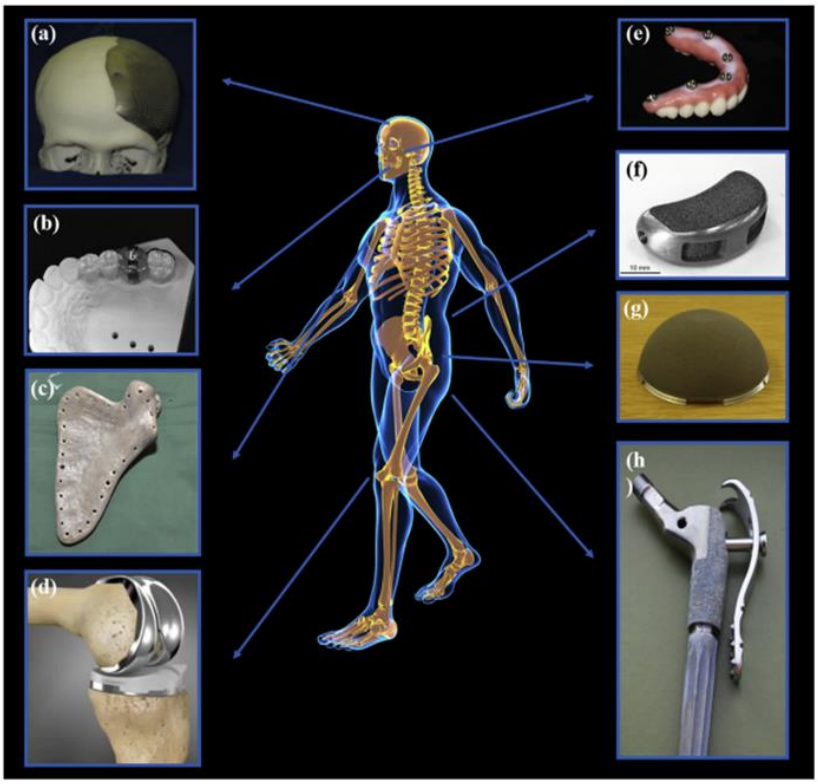

Figure 2.5. Examples of biomedical implants: (a) cranial prosthesis, (b) surgical guide, (c) scapula prosthesis, (d) knee prosthesis, (e) dental implants, (f) interbody fusion cage, (g) acetabular cup and (h) hip prosthesis (Ni et al., 2019).

2.1.2 Titanium alloy in dental applications

Tooth loss is common and can occur due to disease or trauma, consequently dental implants have a long-standing history for replacing missing teeth (Mijiritsky et al., 2013; Searson et al., 2019). Dental implants originated in ancient Egypt when carved seashells or stones were put into the human jawbone to replace missing teeth (Gaviria et al., 2014). Other reported early implants included noble metals and were created to resemble the shape or function of natural tooth roots (Lee et al., 2005). During the Middle Ages, dental implantation was done with allografts (biological materials, such as bones or tissues, obtained from human donors) and xenografts (biological materials sourced from animals, typically pigs or cows) (Gaviria et al., 2014), although Sullivan (2021) stated that this caused infections and even deaths. **Figure 2.6**

shows a dental implant (Xin et al., 2022). In 1957, Per-Ingvar Brånemark, a Swedish orthopaedic surgeon, discovered that bone can grow near titanium and adhere to it without rejection, which was a significant advance in dental implantology (Gaviria et al., 2014).

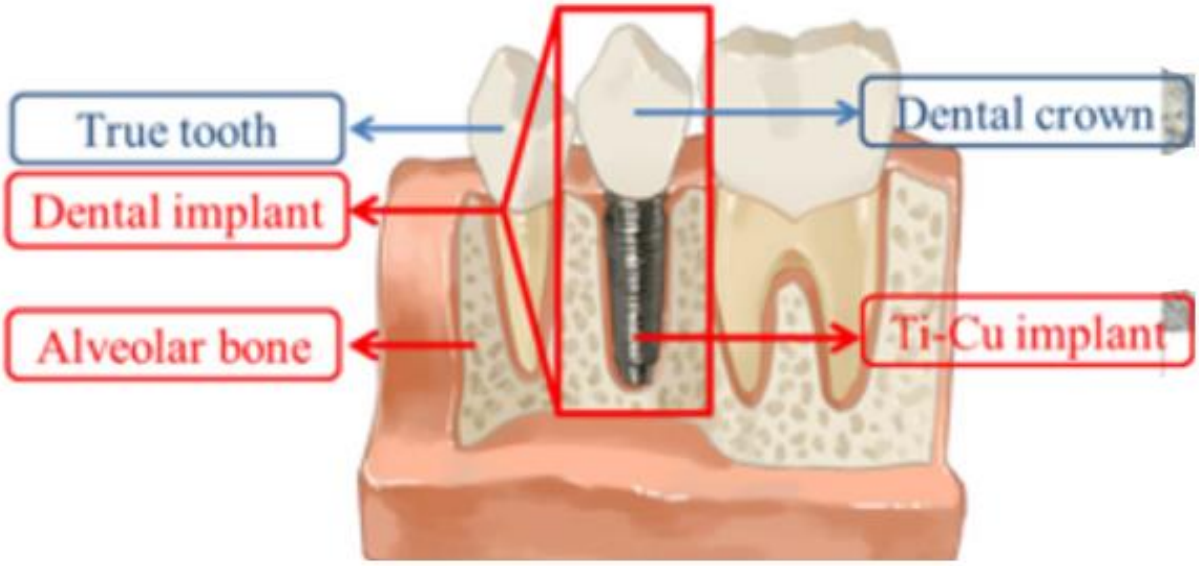

Figure 2.6. Dental implant (Xin et al., 2022).

The rising demand for dental implants, medical devices used to replace missing or damaged teeth, in South Africa is driven by increased oral health awareness and an ageing population (Insights10, 2024). This has led to growing interest in optimising implant materials for clinical success. Titanium alloys play a crucial role in advancing dental implants by providing long-term functional stability and biocompatibility (Gaviria et al., 2014). Dental implants must integrate effectively with bone tissue by osseointegration, ensuring stability and long-term viability (Anil et al., 2011). This interaction is essential to prevent clinical failure, which can occur if a fibrous soft tissue capsule forms around the implant, blocking biomechanical attachment (Heinemann et al., 2015). Upon implantation, two possible reactions may occur: the undesirable formation of a fibrous capsule, which leads to clinical failure, or successful osseointegration, where direct bone-implant contact occurs without connective tissue interference (Heinemann et al., 2015).

The surface roughness of titanium implants affects their osseointegration rate and biomechanical stability (Le Guéhennec et al., 2007). While higher surface roughness can enhance mechanical interlocking between the implant and bone, it also increases the risk of

bacterial colonisation (where oral bacteria attach, multiply and form clusters on the implant surface) (Le Guéhennec et al., 2007; Alvarez et al., 2020). This colonisation leads to biofilm formation, where bacteria create a protective layer of extracellular polymeric substances (EPS) that adhere to the surface and resist immune responses and antibacterial treatments (Zhang and Li, 2019). Biofilm formation can lead to peri-implantitis, an inflammatory condition that causes bone loss and compromises the stability of the implant (Chen et al., 2021).

High compressive and tensile strengths are essential for biomedical implants to prevent fractures and ensure long-term functional stability (Saini et al., 2015). However, increased strength results in reduced ductility (Leyens and Peters, 2003). Ductility is essential for shaping implant materials, allowing them to undergo plastic deformation without breaking during processes like forging or moulding. Saini et al. (2015) recommended a ductility of 8% for dental implants. While a lower elongation might suffice in some cases, ductility becomes less critical once the implant is shaped, with strength taking precedence to ensure durability and resistance to fracture during use. However, titanium alloys used in the medical field should have higher elongation, between 10% and 20% (Niinomi, 1998), to meet the flexibility for load-bearing implants.

In all biomaterials, including Ti alloys, fracture toughness is important as it affects the fatigue resistance of the alloy (Li et al., 2005). Fatigue resistance is critical in biomedical alloys because poor fatigue resistance can lead to mechanical failure, which can cause inflammation and other complications (Leyens and Peters, 2003). Fatigue deformation in biomedical implants can cause the fracturing of the protective oxide layer, exposing the base metal to corrosive environments (Li et al., 2005). This exposure accelerates corrosion, compromising the implant's structural integrity and causing biological reactions such as inflammation.

In clinical dentistry, there are four main types of dental implant designs (Han et al., 2009).

- Subperiosteal: the implant is positioned beneath the periosteum, the membrane covering bones and is used when bone height or density is inadequate for other implants. It consists of a metal framework on the bone beneath the gums as an attachment point for prosthetic teeth.

- Blade: this implant is flat and blade-shaped, intended for insertion directly into the jawbone, conventionally used when the bone width is narrow, offering a stable foundation for attaching prosthetic teeth.
- Ramus frame: these implants are anchored to the mandibular ramus, the posterior part of the lower jawbone. They are used when there is insufficient bone in the main body of the mandible but adequate bone in the ramus region.
- Endosseous: these implants are the predominant type in modern dentistry. Surgically inserted directly into the jawbone, they integrate with the bone by osseointegration, forming a robust foundation for artificial teeth or dental prostheses (Han et al., 2009).

The focus is on endosseous implants, which are the most widely used type in modern dentistry (Gaviria et al., 2014). They are usually screw-shaped and placed into the mandible (lower jawbone, which is the largest and strongest bone in the face and holds the lower teeth in place and is crucial for chewing, speaking and providing support to the lower face) or maxilla (the upper jawbone, which consists of two symmetrical halves that form the upper jaw and support the upper teeth).

Dental implants are designed to have mechanical stability, ensuring they are securely anchored in the jawbone upon placement, while promoting osseointegration (Javed et al., 2013). Endosseous implants have three main macro-designs: screw-shaped threads, solid body press-fit designs (such as conical or cylindrical) and designs with porous coatings (Stanford, 2008). Each configuration affects the long-term biomechanical properties at the bone-implant interface, which determines the success or failure of the implant.

When dental implants do not effectively transfer forces to the surrounding bone, this may result in bone atrophy (the gradual loss of bone density and mass due to insufficient mechanical loading) or hypertrophy (an increase in bone density and mass due to excessive stress at the bone-implant interface) (Gaviria et al., 2014). Consequently, the implant design must promote bone growth and ensure an even distribution of stress to the surrounding bone matrix, as this balance is crucial for maintaining bone health around the implant site.

The screw thread implant is the most used root implant type due to its effectiveness and strong initial retention (Kan et al., 2005). As shown in **Figure 2.7**, various thread design

characteristics, including pitch, height and shape (either square or V-shaped), affect the performance of the implant (Lee et al., 2005). While the implant shape does not affect cortical bone, which is the dense, strong outer layer of bone (Geng et al., 2004), the thread design affects trabecular bone. Trabecular bone in the jawbones is highly porous (with 75–95% porosity) and consists of a network of interconnected rods and plates, known as trabeculae, surrounding spaces that may contain bone marrow (Geng et al., 2004; Wunner et al., 2017). Chun et al. (2004) found that increasing implant length and reducing pitch length lowered maximum effective stresses, emphasising the importance of minimising bone stress to maintain implant stability.

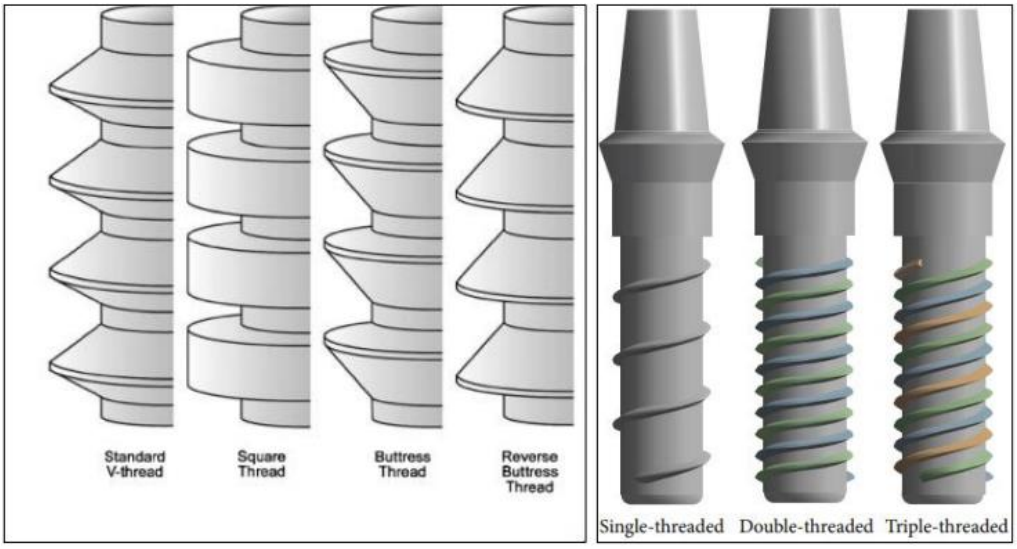

Figure 2.7. Implant thread pattern types (Moulyashree and Mahantesha, 2023).

Dental implants have many necessary properties for their success (Seth and Kalra, 2013). Biocompatibility is one of the most critical properties (Gaviria et al., 2014) and is determined by the material's physical, chemical and mechanical qualities and application. Dental implants are tested for biocompatibility by measuring the degree of osseointegration between the implant and the tissues (Searson et al., 2019). Factors that affect osseointegration are given in **Figure 2.8** (Gaviria et al., 2014).

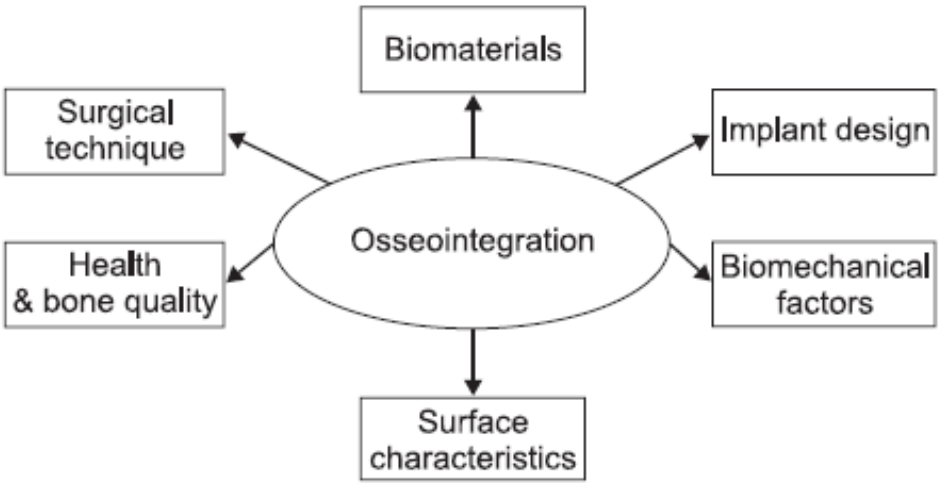

Figure 2.8. Factors that affect osseointegration (Gaviria et al., 2014).

2.1.3 Corrosion behaviour of titanium alloys

Degradation of metal implants is undesirable for two main reasons: it can weaken the implant's structural integrity and released degradation products may trigger adverse biological reactions in the host (Joshua et al., 1998). Degradation can occur due to electrochemical dissolution, wear, or a combination of both. Electrochemical processes include general corrosion, affecting the entire implant surface uniformly, or localised corrosion, which affects shielded areas (crevice corrosion) or random surface sites (pitting corrosion). Corrosion can lead to implant failure after its initial success (Olmedo et al., 2009). Electrochemical and mechanical processes, such as stress corrosion cracking, corrosion fatigue and fretting corrosion, can interact, leading to early structural failure and increased release of metal particles and ions (Joshua et al., 1998).

Titanium alloys are among the most widely used metals in direct contact with body tissues. These biomaterials are highly reactive when exposed to air or fluids, quickly forming a titanium dioxide (TiO_2) layer (Olmedo et al., 2009). This oxide layer minimises interaction between the biological environment and the metal and is important in determining the implant's biocompatibility and the body's response (Olmedo et al., 2009). The oxide layer is a protective surface between the implant and the body, which helps reduce its reactivity and partially prevents corrosion (Jacobs et al., 1998).

Nagay et al. (2022) showed that while the nanoscale amorphous TiO_2 layer on titanium implants offers passivation and is a protective barrier against corrosion under neutral

physiological pH, this barrier is vulnerable in the complex *in vivo* oral environment. Continuous exposure to acidic substances and microbial metabolites can lower the pH, potentially leading to an irreversible breakdown of the passive film. Additionally, the TiO_2 layer has limited tribological resistance and can be easily disrupted under mechanical loading (Dini et al., 2020). Mombelli et al. (2018) showed that prolonged exposure to a corrosive environment and wear from implantation can lead to the release of metallic ions and particles, potentially causing serious biological problems like peri-implant diseases or in severe cases, systemic toxicity (**Figure 2.9**) (Nagay et al., 2022).

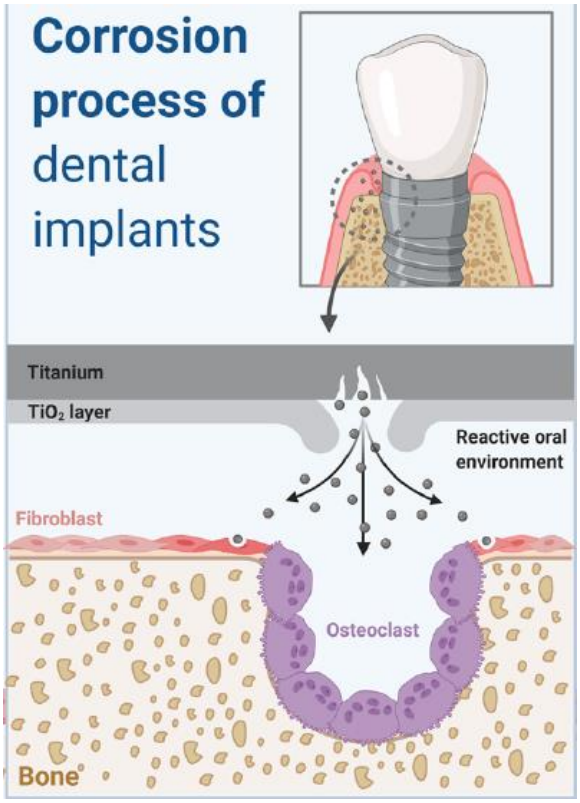

Figure 2.9. Schematic diagram of biochemical mechanisms involved in the corrosion-related interaction between titanium surface (with the oxide layer) and tissue in dental implants (Nagay et al., 2022).

First, the titanium alloy composition needs to be modified to improve the corrosion resistance of dental implants. Some alloying elements form oxides that are less stable and protective than TiO_2, which can weaken the implant's ability to resist corrosion if they are present in high amounts (Cordeiro and Barão, 2017). **Table 2.4** shows that adding an alloying element to titanium can not only alter the oxide layer but also cause phase transformations, resulting in

combinations of the two phases (α and β) such as α, α+β, or β (Nagay et al., 2022). Additionally, the alloying elements may form intermetallic phases, which are distinct chemical compounds that can influence the material's properties (Cordeiro and Barão, 2017). Nagay et al. (2022) disagree with Cordeiro and Barão (2017) on which crystalline phase is most effective for corrosion resistance. The β phase is thought to be more stable and resistant to dissolution than α (Chen and Tsai, 2011). Conversely, titanium alloys with a single α phase have been shown to exhibit better electrochemical performance than α+β and β alloys (Cordeiro and Barão, 2017).

Table 2.4. Effect of alloying elements on titanium alloys' microstructure and electrochemical properties (Nagay et al., 2022), where Rp = polarisation resistance, i_{corr} = corrosion current density, E_{corr} = corrosion potential and E_{pit} = pitting potential.

Alloying Element	**Effect on Microstructure**	**Effect on Electrochemical Parameters**
Zr	Reduces anodic activity, strengthens solid solution and forms ZrO_2 film	Increases Rp, reduces i_{corr}, corrosion rate and capacitance
Ta	Creates stable Ta_2O_5 film and β in the Ti matrix	Reduces pitting, corrosion rate, i_{corr} and improves E_{corr}
Nb	Forms β and α, incorporates Nb_2O_5 in passive film	Enhances cathodic protection, reduces i_{corr} and i_{pass} and increases E_{corr}
Cu	Ti_2Cu precipitation strengthens alloy; a more noble phase.	Increases Rp, reduces i_{corr} with higher Cu
Mn	Promotes α+β microstructure, high concentrations yield a single β phase with TiMn	Enhances cathodic reaction, limited improvement to corrosion resistance
Mg	Forms Ti and Mg phases, increasing Mg lowers E_{corr}	Lowers E_{corr}, increases i_{corr}
Co	Induces α+β structure, high concentrations form Ti_2Co	Displays corrosion behaviour similar to pure Ti
Mo	Smaller primary β dendrites and stabilises acidic oxides	Higher Rp, lower i_{corr} and i_{pass} with increased Mo.
Fe	Promotes β and finer grains	Reduces i_{corr}, increases E_{pit} and Rp

Intermetallic compounds can form localised galvanic cells with the titanium matrix due to differences in electrochemical potential (Cordeiro et al., 2019), which weakens the alloy's electrochemical stability. Thus, single-phase alloys show better electrochemical properties

(Cordeiro et al., 2019). However, for alloys with multiple phases or varying crystallographic orientations, achieving fine grains and uniform distribution of alloying elements is important for maintaining good electrochemical stability (Cordeiro et al., 2019). Fine microstructure helps to evenly surround intermetallic compounds with the matrix, adjusting the cathode/anode area ratio, which reduces galvanic effects and protects the less noble phase from corrosion (Osório et al., 2010; Zhang et al., 2016). Uniform microstructures and enhanced elemental distribution can improve corrosion resistance by stabilising and strengthening the passivation films on titanium-based alloy matrices (Zhang et al., 2016).

Ruthenium, an affordable metal among the platinum group, was added in varying minor amounts to Ti-based alloys as a ternary element for its ability to significantly enhance the corrosion resistance of Ti even in minimal concentrations (Schutz, 1996; Biesiekierski et al., 2014). Ruthenium has a history of use in dental alloys, as has palladium (Biesiekierski et al., 2014). However, Ru was preferred over Pd due to its lower cytotoxicity and concerns about Pd^{2+} which in the form of a chloride salt, has been associated with carcinogenic properties (Yamamoto et al., 1998). Ruthenium has very low solubility in (αTi) (less than 0.1 mass%), leading to the formation of a fine and uniform distribution of noble intermetallic TiRu precipitates throughout the alloy (Schutz, 1996). These precipitates or Ru-enriched surfaces from selective dissolution act as cathodic sites, lowering hydrogen overvoltage and accelerating the reduction of hydrogen ions to hydrogen gas. This cathodic modification shifts the titanium alloy's corrosion potential positively, stabilising the protective TiO_2 film and achieving full passivity (Schutz, 1996; Biesiekierski et al., 2014).

2.1.4 Microstructure, mechanical and biocompatibility of titanium implants

The Ti-6Al-4V alloy is widely used in load-bearing implants due to its high strength, which is better than commercially pure titanium (Hosseini et al., 2012). While pure titanium is highly biocompatible, it lacks sufficient strength for high-stress applications (Elias et al., 2008; Stenlund et al., 2015). This is particularly significant as implant size decreases, where the risk of fatigue fractures becomes more pronounced, making Ti-6Al-4V more suitable (Velasco-Ortega et al., 2014). Although Pure Ti and Ti-6Al-4V have been reported to effectively support bone healing, with no observable histological differences between them and bone and both

materials successfully achieve osseointegration (Palmquist et al., 2009), there are concerns for potential harmful effects of Al and V in Ti-6Al-4V, especially due to ion release from the alloy's surface. This ion release can lead to adverse tissue reactions and immune responses (Morais et al., 2007; Palmquist et al., 2009; Li et al., 2014). Additionally, these ions may inhibit hydroxyapatite formation, potentially reducing the biomechanical anchoring of Ti-6Al-4V implants than with pure titanium (Han et al., 1998; Stenport and Johansson, 2008).

Pure metals of potential alloying elements, including Zr, Ta, Nb, Al, and Mo, have been examined *in vitro* using MC3T3-E1 murine calvaria osteoblast-like cells and GM7373 bovine aortic endothelial cells (Eisenbarth et al., 2004). Zirconium, Ta and Nb showed low toxicity, while Al and Mo demonstrated slightly reduced cell proliferation than Zr, Ta and Nb for both cell types (Eisenbarth et al., 2004). *In vivo* assessments of implants made from pure Ti, Hf, Re, Nb and Ta had similar bone healing responses at 2 weeks. However, by 4 weeks, implants made from Nb, Ta and Re showed a larger bone area than Ti, suggesting that these materials promoted more bone growth. While Ti and Ta implants showed significantly higher bone-implant contact than the other metals, indicating better integration and stability with the bone (Matsuno et al., 2001).

Stenlund et al. (2015) developed a Ti-10.1Ta-1.7Nb-1.6Zr alloy to mimic the α+β Ti-6Al-4V phase proportions and microstructure using low-toxicity elements to enhance its strength and biocompatibility. Thermo-Calc was used to obtain the alloy with the best phase proprtions, selecting Ta and Nb as β-stabilisers and Zr for solution hardening. The Ti-10.1Ta-1.7Nb-1.6Zr implants demonstrated enhanced biomechanical stability over time, significantly improving removal torque measurements from 7 to 28 days than CP-Ti implants.

Histological analysis revealed that bone-to-implant contact (BIC) for Ti-10.1Ta-1.7Nb-1.6Zr implants was similar to CP-Ti at both 7 and 28 days, with no statistically significant differences, but showed more pronounced early bone mineralisation around the implants (Stenlund et al., 2015). Gene expression analysis supported these findings, indicating a faster healing response with Ti-10.1Ta-1.7Nb-1.6Zr implants. This was demonstrated by upregulated expression of bone formation markers, such as runt-related transcription factor-2 (Runx2) and osteocalcin (OC) and bone remodelling markers, including tartrate-resistant acid phosphatase (TRAP) and cathepsin K (CatK), during the early stages of healing. Additionally, the implants demonstrated reduced expression of inflammatory markers, such as interleukin-1 beta (IL-1β) and tumour

necrosis factor-alpha (TNF-α), over time, suggesting a decrease in inflammation as healing progressed.

Several titanium alloys have been developed for biomedical implant applications, such as Ti-6Al-7Nb and Ti-5Al-2.5Fe (Yang et al., 2021). However, challenges remain in achieving optimal mechanical and biological compatibility with the human body. One key problem is that Young's moduli of many titanium alloys, including Ti-6Al-7Nb (~108 GPa), and Ti-5Al-2.5Fe (~128 GPa), are significantly higher than human bone (10–40 GPa). **Table 2.5** lists some of the titanium alloys used in dental applications with their mechanical properties. While adding Al enhances these alloys' strength, it also increases Young's modulus. This mismatch in stiffness between the alloy and bone can lead to stress shielding, where the reduced mechanical load on the surrounding bone results in bone resorption and degradation over time due to disuse (Lee et al., 2002). Furthermore, the stiffness mismatch can cause uneven stress distribution in the bone. Areas subjected to excessive mechanical stress may experience damage to bone cells and tissue, whereas areas with insufficient stress may fail to stimulate bone growth. This imbalance can inhibit bone regeneration, promote bacterial colonisation, and lead to inflammation and bone resorption (atrophy), ultimately resulting in implant loosening (Mohammed et al., 2014).

Table 2.5. Titanium alloys for dental applications and their mechanical properties (Niinomi, 2003; Li et al., 2014).

Alloy	**Process**	**Tensile strength (MPa)**	**Yield strength (MPa)**	**Elongation (%)**	**Vickers hardness (HV)**
Ti–20Cr–0.2Si	Casting	874	669	6	318
Ti–25Pd–5Cr	Casting	880	659	5	261
Ti–13Cu–4.5Ni	Casting	703	–	2.1	–
Ti–6Al–4V	Casting	976	847	5.1	–
Ti–6Al–4V	Superplastic forming	954	729	10	346
Ti–6Al–7Nb	Casting	933	817	7.1	
Ti–Ni	Casting	470		8	190

Several researchers studied alternative alloy compositions to address the stiffness mismatch between titanium implants and human bone. Wang et al. (2018) studied the mechanical

properties of Ti-Mo alloys, finding that Mo additions stabilised β, resulting in a predominantly β microstructure. However, the Young's modulus (83-104 GPa) was higher than for human bone. Qi et al. (2021) investigated the effect of Fe on Ti–6Zr-*x*Fe (*x* = 4, 5, 6, 7 mass%) alloys, showing that Fe improved β stability, with the alloy's tensile strength (748-994 MPa) and Young's modulus (90-94 GPa) increasing with Fe content. Meng et al. (2018) examined the effect of thermo-mechanical treatment on Ti-36Nb-5Zr, finding that tensile strength increased with increased nano-scale α precipitation, while the Young's modulus (60 GPa) remained higher than for bone.

The Ti-Nb-Zr-Sn alloy gained attention for its excellent mechanical properties and biocompatibility (Yang et al., 2021). Hao et al. (2006) developed the Ti-24Nb-4Zr-8Sn (Ti2448) alloy, which has a low Young's modulus of 42 GPa and a high tensile strength of over 850 MPa. In this quaternary alloy, Nb and Ti mix well to form stable β, while Zr and Sn also stabilise the β and prevent the formation of brittle martensite and ω (Niinomi, 1998; Li et al., 2014). Thus, niobium is a key element that stabilizes the β in Ti alloys (Niinomi, 1998; Yang et al., 2021).

Yan et al. (2021) investigated the effects of Nb content (*x* = 16, 20, 24, 28, 36 mass%) on the microstructure, phase composition and mechanical properties of Ti-4Zr–8Sn-*x*Nb alloys. Increasing the Nb content enhanced β stability, so alloys with 16-24 mass% Nb had dual-phase microstructures (α''+ β) and alloys with 28-36 mass% Nb were single-phase β. The β is beneficial to lower Young's modulus, making it more compatible with human bone. Additionally, increased Nb reduces β grain size, resulting in finer and more uniform grains in solution-treated samples, which enhanced mechanical properties by minimising inhomogeneities. At 20–24 mass% Nb, there was a stress-induced martensitic transformation from the β to α'' phase under load, contributing to two yield points in the stress-strain curves. The Ti-24Nb-4Zr-8Sn alloy, with α'' (a metastable orthorhombic structure) and β phases, had the lowest Young's modulus, closely matching that of human bone and potentially reducing stress shielding in implants. However, as the Nb content increased, the β stabilised and prevented the martensitic transformation, gradually increasing Young's modulus above 24 mass% Nb.

Microstructural parameters that are important for the mechanical properties of titanium alloys include the β grain size, α colony size, α lamella thickness and interlamellar β morphology (Filip et al., 2003; Sieniawski et al., 2013) as shown in **Figure 2.10** (Sieniawski et

al., 2013). As the cooling rate increases, the microstructure becomes finer, reducing the α colony size and the thickness of the α lamellae (Sieniawski et al., 2013). Additionally, new colonies may nucleate along β boundaries and also along the boundaries of other colonies, growing perpendicular to the existing lamellae. This gives a distinctive basket-weave or Widmanstätten microstructure (**Figure 2.11) (**Lütjering and Williams, 2007). The colony size of α lamellae with the same crystallographic orientation in α+β Ti alloys is important for the alloy's mechanical properties, as it is the effective slip length (**Table 2.6**) (Ziaja et al., 2001; Gupta et al., 2018). However, the interlocking and overlapping lamellae in the basket-weave microstructure obscure individual colony boundaries, making the measurement of colony size difficult (Sieniawski et al., 2013).

At high temperatures, (βTi) grains in titanium alloys become larger (Sieniawski et al., 2013). When these alloys are slowly cooled from the β region into the α+β region, the α initially forms at β grain boundaries, creating a continuous layer of α along these boundaries (Lütjering et al., 2000). With slower cooling rates, atomic diffusion occurs over long-range distances, resulting in colonies of parallel α plates separated by retained β plates (Tong et al., 2017). The α plates within each colony are aligned crystallographically with parallel crystal orientations, forming a characteristic lamellar structure of alternating α and β plates (Lütjering et al., 2000). **Figure 2.12** shows the microstructure of Ti-6Al-4V below the β transus, where α nucleated at β grain boundaries and extended as lamellae into β grains (Leyens and Peters, 2003). Above the transus, only β is present.

Table 2.6. Mechanical properties of the Ti-6Al-2Mo-2Cr alloy (Sieniawski et al., 2013).

Average thickness of α-phase lamellae (μm)	**YS (MPa)**	**UTS (MPa)**	**σ_f (MPa)**	**Hardness (HV)**
1.7	980	1136	550	340
2	944	1108	575	338
3.6	924	1055	560	336
6.2	922	1024	540	332

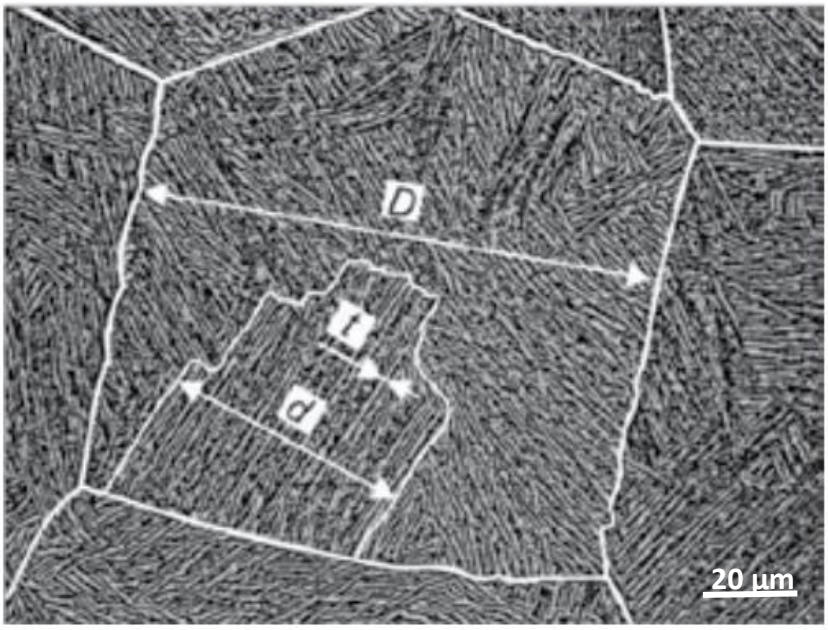

Figure 2.10. SEM-BSE image showing parameters of the lamellar microstructure that was analysed using stereological methods: D = primary β grain size, d = size of the colony of parallel α lamellae, t = thickness of α lamellae (Sieniawski et al., 2013).

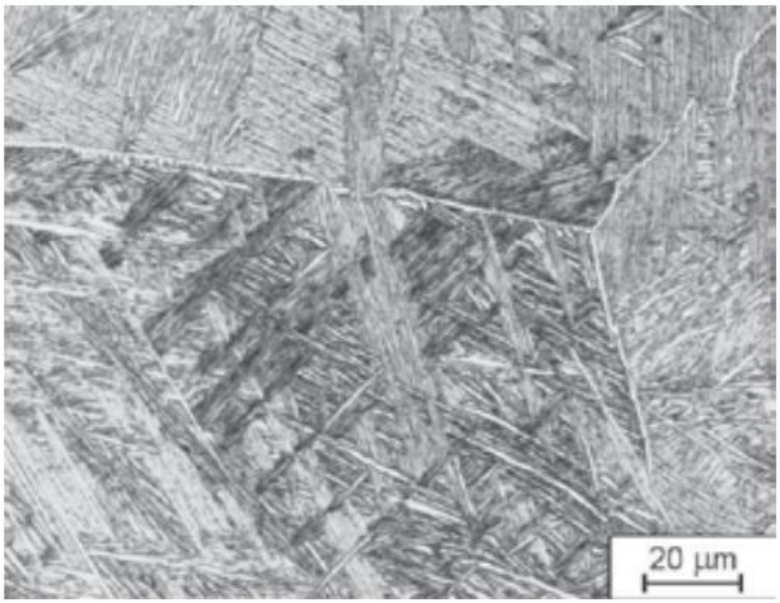

Figure 2.11. SEM-BSE image showing Widmanstätten microstructure of Ti-6Al-4V alloy cooled from the β-phase field at 9°C/s (Sieniawski et al., 2013).

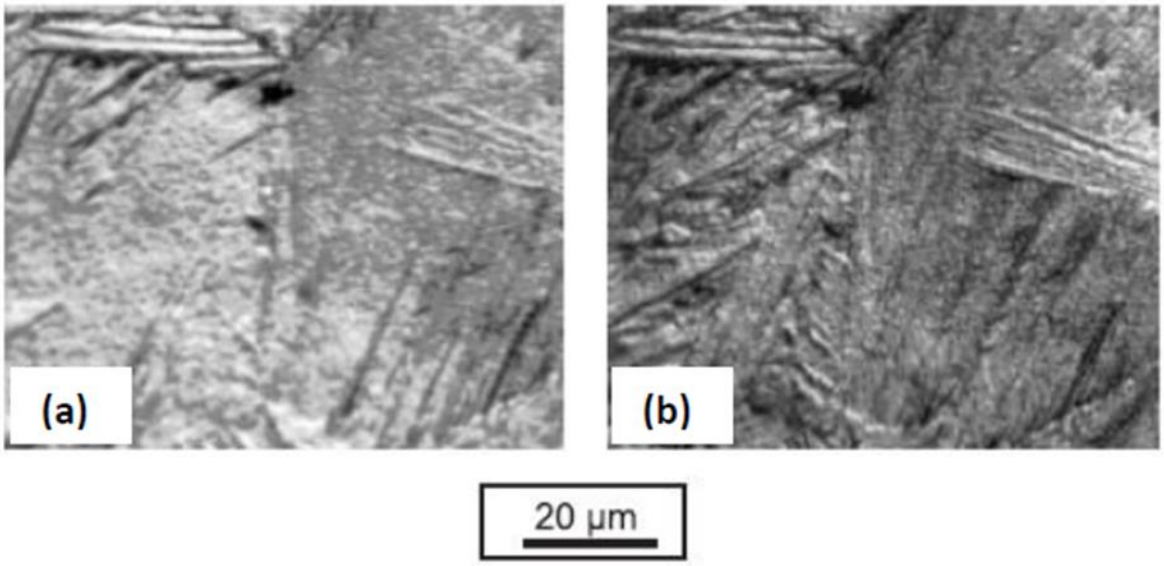

Figure 2.12. SEM-BSE images of Ti-6Al-4V cooled from the β phase field: (a) α growing as lamellae into β grains and (b) colonies of lamellae oriented at different angles (Leyens and Peters, 2003).

2.1.5 Titanium alloys with copper in biomedical applications

Metal ions such as Zn^{+}, Ag^{+} and Cu^{2+} have a wide range of antimicrobial properties and have been used as antibacterial treatments (Grass et al., 2011; Zhang et al., 2014). Copper is preferred in biomedical implants because it has low toxicity and good cytocompatibility (Jin et al., 2015) as well as enhanced antimicrobial properties, improved mechanical performance, better corrosion resistance and maintained biocompatibility (Zhang et al., 2016a).

Titanium-based alloys with copper are excellent biomaterials for biomedical implants due to their biocompatibility, with Cu enhancing mechanical properties such as elongation, modulus, and hardness (Liu et al., 2014a). The main cause of biomedical implant failure is bacterial infection, which can occur after surgical implantation or during the early stages of recovery (Liu et al., 2014b; Seebach and Kubatzky, 2019). These infections interfere with the healing process and may lead to implant failure, as they are difficult to treat due to biofilm formation, antibiotic resistance and the limited immune response at the implant site (Liu et al., 2014b; Seebach and Kubatzky, 2019).

Zhang et al. (2011) found that Ti_2Cu is responsible for anti-bacterial properties. Zhang et al. (2013) added copper to titanium alloys for its antibacterial properties, effectively reducing bacterial activity and lowering infection risks. Zhang et al. (2013) showed that titanium alloys

with 10 mass% copper achieved high antibacterial rates (>99%). They used high purity titanium powder (99.99 mass%) and 10 mass% copper powder (99.99 mass% purity) ball milled for 3–6 h and hot pressure sintered into samples. The resulting alloy had the intermetallic Ti_2Cu phase, and X-ray diffraction showed both (αTi) and Ti_2Cu phases in the alloy (**Figure 2.13**). Zhang et al. (2016a) advised that a minimum of 3 mass% Cu was needed for a good antibacterial rate.

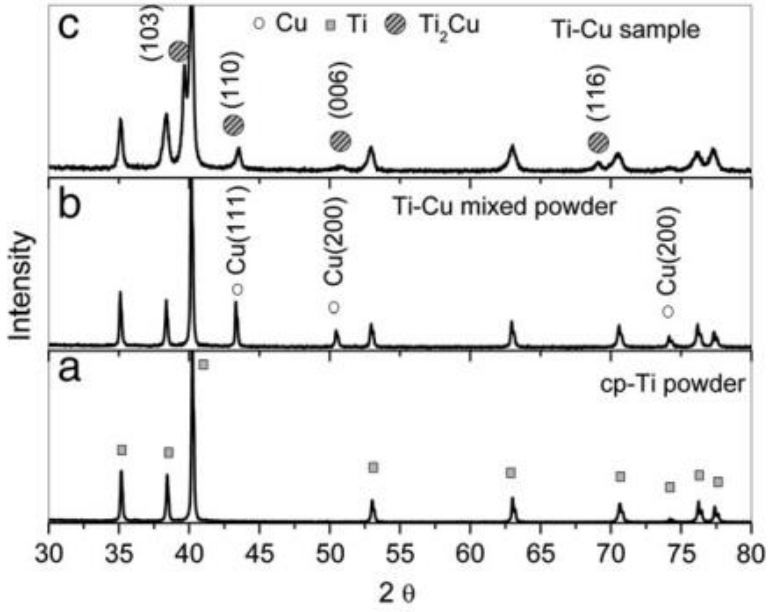

Figure 2.13. XRD patterns of: (a) Ti powder, (b) Ti–Cu mixed powder and (c) Ti–Cu sample (Zhang et al., 2013).

The Ti_2Cu phase is beneficial for antibacterial performance and enhances biocompatibility, mechanical strength although it can reduce ductility (Kikuchi et al., 2003; Lui et al., 2014; Zhang et al., 2016b). Zhang et al. (2015) demonstrated that the antibacterial rate of Ti-Cu alloys was affected by Cu content, and at least 5 mass% Cu gave a high antibacterial rate (>99%). This was attributed to the release of copper ions from the alloy surface, which disrupts bacterial cells by attacking bacteria's cell walls and membranes, producing cytoplasm leakage and nucleus oxidation (Ookubo et al., 1998) as shown in **Figure 2.14** (Liu et al., 2016). However, excess copper intake causes stomach upsets, nausea and diarrhoea and can lead to tissue injury and disease (Liu et al., 2014a). Copper is a heavy metal, so moderate amounts are recommended, less or equal to 5 mass% Cu, because in excess, it could be toxic in the long term (Rathbone et al., 2011; Dzogbewu and du Preez, 2021).

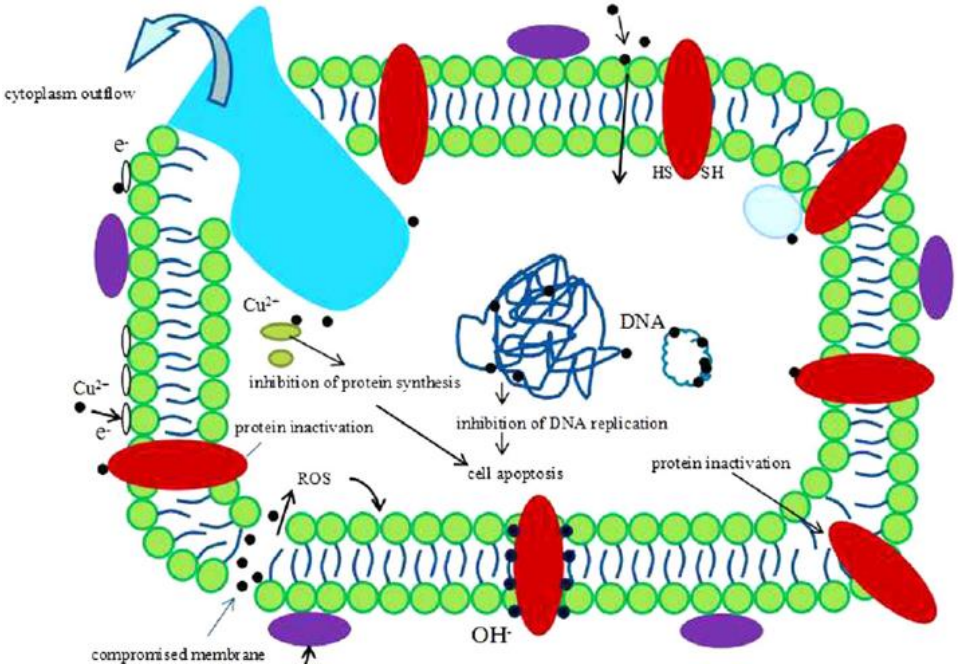

Figure 2.14. Schematic diagram of potential antibacterial activity of Cu^{2+} from Ti-Cu alloy (Liu et al., 2016).

Liu et al. (2018) demonstrated that Ti-5 mass% Cu had strong antibacterial and anti-biofilm properties against oral bacteria, such as *Porphyromonas gingivalis* and *Streptococcus mutans* (**Figure 2.15**). After 24 hours, the Ti-Cu surface showed smaller bacterial clusters and lower population densities of *S. mutans* (**Figure 2.16(b)**) and *P. gingivalis* (**Figure 2.16(d)**) than pure titanium (Liu et al., 2016). Additionally, bacterial cells on the Ti-Cu surface displayed abnormal morphology, with signs of internal leakage, suggesting potential damage due to surface interaction.

To assess the vitality of the biofilms, DAPI (4',6-diamidino-2-phenylindole) was used as a marker for live cells (Liu et al., 2016). This cell-permeable fluorescent dye binds to double-stranded DNA, forming a stable fluorescent complex, which allows the live cells to be seen. The Ti-Cu surfaces exhibited less DAPI staining than commercially pure titanium (CP-Ti) for both *S. mutans* (**Figure 2.15(e), (f)**) and *P. gingivalis* (**Figure 2.15(g), (h)**), indicating reduced cell viability on the Ti-Cu surfaces. The Ti-5Cu (mass%) alloy demonstrated effective and long-lasting bactericidal activity against *S. mutans* and *P. gingivalis*, which is crucial in decreasing biofilm development, inflammatory response and bone defects. The alloy reduced bacterial adherence and biofilm development, was biocompatible and released little Cu^{2+}, significantly less than the minimum daily intake of Cu (WHO, 1982; Liu et al., 2016).

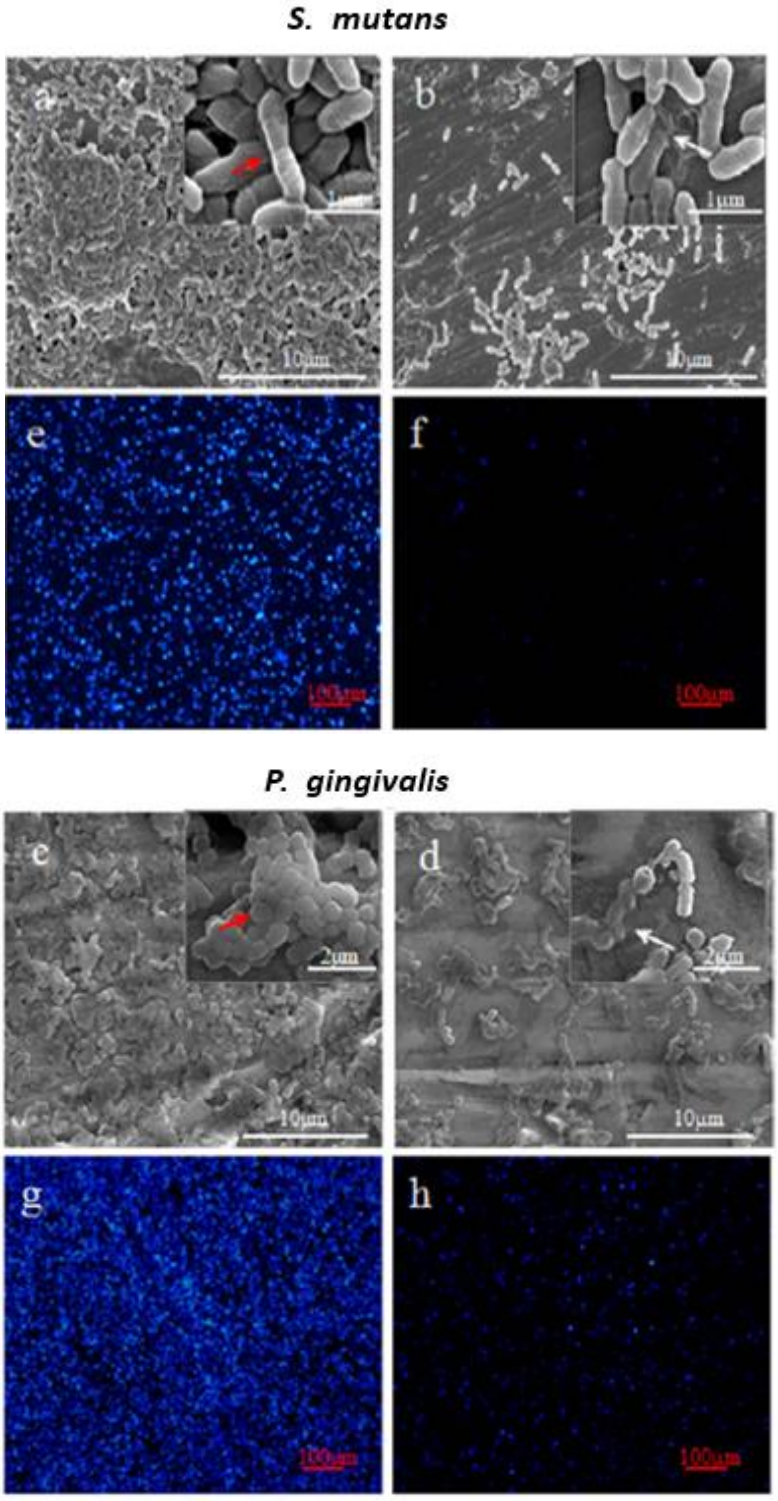

Figure 2.15. SEM-SE micrographs (a, b, c, d) and DAPI images (e, f, g, h) of *S. mutans* and *P. gingivalis* on Ti and Ti-5Cu alloy surface after 24-hour co-culture showing damaged cells (white arrows) on the Ti-Cu alloy, while cells on the Ti surface had normal morphology (red arrows) (Liu et al., 2016).

Ren et al. (2014) studied the corrosion and cell viability of as-cast Ti-6Al-4V-*x*Cu (where *x* = 1 - 5 mass% Cu) and found that adding Cu produced alloys with antibacterial properties, showing a reduction in bacterial growth, good corrosion resistance and cytocompatibility. The antibacterial properties were attributed to the preferential release of copper ions due to galvanic corrosion between the Ti_2Cu intermetallic phase and the α+β matrix. The antibacterial properties of copper were also investigated by adding it to the commonly used α+β Ti-6Al-4V alloy (Bolzoni and Yang, 2019). They found adding Cu could lower infection rates associated with surgical implants due to the release of Cu ions. Titanium-copper alloys have good corrosion resistance due to the formation of TiO_2 on the surfaces, although they are not immune to corrosion (Hu et al., 2012; Masia et al., 2021; Dyal Ukabhai et al., 2022).

Corrosion causes the copper content to decrease, with released Cu ions into the electrolyte (Xin et al., 2022). The Ti-*x*Cu (*x* = 0.5, 1, 2, 5 and 10 mass% Cu) alloys demonstrated good mechanical, anti-corrosion and antibacterial properties (Zhang et al. 2016b). Zhang et al. (2013) and Lui et al. (2014) showed that the Ti-Cu alloys had greater corrosion resistance than CP-Ti. **Figure 2.16** shows that corrosion rates reduced as Cu content increased (Liu et al., 2014a). The Ti-Cu alloys require a minimum Cu content of 3 mass% to achieve effective antibacterial properties (Wang et al., 2019), while others suggest that at least 5 mass% is needed for optimal antibacterial properties (Liu et al., 2014a; Ma et al., 2016; Zhang et al., 2016a). Additionally, Ti-Cu alloys with at least 3-5 mass% Cu had sufficient Ti_2Cu to exhibit excellent antimicrobial properties (Zhang et al., 2013; Zhang et al., 2016a, 2016b; Wang et al., 2019). Although Ti_2Cu improved mechanical strength and antibacterial properties, it decreased ductility (Lui et al., 2014; Zhang et al., 2016b). Chang et al. (2020) found that acicular Ti_2Cu precipitates in Ti-5Al-2.5Cu formed at the grain boundaries had twice the antibacterial activity.

Spotose (2023) developed the Ti-6Ta-1.5Zr-0.2Ru-5Cu (mass%) alloy as a potential (α+β) titanium alloy for dental applications. The Ti-6Al-4V, a widely used (α+β) alloy and Ti-10.1Ta-1.7Nb-1.6Zr alloy (Stenland et al., 2025) were used as references, with aluminium and vanadium replaced by non-toxic elements to maintain phase proportions. The Ti-6Ta-1.5Zr-0.2Ru-5Cu (mass%) alloy was cast and had the targeted phases α, β and Ti_2Cu, with hardness values comparable to Ti-6Al-4V (Spotose, 2023). **Figure 2.17** shows the microstructure of Ti-

6Ta-1.5Zr-0.2Ru-5Cu (mass%), with retained βTi surrounded by fine lath-like structures (Spotose, 2023).

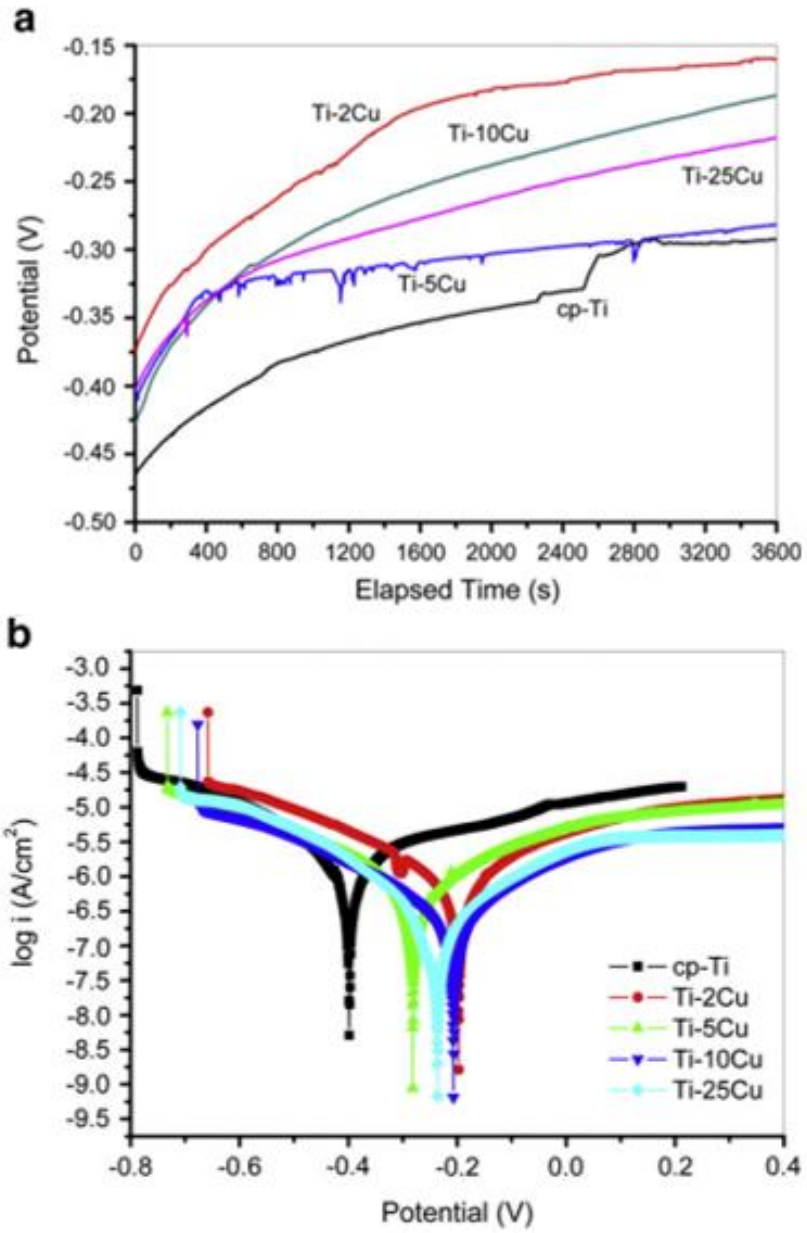

Figure 2.16. Corrosion results of Ti–Cu alloys with different Cu contents: (a) OCP and (b) Tafel curves (Liu et al., 2014a).

Spotose (2023) added Ta as a β-stabilising element to replace V (Chandrasekaran and Xia, 2005), while Zr was added as a solution-hardening element, improving both the material's strength and corrosion resistance by the formation of a protective passive film (Eisenbarth et al., 2004; Nagay et al., 2022). Ruthenium, a non-toxic metal, was also added to enhance

corrosion resistance (Allardyce and Dyson, 2001). In dental implants, corrosion resistance is important due to the presence of various electrolytes and corrosive species in the mouth. To evaluate the corrosion resistance of Ti-6Ta-1.5Zr-0.2Ru-5Cu (mass%) alloy, testing was performed in phosphate-buffered saline (PBS) solution (Spotose, 2023) and the corrosion rate was below 0.13 mm/year, which is the recommended corrosion rate for biomedical applications (Bhola et al., 2011). Furthermore, copper was added to improve the alloy's antibacterial properties, as copper promotes antimicrobial activity in titanium alloys (Liu et al., 2014b; Zhang et al., 2016a).

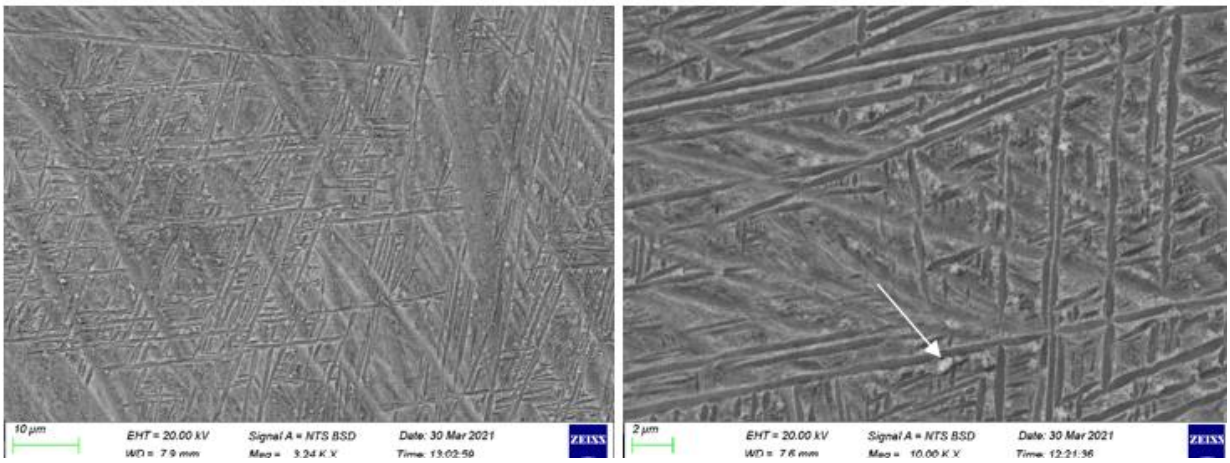

Figure 2.17. SEM-BSE images as-cast Ti-6Ta-1.5Zr-0.2Ru-5Cu (mass%) (Spotose, 2023), (a) low magnification showing (αTi) needles (dark), (βTi) matrix (medium) and (b) high magnification Ti_2Cu (white arrow).

2.2 Additive Manufacturing

2.2.1 Additive manufacturing Methods

Additive manufacturing methods are classified according to the nature and the overall condition of the feedstock and by the binding mechanism between the joined layers of material (Gebhardt, 2007). In metal AM, a powder feedstock or wire is melted by the energy input of a laser or electron beam and transformed layer by layer into a solid part of nearly any geometry (Herzog et al., 2016). The AM process is divided into two categories: powder bed fusion and directed energy deposition (DED) (**Figure 2.18**). Powder bed fusion (PBF) uses an

electron or laser beam to fuse and sinter metallic powders layer by layer in a pre-paved powder bed (**Figure 2.18(a)**). Examples include laser beam melting (LBM), electron beam melting (EBM) and laser metal deposition (LMD) (Murr et al., 2012; Sing et al., 2016). The LBM process is also known as selective laser melting (SLM) (Herzog et al., 2016) or laser powder bed Fusion (LPBF) (Yadroitsev et al., 2021). In DED, a high-energy beam, such as a laser or electric arc, is directed coaxially with metallic powder or wire to melt layers on a substrate, building them layer by layer. Examples include laser-engineered net shaping (LENS) and wire arc additive manufacturing (WAAM) (Saboor et al., 2017) (**Figure 2.18(b)**). The main parameters between PBF and DED are summarised in **Table 2.7** (Liu et al., 2022).

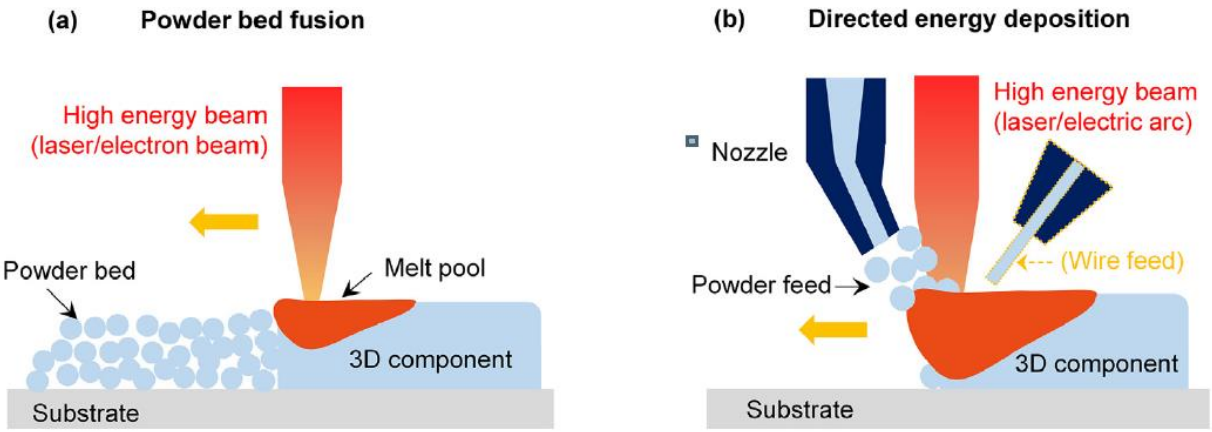

Figure 2.18. Schematic diagrams for additive manufacturing: (a) powder bed fusion (PBF) and (b) directed energy deposition (DED) (Liu et al., 2022).

Printing of AM Ti-6Al-4V, particularly by EBM and LMD, achieved over 99% theoretical density with optimal processing parameters (Yan and Yu, 2015). This high density was achieved by solidification from liquid, rather than conventional sintering, as shown in the time-temperature-transformation (TTT) diagram in **Figure 2.19.** The diagram shows how cooling rates and oxygen levels affect phase formation, which is essential for understanding the phases formed during manufacturing and tailoring the microstructural properties of AM Ti-6Al-4V components (Malinov et al., 2000).

Table 2.7. Parameters of fusion-based additive manufacturing techniques (Liu et al., 2022).

AM	**Powder bed fusion**		**Directed energy deposition**	
Techniques	**SLS**	**EBM**	**LENS**	**WAAM**
Parameters	Laser power, scan speed, Hatch spacing and layer thickness	Electron beam power, scan speed, Hatch spacing, layer thickness and pre-heat temperature	Laser power, power feed rate, scan speed, hatch spacing and layer thickness.	Wire diameter, Wire feed rate, travel speed and arc power.
Output power (W)	100 - 600	500 - 3000	1000 - 3000	1000 - 5000
Beam spot size (mm)	0.04 - 0.5	0.4 - 1	1 - 3	1 - 10
Characteristics size of the melt pool width.	~0.1	~0.1	~0.1	~1
Temperature gradient (K/mm)	10^3 - 10^4	10^2 - 10^3	10^2 - 10^4	10 - 200
Cooling rates (k/s)	10^5 - 10^7	10^3 - 10^5	10^3 -10^4	10^2 - 10^3
Main feature	High precision and broad applicability	Vacuum chambers help reduce residual stress	Multi-material printing enables the fabrication of large components	High deposition rates allow fabrication of large components

The microstructure of Ti-6Al-4V produced by electron beam melting (EBM) consisted of coplanar α and β phases with colony and basketweave morphologies within columnar prior β grains (Al-Bermani et al., 2010; Kok et al., 2015). The α' martensite, which enhanced strength and hardness, was also present (**Figure 2.20**) (Al-Bermani et al., 2010; Kok et al., 2015). Controlled microstructure, process optimisation and controlled cooling rates in EBM ensure uniformity throughout the built component, resulting in consistent mechanical properties. In contrast, laser metal deposition (LMD) produces α+β or α martensite needles within β grains (**Figure 2.16**), but the sizes are non-uniform and vary along the build direction due to higher cooling rate gradients than EBM (Liu and Shin, 2019). As a result, LMD-fabricated Ti-6Al-4V exhibited significantly higher strength due to its finer microstructure (Thomas et al., 2016).

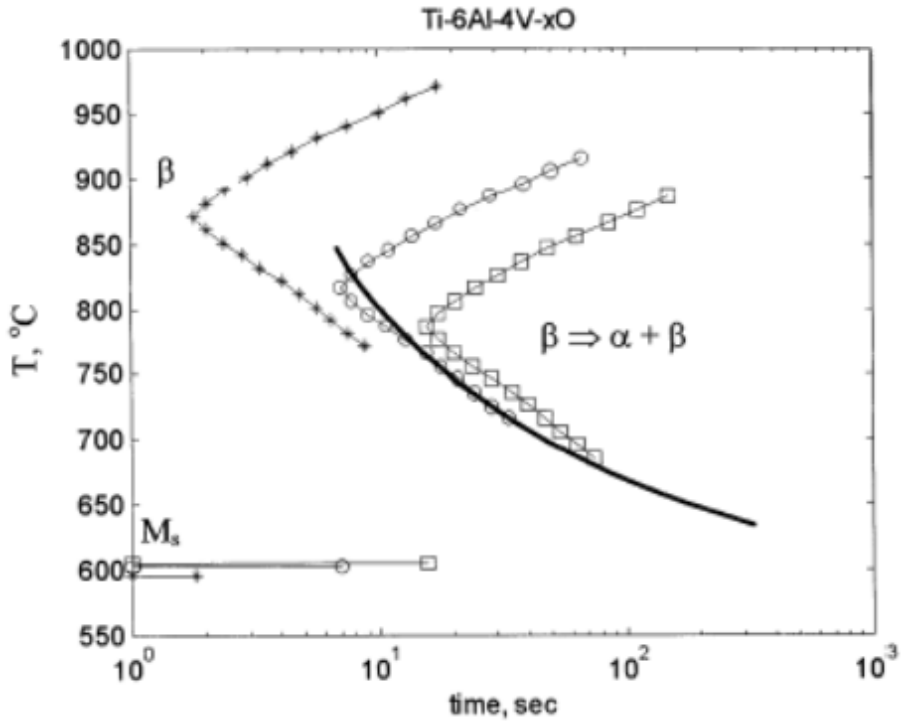

Figure 2.19. Time-temperature-transformation (T-T-T) curves for Ti-6Al-4V: open squares = 0.05 mass% O, circles = 0.1 mass% O, crosses = 0.2 mass% O, solid line from empirical data, showing oxygen content reduced M_s (Yan and Yu., 2015).

Rashid et al. (2022) studied the mechanical properties of Ti-6Al-4V made by LMD and EBM, finding that both techniques gave similar-sized columnar prior β grains (**Figure 2.20**). However, differences in cooling rates gave distinct α morphologies, which affected hardness. In the LMD sample, the bottom layers had the finest α laths, giving higher hardness due to restricted slip length and solid solution strengthening from V in (βTi). Hardness gradually decreased along the build direction as the α laths coarsened. In contrast, the EBM sample showed consistent α lath widths throughout the build, resulting in more uniform hardness. Despite comparable α lath widths in the middle and top regions, the LMD sample was slightly harder than the EBM sample, due to the faster cooling rates and residual strains associated with LMD.

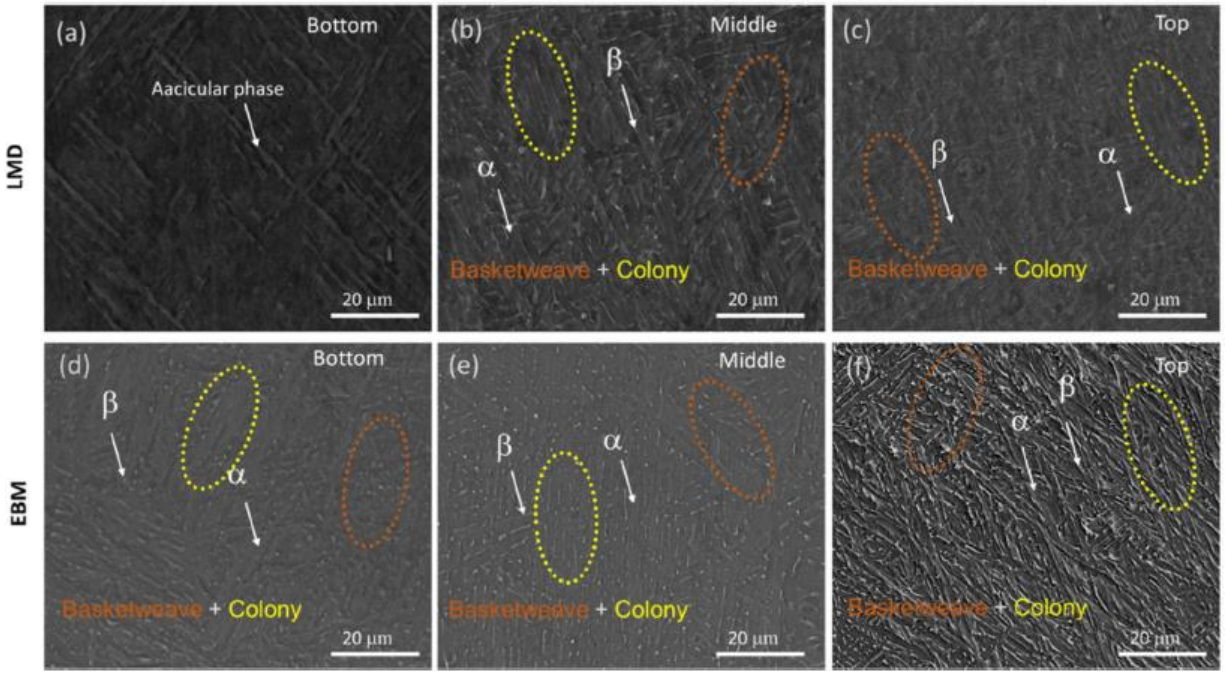

Figure 2.20. SEM-BSE images of Ti-6Al-4V fabricated using laser metal deposition (LMD) and electron beam melting (EBM) in three layers: (a-c) LMD (bottom, middle, top) and (d-f) EBM (bottom, middle, top), showing basketweave morphology (red ellipses) and colony morphology (yellow ellipses). The acicular phase shown (white arrow) in the bottom layer of the LMD sample. (Rashid et al., 2022).

The higher tensile strength of LMD samples than EBM samples was also attributed to a high dislocation density in (αTi) of the LMD samples, which can introduce barriers along slip planes and increase resistance to dislocation motion, thus enhancing strength and work hardening (Rashid et al., 2022). Conversely, EBM samples had more colony-type α+β morphology, resulting in a more gradual decrease in the hardening rate ($d\sigma/d\varepsilon$) than LMD samples. The high dislocation density in the deformed (αTi) of LMD samples led to hardening saturation, where entangled dislocations created barriers that limited further dislocation movement (Kocks and Mecking, 2003). Once saturation was reached, strain localisation occurred, leading to premature failure by shear band formation (**Figure 2.21**) (Rashid et al., 2022).

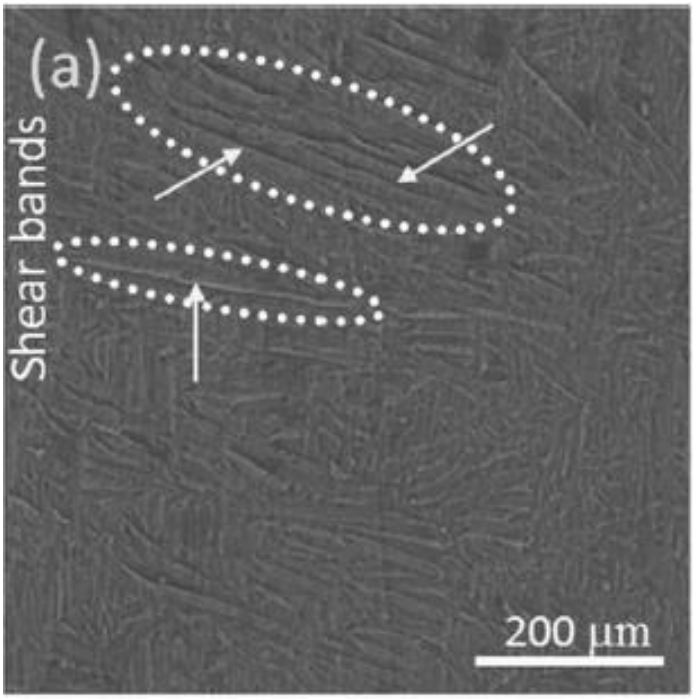

Figure 2.21. SEM-BSE micrograph of LMD showing shear band formation (Rashid et al., 2022).

To enhance the performance of Ti-6Al-4V manufactured by EBM or LMD, several strategies can be implemented. For LMD-manufactured alloys, reducing hardness gradients by controlled heat treatments is crucial, while ensuring these treatments do not compromise overall hardness (Rashid et al., 2022). Although these alloys exhibit optimal strength and hardness, improving ductility requires minimising pore volume and increasing the colony-type α+β microstructure. Conversely, EBM-manufactured alloys, are known for their homogeneous microstructures and uniform mechanical properties. To further enhance their strength, strategies aimed at enhancing strength without increasing cooling rates are preferred, as higher cooling rates lead to undesirable microstructural changes that negatively affect material performance.

Laser metal deposition (LMD) is a family of AM techniques that includes LPBF, which was first proposed in the early 1990s (Yadroitsev et al., 2021). The process was called selective laser sintering (SLS) in 2001 rather than LPBF (Ni et al., 2019). In LPBF, a high-powered laser melts metal powder layer by layer, building parts directly from a 3D model within a vacuum or inert gas to prevent oxidation (Yadroitsev et al., 2013). The LPBF process is known for producing highly detailed, complex geometries with excellent surface finish and accuracy, making it ideal for high-strength parts in aerospace, automotive and biomedical applications (Ni et al., 2019).

Its finer microstructure results in enhanced tensile strength. However, LPBF has limitations, including slower build rates, higher costs and problems with porosity and residual stresses (Ni et al., 2019). Despite these, it remains valuable for industries requiring high-performance, complex parts. Other examples of LMD are summarised in **Table 2.8** (Ni et al., 2019).

2.2.2 Feedstock preparation

The preparation of feedstock powder particles is essential for the LPBF process, as powder purity and quality determine the quality of the manufactured components. Features that are affected by the powder feedstock's quality include: (i) defects in the components, (ii) consistency between builds and (iii) reproducibility across AM machines (EPMA, 2019). Spherical powders are preferred for LPBF to improve flowability, enable uniform layer spreading and enhance loose packing density (Anderson et al., 2018; Yadroitsev et al., 2021). In LPBF, powder properties such as thermal conductivity, flowability and melting point affect process parameters like laser power and scanning speed, which in turn affect the final build quality (Yadroitsev et al., 2021).

Metallic powders are produced using various methods, one of which is atomising solid metallic feedstock (Yadroitsev et al., 2021). During atomisation, the metal is melted and passed through a nozzle, where a high-pressure fluid jet rapidly strikes the nozzle's end, breaking the metal into fine particles, as shown in **Figure 2.22** (Yadroitsev et al., 2021). The methods differ in the atomisation medium: gas, water, and plasma. Characteristics of each medium are summarised in **Table 2.9** (Anderson et al., 2018). The type of fluid used in atomisation affects the powder characteristics. Water jets cool the metal rapidly, producing less spherical particles with wider size distributions (Dawes et al., 2015; Yadroitsev et al., 2021). In contrast, inert gas jets create more uniform, spherical particles. Powders from gas or plasma atomisation are more uniform and spherical, with a narrower size distribution (Dawes et al., 2015; Yadroitsev et al., 2021).

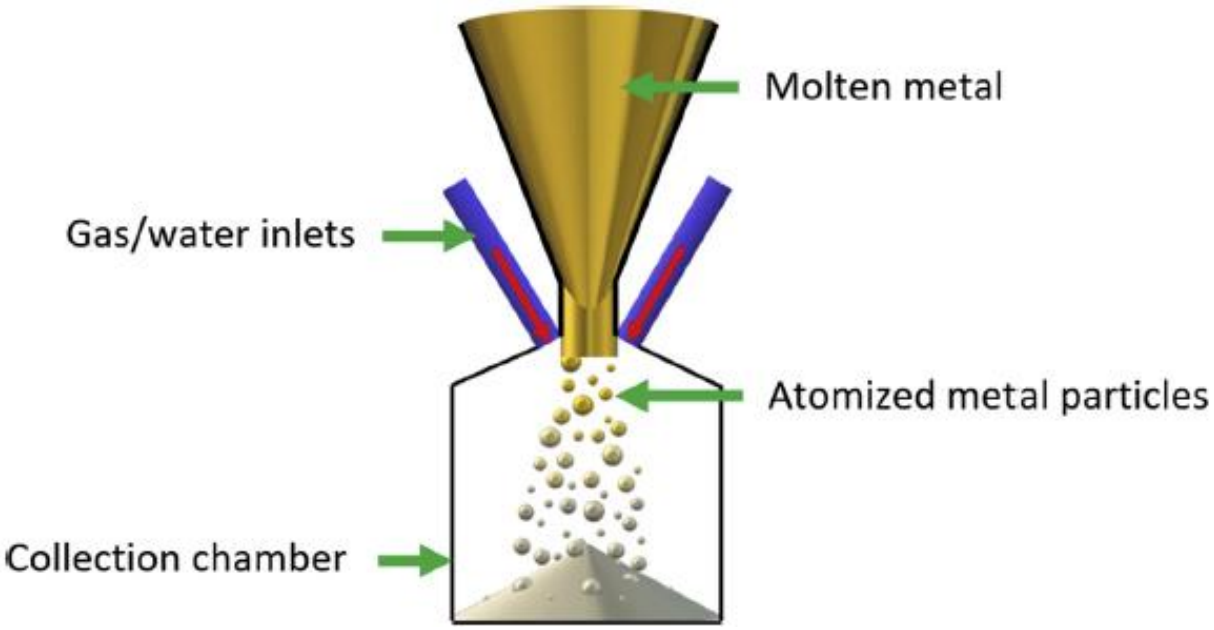

Figure 2.22. Schematic diagram showing powder atomisation (Yadroitsev et al., 2021).

Plasma atomisation involves rapidly heating the feedstock material inside the nozzle, unlike gas and water atomisation, which atomises molten metal (Dawes et al., 2015; Yadroitsev et al., 2021). Plasma atomisation offers two key advantages: feedstock material can have smaller volumes, such as wire or powder, which melts faster than larger ingots or bars and the metal spends less time at high temperatures, reducing the potential for chemical reactions with the surrounding atmosphere (Dawes et al., 2015; Yadroitsev et al., 2021).

The LPBF process requires powder to be uniformly spread across the substrate, ensuring a high packing density (Vanock et al., 2019). Particles of ~1 to ~2 µm are difficult to evenly distribute across a substrate as they easily agglomerate. Conversely, coarse powders of >60 µm, can form a thick layer and require a larger focal spot (Yadroitsev et al., 2021). This can result in decreased manufacturing accuracy and increased porosity, which impairs the mechanical properties of the final parts (Yadroitsev et al., 2021). To produce a high-quality part with maximum density and minimal porosity in LPBF, the powder particles should be fine and within 15 - 45 µm. This particle size range ensures the proper layer thickness during the process, which is crucial for achieving optimal build quality (Sutton et al., 2017). However, AMAZEMET (AMAZEMET, 2022) can atomise powder using ultrasound, and the powder may have a size range of 10 - 100 µm.

Table 2.8. Summary of Powder Bed fusion methods for biomedical applications (Ni et al., 2019).

Technique name	**Applicable metals**	**Processing parameters**	**Advantages**	**Limitations**
Selective laser sintering (SLS)	Ti alloys, Co-Cr, stainless steel, Ni-Ti	Powder laser sintering in Ar/N_2, CO_2 laser (9.2 – 10.8 µm), unidirectional/bidirectional scan	Wide material range, high material utilisation, no support structures	Porous internal structure and rough surface finish require post-processing; precision limited by particle size
Selective laser melting (SLM)	Almost all metal alloys	Laser melting, 10–45 µm powder, inert Ar/N_2, unidirectional/bidirectional scanning	Customisable part properties, low direct cost	Expensive, slow process, limited speed
Laser direct metal deposition (LDMD)	Almost all metal alloys	Nd:YAG/fibre laser (1.064 – 1.09 µm), 20 – 200 µm powder, inert Ar/N_2, various scan modes	Reduced assembly time, good mechanical properties, low roughness	Size restriction, low dimensional accuracy
Selective electron beam melting (SEBM)	Almost all metal alloys	Electron beam, vacuum chamber, He gas, 45 – 106 µm powder, spot mode	High density, high strength, fewer impurities, brittle material fabrication	Vacuum required, poor surface finish, post-processing, expensive
Laser-induced forward transfer (LIFT)	Cr, W, Au, Ni, Al	Pulse laser/layer	Small-scale production, simultaneous multiple parts	Low accuracy, small-batch production only
Atomic diffusion additive manufacturing (ADAM)	Stainless steel, Ti alloys	Metal powder wrapped in a plastic binder	High accuracy (95–99% density), low cost, high-quality surfaces, isotropic performance	Long lead times for strong parts.
Nanoparticle jetting (NPJ)	Ti alloys	Inkjet nozzle, metal nanoparticles in liquid ink	High production speed, low cost, high resolution (1 µm), excellent surface finish	Lower temperature tolerance than conventional metal 3D printing
Inkjet 3D printing (3DP)/binder jetting	Ti alloys	Fine water jet/metal powder binder	Low cost, wide material range, simple operation	Low precision

Table 2.9. Characteristics of powder atomisation medium for LPBF (Anderson et al., 2018).

Manufacturing process	**Particle size (µm)**	**Advantages**	**Disadvantages**	**Metal used**
Water atomisation	0 – 500	Converts ingots to a range of particle sizes, enabling material customisation	Post-processing required to remove water due to irregular particle morphology, such as satellites, wide particle size distribution (PSD) with low yield in 20 – 150 µm range	Non-reactive metals
Gas atomisation (Including Electrode Induction Melting Gas Atomisation (EIGA)	0 – 500	EIGA allows wide range of alloys, requires only ingot-form feedstock, high throughput with various particle sizes. Effectively processes reactive powders, produces spherical particles.	Wide PSD, satellites, low powder yield for 20 – 150 µm	Ni, Co, Fe, Ti (EIGA), Al
Plasma atomisation	0 – 200	Highly spherical particles	Requires wire or powder feedstock. High cost	Ti (Ti-6Al-4V most common)
Plasma rotating electrode process	0 – 100	High-purity and highly spherical powders	Low productivity and high cost	Ti
Centrifugal atomisation	0 – 600	Wide range of particle sizes, narrow PSD	High cost: Requires very high speed for fine powder	"Exotics", Solder pastes, zinc from alkaline batteries, Ti, steel shot

Ultrasound liquid atomisation was introduced in 1927 and Stamm (2019) reported the first use of this technique to produce metal powders in 1964 (Lierke and Griesshammer, 1967). It uses ultrasonic vibrations to create Rayleigh wave instability, resulting in the formation of small liquid droplets which cool into solid metal powder (Sun et al., 2017). Lierke and Griesshammer (1967) used vibrational frequencies up to 0.8 MHz to atomise metals with melting temperatures up to 700°C. This process can produce high-quality powders at lower costs than gas and plasma atomisation (Sun et al., 2017). The powders are more spherical than from gas atomisation as shown in **Figure 2.23**. The components of the system include an ultrasonic stack, an arc-melting system and a vacuum chamber as shown in **Figure 2.24.**

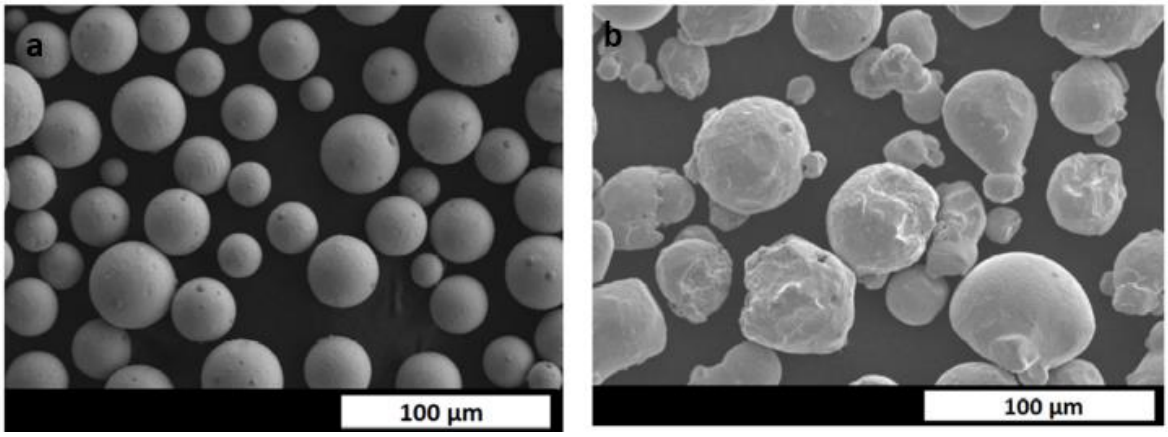

Figure 2.23. SEM-SE images of: (**a**) <50 µm particle size ultrasonically atomised powder and (**b**) gas-atomised powder (Żrodowski et al., 2021).

Ultrasound atomisation is a solid-to-liquid process that can be used to melt non-reactive or low-melting-point materials in a crucible (e.g. Sn, Zn, Mg, Pb and Al alloys), or metals can be poured into the vibrating element or melted directly into the sonotrode for highly reactive or high-melting-point materials (e.g. Fe, Ti and Pt-based alloys) (AMAZEMET, 2022). The basis of ultrasonic atomisation depends on the material's surface wettability and the amplitude of ultrasonic vibrations (Lierke and Griesshammer, 1967). As the amplitude increases, the liquid droplets become smaller. Additionally, both the frequency of the ultrasonic waves and the properties of the liquid affect the droplet size. These liquid droplets are ejected from the melt within the thin film of liquid on the sonotrode surface (AMAZEMET, 2022).

Ultrasound atomisation operates at a lower pressure (~1.1 bar) than gas atomisation (15 - 60 bar), leading to reduced costs and smaller volumes (Bałasz et al., 2023). It is also cost-effective and fast, as it produces droplets at lower speeds, making it suitable for manufacturing small to medium quantities of high-end or customised alloys (Bałasz et al., 2023). Ultrasonic atomisation reduces residual porosity in metal powders, enhancing their quality and making them suitable for high-performance applications, such as those involving titanium alloys (Tammas-Williams et al., 2017; Bałasz et al., 2023). Reducing porosity minimises the need for expensive post-processing techniques, such as hot isostatic pressing (HIP) (Bałasz et al., 2023).

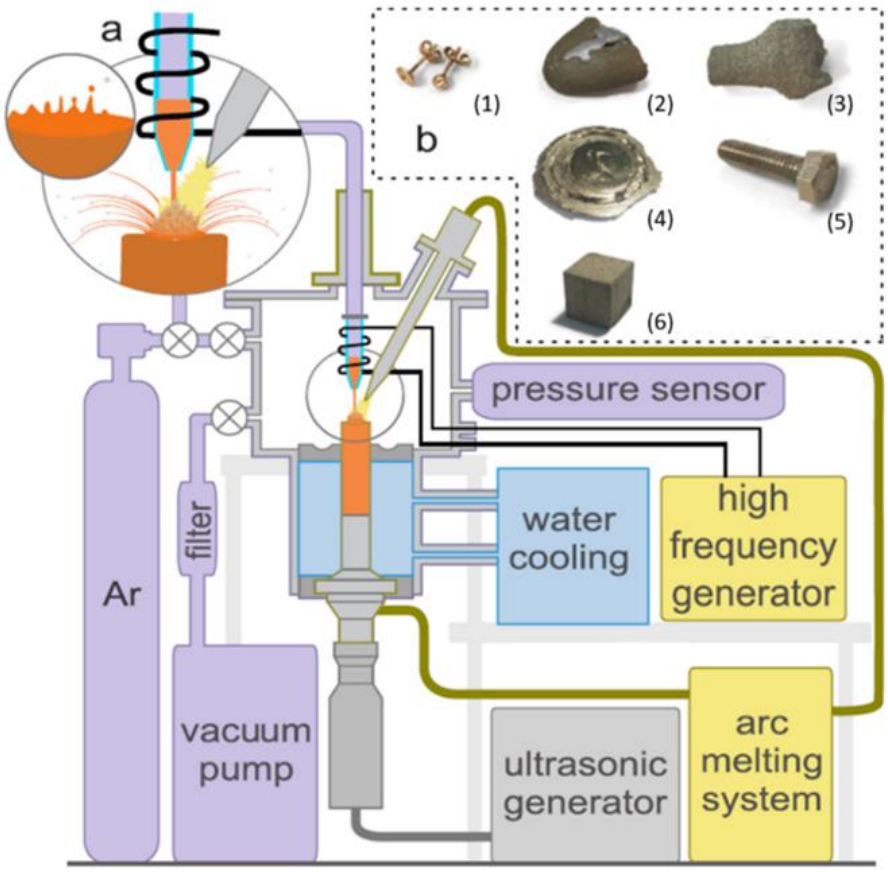

Figure 2.24. Process diagram and experimental set-up: (**a**) material feedstock and (**b**) (1) Au-based alloy earrings, (2) AMZ4 (Heraeus GmbH) Zr-based metallic glass, (3) slabs of Ni–Mn–Ga magnetocaloric alloy, (4) forged equiatomic Fe–Cr–Mn–Ni high entropy alloy, (5) AISI 304 steel as a M10 bolt, (6) Grade 2 titanium porous implant (Żrodowski et al., 2021).

Compared to gas atomisation, ultrasonic atomisation has a narrow particle size distribution which allows up to 80% of the produced powder to be used (AMAZEMET, 2022). The ultrasonic frequency used is the main factor that determines the PSD of the final powder. For LPBF, powder with an average particle size (D_{50}) of 45 – 60 µm can be produced at a frequency of 40 kHz and an electric arc or concentrated plasma is used to carry out the atomisation under inert argon gas (Żrodowski et al., 2021). The powder that is produced is collected in an airlock container which is sealed in argon to prevent contamination, as reactive metals like titanium are sensitive to oxygen and moisture, and for safe handling.

2.2.3 Laser powder bed fusion

2.2.3.1 Properties of LPBF

Laser power bed fusion (LPBF) was invented in 1986 by Carl Deckard and Joe Beaman (Beaman et al., 2020; Yadroitsev et al., 2021). High degrees of freedom provided by LPBF enable the construction of objects with distinctive geometries and intricate internal structures (Tofail et al., 2018). Also, LPBF can produce complex and customised gradient structures by integrating multiple materials into a single, fully functional part (Yadroitsev et al., 2021). These features are extremely advantageous and have encouraged the rapid development of this technology and its widespread acceptance in several industries recently (Tofail et al., 2018). Laser powder bed fusion can create parts with varying material properties (gradient structures) within a single build, tailoring areas for specific strengths or flexibility (Yadroitsev et al., 2021). It combines multiple components into one functional piece, reducing assembly and improving durability. **Figure 2.25** shows the LPBF part-making process, from CAD design to machine set-up and laser-material interaction (Yadroitsev et al., 2021).

The LPBF process may be affected by more than 130 input parameters, e.g., build environment parameters (shield gas properties), laser beam properties (mode and wavelength), materials properties (e.g., density, melting point, thermal conductivity, particle size distribution and absorption coefficient of laser radiation) (Rehme and Emmelmann, 2005). Laser power, focus spot diameter, scanning speed, powder layer thickness and atmospheric oxygen content are all variable or controlled system parameters (Rehme and Emmelmann, 2005). **Figure 2.26** shows the four main parameter categories that affect LPBF component quality (Yadroitsev et al., 2021): machine-based, material-based, process and post-treatment parameters. The LPBF machine operator must possess the skills and knowledge to perform all these activities and interactions with the LPBF system, including proper handling of powder, parameter selection and building strategies.

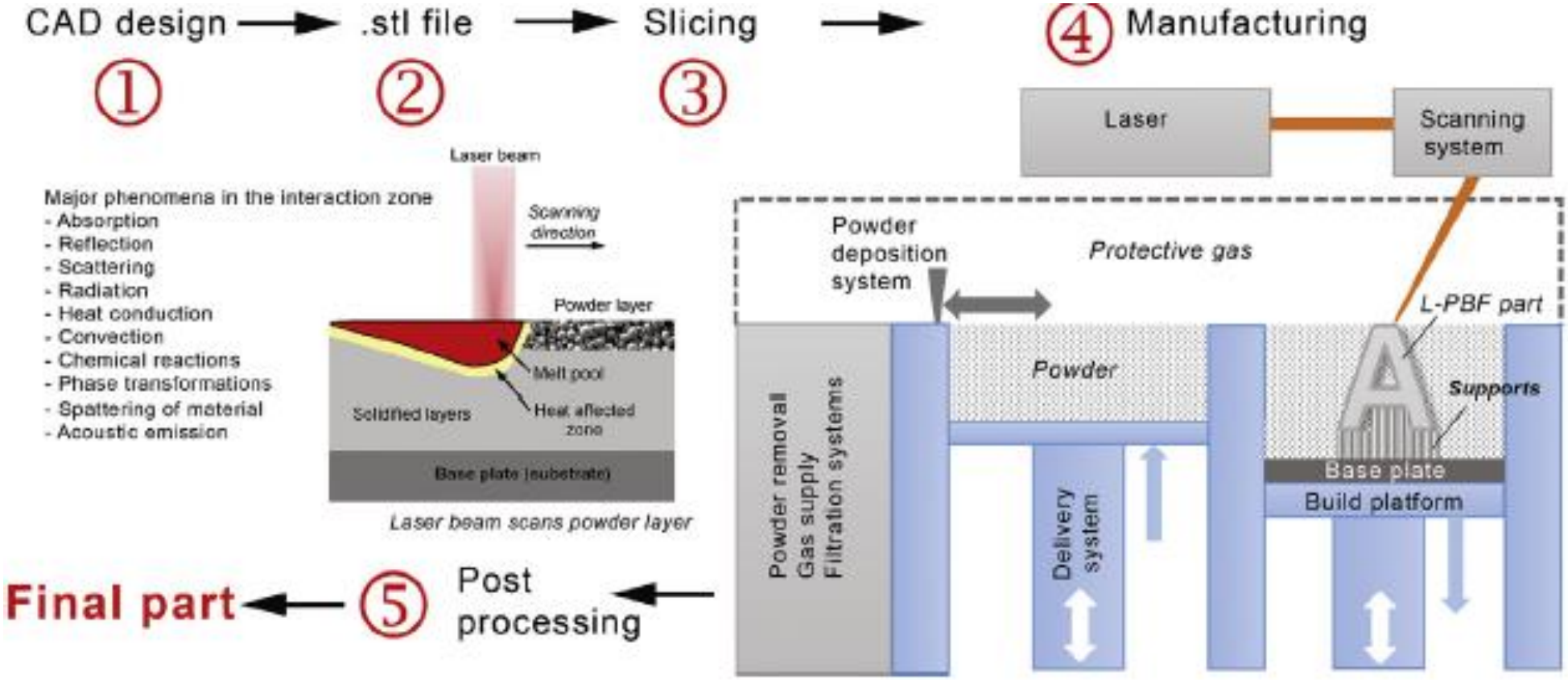

Figure 2.25. Process flow diagram for creating parts with LPBF, including designing in CAD, setting up the LPBF machine and laser-material interaction process (Yadroitsev et al., 2021).

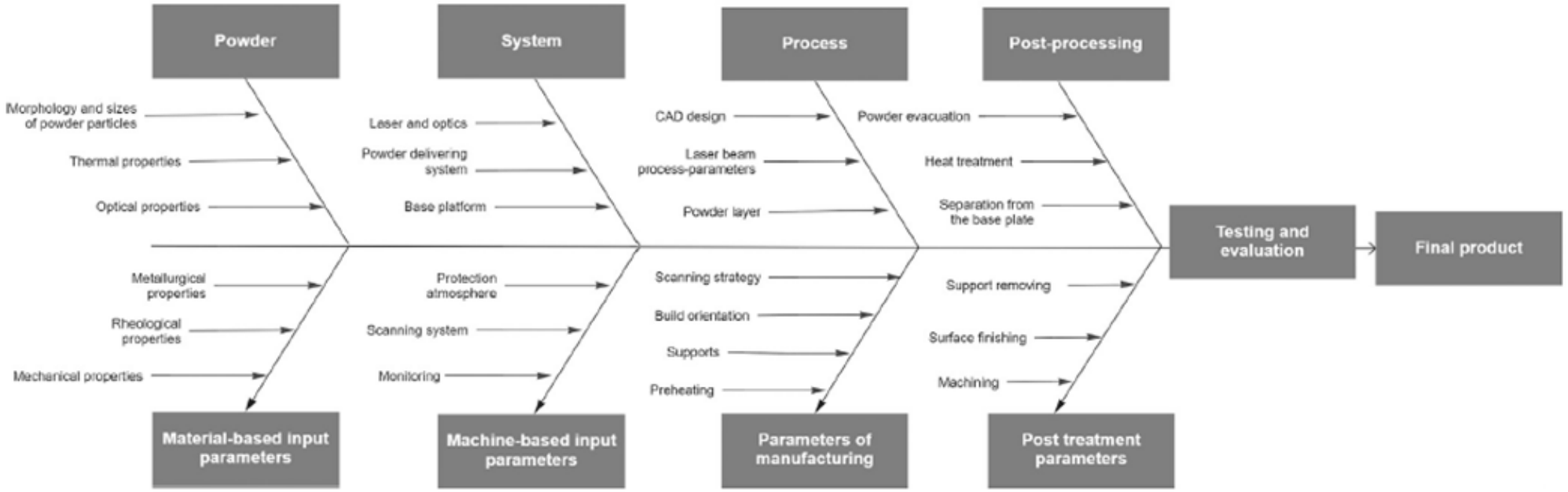

Figure 2.26. Main parameters affecting the quality of LPBF components (Yadroitsev et al., 2021).

The LPBF process offers high precision and flexibility, enabling the production of intricate parts with fine details that are difficult to achieve using conventional methods (Yadroitsev et al., 2021). This precision is achieved by controlling laser energy and powder distribution, allowing for complex geometries and fine features (Tofail et al., 2018). It also produces parts with high material density and excellent surface finish, making it ideal for aerospace, medical and automotive applications (Yadroitsev et al., 2021). Additionally, it can create fully dense parts without additional support, reducing material waste and enhancing sustainability (Rehme and Emmelmann, 2005). The LPBF process's ability to work with various materials, such as metals and composites, increases its potential for creating advanced components. Additionally, ongoing improvements in machine speed and material properties are expanding the technology's applications (Tofail et al., 2018)

2.2.3.2 Optimisation of printing parameters of LPBF

The development of guidelines for optimising parameters has allowed the production of high-quality, defect-free components with improved mechanical properties (Carrozza et al., 2021). Understanding the relationships between processing parameters, geometry and the resulting microstructure is important, as the microstructure directly affects the mechanical and physical properties, therefore affecting the performance of LPBF-manufactured parts (Yadroitsev et al., 2021; Svetlizky et al., 2022).

To understand how laser power and scan speed parameters affect the LPBF components, linear energy density (LED), which is the ratio of laser power to the deposition scan speed was used (Gonnabattula et al., 2024). The geometry of the melt pool, rate of heating and cooling and thermal dynamics (referring to the heat flow and temperature changes during the process) were all affected by linear energy density, which affected the microstructure and mechanical properties of the produced parts (Gu et al., 2012). For a given laser power and scan speed, using a finer laser spot size locally concentrated the heat source, which may have produced more energy than larger spot size lasers.

Planar Energy Density (PED, ratio of laser power to scan speed and beam diameter) provides a better knowledge of the deposition than LED (Gonnabattula et al., 2024). Planar energy density plays an important role in component design, as it directly affects the melt pool

geometry (width and depth) and stability, which are essential for producing defect-free parts. Adjusting PED allows control over melt pool shape and dimensions, ensuring strong adhesion between the printed tracks and the substrate, while preventing problems like porosity and cracking. Optimising PED is important to achieve desired component properties and ensure consistent quality throughout the build process.

In LPBF, single tracks are printed to evaluate the effect of different combinations of process parameters on the microstructures and geometrical characteristics (Gonnabattula et al., 2024). The basic structural unit of 3D LPBF objects is a single track; several single tracks combine to form a single layer, and many single layers form a three-dimensional object. This method assists in identifying the optimum process parameters that can be used subsequently to fabricate complex parts. Most of the research on process parameter optimisation uses a laser spot size of at least 1 mm. The efficiency of deposition is affected by the laser's spot size, which is critical to developing process maps for each time a different type of laser is used.

The main contributing factors to the deterioration of the surface topography along the single-track profile are the adhesion of partially melted powder particles and ripple development (Simson and Subbu, 2022) as shown in **Figure 2.27.** Ripples are small, periodic surface distortions along the laser scan path, caused by fluctuations in the laser's interaction with the powder bed or rapid thermal cycles during printing. These distortions can impair the surface finish and overall quality of the part. Simson and Subbu (2022) formed tracks successfully with continuous deposition and homogeneous track width when the LED was >0.22 J/mm. At constant LEDs of 0.25 J/mm, the number of particles stuck to the surface reduced as laser power and scanning speed increased because when scanning speed increased, the lateral border solidified quickly (Simson and Subbu, 2022). The surface topography of a single track with constant LED power and scanning speed is shown in **Figure 2.28**.

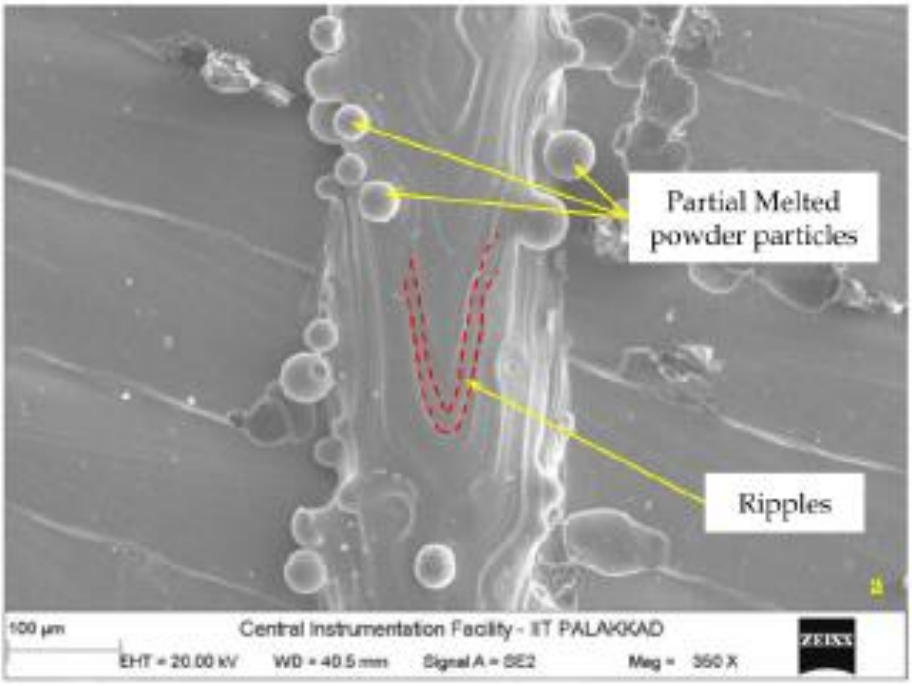

Figure 2.27. SEM-SE image of single-track showing adhered partially melted powder particles and solidification ripples (Simson and Subbu, 2022).

A laser beam, powder and substrate system involve energy absorption, reflection, radiation, heat transfer, phase changes, fluid movement from surface tension gradients and mass transfer within the molten pool and chemical reactions (Yadroitsev et al., 2013). Process parameter changes can lead to several unfavourable outcomes, including irregular sintered tracks (Niu and Chang, 1999) and balling (Tolochko et al., 2004). Manriquez-Frayre and Bourell (1991) defined balling as molten material solidifying as spherical droplets (balls) rather than forming smooth, flat surfaces. Rayleigh identified this phenomenon, also known as Plateau-Rayleigh capillary instability, as the tendency of a liquid cylinder to minimise surface area, by causing the melt pool to fragment into a series of droplets (Rayleigh, 1878; Yadroitsev et al., 2021).

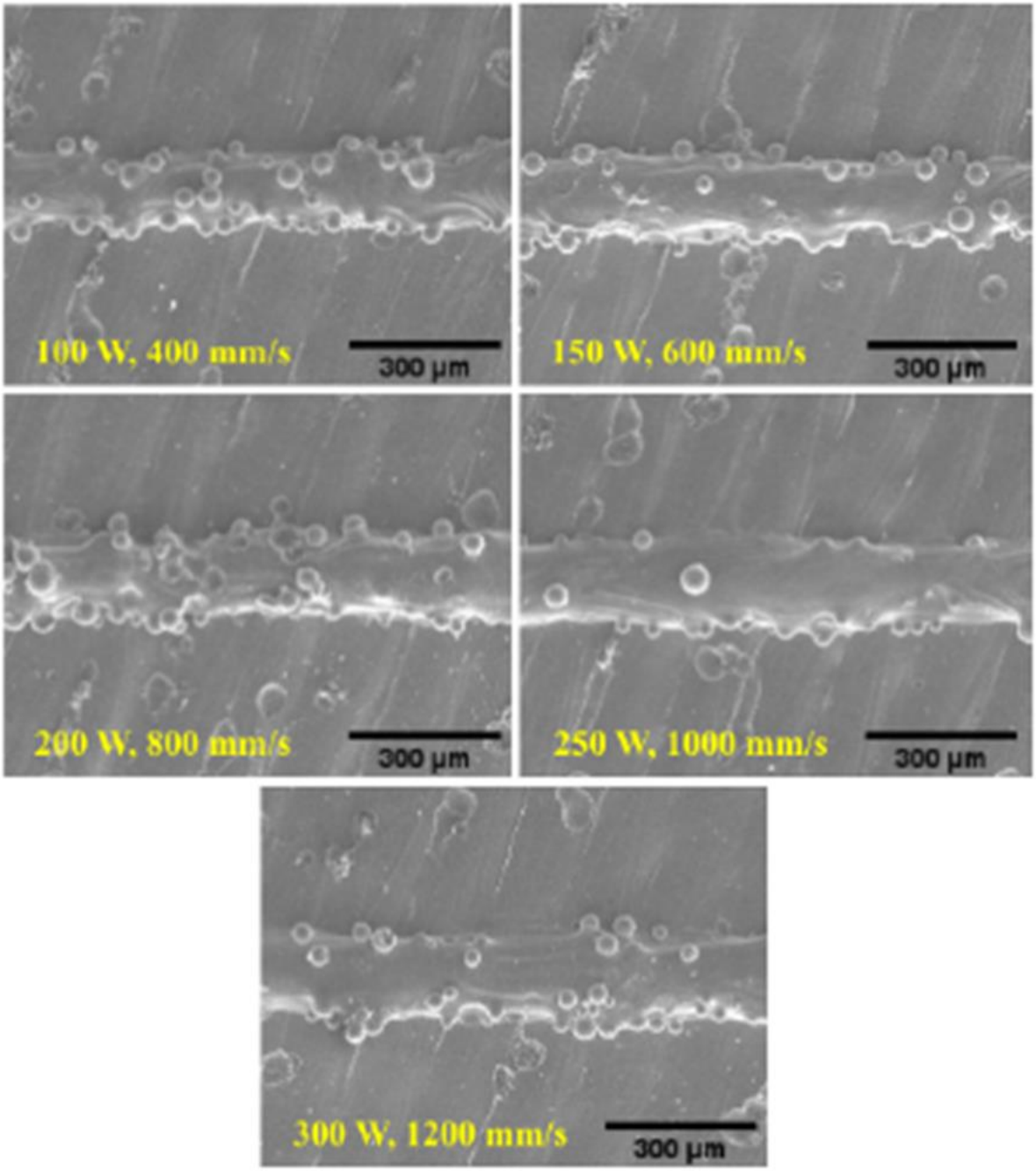

Figure 2.28. SEM-SE images showing the effect of laser power and scanning speed on single-track surface topography at constant LED (Simson and Subbu, 2022).

Figure 2.29 shows balling (Yueling et al., 2018). Mumtaz and Hopkinson (2010a) identified the satellite molten droplets (small droplets that form around and on the main molten track) (**Figure 2.30)** as surface defects. If these droplets are not fully integrated into the molten track during solidification, they can cause porosity and increase surface roughness, leading to imperfections and reducing the quality and mechanical properties (Mumtaz and Hopkinson,

2010a). Yadroitsev et al. (2013) recognised that each metal powder has specific process parameters that determine whether the tracks formed are stable or unstable.

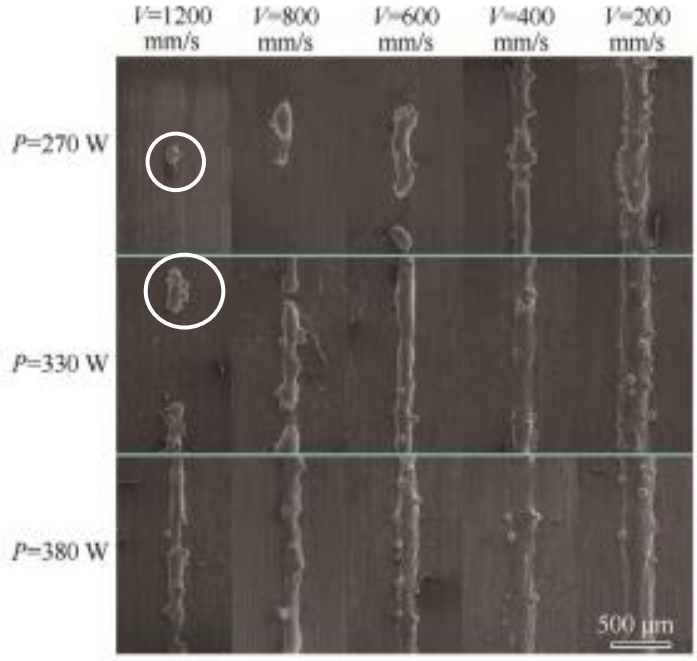

Figure 2.29. SEM-BSE images of single-track surface morphologies at varying scanning speeds (V) and laser powers (P), with white circles showing balling (Yueling et al., 2018).

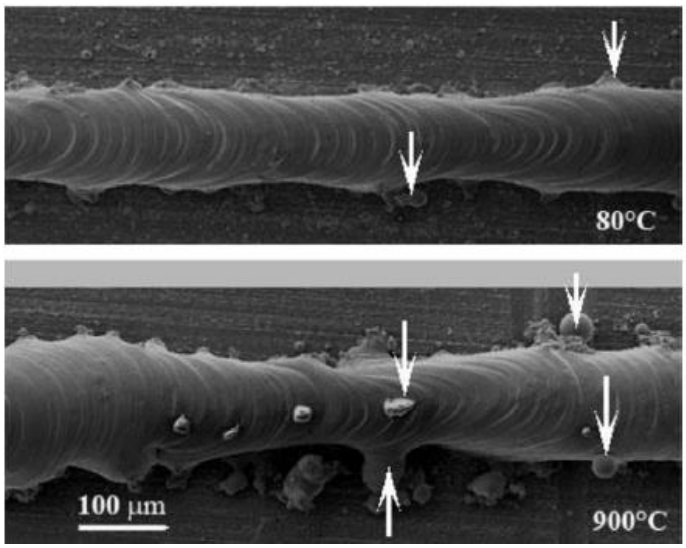

Figure 2.30. SEM-SE images of top views of single tracks on the substrate for 80°C and 900°C preheating at 0.12 m/s scanning speed, with white arrows indicating satellites (Yadroitsev et al., 2013).

2.2.4 Additive Manufacturing in Biomedical Applications

Additive manufacturing (AM), or 3D printing, was established in the 1980s (Ahangar et al., 2019). As defined by ASTM (2009), AM is the process of joining materials to create objects from 3D model data, typically layer by layer, in contrast to subtractive manufacturing, which involves cutting, hollowing, or removing parts from a block, bar or rod (ASTM, 2009; Yadroitsev et al., 2021). The core concept of AM is the use of computer-generated models as a guide for material layer deposition in three dimensions (Ahangar et al., 2019). Other terms for additive manufacturing include additive fabrication, additive techniques, additive layer manufacturing, layer manufacturing and freeform fabrication (Yadroitsev et al., 2021). Additive manufacturing has recently gained prominence as a cost-effective method for fabricating geometrically complex objects (Ahangar et al., 2019), particularly in biomedical engineering, where complex shapes are required and difficult to achieve using conventional techniques.

Dental implants are small with complex shapes and are expensive to manufacture using conventional casting and powder metallurgy methods (Saha and Roy, 2022). Multiple steps in conventional machining make it difficult and time-consuming to modify a finished product (Zadpoor, 2017). During these processes, titanium alloys such as Ti-6Al-4V are reactive, leading to material loss due to oxidation and degradation as they tend to form oxides or degrade due to chemical reactions. Additionally, titanium alloys like Ti-6Al-4V are less deformable, making them difficult to shape. However, AM can produce complex shapes for metallic implants (Ryan et al., 2021). Customised 3D-printed implants have favourable surgical outcomes, reducing hospital stays, operation times and medical costs (Ni et al., 2019).

The medical industry's supply chain has been enhanced by AM, which integrates mass production with tailored fabrication, using scanning and imaging technologies to provide quick, affordable and efficient medical treatment solutions (Ni et al., 2009). The AM technologies offer the potential to control the internal shape or microarchitecture of the generated implants (**Figure 2.31**) (Zadpoor and Malda, 2017). Other geometrical features, such as the sign and intensity of curvature, affect tissue regeneration rates, positively affecting integration (Zadpoor and Malda, 2017). Tan et al. (2017) demonstrated that porous titanium alloys have high implant success due to their promotion of human bone cell formation, creating strong twist-locks between implants and bone.

Porous Ti-based implants have lower elastic moduli, enhancing better stress transfer between bone and implant (Li et al., 2014). The pores promote biological fixation by allowing bone to grow into the implant's structure, while interconnected pore structures support stable blood flow for new bone tissue (Li et al., 2006). The interconnectivity also aids in the circulation of other bodily fluids. High porosity is crucial for promoting cell viability, adhesion, growth and differentiation (Li et al., 2006; Li et al., 2014), although increased porosity can reduce yield strength and tensile strength (Li et al., 2014).

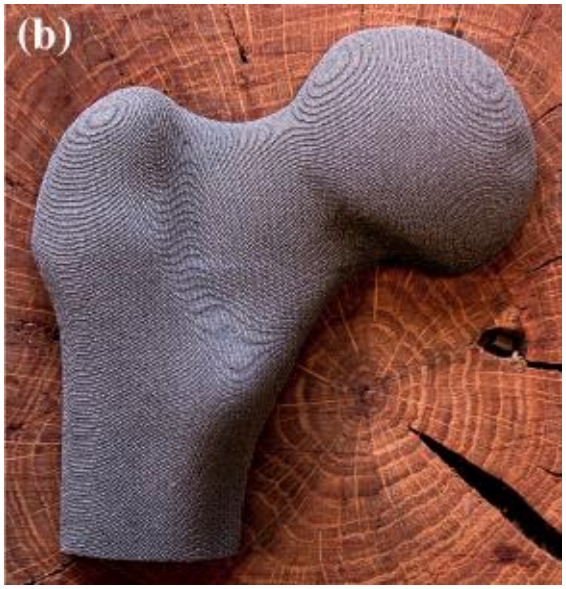

Figure 2.31. AM manufactured Ti-6Al-4V femur (Zadpoor and Malda, 2017).

2.3 Literature review summary and the design of this project

The literature review showed the potential of Ti-Cu alloys in additive manufacturing for dental applications, showing their ability to enhance biocompatibility, antibacterial properties and mechanical strength (Liu et al., 2014). Titanium alloys, particularly Ti-6Al-4V, have been widely used in biomedical applications due to their high strength, corrosion resistance and biocompatibility, which are critical for dental implants (Leyens and Peters, 2003). However, this alloy has concerns due to the cytotoxicity of aluminium and vanadium, which can pose health risks when released into the body (Morais et al., 2007; Palmquist et al., 2009; Li et al., 2014).

The addition of copper to titanium alloys has shown significant antibacterial properties, attributed to the Ti_2Cu phase (Zhang et al. 2013). This phase reduces biofilm formation and bacterial adhesion, particularly against oral pathogens like *Streptococcus mutans* and *Porphyromonas gingivalis*, which are common causes of implant-related infections (Liu et al., 2016). Liu et al. (2014b) and Zhang et al. (2016a) showed that 3 - 5 mass% copper is necessary to achieve optimal antibacterial effects while maintaining mechanical properties. However, excessive copper content can reduce ductility (Kikuchi et al., 2003; Liu et al., 2014; Zhang et al., 2016b), and optimising copper content and processing parameters is essential to balance antibacterial properties. Ruthenium is added in smaller amounts to increase the corrosion resistance without changing its microstructure (Schutz, 1996; Spotose 2023). The Ti-6Ta-1.5Zr-0.2Ru-5Cu (mass%) alloy, developed by Spotose (2023) as a promising (α+β) titanium alloy in its as-cast state, was selected for the current study to evaluate whether it retains similar properties when produced by additive manufacturing.

Additive manufacturing (AM) techniques, particularly laser powder bed fusion (LPBF), have proven effective for fabricating Ti-Cu alloys (Ni et al., 2019). These methods enabled control of microstructure, mechanical properties and customisation of complex geometries, making them ideal for dental implants. AM also allows for controlled porosity, which promotes osseointegration, a critical factor for implant stability and longevity (Ni et al., 2019; Zadpoor and Malda, 2017).

To manufacture alloys using AM requires powder atomisation to ensure spherical particles with a uniform size distribution for consistent layer spreading and minimising defects (Sutton et al., 2017). Ultrasound atomisation was chosen because it offers control over particle size and distribution. It is more energy-efficient than gas and water atomisation, as it does not rely on high-pressure gases or water jets (Ni et al., 2019; Żrodowski et al., 2021). This method provides better microstructure control, reducing porosity and inconsistencies, making it ideal for biomedical implants. It is also suited for low-melting-point, viscous, and oxidation-sensitive metals (Żrodowski et al., 2021; AMAZEMET, 2022). Additionally, ultrasound atomisation minimises material waste and environmental impact, making it a cost-effective and sustainable alternative to traditional atomisation techniques (AMAZEMET, 2022).

Additive manufacturing requires parameter optimisation to ensure high-quality, defect-free, and reliable parts while improving efficiency and reducing waste. The single-track method

enables direct assessment of process stability by observing how parameters like laser power, scan speed and beam diameter affect track formation, wetting behaviour and defect formation (Gonnabattula et al., 2024). It minimises material and energy waste by using small-scale testing instead of full-layer prints, making parameter optimisation faster and more efficient (Blakey-Milner et al., 2021). This approach provides valuable insights into melt pool dynamics, ensuring defect-free builds and is particularly beneficial for new alloy development in processes like LPBF.

Chapter 3. Experimental Procedure

This chapter presents the experimental procedure used to characterise powders, manufacture samples and evaluate the properties of the printed Ti-6Ta-1.5Zr-0.2Ru-5Cu (mass%) alloy. The methodology covers powder preparation, atomisation and sample production using laser powder bed fusion (LPBF). Post-processing analyses, including microstructural, mechanical, antibacterial and corrosion tests, were done to assess the alloy's suitability for biomedical applications.

3.1 Powder manufacturing and characterisation

3.1.1 Powder Manufacturing

Pure elemental powders (**Table 3.1**) were mixed in the correct ratio for Ti-6Ta-1.5Zr-0.2Ru-5Cu (mass%). A total mass of 100 g was mixed, and the powders were blended in a WAB T2C Turbula mixer for 30 minutes to obtain a good mixture, followed by compaction with an Instron 1175 testing machine with a maximum load of 70 kN and a crosshead speed of 20 mm/min.

Table 3.1. Powder specifications.

Element	**Purity (with trace metals)**	**Size**	**Company**
Titanium	99.98%	<45 µm	Labchem
Tantalum	99.99%	<-60+100 mesh	Labchem
Zirconium	99.98%	Average particle size: 2 - 3 µm, packed in water	Labchem
Ruthenium	99.99%	<45 µm	Merck
Copper	99.99%	<45 µm	Merck

Ultrasonic atomisation was done using a rePowder system (AMAZEMET, Poland), Żrodowski et al., 2021), with a molybdenum alloy sonotrode at 40 kHz, with fixed 155 A current and 100 - 130% amplitude of the sonotrode at 180 - 280 W, 7 L/min argon gas flow (to prevent oxidation) and the blower set at 13 - 17% maximum power. The whole process was carried out in an argon atmosphere. The powder produced was collected in an airlock container which was sealed under argon for safe handling.

3.1.2 Power Characterisation

A Malvern Mastersizer Hydro 200MU (at the University of the Witwatersrand) was used for particle analysis and the average of the three runs was recorded before and after the atomisation. The atomised powder was mounted in polyfast phenolic hot mounting resin with carbon filler, ground on 1200 grit grinding paper, and polished to ~1 µm to obtain the powder's cross-sections. The cross-sections were characterised by scanning electron microscopy with energy dispersive X-rays (SEM-EDX). The EDX was done on ten different cross-sectional areas of 1 mm^2 to obtain the bulk composition.

3.2 Single tracks

3.2.1 Printing of the Single Tracks

Single tracks of Ti-6Ta-1.5Zr-0.2Ru-5Cu (mass%) atomised powder of 30 - 60 µm size were printed using an AconityMIDI system using different parameters (**Table 3.2**). The single tracks were LPBF-printed on squares consisting of 20 layers of this alloy, on a 1 mm thick Ti-6Al-4V disc used as the substrate, (**Figure 3.1**) to prevent the substrate melting and chemical compositions changing. Subgroups of five single tracks, each with a different parameter combination, listed in **Table 3.3**, were printed on eight supporting squares. also shows the directions of argon gas for oxidation prevention, melting and recoating (the blade used to coat a layer of powder during LPBF). Squares were cut to separate single tracks for analysis.

Single-track experiments were conducted across a wide processing window, following parameter ranges of Wang et al. (2017) and equipment constraints, such as the laser power and scan speed limits of the AconityMIDI equipment. The scan speed range was limited by melt pool instability. Layer thickness and hatch spacing were selected to ensure a high remelting ratio across layers along the build direction (Z-axis). The final parameters were compared to parameters ranges of Wysocki et al. (2017) to ensure continuous and defect-free melt tracks.

Table 3.2. Printing parameter ranges for the single tracks.

Laser power (W)	Scanning speed (mm/s)	Beam diameter (mm)	Linear energy density (J/mm)	Planer energy density (J/mm^2)
120 - 280	200 - 1200	0.08 - 0.36	0.120 - 0.788	0.600 - 9.844

Table 3.3. Parameters for printing single tracks.

Number	Laser power (W)	Scanning speed (mm/s)	Beam diameter (mm)	Linear energy density (J/mm)	Planar energy density (J/mm^2)
1	171	600	0.08	0.285	3.563
	171	400	0.08	0.428	5.344
	171	600	0.15	0.285	1.900
	171	400	0.15	0.428	2.850
	171	200	0.15	0.855	5.700
2	157.5	1200	0.08	0.131	1.641
	157.5	1000	0.08	0.158	1.969
	157.5	800	0.08	0.197	2.461
	157.5	600	0.08	0.263	3.281
	157.5	400	0.08	0.394	4.922
3	157.5	1200	0.15	0.131	0.875
	157.5	1000	0.15	0.158	1.050
	157.5	800	0.15	0.197	1.313
	157.5	600	0.15	0.263	1.750
	157.5	400	0.15	0.394	2.625
4	157.5	600	0.22	0.263	1.193
	157.5	600	0.15	0.263	1.750
	157.5	600	0.08	0.263	3.281
	120	1000	0.15	0.120	0.800
	120	1000	0.08	0.120	1.500
5	315	1200	0.08	0.263	3.281
	315	1000	0.08	0.315	3.938
	315	800	0.08	0.394	4.922
	315	600	0.08	0.525	6.563
	315	400	0.08	0.788	9.844
6	315	1200	0.15	0.263	1.750
	315	1000	0.15	0.315	2.100
	315	800	0.15	0.394	2.625
	315	600	0.15	0.525	3.500
	315	400	0.15	0.788	5.250
7	157.5	600	0.36	0.263	0.729
	157.5	600	0.29	0.263	0.905
	157.5	600	0.22	0.263	1.193
	157.5	600	0.15	0.263	1.750
	1575	600	0.08	0.263	3.281
8	280	1200	0.36	0.233	0.648
	280	1200	0.29	0.233	0.805
	280	1200	0.22	0.233	1.061
	280	1200	0.15	0.233	1.556
	280	1200	0.08	0.233	2.917

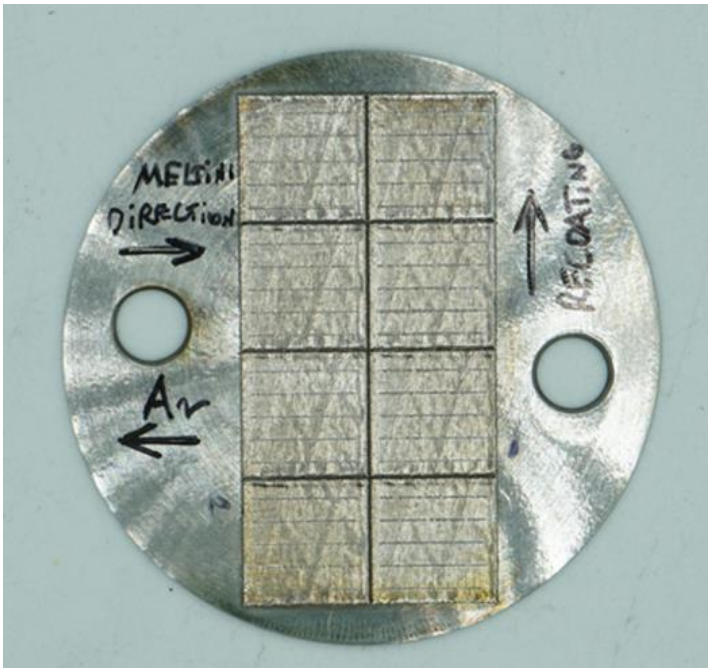

Figure 3. 1. Photograph of the Ti-6Al-4V substrate disc with eight LPBF squares supporting five horizontal single tracks each, showing directions of argon gas flow, melting and recoating.

3.3 LPBF-manufactured and as-cast samples: manufacturing and characterisation

3.3.1 As-cast manufactured sample

Elemental powders were weighed and mixed in the Ti-6Ta-1.5Zr-0.2Ru-5Cu (mass%) ratio. The mixture was melted under vacuum using the arc-melting module of rePowder and cast into bars with dimensions of 62 mm in length and ~15 mm in diameter. Arc-melting was performed in a cold crucible using a plasma arc to ensure compositional homogeneity. These bars were prepared for subsequent processing by ultrasonic atomisation, which is described in Section **3.1.1**.

3.3.2 Printing of LPBF-manufactured samples

The Ti-6Ta-1.5Zr-0.2Ru-5Cu (mass%) cuboid (length 10 mm, width 10 mm and height ~1.2 mm) samples were manufactured using the AconityMIDI system with the ultrasonically atomised powder (Section 3.1.1). The samples were manufactured using the parameters listed in **Table 3.4**.

The 5 mm long tracks, with 0.1 mm overlap, were printed with the scanning direction against the argon flow to ensure effective extraction of fumes and spatter. To achieve remelting,

where the laser beam re-melts a previously solidified layer, the following parameters were applied: 280 W laser beam, 3000 mm/s scanning speed and 0.08 mm beam diameter. After fabrication, the cuboids were removed from the substrate using an electric cutter for further analysis.

Table 3.4. LPBF process parameters for cuboid samples.

Laser Powder (w)	Scanning Speed (mm/s)	Beam diameter (mm)	Layer thickness (mm)	Hatching (mm)	Linear energy density (J/mm)	Planar energy density (J/mm^2)	Volumetric energy density (J/mm^3)	Rotation (°)
157.5	600	0.15	0.03	0.05	0.26	1.75	175	67

3.3.3 Density calculations

The density of the samples was measured using Archimedes' principle using the ASTM B962-17 standard (ASTM, 2017). Three samples were tested, with five measurements conducted on each sample, and the averages obtained were used as representative values. An ADAM Luna Precision Balance-LPB 223i scale was used to measure the mass. The samples were weighed in air to obtain the dry mass (m) and in distilled water to determine the suspended mass (M). The density was calculated using Equation 3.1 (Kaoushik et al., 2023).

Density of the sample $=\left\{\frac{m}{m-M}\right\}(\rho-\rho_O)+\rho_O$ (Equation 3.1)

where ρ = density of distilled water at room temperature and ρ_O = density of air.

Theoretical density was calculated based on the individual elements in the alloy.

Percentage of densification $=\frac{True\ density\ of\ the\ sample}{Theoritical\ density\ of\ the\ sample}\times 100$ (Equation 3.2)

The estimated porosity was calculated using Equation 3.3 (Gong et al., 2014).

$R_D = 1-\frac{\rho DS}{\rho TD}$ (Equation 3.3)

where R_D = porosity, ρ_{DS} = true density and ρ_{TD} = theoretical density.

The theoretical density of Ti-6Ta-1.5Zr-0.2Ru-5Cu (mass%) was calculated from Equation 3.4, as 4.86 g/cm^3.

$$100\ \text{wt\%} \times \left(\frac{87.3\ mass\%}{4.51} + \frac{6\ mass\%}{16.65} + \frac{1.5\ mass\%}{6.51} + \frac{0.2\ mass\%}{12.37} + \frac{5\ mass\%}{8.92}\right)^{-1} \quad \text{(Equation 3.4)}$$

3.3.4 Microstructural analysis and phase identification of LPBF and as-cast samples

The LPBF cuboids and the as-cast sample were mounted (METCO, Bainmount Twin H auto, Specimen Mounting Press) using polyfast phenolic hot mounting with carbon filler resin. The process involved heating the material to 180°C for 5 minutes and cooling for 4 minutes under a pressure of 250 bar, using water as the coolant. The mounted samples were ground and polished using an automatic SAPHIR 520. Grinding was done using silicon carbide (SiC) grinding paper with different particle sizes (grades) and water as a coolant. Polishing was done using MD-Chem polishing cloth and colloidal silica as a lubricant to give a mirror-like surface. **Table 3.5** summarises the metallographic procedures.

Table 3.5. Grinding and polishing steps for Ti-6Ta-1.5Zr-0.2Ru-5Cu (mass%) alloys**.**

Parameters	**Steps**				
Abrasive Discs (Silicon Carbide P Grade) / Polishing cloth	P240	P500	P800	P1200	MD-Chem cloth with a particle size of 0.04 µm
Lubricant	Water	Water	Water	Water	Colloidal silica
The speed at the counter direction (rpm)	240	200	200	200	150
Force (N)	25	25	25	25	20
Time (min)	15	15	15	15	30

The mixed elements were characterised before and after atomisation, as well as single tracks, LPBF-manufactured samples and as-cast samples. A high-resolution Carl Zeiss Sigma Field Emission Gun Scanning Electron Microscope (FEG-SEM 500), equipped with BSE (backscattered electron), SE (secondary electron), and EDX (energy dispersive X-ray) detectors, was used for microstructural and compositional analysis (SE, BSE, and EDX signals were selected to provide complementary information: SE for surface morphology, BSE for

compositional/phase contrast, and EDX for elemental compositions). Data analysis was performed using ZEISS Smart SEM software, with the electron high tension (EHT) set to 20 kV (to ensure sufficient penetration depth and efficient excitation of X-rays from heavier alloying elements (Ta, Zr, Ru). Elemental composition analysis was performed with an OXFORD INSTRUMENT x-act PentaFET Precision EDX detector, and the data were analysed using Oxford INCA software. ImageJ software was used to calculate the average lath widths.

Phase identification was conducted using X-ray diffraction (XRD) on a Bruker XRD D2 Phaser. The instrument used Co-Kα radiation (wavelength = 1.78899×10^{-10} m) and was operated at 50 kV and 25 mA. The scans were performed within a 2θ range of 10 – 90° over 20 minutes to determine the phases present in the samples.

3.3.5 Hardness testing

Hardness testing of the LPBF and as-cast samples was done using a Vickers FutureTech Microhardness FM 700 machine, with a 500 gf load and a 10 s dwell time. The first set of hardness measurements was taken along a line across the sample, with indentations spaced 20 µm apart. In the second test, ten random indentations were made at various points. Mean and standard deviations were calculated, and the tests followed ASTM E384-17 standards.

3.3.6 Anti-bacterial testing

The tests were *in vitro* (outside of a living organism) bacteriostatic and conducted in a controlled laboratory environment to evaluate the specimens' ability to inhibit bacterial growth.

3.3.6.1 Bacterial culture

A Gram-positive bacterial strain, *Staphylococcus aureus*, was used because of its role in healthcare-associated infections, particularly in implants (Leaper et al., 2010). Its ability to form biofilms and resist antibiotics, including methicillin-resistant strains (MRSA), makes it essential for evaluating the antimicrobial properties of materials. To prepare the culture, 10 µL of a bacterial suspension was added to 10 mL of sterilised Lysogeny Broth (LB) broth (Sigma-Aldrich, Missouri, USA) and the mixture was incubated overnight at 37°C. After incubation,

the suspension was centrifuged to separate the bacteria and resuspended in 10 mL of fresh LB broth. The bacterial solution was subsequently diluted to an optical density (OD) of 0.2 at 600 nm using a UV–VIS spectrophotometer (UVmini-1240, Shimadzu, Kyoto, Japan). A working bacterial solution with a concentration of 10^5 colony-forming units (CFU)/mL was prepared by adding 40 µL of the bacterial suspension to 40 mL of LB broth.

3.3.6.2 Colony forming unit (CFU) assay

Three separate samples were taken from each group: as-cast, LPBF-manufactured, pure copper and Ti-6Al-4V. The samples were placed in individual testing tubes for sterilisation using the water vapour in a CertoClav, which was heated up to 121°C and a pressure of 100 bar for 30 minutes, then cooled for 45 minutes. The samples were then transferred to a sterile 24-well plate and 1.5 mL of the prepared bacterial solution was added to each well. The plate was incubated at 37°C for 24 hours. Once the incubation period ended, the samples were placed in 1 mL of phosphate-buffered saline (PBS, Sigma-Aldrich, Missouri, USA) and vortexed in a mini vortexer for 2 minutes each to detach the bacteria adhering to the samples' surfaces. These bacterial solutions were then subjected to a three-step 10-fold dilution, with each 20 mL dilution plated onto LB-agar plates. The agar plates were incubated overnight to allow the formation and counting of bacterial colonies.

Equation 3.5 was used to calculate the colony forming units (CFU) (Fowler et al., 2019):

$$\text{CFU/ml} = \frac{Number\ of\ colonies \times dilution\ factor}{volume\ o\ f\ culture\ plated\ into\ petri\ dish} \quad \text{(Equation 3.5)}$$

The antibacterial rate was calculated from Equation 3.6 (Xie et al., 2022):

$$\text{Antibacterial rate} = \frac{CFU\ Control - CFU\ Sample}{CFU\ Control} \times 100 \quad \text{(Equation 3.6)}$$

The Ti-6Al-4V was used as the positive control while copper was used as the negative control as it would kill all the bacteria.

3.3.7 Corrosion testing

The corrosion tests were performed using a three-electrode electrochemical cell connected to an Autolab potentiostat. Each alloy sample was the working electrode, a graphite rod was used as the counter electrode and a saturated calomel electrode (SCE) was the reference electrode. A Luggin probe with a salt bridge that connected to the calomel electrode was included in the cell set-up. The calomel electrode saturated with 3M KCl^- (SCE) was positioned between the working electrode and the reference electrode.

Copper wires were soldered on the samples for electrical connection. The samples were mounted in a non-conductive epoxy resin. The surface exposed to the electrolyte was ground with 1200 grade silicon carbide paper and rinsed with deionised water. The open circuit potential (OCP) tests in the phosphate-buffered saline (PBS) solutions were conducted for 3600 seconds after immersion until it stabilised. Afterwards, potentiodynamic polarisation tests were performed at room temperature, at a scan rate of 0.167 mV/s in the potential range of 250 mV to 1500 mV at a scan speed of 10 mV/min without reversing the scanning direction.

The PBS solution was prepared using the procedure described by Fowler et al. (2019) to have a pH of 7.4. Deionised water and the following salt concentrations were used to create the PBS in a 1-litre flask:

- 8 g/L of sodium chloride (NaCl)
- 0.2 g/L of potassium chloride (KCl)
- 1.44 g/L of sodium hydrogen phosphate (Na_2HPO_4)
- 0.24 g/L of potassium dihydrogen phosphate (KH_2PO_4).

The solution was heated and kept at 37 ± 1°C before the tests, and a thermostat submerged in the solution was used to ensure exact temperature control. Nitrogen gas (N_2) was used to purge the PBS solution to remove oxygen and create anaerobic conditions. A new solution was prepared for each sample tested to maintain consistency and reliability in the experiments. The corrosion tests were conducted following the ASTM G59 standard.

The corrosion rates were calculated using Equation 3.7 following the ASTM G102 standard.

$$\text{Corrosion rate} = K_1(i_{corr}EW)/(\rho) \qquad \text{(Equation 3.7)}$$

where: i_{corr} = corrosion current density (mA/cm²), K = 3.27 mm/(mA·cm·y), EW = equivalent weight of the material = 13.02 g, ρ = density of the alloy = 4.86 g/cm³.

Chapter 4. Results

This chapter presents the experimental results including characterising powder particles, single tracks, LPBF-manufactured samples and as-cast samples using SEM-EDX and XRD. Additive manufactured and as-cast Ti-6Ta-1.5Zr-0.2Ru-5Cu (mass%) alloy samples were tested for hardness, anti-bacterial and corrosion resistance.

4.1 Powder Characterisation

The SEM-BSE images of the starting elemental powders show irregular shapes (**Figure 4.1**). The order of contrasts from lightest to darkest (based on atomic number) is Ta, Ru, Zr, Cu and Ti. The titanium powder particles were larger than those of Ta and Cu, which tended to agglomerate together. The Zr and Ru particles were not visibly distinguishable, likely due to their smaller amounts in the mixture. The EDX maps of the blended powder **(Figure 4.2)** shows that it was mixed well, and all the starting elements were present.

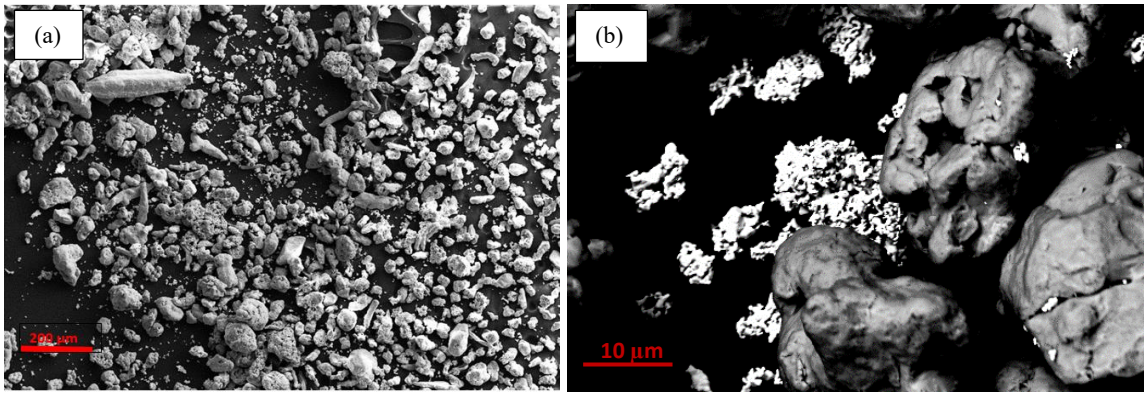

Figure 4.1. SEM-BSE images of blended elemental powders of Ti, Ta, Zr, Ru and Cu before atomisation: (a) lower and (b) higher magnification: Ta (light contrast) and Ti (dark).

Figure 4.3(a) shows SEM-BSE images of the powders after atomisation, indicating that they were mostly spherical within the size range (10 - 100 µm) required for LPBF (Żrodowski et al., 2021. However, at higher magnification (**Figure 4.3(b**)), many particles still appeared spherical, while some showed irregular shapes. **Figure 4.4** shows the EDX maps of powder particles after atomisation**.** Error! Reference source not found. lists the EDX results of the powder after atomisation, showing that there was more Ru and Cu and less Ti, Ta and Zr than expected.

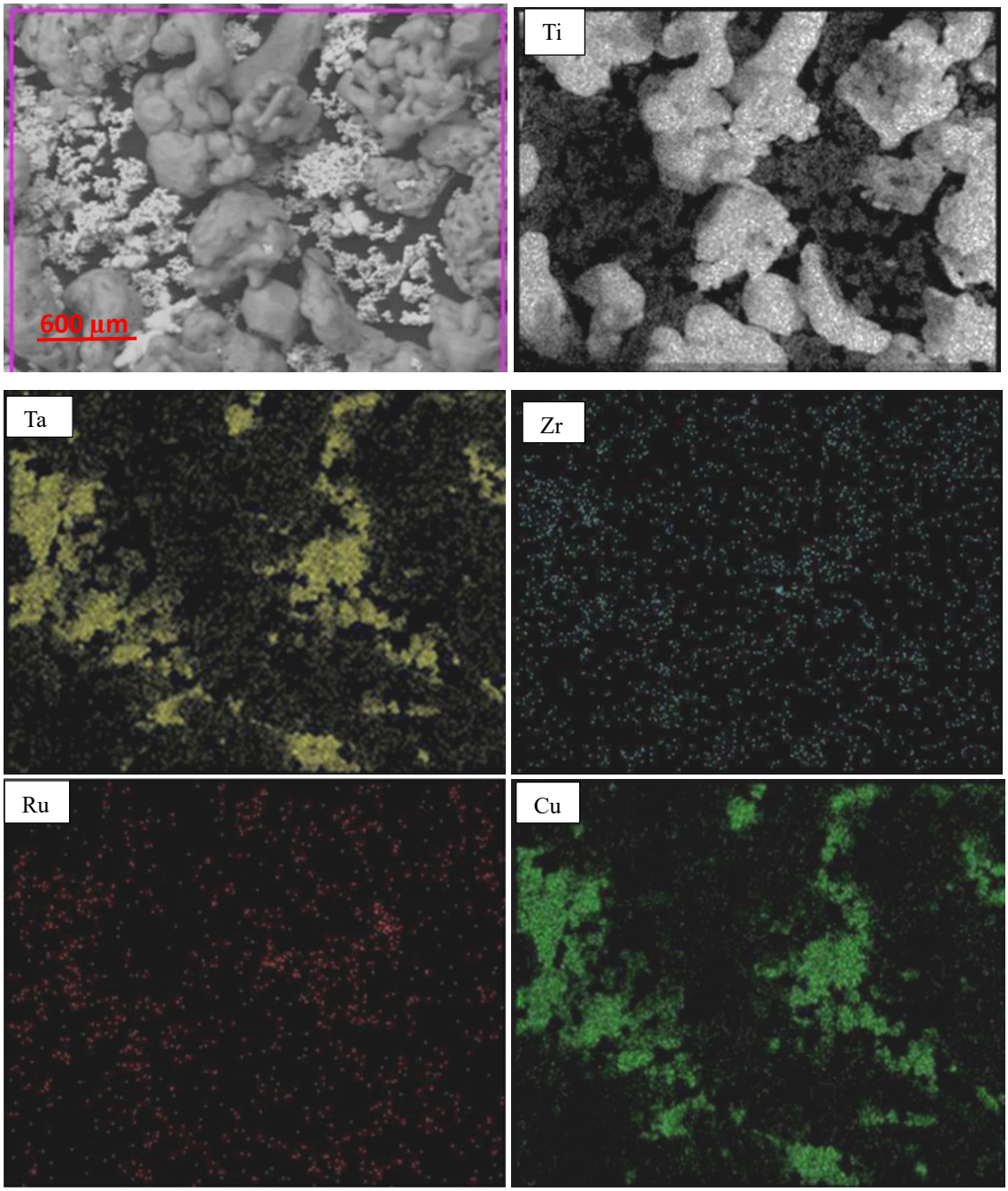

Figure 4.2. X-ray maps of the blended powder of Ti, Ta, Zr, Ru and Cu before atomisation.

Table 4.1. EDX results for atomised Ti-6Ta-1.5Zr-0.2Ru-5Cu (mass%) powder.

Composition	**Ti**	**Ta**	**Zr**	**Ru**	**Cu**
Atomised	83.5 ± 0.3	4.6 ± 0.1	0.24 ± 0.1	0.5 ± 0.1	11.3 ± 0.3

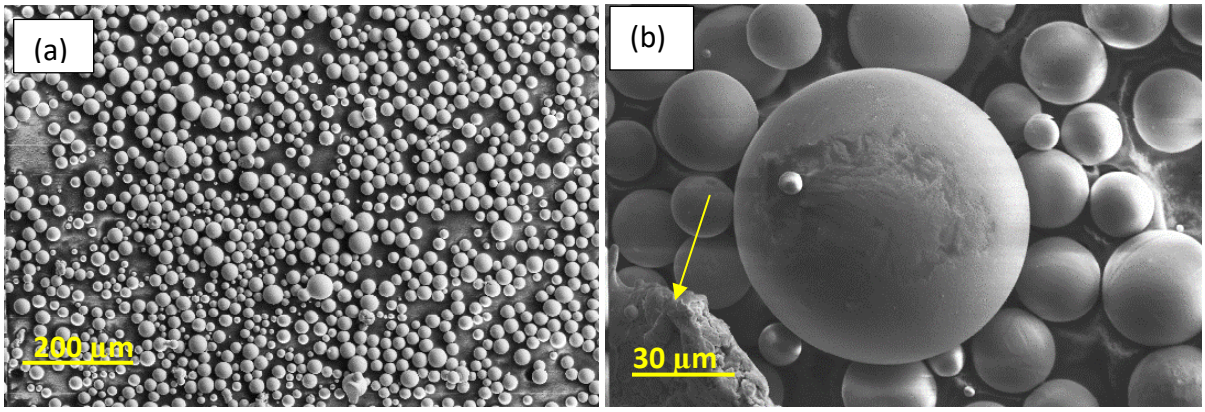

Figure 4.3. SEM-SE images of Ti-6Ta-1.5Zr-0.2Ru-5Cu (mass%) powder after atomisation: (a) lower and (b) higher magnification showing large spherical particles and an irregular particle (shown by the yellow arrow).

Figure 4.5 shows the X-ray maps of the cross-sections of the powder and **Table 4.2** shows EDX results of the cross-sections after atomisation. The X-ray maps of the powder particles show that alloying occurred during atomisation and the distribution of elements was homogeneous. **Figure 4.6** shows SEM images of the cross-sections of the atomised powder at lower and higher magnifications, displaying minor internal porosity, with an irregular particle exhibiting regions of different phases. **Figure 4.6(b)** shows dendrites.

The areas shown by the squares in **Figure 4.7** are examples of the scans on ten different particle cross-sections and the average results are recorded in **Table 4.2**.

Table 4.2. Targeted composition and EDX results for area scans of cross-sections of atomised Ti-6Ta-1.5Zr-0.2Ru-5Cu (mass%) powder particles.

	Ti	**Ta**	**Zr**	**Ru**	**Cu**
Targeted	87.3	6	1.5	0.2	5
Larger spherical particles	88.0 ± 0.4	6.9 ± 0.4	0.1 ± 0.6	0.2 ± 0.1	4.8 ± 0.2
Smaller irregular particles	87.2 ± 0.5	5.2 ± 0.6	0.0 ± 0.0	0.0 ± 0.0	7.6 ± 0.8

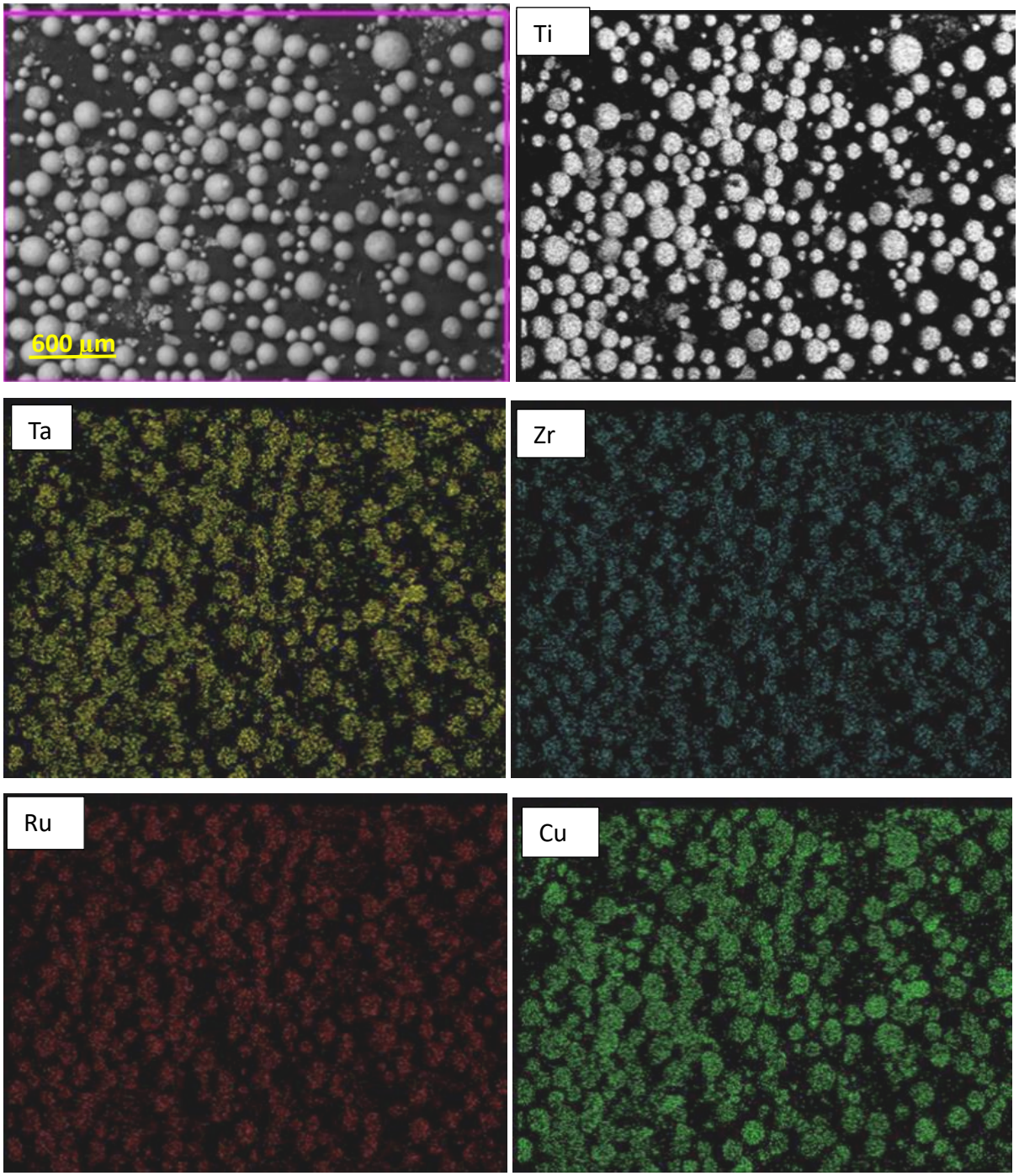

Figure 4.4. X-ray maps of the atomised Ti-6Ta-1.5Zr-0.2Ru-5Cu (mass%) powder.

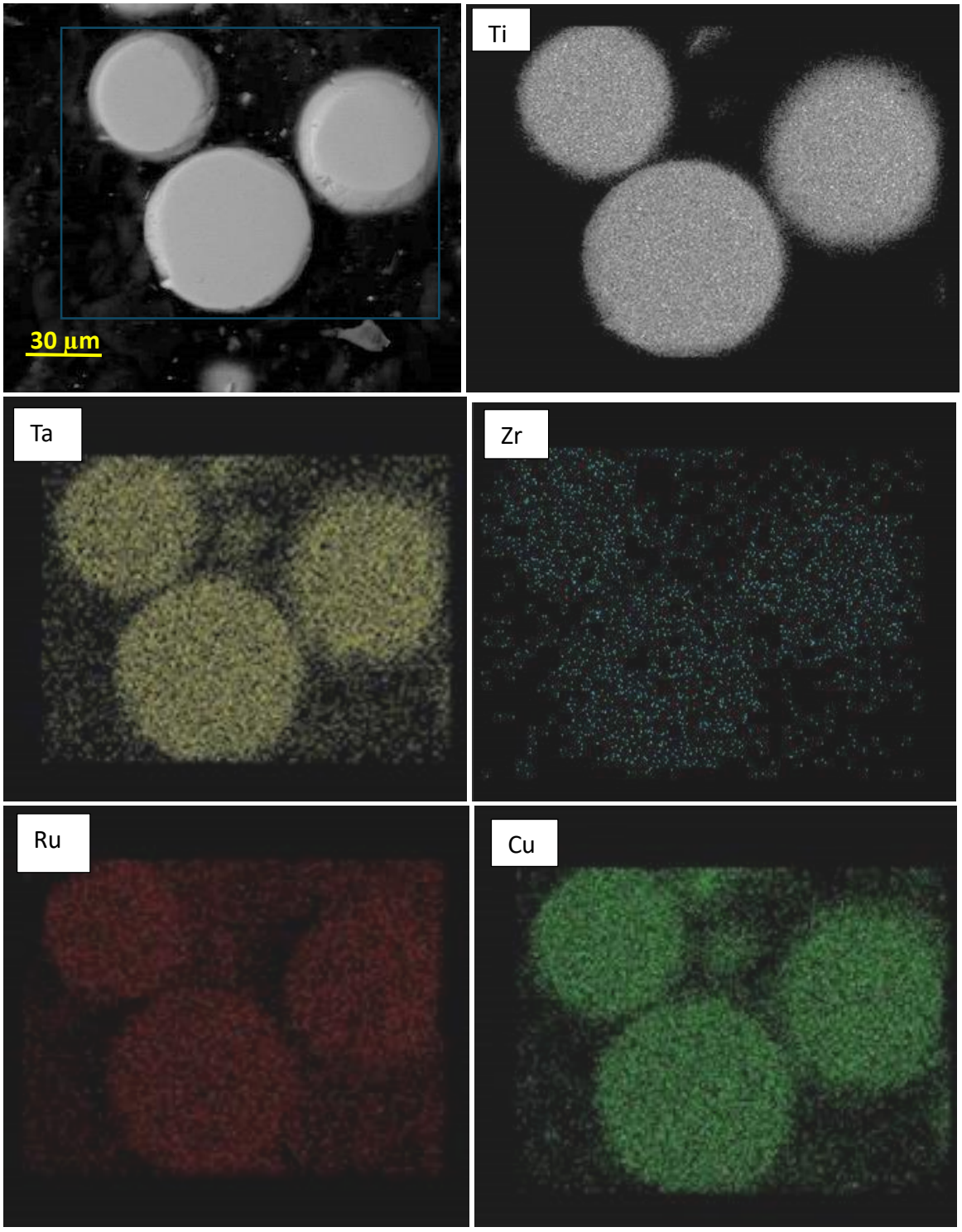

Figure 4.5. X-ray maps of cross-sections of three Ti-6Ta-1.5Zr-0.2Ru-5Cu (mass%) atomised powder particles.

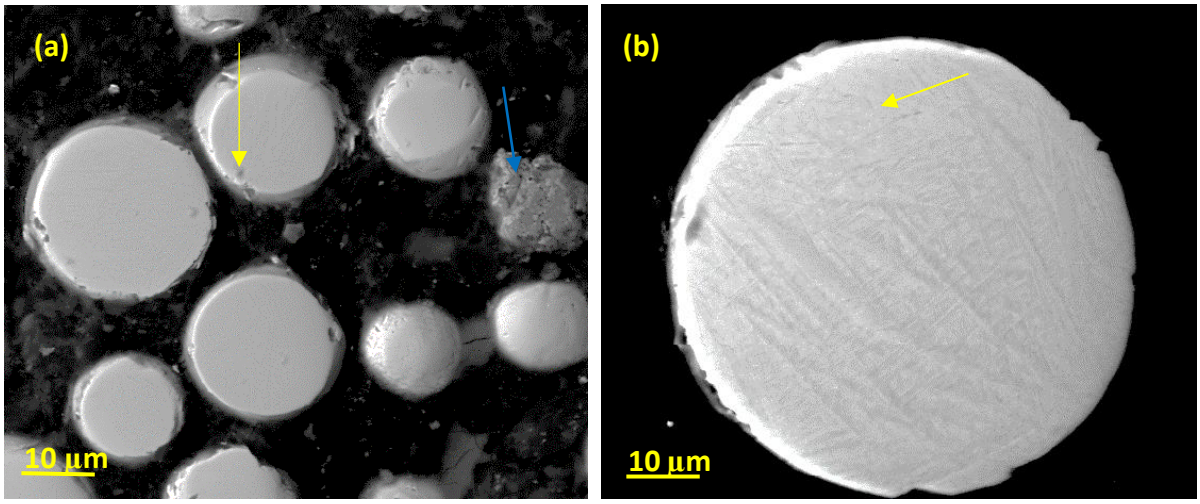

Figure 4.6. SEM-BSE images of cross-sections of Ti-6Ta-1.5Zr-0.2Ru-5Cu (mass%) powder, yellow arrows show internal porosity, and blue arrow shows an irregular particle.

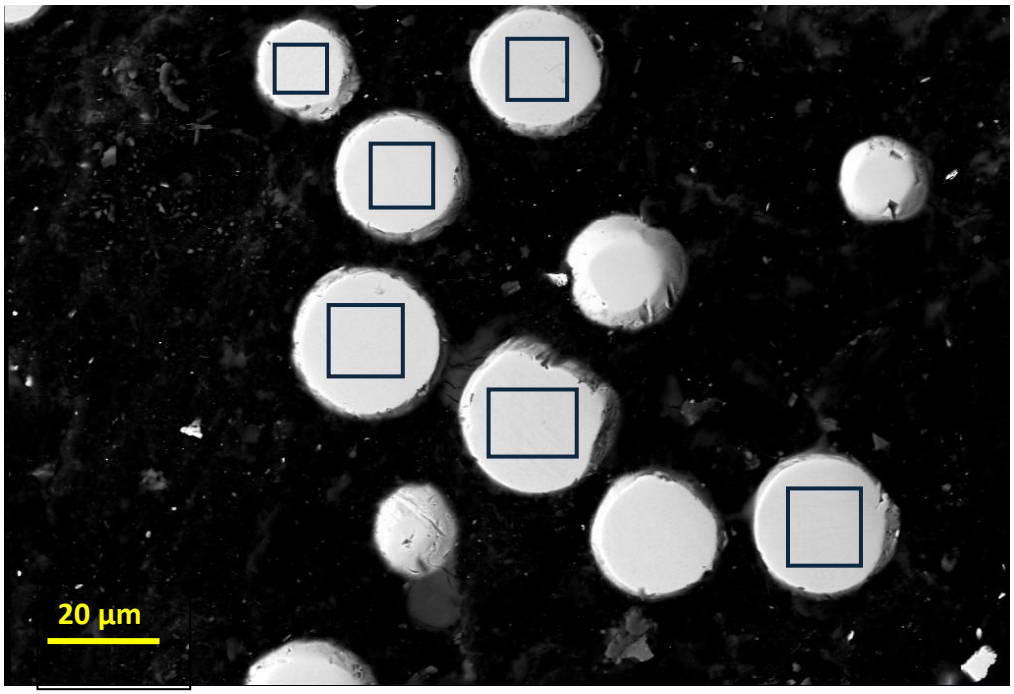

Figure 4.7. SEM-BSE image indicating the areas of the EDX analyses on cross-sectioned atomised powder particles.

Figure 4.8 show the X-ray line scans of cross-sections of a spherical powder particle showing that there was a decrease in titanium towards the edges of the particle. **Figure 4.9** shows line scans of an agglomerated powder particle indicating the homogeneous distribution of the

elements. **Figure 4.10** shows irregular and spherical powder particles agglomerated with less titanium at the edges of both particles.

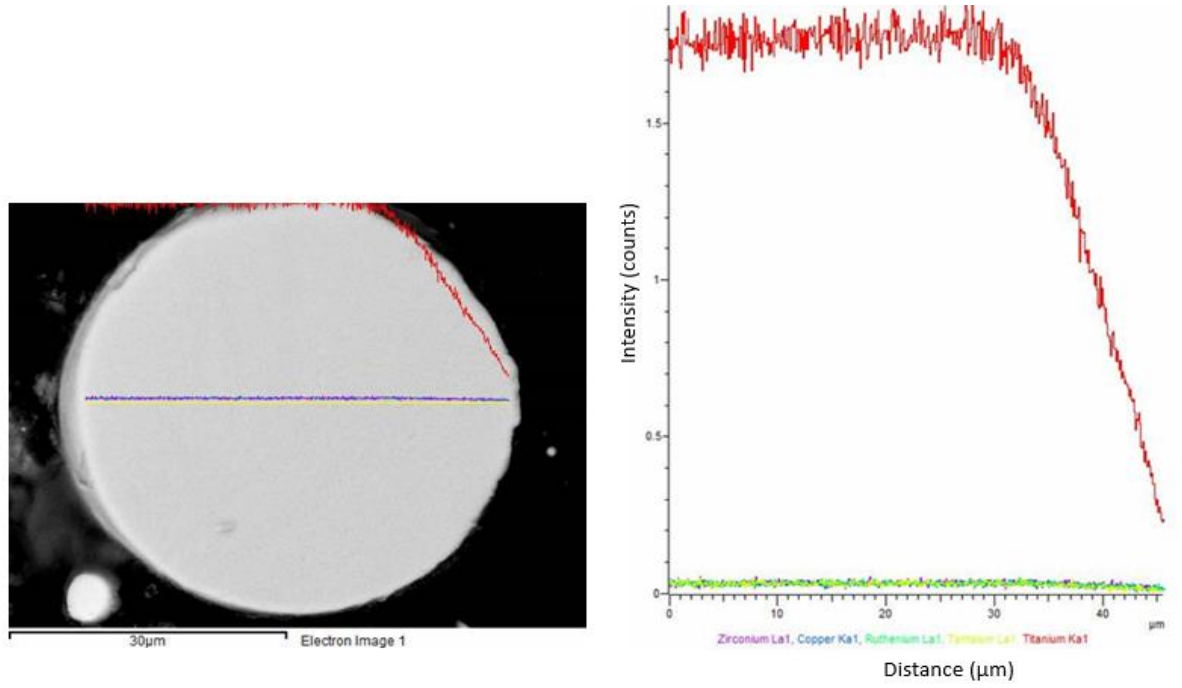

Figure 4.8. X-ray line scans of a cross-section of a single spherical powder particle.

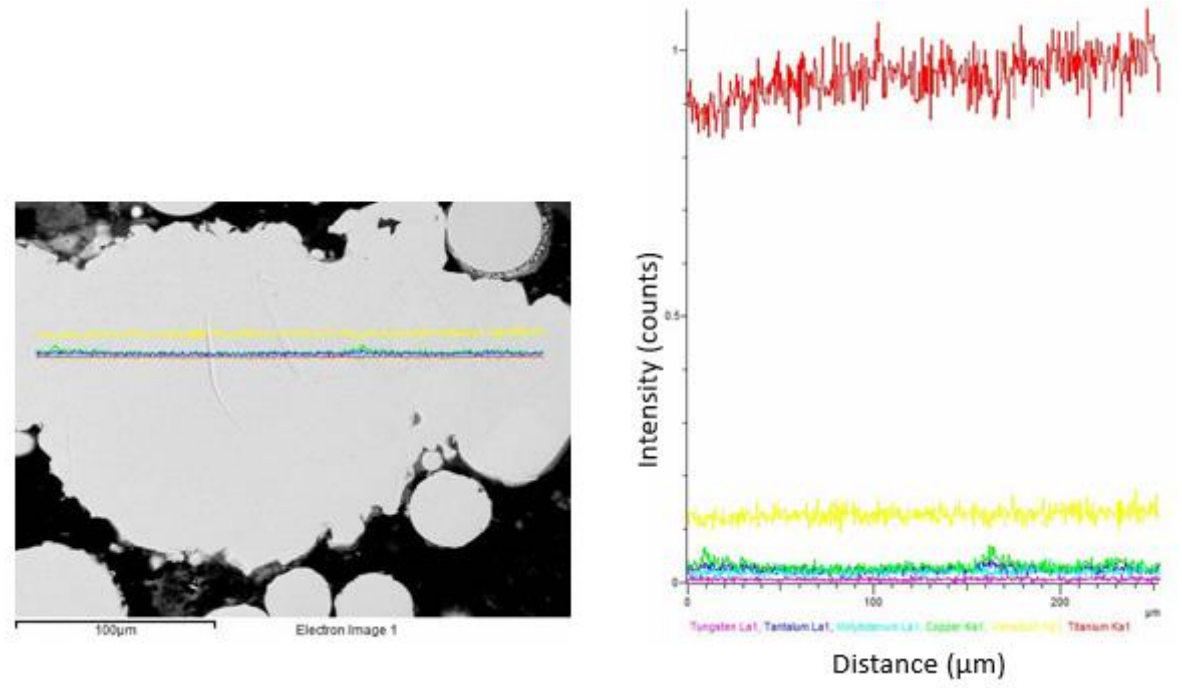

Figure 4.9. X-ray line scans of a cross-section of an agglomerated powder particle.

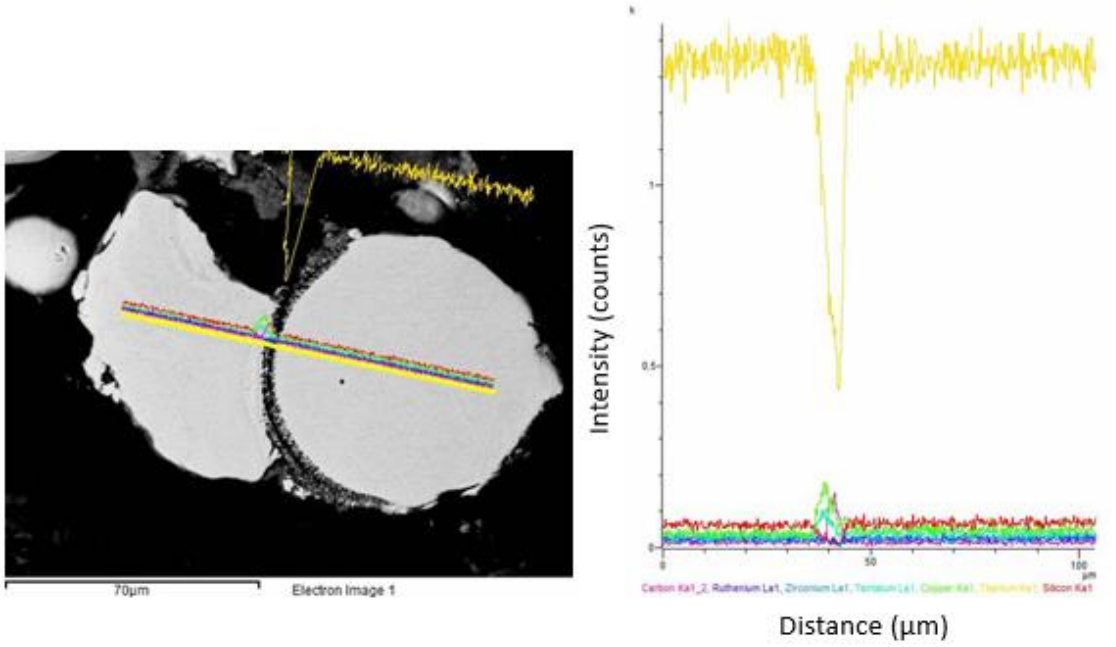

Figure 4.10. X-ray line scans of a cross-section of irregular and spherical powder particles.

Particle size distributions of the blended elemental powder before atomisation are shown in **Figure 4.11.** There was a large peak at ~50 µm and two small peaks at ~9 µm and ~250 µm. **Figure 4.12** shows the particle distribution after atomisation, with no particles below 10 µm, a main peak at ~55 µm and a smaller peak at ~800 µm. **Figure 4.13** shows some agglomerated spherical particles.

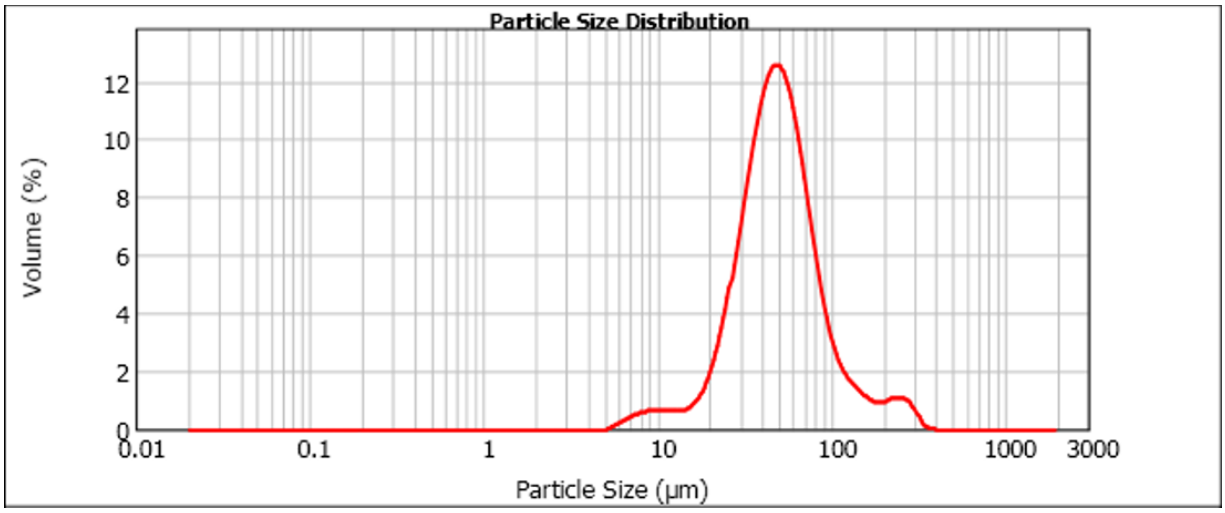

Figure 4.11. Particle size distribution of blended elemental powders of Ti, Ta, Zr, Ru and Cu before atomisation.

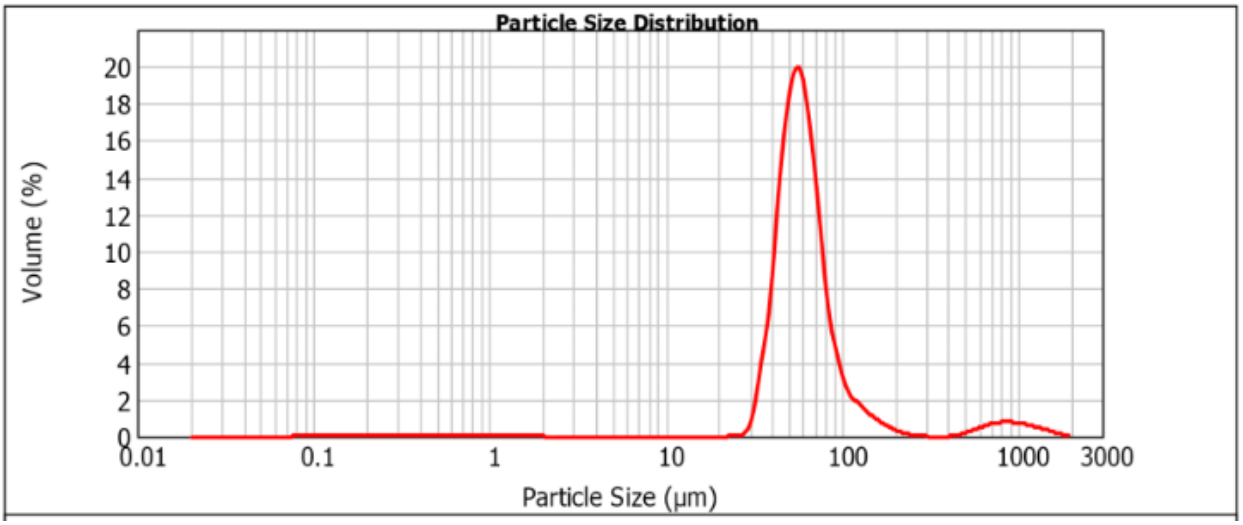

Figure 4.12. Particle size distribution of Ti-6Ta-1.5Zr-0.2Ru-5Cu (mass%) powder after atomisation.

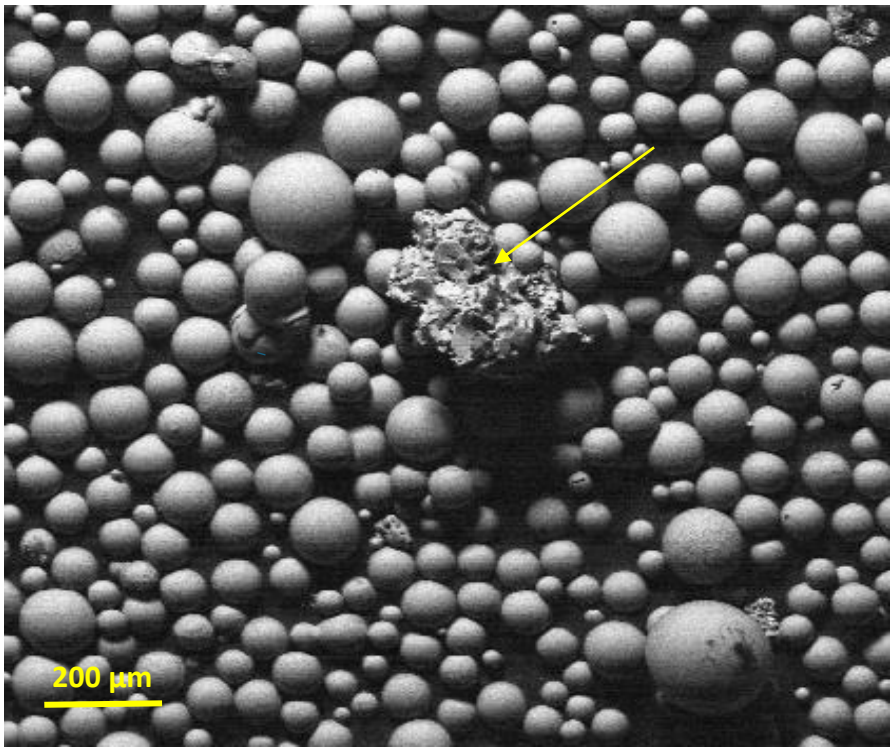

Figure 4.13. SEM-BSE image showing an agglomeration of particles.

Figure 4.14 shows XRD results of the blended elemental powders of Ti, Ta, Zr, Ru and Cu before atomisation, with major peaks of (αTi). Conversely,

Figure 4.15 (after atomisation), displays (αTi), (βTi) and Ti_2Cu peaks. **Table 4.3** is a summary of the particle size distributions before and after atomisation.

Table 4.3. Average particle size distributions of blended powder and after atomisation.

	D_{10}	D_{50}	D_{90}
Blended elemental powder	25.1	48.6	100.6
After atomisation	40.7	58.3	106.9

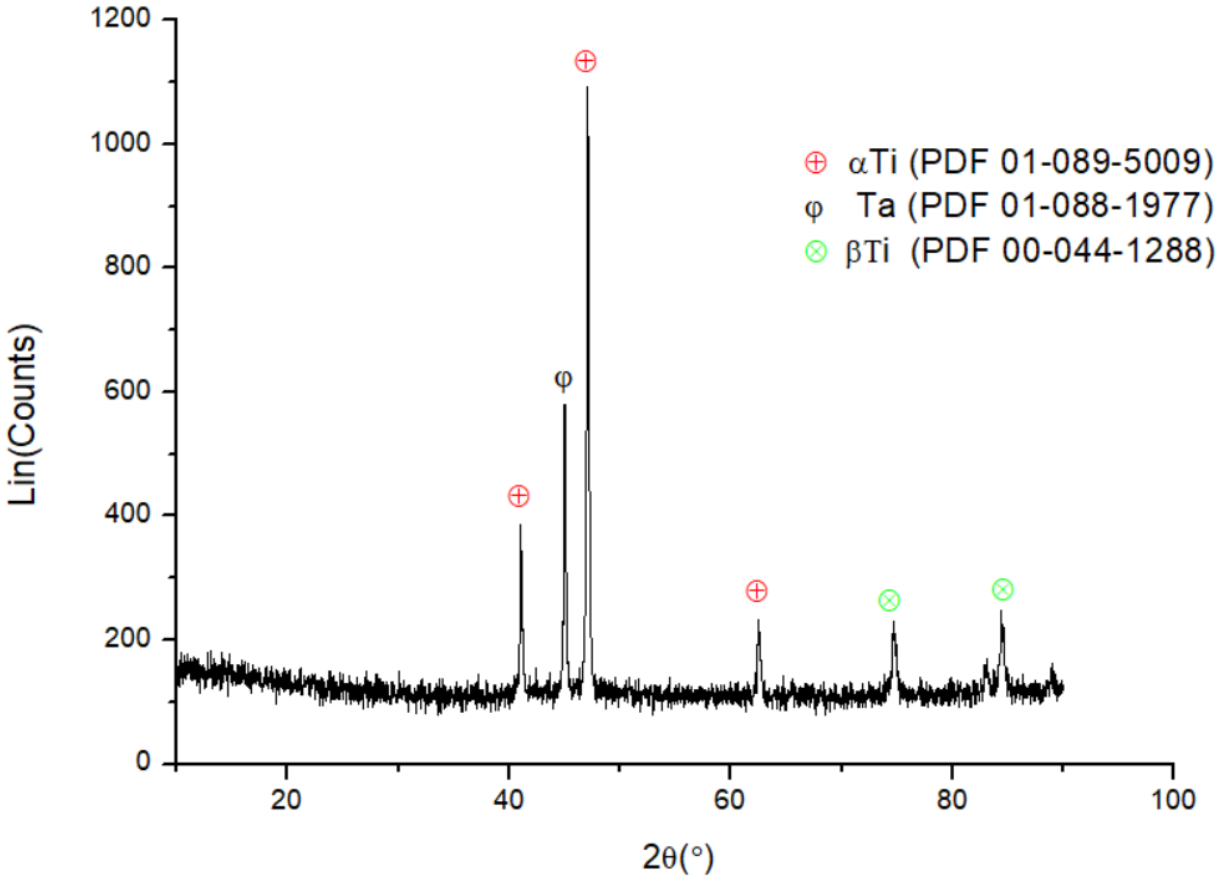

Figure 4.14. XRD pattern for blended elemental powder before atomisation.

4.2 Characterisation of single tracks

Figure 4.16 shows the morphology of the single tracks of Ti-6Ta-1.5Zr-0.2Ru-5Cu (mass%) for constant laser power and beam diameter at varying scanning speeds. The unmelted spherical particles in **Figure 4.16(a)** had an average particle size of 51.4 ± 1.9 µm, which was within the 45 - 60 µm particle size range of the atomised powder. The unmelted spherical powders were

randomly distributed in all the samples. Some samples had more unmelted spherical particles, **Figure 4.16(a),** while others had fewer, **Figure 4.16(c)**. **Figure 4.16(d)** shows that the tracks were unstable along the printing direction at higher scanning speeds and "balling" had occurred (shown by the ellipse). The dark particles in **Figure 4.16d** were caused by contamination during the separation of the eight squares using direct wire cutting.

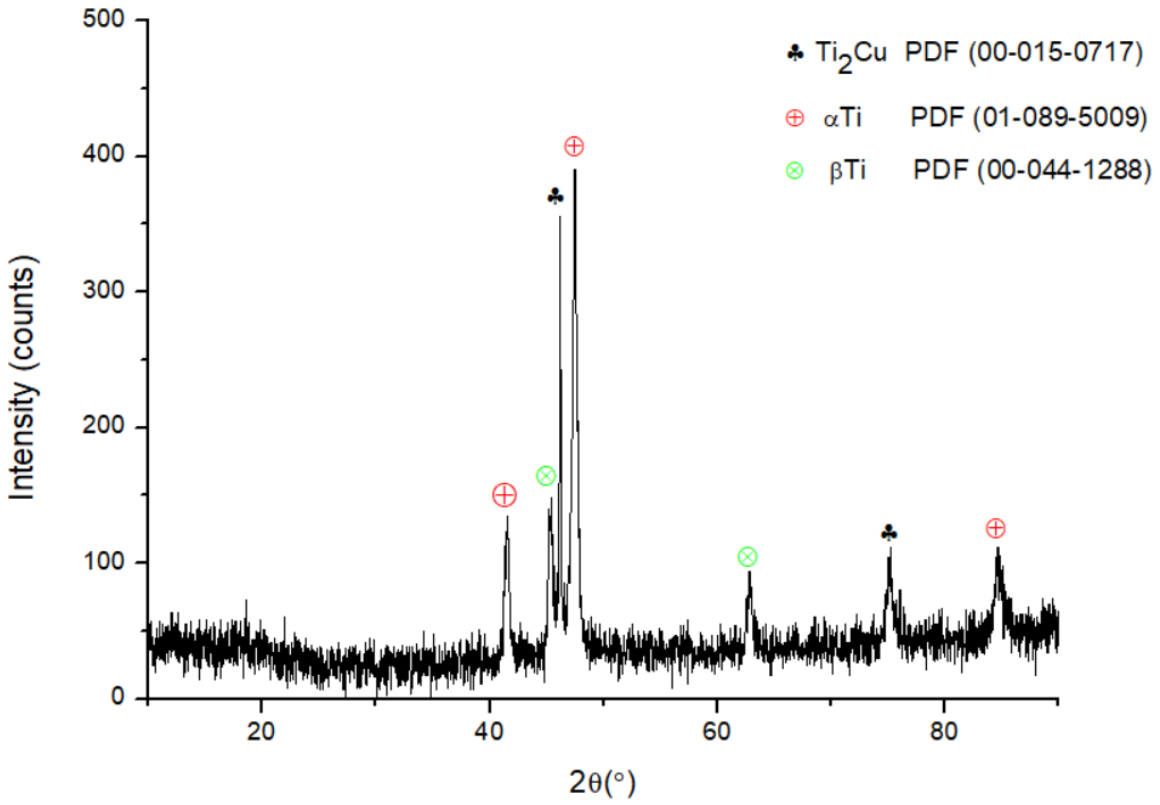

Figure 4.15. XRD pattern for Ti-6Ta-1.5Zr-0.2Ru-5Cu (mass%) powder after atomisation.

Figure 4.17 shows that increasing the laser power and reducing the beam diameter reduced "balling" at higher scanning speeds. **Figure 4.18** shows that balling at higher power and scanning speed increased with increasing beam diameter. **Figure 4.18(c)** and **Figure 4.18(d)** show that lower planer energy density (PED) caused balling.

Table 4.4 shows the EDX results of the best track and the spherical particles on the tracks. These spherical particles had lower Ti and higher Ta, Zr and Cu than the target composition. The particles had the expected Ru, although was lower than that on the best single track.

Table 4.5 lists EDX results of the dark spots on the single tracks showing they were mostly contamination.

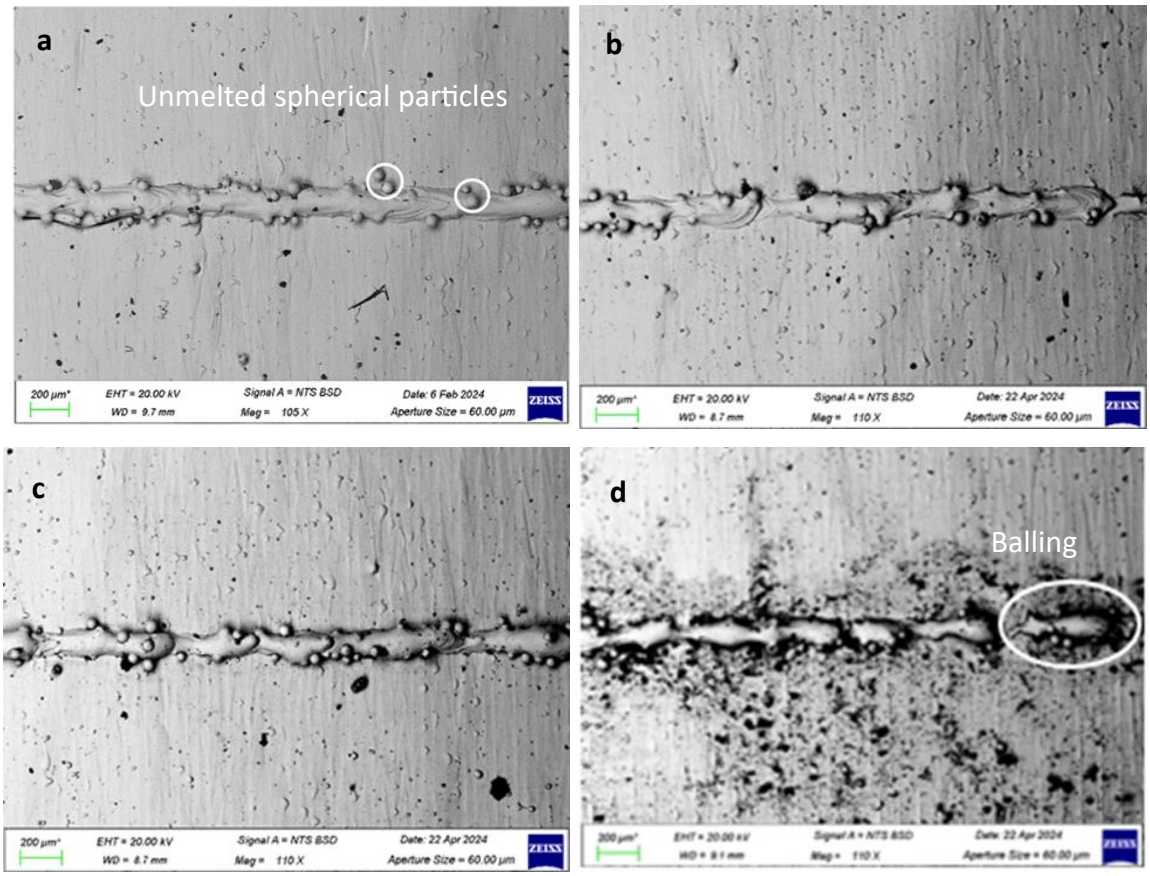

Figure 4.16. SEM-BSE images showing morphology of the single tracks at 157.5 W laser power, 0.15 mm beam diameter and scanning speeds of: (a) 600 mm/s, (b) 800 mm/s, (c) 1000 mm/s and (d) 1200 mm/s. White ellipse indicates balling.

Table 4.4. EDX results of best single track and the spherical particle on the track.

	Ti	Ta	Zr	Ru	Cu
Best single track	83.9±1.6	7.4±0.2	1.7±0.2	0.4±0.1	6.8±1.9
Spherical particle	81.9±0.3	7.4±0.3	1.9±0.1	0.2±0.1	8.6±8.6

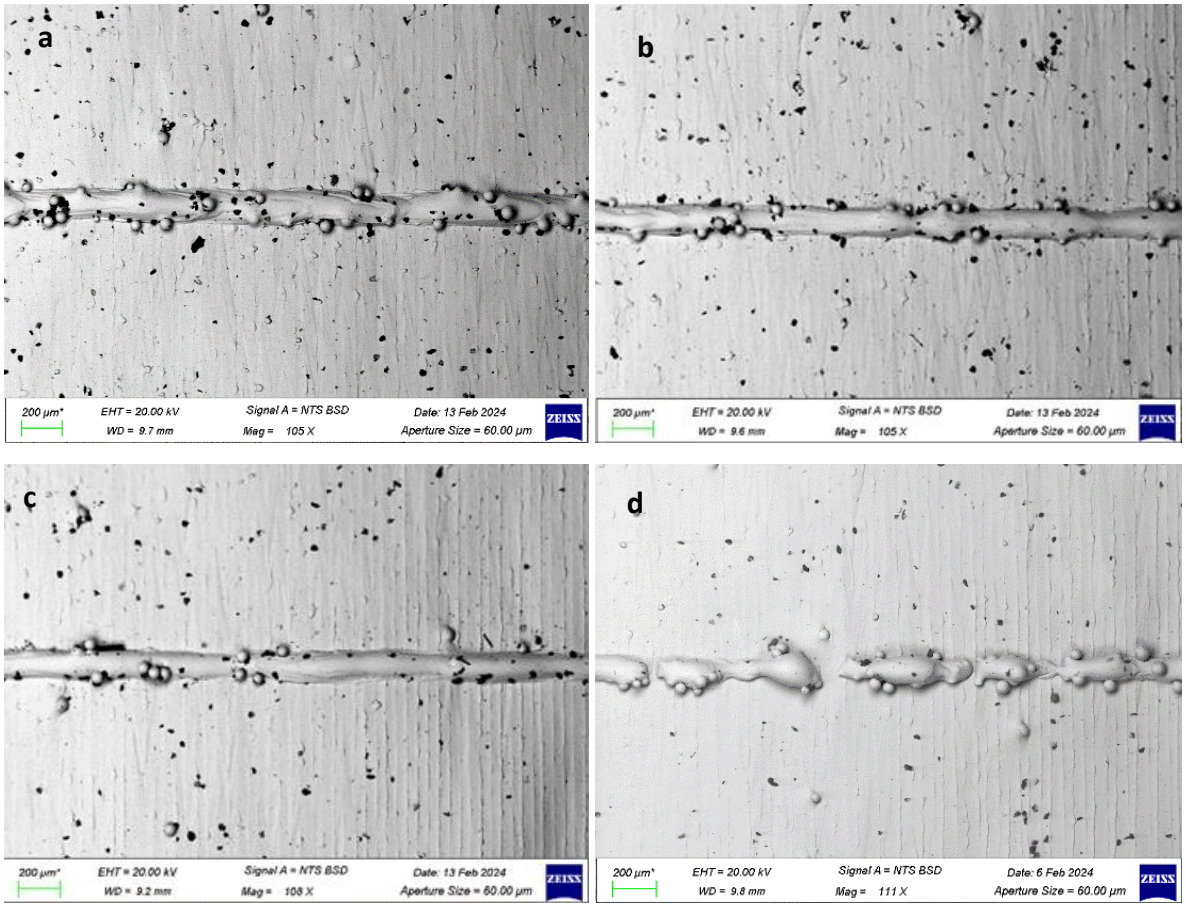

Figure 4.17. SEM-BSE images showing the morphology of single tracks at 315 W laser power, 0.08 mm beam diameter and scanning speeds of: (a) 600 mm/s, (b) 800 mm/s, (c) 1000 mm/s and (d) 1200 mm/s.

Table 4.5. EDX results of dark spots on Ti-6Ta-1.5Zr-0.2Ru-5Cu (mass%) best single track.

Composition	**C**	**O**	**Si**	**Cl**	**K**	**Ti**	**Fe**
Dark spot	42.6±5.6	34±9.4	0.7±0.1	0.6±0.4	3,2±1.4	18±2.8	0.9±0.1

Figure 4.19 shows the XRD pattern of the best single track of Ti-6Ta-1.5Zr-0.2Ru-5Cu (mass%) identifying (αTi), (βTi) and Ti_2Cu peaks. Tantalum, Zr and Ru were not detected, because they had dissolved in the (αTi) and (βTi) solid solutions. To ensure only the single track was scanned, each scan track was isolated by cutting out individual squares from the template, allowing laser exposure to only the intended region. The cross-section of the single tracks was not done because they were too small; grinding them would have removed them from the substrate.

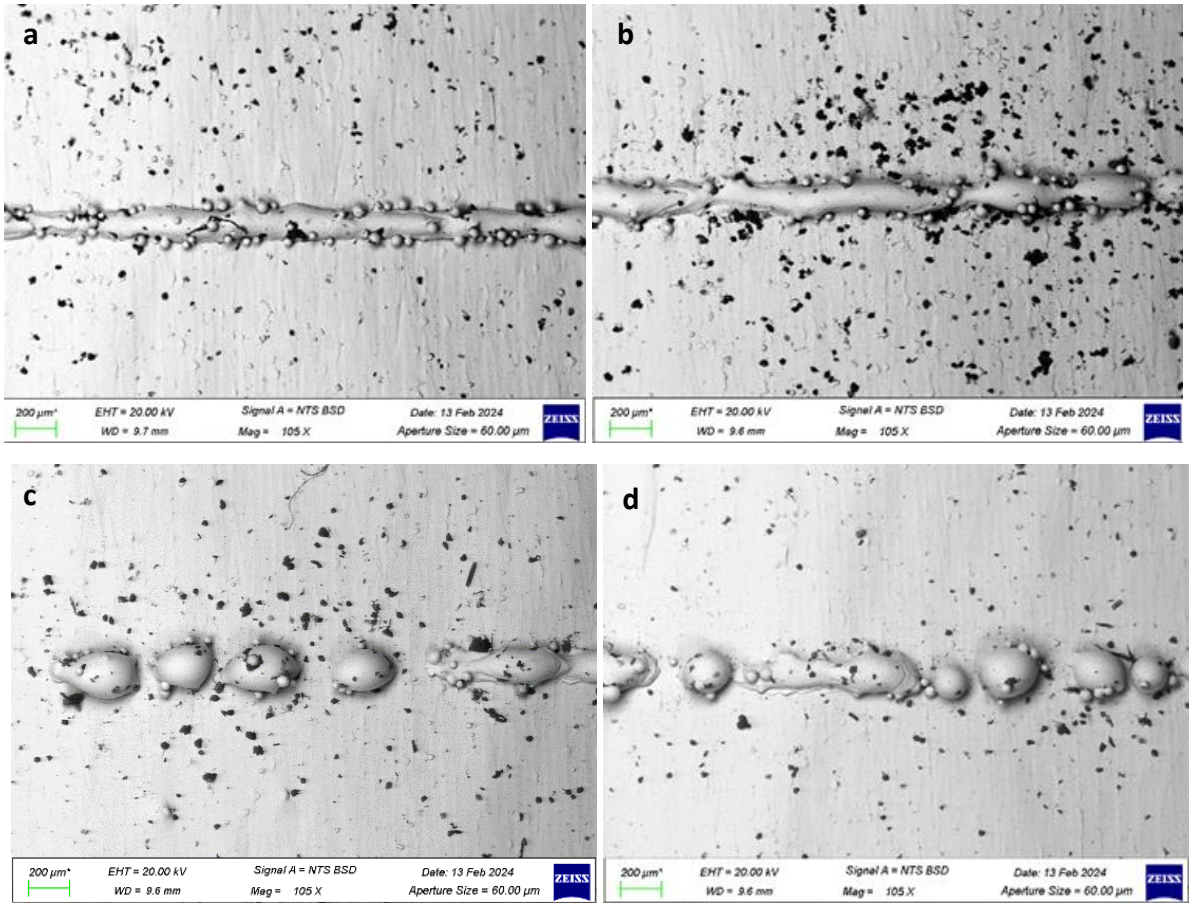

Figure 4.18. SEM-BSE images showing the morphology of the single tracks at 280 W laser power and 1200 mm/s scanning speed for beam diameter: (a) 0.15 mm, (b) 0.22 mm, (c) 0.29 mm and (d) 0.3 mm.

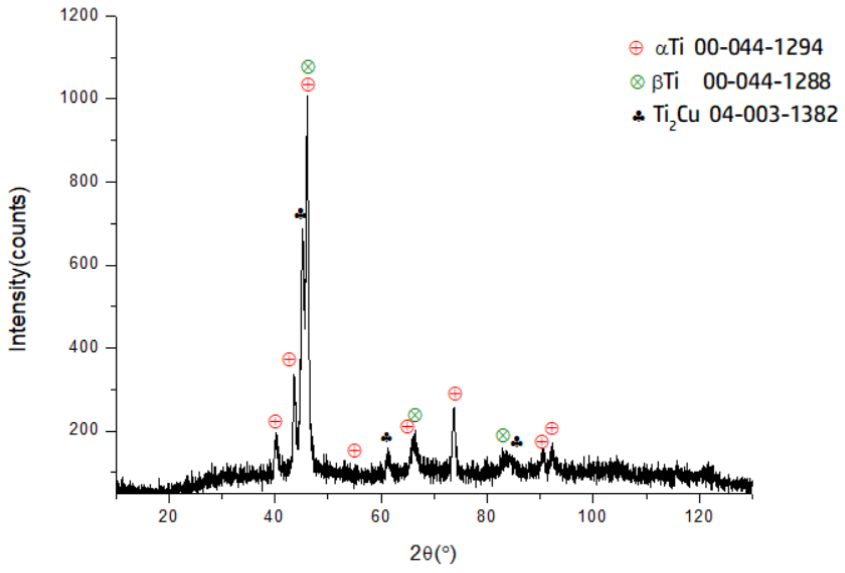

Figure 4.19. XRD pattern of the best single track of Ti-6Ta-1.5Zr-0.2Ru-5Cu (mass%).

4.3 Characterisation of LPBF-manufactured cuboids and as-cast samples

4.3.1 Density testing

The true density of the samples and their densification percentages were calculated and are listed in **Table 4.6**.

Table 4.6. Densities of the LPBF-manufactured samples.

Sample	Mass in air (g)	Mass in distilled water(g)	True density (g/cm^3)	Densification (%)
1	1.08 ± 0.01	0.85 ± 0.01	4.69 ± 0.05	96.40 ± 0.01
2	1.10 ± 0.01	0.87 ± 0.01	4.68 ± 0.06	96.20 ± 0.01
3	0.99 ± 0.02	0.78 ± 0.02	4.68 ± 0.03	96.30 ± 0.01

Sample 1 had the highest densification, with a calculated porosity of 0.04 attributed to its high densification. **Figure 4.20** shows an SEM image of an LPBF-manufactured cuboids, showing the porosity on the areal view, while **Figure 4.21** shows a cross-section of the cuboids with unmelted powder particles and pores.

4.3.2 Microstructural and XRD analysis

Figure 4.22 shows that the as-cast sample had coarser (βTi) grains with coarse (αTi) on the grain boundaries and fine (αTi) within the grains. **Figure 4.23** shows an LPBF horizontal cross-section, with (αTi) along the prior (βTi) grain boundaries and as small precipitates in the (βTi) equiaxed grains. **Figure 4.24** shows a vertical cross-section of LPBF cuboids, with (αTi) precipitated along the grain boundaries and within the (βTi) matrix. The alignment of these grains indicates directional solidification, although some variation in orientation was observed. The as-cast sample (**Figure 4.22**) mainly consisted of (αTi) needles, while the LPBF-manufactured horizontal cross-section samples (**Figure 4.23**) had primary (βTi) with (αTi) precipitating along the grain boundaries and forming coarse Widmanstätten needles within the grains. The average lath width of as-cast was 1.3 ± 0.6 µm and LPBF was 0.45 ± 0.19 µm.

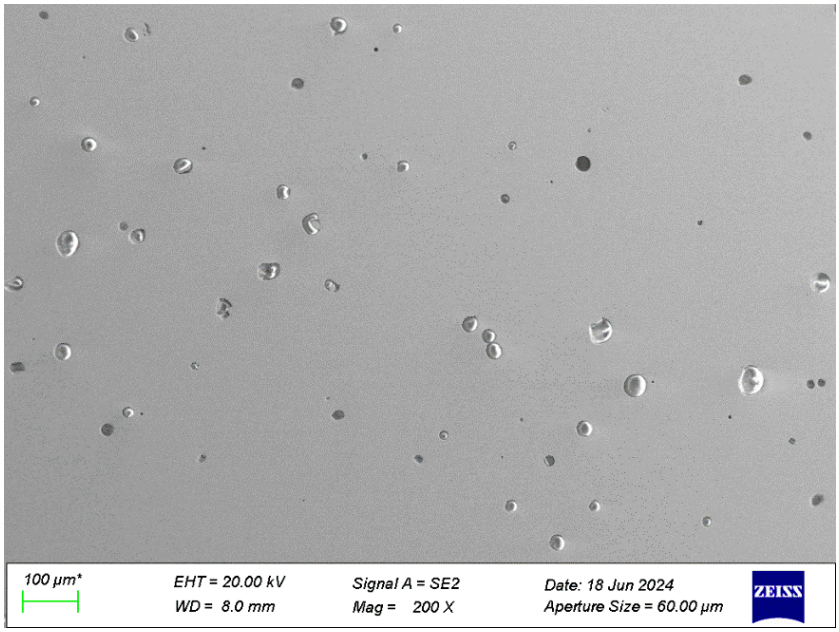

Figure 4.20. SEM-SE image showing porosity within the LPBF sample.

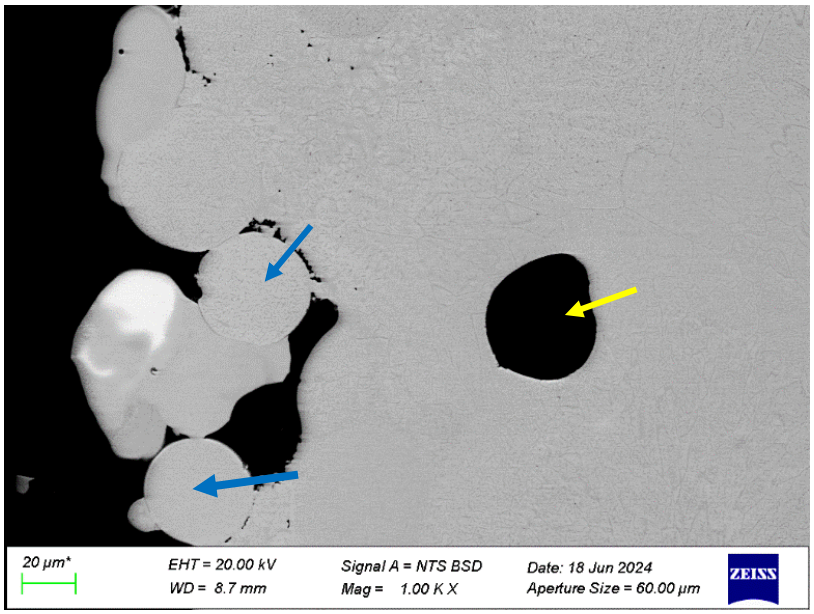

Figure 4.21. SEM-BSE image showing the side of the LPBF sample: yellow arrow indicates a pore, blue arrows show unmelted powder particles and the light region is probably unmelted tantalum.

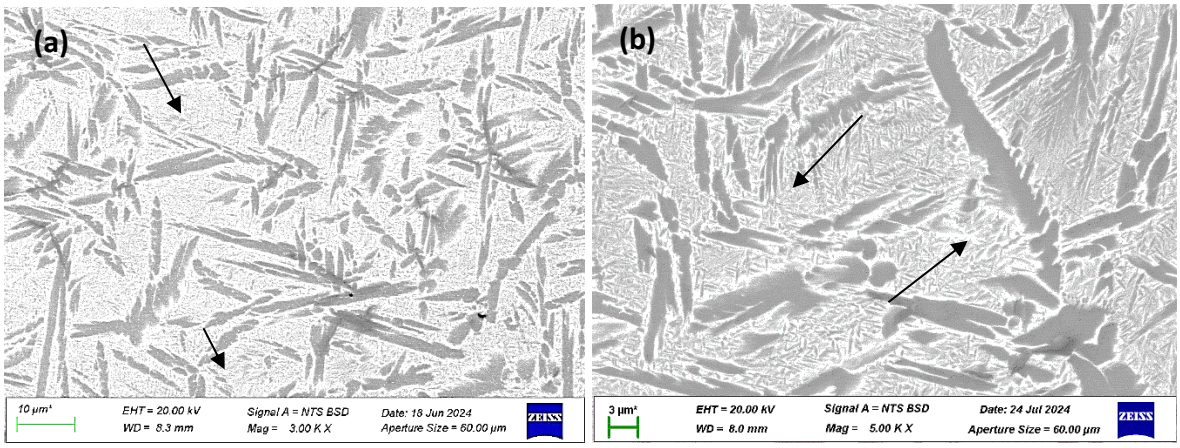

Figure 4.22. SEM-BSE images of as-cast Ti-6Ta-1.5Zr-0.2Ru-5Cu (mass%): (a) lower magnification: (βTi) (light) grains with (αTi) (dark) precipitated on grain boundaries and within and (b) higher magnification. Black arrow indicates Ti_2Cu precipitates.

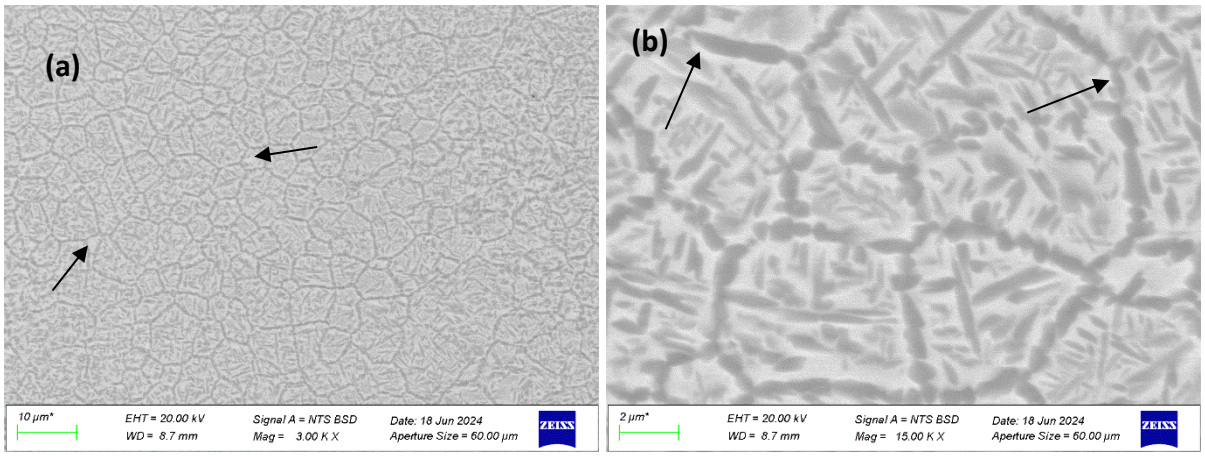

Figure 4.23. SEM-BSE images of Ti-6Ta-1.5Zr-0.2Ru-5Cu (mass%) LPBF horizontal cross-section: (a) low magnification showing equiaxed (αTi) along (βTi) grain boundaries and within the grains and (b) high magnification, (βTi) (light contrast) and (αTi) (dark contrast); the black arrow indicates Ti_2Cu precipitates (very light contrast).

Table 4.7 shows the EDX results for each sample. The LPBF sample had lower Cu and higher Ta compositions than the as-cast sample, while both samples showed similar Ti, Zr and Ru compositions. The as-cast (Spotose, 2023) sample had the expected Ti and Ru, with higher Ta and Zr and lower Cu.

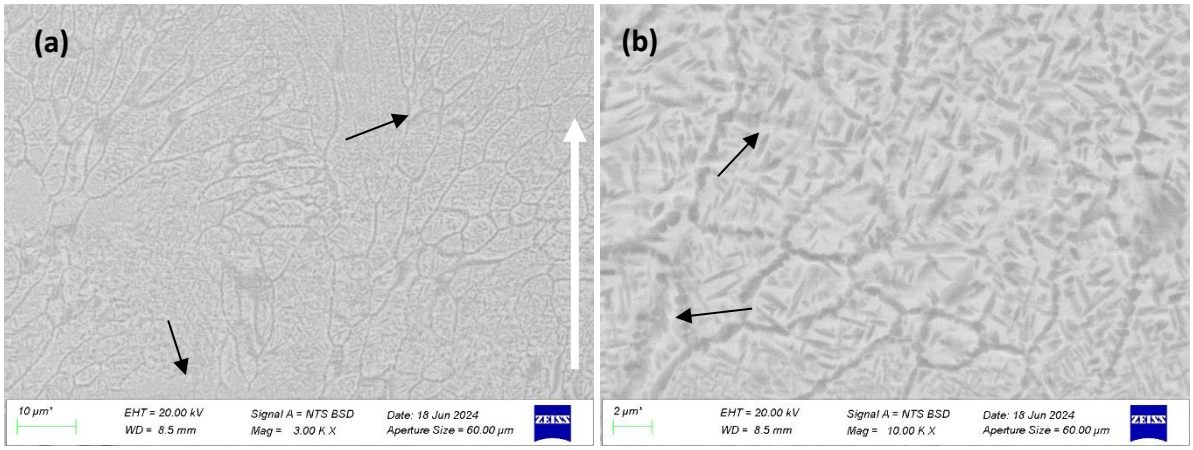

Figure 4.24. SEM-BSE images of LPBF Ti-6Ta-1.5Zr-0.2Ru-5Cu (mass%) vertical cross-section: (a) low magnification showing (αTi) along (βTi) grains and (b) high magnification, (βTi) (light) and (αTi) (dark). White arrow indicates build direction.

Table 4.7. Areal EDX results of LPBF, as-cast and as-cast (Spotose,2023) samples of Ti-6Ta-1.5Zr-0.2Ru-5Cu (mass%).

Alloy	**EDX (mass %)**				
	Ti	**Ta**	**Zr**	**Ru**	**Cu**
As-cast	84.4±0.5	6.4±0.2	1.4±0.2	0.4±0.2	7.4±0.3
As-cast (Spotose, 2023)	86.0±1.6	7.4±0.9	2.0±0.8	0.4±0.6	4.5±1.5
LPBF:Horizontal	84.5±0.8	8.9±0.6	1.5±0.1	0.3±0.2	4.8±0.3
LPBF: Vertical	85.4±0.4	8.3±0.4	1.6±0.2	0.1±0.1	4.7±0.2

Table 4.8 shows the EDX results of the light and dark phases in the as-cast Ti-6Ta-1.5Zr-0.2Ru-5Cu alloy (mass%). The light phase (βTi) had low Ti and high Cu content. The Ru and Ta were close to the target composition, while Zr was lower than expected. However, the dark phase (αTi) had higher Ti and lower copper while Zr, Ta and Ru had target compositions.

Table 4.8. EDX results of as-cast light and dark phases of Ti-6Ta-1.5Zr-0.2Ru-5Cu (mass%).

Phase	**EDX (mass%)**				
	Ti	**Ta**	**Zr**	**Ru**	**Cu**
Light (βTi)	84.5±0.9	6.4±0.4	1.0±0.1	0.3±0.1	7.8±0.5
Dark (αTi)	88.3±4.4	5.5±0.9	0.8±0.2	0.2±0.1	5.2±3.3

Figure 4.25 shows the XRD pattern of the LPBF sample with hcp (αTi) as the major phase with peaks at 2θ = ~42°, ~44°, ~47°, ~63°, ~75° and ~86°. The bcc (βTi) has peaks near 2θ = ~67° and ~84° were also present showing (βTi) was retained due to the rapid cooling of the LPBF sample. Peaks at 46° and 51° indicated the Ti_2Cu phase. **Figure 4.26** shows the XRD pattern of the as-cast sample with (αTi) peaks at 2θ = ~42°, ~45°, ~47°, ~63° and ~75°. A less intense peak at 2θ = ~84° was for (βTi) although in smaller amounts. Peaks near 2θ = ~33°, ~46° and ~51° correspond to Ti_2Cu.

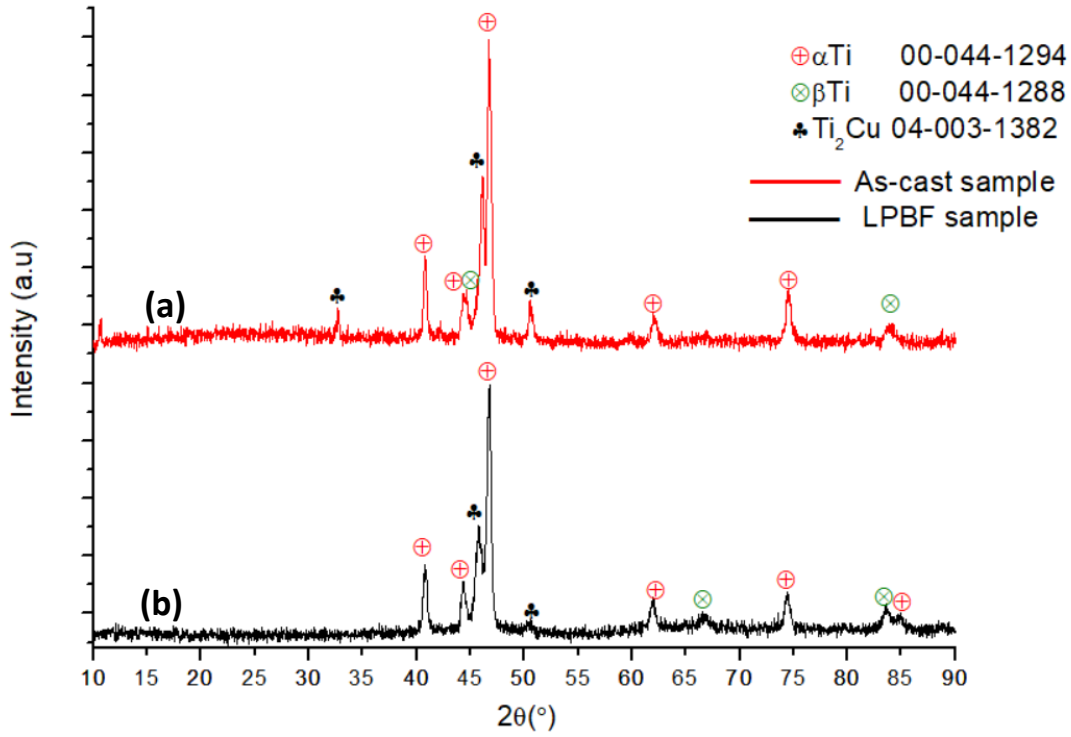

Figure 4.25. XRD patterns of LPBF-manufactured and as-cast Ti-6Ta-1.5Zr-0.2Ru-5Cu (mass%).

4.3.3 Hardness testing

Figure 4.26 shows the hardness profile across the samples. **Figure 4.27** is the photograph, taken using a stereomicroscope, showing the samples used to generate the hardness profile, with the indentations spaced 0.70 ± 0.02 mm apart. The LPBF sample had higher hardness, except at distances of 0.484 mm and 3.91 mm from the edge of the sample. The LPBF sample showed more hardness variability, fluctuating between ~350 $HV_{0.05}$ and ~450 $HV_{0.05}$, whereas

the as-cast sample showed a more consistent hardness of ~350 $HV_{0.05}$. However, for the LPBF sample, after the initial variations, the hardness was similar to that of as-cast sample. **Figure 4.28** shows that for random hardness measurements, the LPBF sample had higher hardness than the as-cast sample for all the indentations. The LPBF sample had a mean of 393.54 ± 16.72 $HV_{0.05}$, while as-cast sample had 360.05 ± 11.02 $HV_{0.05}$ with a lower variation.

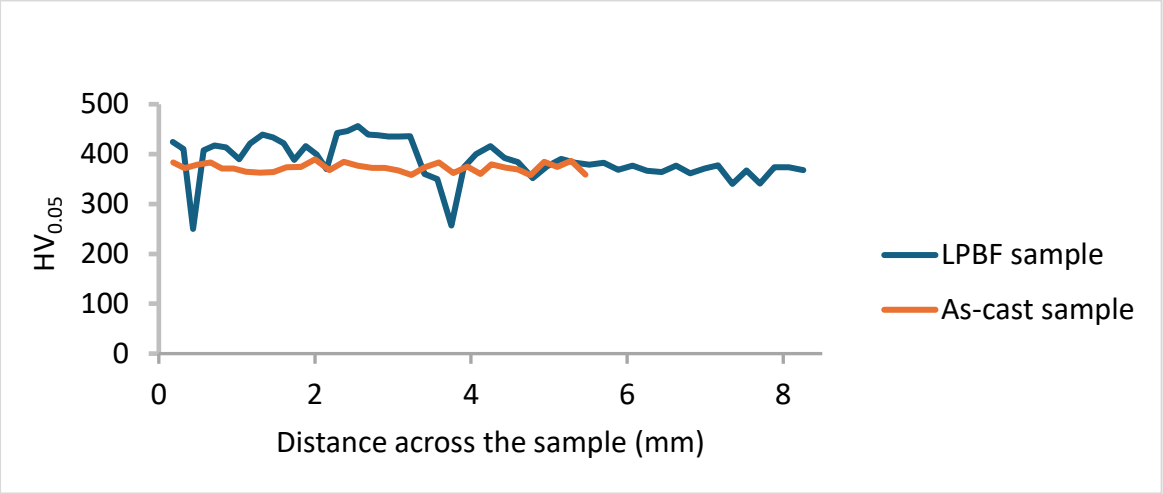

Figure 4.26. Hardness profile for LPBF and as-cast samples measured from the edge.

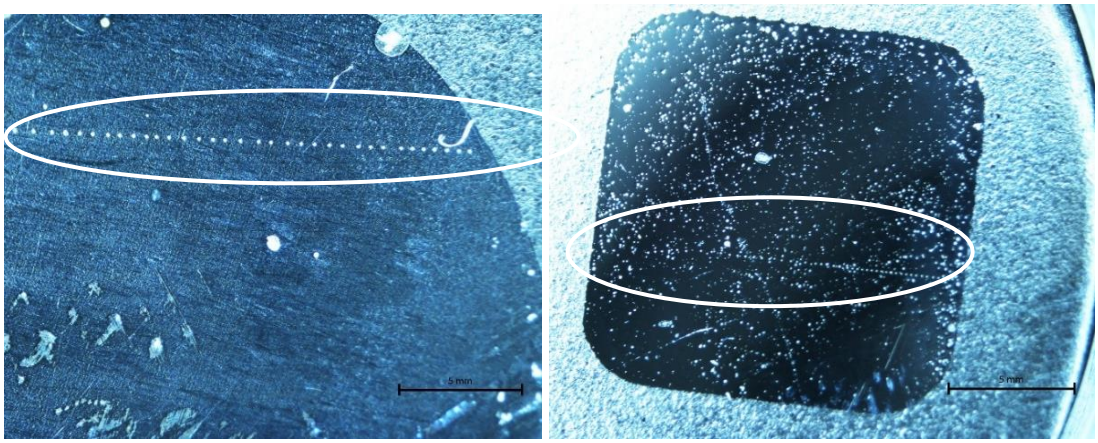

Figure 4.27. Photographs of: (a) as-cast sample and (b) LPBF-manufactured sample showing indentations inside the white ellipses.

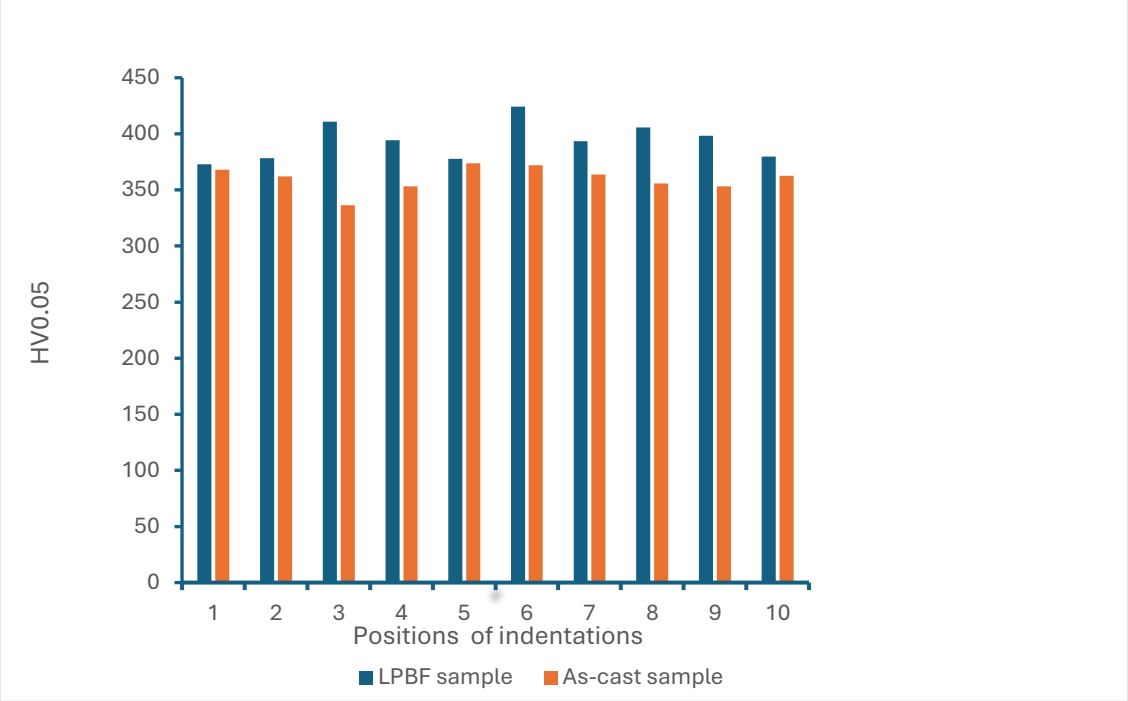

Figure 4.28. Hardness values from random indentations across the samples.

4.3.4 Anti-bacterial testing

The colony counts for the three samples were determined using the third 10-fold dilution, as it provided countable colonies (**Figure 4.29**). Due to the high concentration of colonies, both the first (10^1) and second 10-fold (10^2) dilutions were not used (**Figure 4.30**).

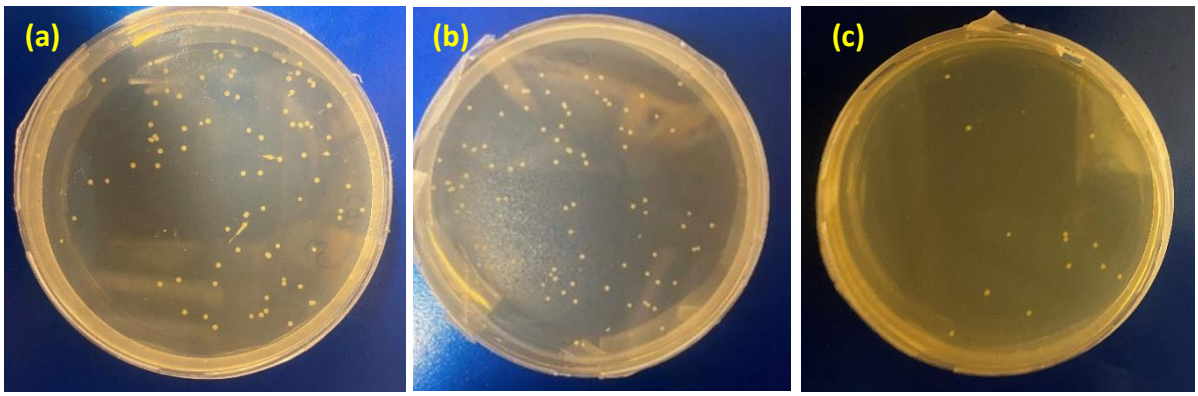

Figure 4.29. Photographs of bacteria count tests after 24 hours: (a) LPBF, (b) as-cast, and (c) Ti-6Al-4V samples, all conducted with three iterative 10-fold dilutions from the second test.

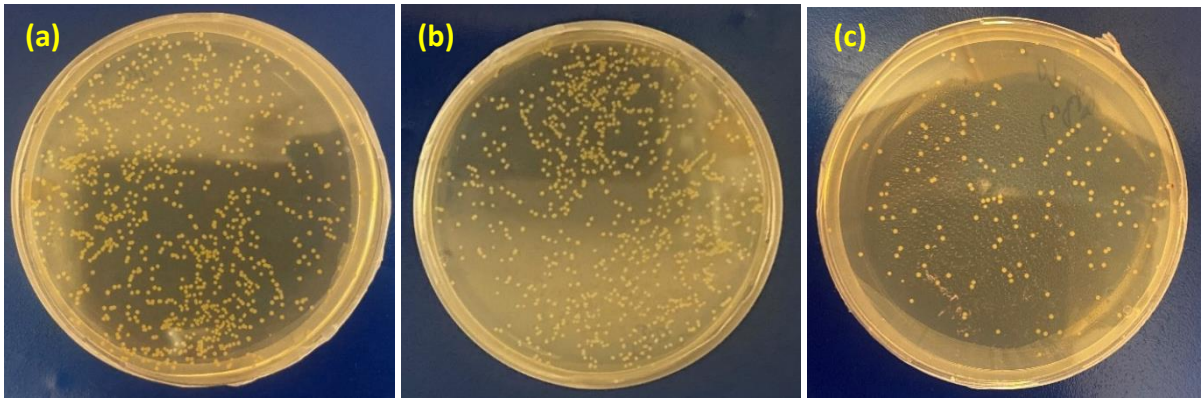

Figure 4.30. Photographs of bacteria count tests after 24 hours: (a) LPBF, (b) As-cast and (c) Ti-6Al-4V samples, all conducted with two iterative 10-fold dilutions from the second test.

Figure 4.31 shows the number of colonies in each sample. The LPBF samples had lower counts than the as-cast samples, with increases observed in the second and third runs ("run" refers to each test done). The highest colony counts were found in the as-cast samples, indicating low antibacterial rates. The Ti-6Al-4V samples had the highest counts in the fourth run, but lower counts in the other runs and higher standard deviations. Conversely, the copper samples had no colonies in all runs, indicating high antibacterial rates.

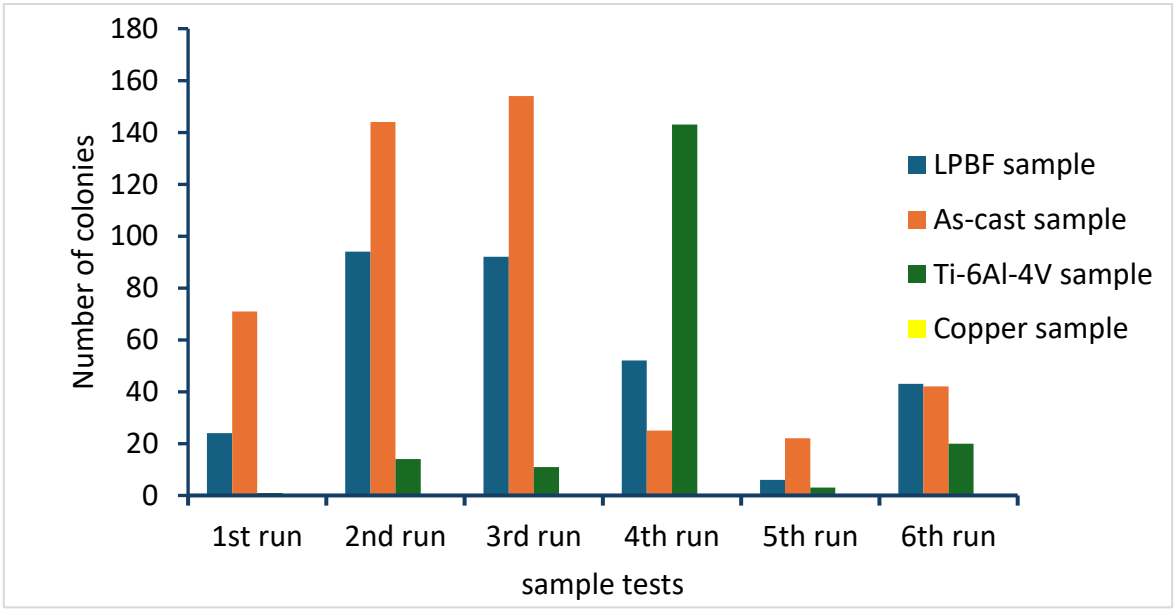

Figure 4.31. Number of colonies counted on each sample in the third 10-fold dilution test (there were no colony counts for copper sample).

Figure 4.32 shows the colony forming units (CFU) counts from multiple experimental runs with significant differences in bacterial adhesion and colony formation across each sample, with similar trends to **Figure 4.31**. The LPBF samples had a lower average CFU count than as-cast samples (**Table 4.9**). These averages were calculated from six tests, with three samples tested twice each.

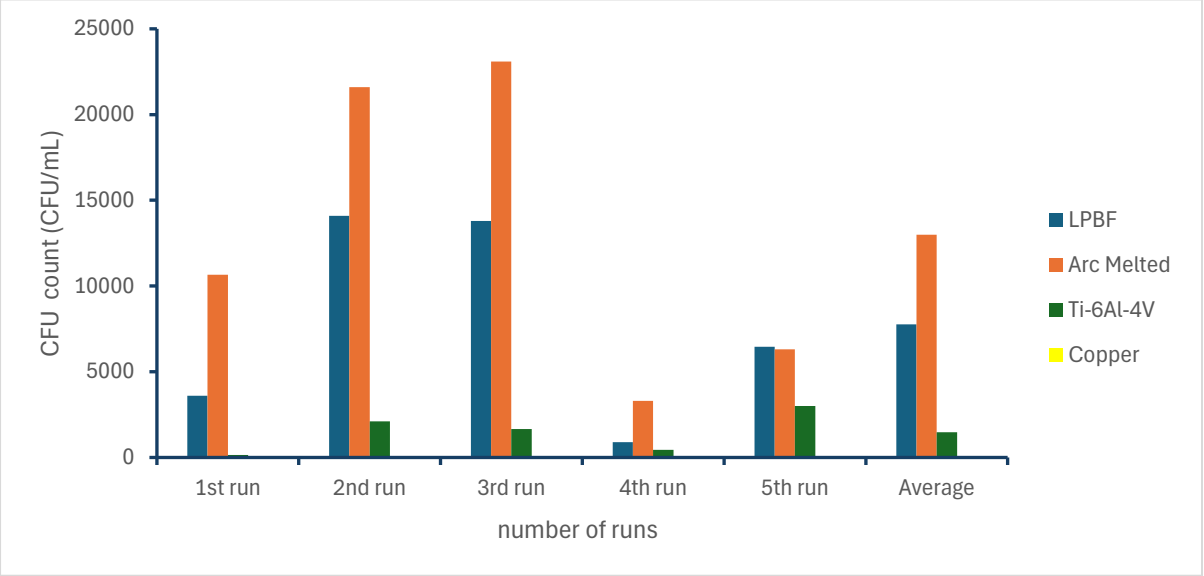

Figure 4.32. Colony-forming unit (CFU) counts of each sample bacteria after 24 hours (there were no colony counts for copper sample).

Table 4.9. Comparison of average colony-forming unit (CFU) counts for different samples.

Sample	**Average CFU Count (CFU/mL)**	**Observations**
LPBF-manufactured	7770 ± 5974	Better antibacterial properties
As-cast	12990 ± 8950	Higher bacterial adhesion and colony formation
Ti-6Al-4V	1470 ± 1178	Moderate antibacterial properties
Pure Copper	0 ± 0	Killed all the bacteria

The antibacterial rate could not be calculated using averages, as the control samples (Ti-6Al-4) had fewer colony counts than the Ti-6Ta-0.5Zr-0.2Ru (mass%) alloy and would result in negative antibacterial rate. However, as shown in **Figure 4.32**, this was not consistent across all experimental runs.

4.3.5 Corrosion test results

4.3.5.1 Open circuit potential profiles

Figure 4.3 shows the open circuit potential (OCP) curves for Ti-6Ta-1.5Zr-0.2Ru-5Cu (mass%) alloys manufactured by as-cast and LPBF methods. The as-cast alloy shows higher and more stable OCP, stabilising ~–0.12 V, indicating the formation of a stable passivation oxide layer (Abou Shahbha et al., 2011). In contrast, the LPBF-manufactured alloy started at a more negative potential and had fluctuations, including a sharp dip at around ~900 s and a gradual decrease after 2500 s. This indicated the breakdown in passive film and then repassivation, indicating potential instability or thinning of the passive film.

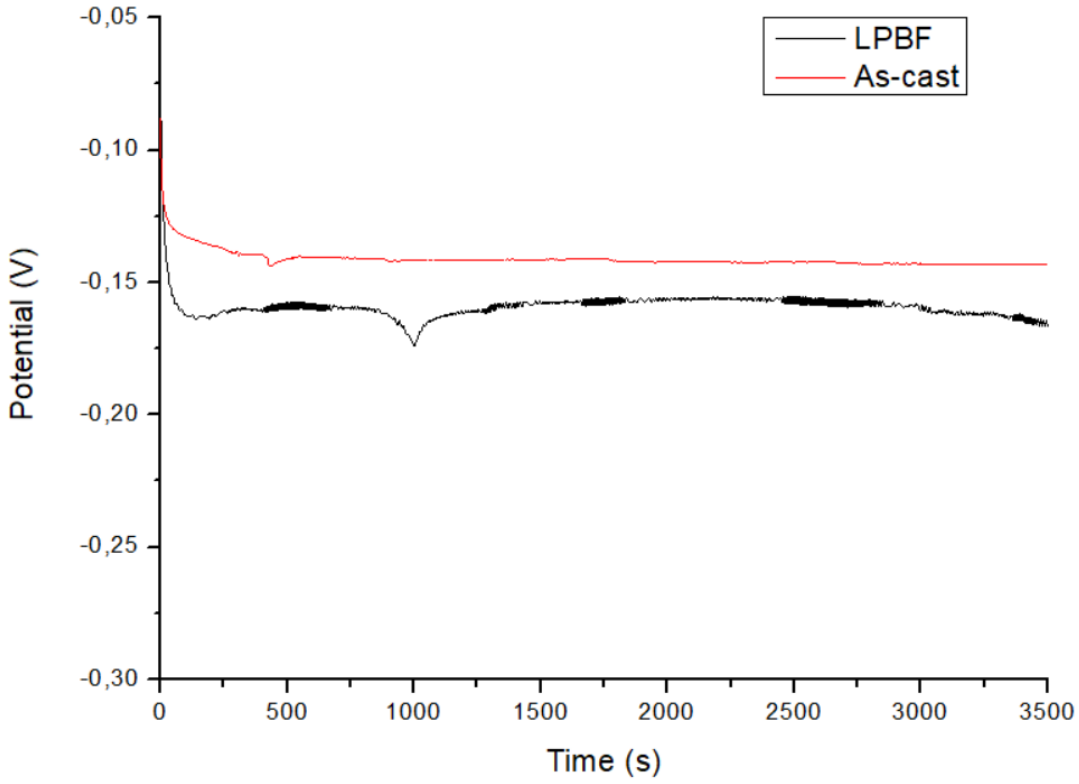

Figure 4.33. OCP profiles of the Ti-6Ta-1.5Zr-0.2Ru-5Cu (mass%) alloys in phosphate-buffered saline solution.

4.3.5.2 Potentiodynamic polarisation curves

Figure 4.34 shows the potentiodynamic polarisation curves for the Ti-6Ta-1.5Zr-0.2Ru-5Cu (mass%) alloys. The as-cast sample exhibited a more positive corrosion potential (E_{corr}),

indicating a lower thermodynamic tendency to initiate corrosion. The LPBF-manufactured and as-cast samples exhibited similar passive current densities (I_{pass}), indicating comparable passive film stability. Although the LPBF alloy had a slightly lower E_{corr}, it had a broader passive region and spontaneous passivation, suggesting improved long-term corrosion resistance. The corrosion current density (I_{corr}) was lower for LPBF sample than the as-cast sample, shown by the Tafel extrapolation curves intersection of the polarisation curves (**Figure 4.34**). This lower I_{corr} implied a reduced corrosion rate, showing the superior electrochemical stability of the LPBF-manufactured alloy.

The corrosion rates of the samples were calculated from potentiodynamic polarisation curves (**Figure 4.34**) using the Tafel extrapolation method (Choubey et al., 2004). **Table 4.10** shows that the as-cast sample had a higher corrosion rate than the LPBF manufactured sample.

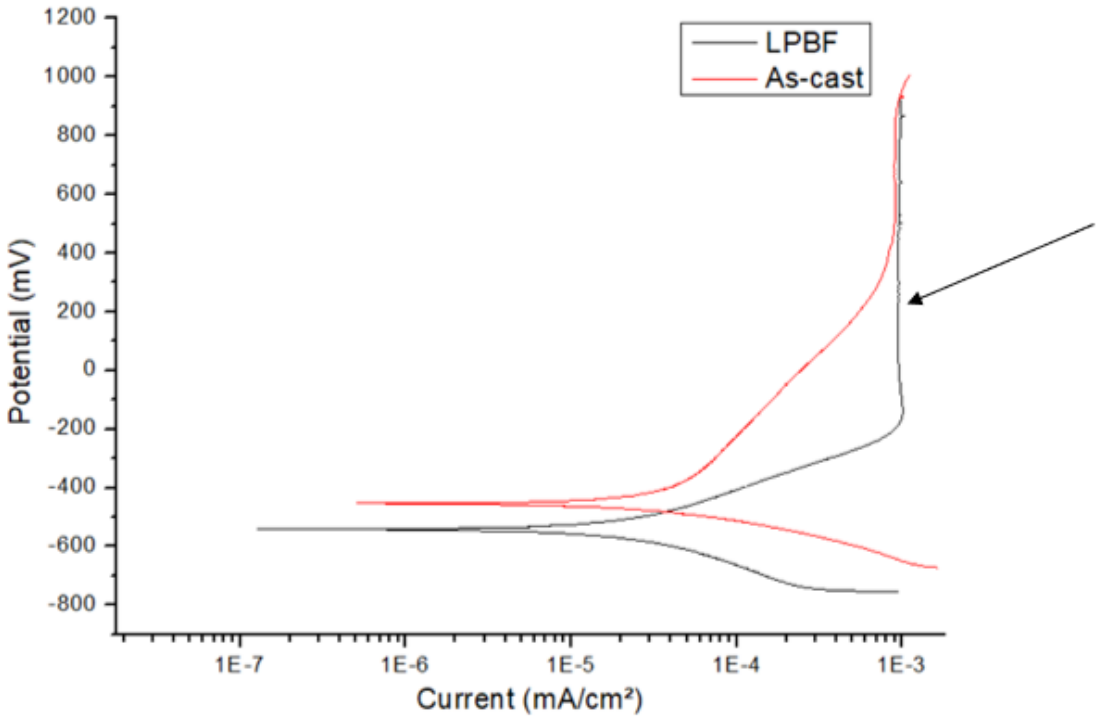

Figure 4.34. Potentiodynamic polarisation curves of Ti-6Ta-1.5Zr-0.2Ru-5Cu (mass%) alloys in phosphate-buffered saline solution, black arrow shows broader passive region in LPBF.

Table 4.10. Polarisation results of the Ti-6Ta-1.5Zr-0.2Ru-5Cu (mass%) alloy.

Manufacturing technique	**E_{corr} (mV)**	**I_{corr} (mA/cm^2)**	**Corrosion rate (mm/year)**
As-cast	-471.25 ± 46.26	3.74E-05 ± 8.69E-06	3.27E-03 ± 7.62E-05
LPBF	-573.05 ± 37.69	2.65E-05 ± 7.09E-06	2.32E-3 ± 6.21E-05

4.3.5.3 Characterisation of corroded samples

Figures 4.35 and 4.36 show the corroded surfaces of the as-cast and LPBF alloys after exposure to PBS solution at 37 ± 1°C. Prior to corrosion testing, the as-cast and LPBF samples had similar surface roughness and morphology due to same sample preparation. After corrosion testing, the observed differences in surface roughness and morphology were due to corrosion. **Figure 4.36(b)** had pores from casting that acted as sites for corrosion. **Figure 4.35(a)** shows scattered corrosion products on the sample surface, while in **Figure 4.35(b)**, shows a pore covered by corrosion products and unmelted powder particles.

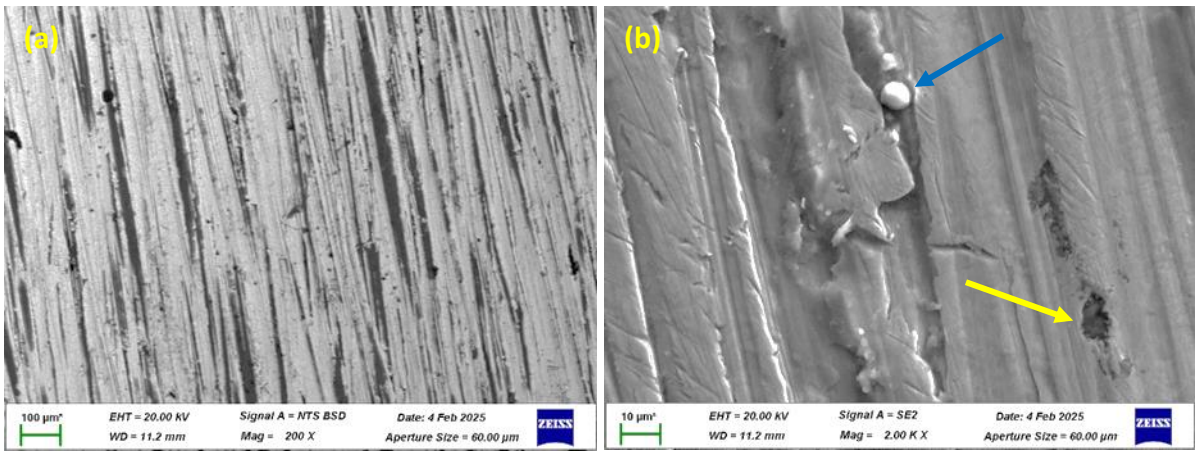

Figure 4.35. SEM-SE images of as-cast Ti-6Ta-1.5Zr-0.2Ru-5Cu (mass%) after corrosion tests: (a) lower magnification and (b) higher magnification: Yellow arrow indicates pore from casting and blue arrow indicates a precipitate from PBS solution.

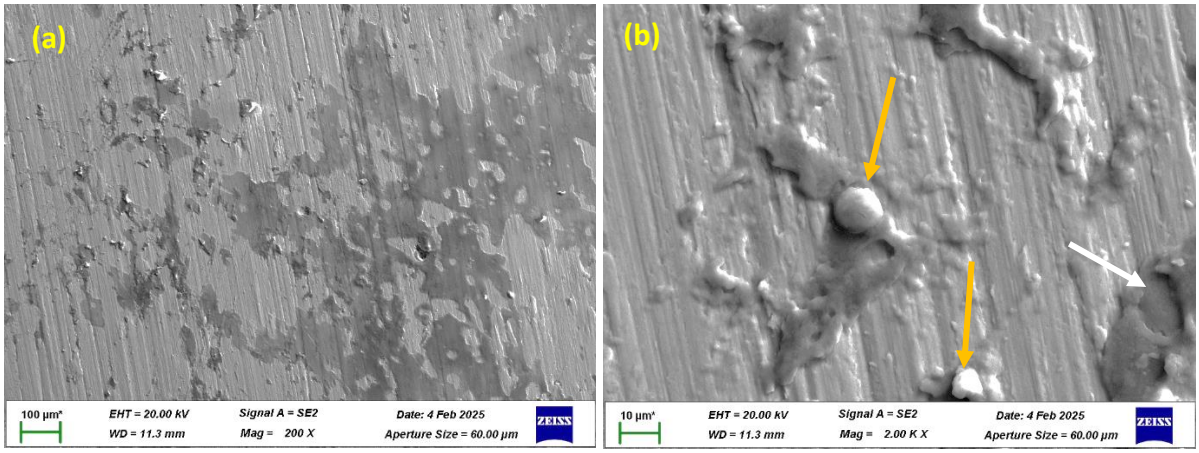

Figure 4.36. SEM-SE images of LPBF Ti-6Ta-1.5Zr-0.2Ru-5Cu (mass%) after corrosion tests: (a) low magnification showing scattered corrosion products on the surface (dark contrast) and (b) high magnification showing unmelted powder particles (orange arrows) and a pore (white arrow).

Table 4.11 shows the EDX analyses of both samples, showing that the dark regions comprised elements from the PBS solution (chlorine, potassium, calcium and sodium). These elements were also detected within a pore, suggesting that the PBS solution became entrapped in the casting defect. The presence of O and C on both samples indicated the formation of oxide and carbon-based corrosion products. The large standard deviations in Ti, O and C compositions across different regions indicated significant surface heterogeneity. This variability showed uneven corrosion and localised oxide formation, particularly in the dark regions. The as-cast sample did not show any detectable Ru after corrosion, possibly due to its low initial concentration.

Table 4.11. EDX results of as-cast and LPBF Ti-6Ta-1.5Zr-0.2Ru-5Cu (mass%) after corrosion tests.

Alloy	**EDX results (mass%)**										
	Ti	**Ta**	**Zr**	**Ru**	**Cu**	**O**	**C**	**Na**	**Cl**	**Ca**	**K**
As-cast (Areal)	63 ± 5.0	4.4 ± 0.1	0.9 ± 0.4	-	3.4 ± 0.8	21.5 ± 5.7	6.5 ± 0.1	0.3 ± 0.1	-	-	-
As-cast (Light region)	80.7 ± 4.0	4.2 ± 1.2	1.4 ± 0.4	-	3.2 ± 0.1	6.1 ± 1.1	4.0 ± 0.4	-	-	-	-
As-cast (Dark region)	19.3 ± 5.2	1.5 ± 0.8	0.5 ± 0.4	-	1.0 ± 0.1	50.2 ± 0.4	25.0 ± 5.8	1.5 ± 1.2	0.2 ± 1.9	0.2 ± 0.1	0.6 ± 0.7
LPBF (Areal)	55.1 ± 4.2	4.0 ± 0.3	0.7 ± 0.5	0.1 ± 0.1	2.7 ± 0.2	33.0 ± 4.6	3.9 ± 3.5	0.4 ± 0.2	0.1 ± 0.1	-	-
LPBF (Light region)	76.3 ± 0.8	5.7 ± 0.4	1.4 ± 0.1	0.1 ± 0.1	3.6 ± 0.2	12.9 ± 2.4	-	-	-	-	-
LPBF (Dark region)	26.2 ± 6.9	1.5 ± 0.4	1.3 ± 0.3	0.1 ± 0.1	1.1 ± 0.3	58.6 ± 5.0	8.6 ± 3.0	1.2 ± 0.2	0.5 ± 0.1	0.5 ± 0.1	0.4 ± 0.1

Chapter 5. Discussion

5.1 Powder characterisation

The Ru and Zr particles occurred in minor proportions in the powders, hence they were not discerned (**Figure 4.1(a)**). **Figures 4.4** and **4.6(a)** show spherical particles, although there were also irregular particles. This may have been caused by the collision of the droplets with each other causing distortions. The non-spherical shape could also be caused by incomplete spheroidization whereby the powder particles retain their previous shape and form ellipsoidal or other irregular shapes (Qi et al., 2021). **Figure 4.6**(**b**) shows fine dendrites due to rapid cooling during the atomisation.

Before atomisation, Zr was weighed along with the liquid in which it was stored to prevent oxidation. As a result, a lower concentration of Zr is listed in **Table 4.1**. The EDX results in **Figure 4.9** show that Ru was not detected, possibly due to its loss during atomisation. Given that Ru was the heaviest element in the sample, it may have settled at the bottom of the melt. Additionally, since ruthenium was deliberately present in small proportions, its distribution may not have been homogeneous, making it less likely to be detected in localised EDX analysis.

The decreased titanium concentration towards the particle boundaries, as shown in **Figures 4.8** and **4.10**, was attributed to inhomogeneous distribution and element segregation during rapid cooling. As the alloy cools quickly, the titanium and copper elements do not have sufficient time to diffuse evenly throughout the alloy, leading to regions with distinct elemental concentrations. The titanium-rich regions tend to stabilize as the αTi phase, while the copper-rich areas promote the formation of the Ti_2Cu phase, both of which are thermodynamically stable in the alloy.

Large particles formed by agglomeration of smaller particles (**Figure 4.13)** had not been atomised correctly. Möller et al. (2022) attributed the phenomenon to “splintering” of the feedstock material before melting. It is likely that the splintered particles, having high surface areas, would combine to form the larger particles and reduce the surface area, even if not atomised properly. Möller et al. (2022) also observed composite particles which formed by spattering of liquid that was ejected from the arc and landed on other particles. In this work, agglomerations of small particles of different compositions were observed **Figure 4.12(a)**. This

could explain some of the irregularly shaped particles containing only Ti, Ta and Cu (**Table 4.2**). These likely formed during the agglomeration of smaller particles with these specific compositions. **Figure 4.12(a)** shows that some spherical particles were included in the agglomeration.

The XRD pattern for powders after atomisation displays peaks for αTi, βTi and Ti_2Cu (**Figure 4.15**). This Ti_2Cu phase is important for antibacterial properties of the alloys (Zhang et al., 2013), which is beneficial for biomedical applications. Before atomisation, Zr and Ru were not expected to have been detected since their concentrations were below the 4 vol.% detection limit for XRD. However, Cu should have been detected, albeit with low peaks. Since the background intensity was high (due to small particle sizes), the Cu peaks were possibly obscured.

Figure 4.11 shows that the original particle size distribution was relatively fine but not uniform, with some larger particles. The narrower particle size distribution (**Figure 4.12)** shows that atomisation reduced the particle size range. However, the presence of a few larger particles, indicated by the second smaller peak, suggests that the atomisation process was not entirely efficient. After atomisation, some of the smaller particles agglomerated, forming larger clumps that were more difficult to disintegrate. This agglomeration may have been caused by moisture or electrostatic attraction (Rescaglio et al., 2017). The powder's PSD after atomisation (**Figure 4.12**) could have been narrower if a #200 μm sieve had been used to remove these agglomerated powders.

The manufactured powders were suitable for the next step, as they were spherical and met LPBF requirements. SEM images (**Figure 4.13**) showed a higher proportion of spherical particles, and the size range was small (**Figure 4.12**), both giving good flowability.

5.2 Single tracks

Balling (**Figure 4.16(d))** is a surface defect which occurs due to severe instability of the molten pool, induced by the high melt viscosity under relatively low energy density (Gonnabattula et al., 2024). This defect decreases surface quality and densification (Dai et al., 2020). Gao et al. (2019) identified high scanning speed as a key factor contributing to balling as identified in

Figure 14.16(d) and **Figure 14.17(d)**. Under these conditions, balling is primarily due to the large Marangoni convection and liquid capillary instability within the molten pool. Balling is caused by insufficient contact of the melt with the solid substrate and occurs with limited energy input due to high scanning speeds (Gao et al., 2019).

High power and lower scanning speed result in higher laser energy density (LED), which causes porosity (Gonnabattula et al., 2024). Conversely, **Figure 4.17(d)** shows that high scanning speed resulted in balling, indicating defect formation at different scanning speeds through distinct mechanisms. Guo et al. (2018) studied single-track fabrication of niobium and titanium alloys finding that when laser energy density increased, the track width and substrate penetration also increased. This occurred in the current work because when the LED increased, the tracks were more even. Conversely, Gong et al. (2014) reported that high laser power with low scanning speed can cause excessive energy input, leading to melt pool overheating, evaporation and defects. However, in **Figure 4.17(a)-(b**), the single track appeared even and continuous, suggesting that defect formation depends on material properties and processing parameters.

The single track shown in **Figure 4.16(a)** was the best single track, with an even, continuous and smooth surface. Although the tracks in **Figure 4.17(a)-(c)** also appear satisfactory, they were produced using a high LED, which can lead to increased porosity (Gonnabattula et al., 2024). However, no porosity was observed on the surface. The tracks were not sectioned, so internal porosity was not assessed. The best parameters were identified as 157.5 W laser power, 600 mm/s scanning speed, 0.15 mm beam diameter, 0.263 J/mm linear energy and 1.750 J/mm^2 planar energy density.

Figure 4.19 shows the peak of Ti_2Cu, which is wanted as it enhances the antibacterial properties of the alloys (Zhang et al., 2013). Although Canale and Servant (2022) identified Ti_3Cu upon solidification and Fowler (2019) found it in a 5 mass% Cu sample, the XRD peaks of Ti_2Cu and Ti_3Cu are so similar that they are indistinguishable at low amounts. The Ti_3Cu phase was considered unstable (Dyal Ukabhai et al., 2022). This instability was shown by diffusion couple studies (Dziadon and Konieczny, 2004; Song et al., 2009), which found only Ti_2Cu and TiCu, with no trace of Ti_3Cu. Additionally, Klotz and Liu (2007) found that annealing a Cu-Ti diffusion couple at 800°C for 864 hours failed to produce Ti_3Cu, showing its instability,

even under typical processing conditions. Therefore, given its instability (Dyal Ukabhai et al., 2022), it is not surprising that Ti_3Cu did not form in this alloy.

5.3 Comparison between LPBF and as-cast manufactured alloy samples

5.3.1 Density

The notable pores observed in Ti-6Ta-1.5Zr-0.2Ru-5Cu (mass%) (**Figure 4.20**) manufactured by LPBF led to reduced density, the pores were likely due to incomplete melting, which resulted in both poor bonding and overlap between adjacent tracks. Insufficient overlap can create gaps or cause pooling. According to Biamino et al. (2011) and Singla et al. (2021), high solidification rates can prevent the evaporation of gas bubbles from molten powder particles, trapping argon and leading to porosity. Porosity can also originate from entrapped inert gas within the powder stock during atomisation (Chen et al., 2018). Gona et al. (2014) found that reduced energy density or wider hatch spacing can decrease overlap, affecting wettability and thermal conductance. Furthermore, incomplete melting combined with low laser energy input can trap unfused powder particles within the solid material, resulting in porosity (Gona et al., 2014). Low energy input limits heat penetration, hindering fusion between layers and powder particles. The molten pool's surface tension fails to fully wet and incorporate unmelted particles and rapid solidification retains these gaps as pores.

Porosity in LPBF can be affected by various factors related to scanning. The 67° rotation between layers, designed to minimise anisotropy and layer defects, can cause misalignment and gaps if not properly controlled. Ali et al. (2018) recognised that unsuitable overlap and rotation may lead to thermal mismatches between layers, which can also contribute to porosity. Nkosi and Sacks (2023) reported that bidirectional alternating scanning with a 67° rotation led to porosity due to the laser being turned off during transitions, resulting in unmelted powder particles and poor fusion. The 67° rotation strategy could be beneficial, although improper implementation of scanning parameters can introduce thermal inconsistencies and scan interruptions, increasing porosity, so it needs careful use.

5.3.2 Microstructures and chemical compositions of the manufactured alloys

The microstructure of the Ti-6Ta-1.5Zr-0.2Ru-5Cu (mass%) alloy manufactured by LPBF (**Figure 4.23**) had finer microstructure than as-cast samples (**Figure 4.22**), a difference attributed to the faster cooling rates in LPBF samples, which range from 10^5 to 10^7 K/s, than slower cooling rates of arc-melting, ranging between 10^2 and 10^3 K/s (Liu et al., 2022; Yadroitsev et al., 2021; Dawes et al., 2015). The (αTi) phase preferentially formed along (βTi) grain boundaries because it is a phase transformation and the grain boundaries provide more space (i.e. a looser structure), which enhances diffusion and facilitates phase growth. The Ti-enriched boundaries provide favourable sites for (αTi) nucleation, resulting in the observed microstructures (Greer, 2016). The coarser needles in the as-cast grains (**Figure 4.22**) were due to slower cooling during solidification, whereas LPBF samples cooled rapidly, producing a fine grain microstructure, **Figure 4.23(a)**. While the rapid cooling rates and steep thermal gradients of LPBF can affect solidification, they do not alter the two-phase nature of the alloy. The processing conditions may lead to changes in the morphology, such as finer precipitates of (αTi) along grain boundaries and within the (βTi) grains. The alignment of most of the grains along the build direction (**Figure 4.24(a)**) resulted from the directional heat flow and repeated melting-solidification cycles during the layer-by-layer deposition, driving columnar grain growth parallel to the thermal gradient (Pesode and Barve, 2023). This anisotropic grain structure can introduce anisotropy in mechanical properties, such as tensile strength and fatigue resistance (DebRoy et al., 2018).

Spotose (2023) observed a residual dendritic microstructure in an as-cast Ti-6Ta-1.5Zr-0.2Ru-5Cu (mass%) alloy, and there was subsequent growth of needle-like (αTi) and colonies of parallel laths. Additionally, there were Ti_2Cu precipitates. The as-cast microstructure showed laths, indicating the formation of a second phase during cooling.

The LPBF microstructure (**Figure 4.23**) shows regions of a lamellar (αTi) within (βTi), characteristic of a Widmanstätten-type morphology. In the as-cast sample (**Figure 4.22**), slower cooling produced larger (αTi) laths within the (βTi) grains, giving a coarse Widmanstätten morphology. In contrast, the rapid cooling of LPBF produced finer (αTi) laths

The LPBF microstructure (**Figure 4.23**) shows regions of lamellar (αTi) within (βTi), characteristic of a Widmanstätten-type morphology. In the as-cast sample (**Figure 4.22**), slow

cooling rates resulted in coarse (βTi) grains due to limited nucleation, which allowed the growth of larger (αTi) laths within the (βTi) grains, producing a coarser Widmanstätten morphology. In contrast, LPBF exhibited smaller (βTi) grains due to more nucleation sites from faster cooling rates, leading to finer (αTi) laths. ImageJ measurements showed this: the average lath width of the as-cast sample was 1.3 ± 0.6 µm, compared with 0.45 ± 0.19 µm for the LPBF sample. Liu et al. (2024) showed that LPBF-produced Ti-*x*Cu alloys exhibited a mixture of martensite (α') and Ti_2Cu (**Figure 5.1**), and transmission electron microscopy (TEM) revealed that nanoscale Ti_2Cu phases precipitated at the interfaces of α' laths in Ti-2Cu, Ti-5Cu, and Ti-8Cu alloys. This agrees with the Ti_2Cu found in the alloys in this study.

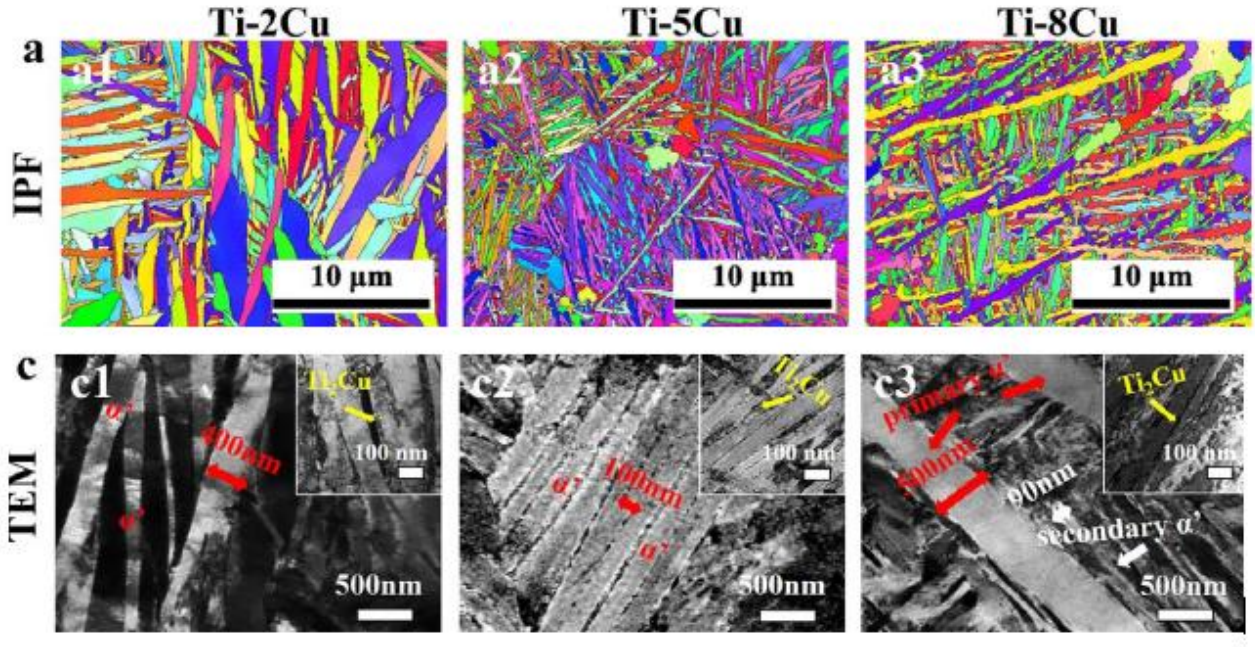

Figure 5.1. IPF maps and TEM images of LPBF-produced Ti-*x*Cu alloys (*x* = 2, 5, 8 wt%), showing finer α' martensite and increased Ti_2Cu precipitation with higher Cu content (Liu et al., 2024)

Hayama et al. (2014) found that slow cooling of as-cast Ti-5Cu (mass%) alloy produced a microstructure with (αTi) and Ti_2Cu phases. The phases were identified by their contrast in BSE imaging, where (αTi) appeared dark and Ti_2Cu appeared light. This microstructure resulted from a eutectoid transformation, although some (αTi) also formed at temperatures above the eutectoid reaction. Similarly, the slow cooling of the Ti-4.5Cu alloy resulted in the (αTi) phase with Ti_2Cu precipitates (Bhaskaran et al., 1985; Bumke et al., 2021). These microstructures resembled those of as-cast sample (**Figure 4.24**), which exhibited (αTi) (dark)

and (βTi) (light)) phases and Ti_2Cu which appeared lighter than (βTi) and was also identified by XRD (**Figure 4.25**).

5.3.2.1 Chemical compositions of the manufactured alloys

In the LPBF samples, the differences between the horizontal and vertical scans were minimal (**Table 4.7**), with only minor variations in Ti, Ta and Cu compositions. This consistency demonstrated that the LPBF process effectively controlled the distribution of alloying elements. The laser scanning strategy influences heat input and cooling rates, which affect elemental segregation (DebRoy et al., 2018). The small variations in Cu content (4.7 ± 0.2 mass% 4.8 ± 0.3 mass%) (**Table 4.7**) affect the antibacterial properties, as the reported minimum Cu content required for effective antibacterial performance varies. While Zhang et al. (2013), using powder metallurgy, suggested a threshold of 5 mass% Cu, Wang et al. (2019), using as-cast, demonstrated antibacterial effects in Ti-Cu alloys with as little as 3 mass% Cu.

In the as-cast sample, Ta and Zr were similar to the targeted composition, although Ru was slightly higher. The cooling rate plays a crucial role in determining the morphology and distribution of Ti_2Cu precipitates. A slower cooling rate promotes the segregation of Cu into the (βTi), leading to a locally higher Cu concentration and facilitating the formation of Ti_2Cu precipitates (Akbarpour et al., 2022). Using Thermo-Calc (**Figure 5.2**), Spotose (2023) showed that the transformation from (βTi) to (αTi) first and would likely occur on the grain boundaries first. Subsequently, Ti_2Cu would nucleate within the grains rather than at the grain boundaries as forms in a eutectoid reaction ((βTi) → Ti_2Cu + (αTi)), as shown **Figure 2.17. Table 4.8** shows that the light phase had more Cu than the dark phase. When the effect of Ta is ignored to distinguish between (βTi) and (αTi) because it was present in the same amounts (~6 mass% Ta). The Ti_2Cu was demonstrated as a small light contrast phase in **Figure 4.22.** Spotose (2013) found that there were only small amounts of light contrast Ti_2Cu within the grains (**Figure 2.17(b)**) and the amounts ~13% agreed with the Thermo-Calc results of Spotose (2023) (**Figure 5.2**).

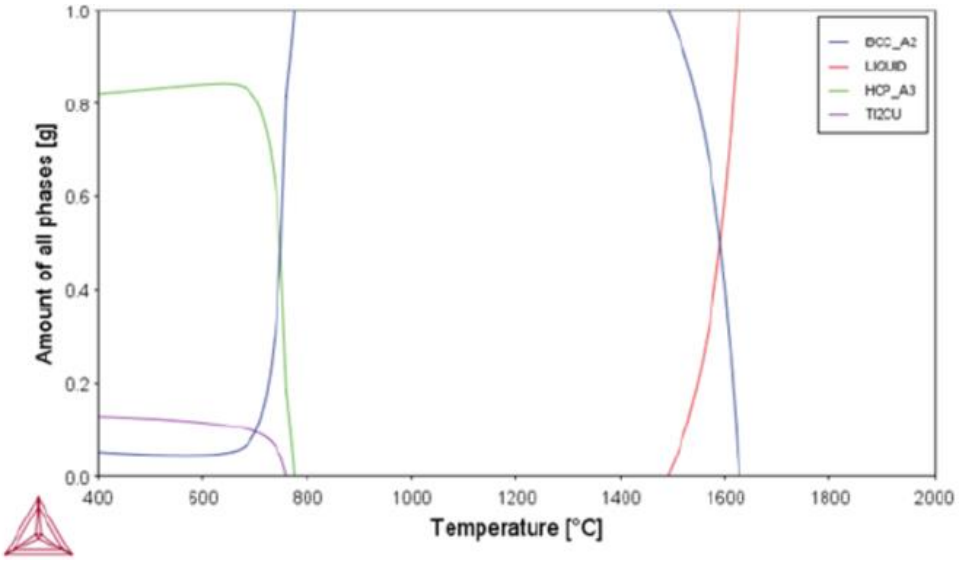

Figure 5.2. Phase proportion diagram of Ti-6Ta-1.5Zr-0.2Ru-5Cu (mass%) (Spotose, 2023).

5.3.2.2 XRD results

The XRD pattern of the as-cast sample (**Figure 4.25(a)**) had narrower peaks due to narrower composition ranges in the phases. In contrast, the LPBF-manufactured sample (**Figure 4.25(b))** showed broader peaks corresponding to a wider compositional range, possibly due to less diffusion and residual stress The as-cast sample showed higher intensity, sharp Ti_2Cu peaks, indicating a higher fraction of Ti_2Cu precipitates and the slower cooling rate promoted the formation of (αTi), as this phase is stable at lower temperatures (Dyal Ukabhai., 2022). In the LPBF sample, the fewer and broader Ti_2Cu peaks indicate fewer precipitates from rapid solidification, with broadening likely caused by residual stresses from thermal cycling during building (Ni et al., 2019). Additionally, the LPBF process favoured (βTi) retention, reducing the extent of (αTi) formation.

Although **Figure 4.25** shows (αTi), (βTi), and Ti_2Cu peaks, Liu et al. (2023) and Wang et al. (2021) argued that Ti_2Cu and (βTi) peaks in XRD patterns of LPBF-manufactured Ti-5Cu and Ti-6Al-4V alloys were difficult to distinguish. This was due to the low volume fraction of these phases and the potential for small peaks being lost in the background noise. As a result, the observed peaks mainly corresponded to the (αTi) as other phases were likely too minor (less than 4 vol.%) to be detected. The XRD results in this study are consistent with Vilardell et al. (2020) and Goettgens et al. (2023), showing similar phases, with differences in peak intensities due to different phase proportions.

The smaller (βTi) peak (2θ = ~84°) in **Figure 4.25(b)** than in **Figure 4.25(a)** was because LPBF-manufactured Ti alloys retained (βTi) due to the localised reheating during the layer-by-layer processing, where previously deposited layers partially re-melted. This stabilised (βTi), making it more prevalent in LPBF-processed than as-cast samples (Cao et al., 2023).

5.3.3 Hardness

The higher hardness in the LPBF-manufactured sample was due to faster cooling rates, which resulted in a finer grain structure with smaller (αTi) grains. As shown in **Figure 4.28** and **Figures 4.22 and 4.23**. These variations resulted from non-uniform heat distribution during rapid laser melting and solidification, inducing high residual stresses and fine microstructures that increased hardness (DebRoy et al., 2018; Cerezo et al., 2024). However, the pores (**Figure 4.20**) at distances (from the sample edge) of 0.5 mm and 39 mm (**Figure 4.26**) weakened the material. The pores reduce hardness by causing localised stress concentrations that facilitate crack propagation (Cobbinah et al., 2020; Cerezo et al., 2024), as well as reducing the cross-sectional area that supported the load. These effects resulted in wavy hardness profiles, as shown in **Figure 4.26**.

The finer microstructure of LPBF-manufactured samples generally increases hardness because smaller grain sizes enhance dislocation density, strengthen the alloy and slow crack initiation and propagation by increasing grain boundary resistance, which diverts and hinders crack growth (Leyens and Peters, 2003). Smaller grains also improve strength and toughness by grain boundary strengthening, following the Hall-Petch effect (Hall, 1951). Wang et al. (2023) found faster cooling gave very fine and lamellar microstructures with β-phase transforming into very thin layers of α' martensite and Ti_2Cu. This created a super-fine microstructure that gave excellent strength and hardness. Conversely, the as-cast (Spotose, 2023) sample had lower hardness but greater consistency, with a standard deviation of ±12 $HV_{0.05}$ versus ±41 $HV_{0.05}$ for the LPBF-manufactured sample. This uniformity was due to the more homogeneous cooling in casting, although the coarser microstructure, with larger grains and reduced overall hardness.

Spotose (2023) reported a hardness of 368 ± 12 $HV_{0.05}$ for Ti-6Ta-1.5Zr-0.2Ru-5Cu (mass%) and the as-cast sample had similar hardness of 373 ± 9 $HV_{0.05}$. The increased homogeneity in

the as-cast sample was likely due to more uniform solidification, which reduced microstructural inhomogeneities. Both the as-cast (Spotose, 2023) and the as-cast sample in this work had lower standard deviations in hardness than the LPBF-manufactured sample (389 ± 41 $HV_{0.05}$). The higher standard deviation in the LPBF sample was due to pores.

The additively manufactured Ti-6Ta-1.5Zr-0.2Ru-5Cu (mass%) exhibited a Vickers hardness of 389 ± 41 $HV_{0.05}$, which is significantly higher than commercially (1) pure titanium (Grade 4), with a hardness of 140-160 HV (Callister and Rethwisch, 2020) and (2) Ti-6Al-4V, which ranges from 330-350 HV (Leyens and Peters, 2003). This increased hardness suggests that Ti-6Ta-1.5Zr-0.2Ru-5Cu (mass%) could provide enhanced wear resistance, potentially improving the durability of dental implants. However, the observed high variation in hardness across the sample indicated significant microstructural heterogeneity. This variability may result in inconsistent mechanical properties, leading to areas of weakness and susceptibility to failure. Such inconsistencies can compromise the overall structural integrity and long-term performance of the implants but could be reduced by post-process annealing (Jamhari et al., 2023).

Annealing in LPBF plays an important role in improving the mechanical properties and overall performance of implants (Jamhari et al., 2023). The rapid cooling rates and non-uniform thermal gradients during LPBF processing often led to residual stresses, pores, and microstructural inhomogeneity, which can cause variability in hardness and affect the use of alloy in the biomedical implant (Nabavi et al., 2024). Post-processing heat treatment such as annealing promotes grain growth and phase transformations, resulting in a more stable microstructure that enhances the hardness and ductility of the alloy (Liu et al., 2020). This process also improves fatigue resistance, which is essential for the long-term performance of implants in load-bearing applications, as the reduction in residual stresses and refinement of microstructures enhances the material's ability to withstand cyclic loading (Marin and Lanzutti, 2023). Additionally, it improves surface properties by reducing defects and enhancing surface finish, which is crucial for biomedical implants, as surface irregularities may lead to corrosion or affect osseointegration (Zhu et al., 2021; Thakur et al., 2022).

5.3.4 Anti-bacterial resistance

The colony-forming unit (CFU) assays for antibacterial testing indicated that LPBF-manufactured samples had better antibacterial performance than as-cast samples (**Figure 4.27**). This can be attributed to the higher number of grain boundaries providing favourable sites for Cu ion release, as well as the finer microstructure and smooth surface, both of which can influence bacterial adhesion and proliferation (Mu et al., 2023). The porous surface (**Figure 4.19**) facilitated the release of Cu ions to combat bacteria (Mitra et al., 2019). The use of pure copper as a positive control meant that it had a strong bactericidal effect, effectively eliminating all bacteria after 24 hours. Conversely, Ti-6Al-4V served as a negative control, expected to have no antibacterial properties. In contrast, the Ti-6Ta-1.5Zr-0.2Ru-5Cu (mass%) sample contains 5 mass% Cu, providing a strong and stable antibacterial effect (Zhang et al., 2016a)

Increased experimental time could have allowed Ti-6Ta-1.5Zr-0.2Ru-5Cu (mass%) to release more copper and kill the bacteria. Hadebe (2022) noted that longer testing times allowed for extended bacterial exposure. However, a potential drawback is that the growth medium, which nourishes the bacteria during the test, may need to be replenished in the well plates, which could interfere with the bacteria's ability to adhere to the sample surface.

Fowler et al. (2019) found that while MC3T3 cells and *Staphylococcus epidermidis* were sensitive to Cu ion concentrations, bacteria could develop resistance, influenced by metal-resistant genes like copper-transporting ATPase *cop*A and multi-copper oxidase (*mco*). Baker et al. (2010) also observed that copper serves as a stress-inducing ion, with concentrations below the MIC value of 200 mM promoting faster bacterial growth than controls without copper. This shows the dose-dependent response of bacteria to copper ions, where concentrations >9×10^{-5} g/ml are toxic to *Staphylococcus epidermidis*, while sub-lethal concentrations between 9×10^{-7} and 9×10^{-6} g/ml can stimulate bacterial growth, potentially as part of a stress adaptation mechanism (Fowler et al., 2019). Ren et al. (2014) demonstrated the antibacterial effectiveness of Ti-6Al-4V-*x*Cu alloys, with antibacterial activity increasing with increasing copper content (*x* = 1, 3 and 5 mass%). The 5 mass% Cu alloy showed significant bacterial elimination, attributed to copper ion release and the antibacterial action of the Ti_2Cu phase. However, excessive copper intake can result in stomach upsets, nausea

and diarrhoea, leading to tissue damage and disease, particularly when copper content is ≥10 mass% (Zhang et al., 2015).

The antibacterial activity of copper involves two mechanisms. The first is direct contact killing, where interaction between the bacterial cell membrane and the copper-containing surface causes membrane rupture and protein inactivation (Liu et al., 2016). The second is ion-mediated toxicity, where Cu^{+} and Cu^{2+} ions released from the alloy surface diffuse into bacterial cells and disrupt vital cellular functions. The LPBF process produced finer microstructure (**Figure 4.23**), which enhanced these mechanisms by increased surface area that improved ion release. Additionally, the surface porosity affects copper ion release and reactivity during corrosion. Compared to as-cast alloys, the LPBF samples had more consistent and effective copper ion diffusion and bacterial interaction (Xu et al., 2023).

5.3.5 Corrosion resistance

The corrosion resistance of Ti-6Ta-1.5Zr-0.2Ru-5Cu alloys varied significantly depending on the manufacturing technique (**Table 4.10**). The as-cast alloy exhibited a more positive corrosion potential (E_{corr}) than the LPBF-manufactured sample (**Figure 4.34**), indicating a lower thermodynamic tendency to initiate corrosion. However, this did not translate into better corrosion resistance, as the as-cast sample showed a slightly higher corrosion current density (I_{corr}), suggesting a higher corrosion rate. Although the as-cast alloy appeared more electrochemically stable based on its OCP behaviour (**Figure 4.33**), the LPBF sample exhibited more spontaneous passivation and a broader passive region, suggesting the formation of a more continuous and adherent passive film. Notably, the LPBF curve exhibited a distinct dip in OCP at around 900 s (**Figure 4.33**), which could have been due to the pores (**Figure 4.36**) inherent to the LPBF process. These defects can locally disrupt the passive film (DelRio et al., 2023), causing a temporary loss in protection. The subsequent partial recovery and gradual decline after 2500 s was due to film reformation over these porous regions. These findings were consistent with Özer and Yılmaz (2023), who reported extended passivation in selective laser-melted Ti-6Al-4V alloys. Thus, while the as-cast alloy showed initial electrochemical stability, the LPBF alloy later exhibited more favourable passivation characteristics, despite transient instability.

The observed electrochemical behaviour of the as-cast and LPBF manufactured Ti-6Ta-1.5Zr-0.2Ru-5Cu (mass%) alloys agreed with Zhan et al. (2024) who found that LPBF processed samples developed thinner and less stable passive films, resulting in slightly poorer initial corrosion resistance than their as-cast counterparts. This showed that the manufacturing process significantly affected the stability and integrity of the passive film, agreeing with the fluctuations in the LPBF alloy's OCP profile (**Figure 4.33**). Both the as-cast and LPBF samples showed surface pores which can act as initiation sites for localised breakdown of the passive film, especially where stress is concentrated such as near grain boundaries or unmelted powder regions (Zhao et al., 2021; DelRio et al., 2023). This interpretation agrees with the fluctuations in the LPBF alloy's OCP profile (**Figure 4.33**), which were likely due to transient disruptions in the passive layer.

The potentiodynamic polarization curves (**Figure 4.34**) revealed that the corrosion rate of the LPBF alloy was lower than that of the as-cast alloy, showing that LPBF samples corroded at a slower rate. This agrees with Choubey et al. (2004), who suggested that, despite initial instability, the LPBF alloy developed a stable passive film that enhanced its long-term corrosion resistance. The lower initial stability of the LPBF alloy's oxide layer can be attributed to rapid solidification, which produced fine microstructures (**Figure 4.23)** and potential residual stresses (Sames et al., 2016), that may have caused the early instability of the oxide films, as grain boundaries and residual stresses can act as active sites for corrosion or slow down initial passivation kinetics (Ralston and Birbilis, 2010; Mazumder et al., 2022). Additionally, the higher surface roughness of the LPBF sample (**Figures 4.20 and 4.21**), due to the manufacturing process (Sun et al., 2014; Khan et al., 2020), could have made the oxide less uniform and less stable. In rougher areas, the oxide film might have formed more unevenly, with thinner or discontinuous areas, making it less protective at first. However, over time, the passive layer stabilised and became more uniform, thus enhancing the long-term corrosion resistance. Both samples had lower corrosion rates than 0.13 mm/year, the acceptable maximum corrosion rate for biomedical implants (Bhola et al., 2011).

While the initial oxide film on the LPBF alloy may have been less stable (indicated by fluctuations in OCP, **Figure 4.33**), the passive layer that eventually formed was assumed to be more protective because of lower passive current density (I_{pass}), **Figure 4.34**, which indicated a more stable passive state and correlates with the reduced corrosion rate. Additionally, the

finer microstructure of the LPBF alloy (**Figure 4.23**) enhanced the stability and protectiveness of the oxide layer, as finer grains provide more nucleation sites for passive film formation (Jelliti et al., 2013). LPBF-manufactured alloys exhibit improved resistance to localised corrosion and lower overall corrosion rates, due to their finer, more homogeneous microstructures (Cao et al., 2021).

The higher oxygen content of the LPBF samples (**Table 4.11**) indicated more extensive oxide formation on the surface. This supports the interpretation that LPBF alloys developed a thicker passive film than the as-cast alloys, giving lower corrosion rates. However, it is important to realise that while a uniform passive layer improves corrosion resistance by limiting ion release (Chen et al., 2023) excessive oxide formation during manufacturing can promote the formation of brittle oxides, potentially compromising mechanical properties (Wei et al., 2011). Moreover, as shown in **Figure 4.36(a)**, uneven oxide distribution could introduce localised defects. If the passive film becomes too thick or brittle, cracking may occur, exposing the substrate to further attack. In addition, oxides penetrating along grain boundaries may weaken the microstructure and increase the risk of embrittlement and mechanical failure (Wang et al. 2022).

Table 4.11 shows that oxygen was present in both samples, indicating regions with corrosion products. Titanium readily develops a protective TiO_2 film (which might be too thin to be detected by EDX) when exposed to oxygen (Zhu et al., 2006; Olmedo et al., 2009), while Ta and Zr stabilise this passive layer and improve corrosion resistance (Bocchetta et al., 2021). The higher oxygen content in the LPBF samples indicated more extensive oxide formation on the surface (**Figure 4.36(a)),** consistent with the finer microstructure promoting rapid TiO_2 formation. While a uniform passive layer improves corrosion resistance by limiting ion release, excessive oxygen uptake in LPBF can promote the formation of brittle oxides and oxygen-enriched phases, which may initiate cracking or flaking at the surface, reducing ductility and fracture toughness (Wei et al., 2011; Chen et al., 2023). In the as-cast sample, oxides were more stable with less variability (**Figure 4.33**), whereas LPBF samples exhibited increased oxygen, suggesting a thicker oxide layer. However, Jelliti et al. (2013) found potentially less homogeneous oxide layers in LPBF samples, which increased susceptibility to localised attack.

EDX analyses of both areal (overall) and light regions on both samples (**Table 4.11**) showed minor losses of Ta and Zr. The higher losses of Cu indicate that some copper was corroded and

released into the surrounding solution. This release is beneficial because antimicrobial activity increases with the concentration of Cu ions (Lui et al., 2014; Zhang et al., 2016a). However, excessive Cu leaching can reduce the alloy's mechanical integrity by promoting the formation of brittle intermetallic phases (Hadebe, 2022). This disruption of chemical homogeneity and passive film stability increases susceptibility to localised corrosion, which may further reduce mechanical strength and compromise the long-term structural integrity and biocompatibility of the implant (Balamurugan et al., 2008; Thakur et al., 2022).

Dark regions exhibited reduced Ti and Cu, and increased O and C **(Table 4.11)**, indicating localised corrosion and formation of TiO_2 and carbonate-based products such as $CaCO_3$. Elevated carbon in as-cast samples likely originated from surface deposits formed during corrosion, including carbonates from reaction with dissolved CO_2 in PBS or adsorbed organic residues (Qiao., 2023). Tantalum and Zr concentrations remained unchanged due to their stable passive films (Bocchetta et al., 2021).

Microstructural differences affected corrosion rates: the as-cast alloy had coarser needle-like (αTi) within large (βTi) grains (**Figure 4.22**), while LPBF alloys had finer, equiaxed (αTi) within (βTi) matrix (**Figures 4.23 and 4.24**). The finer LPBF microstructure promotes faster oxide formation, which can reduce mechanical integrity if oxides penetrate grain boundaries (Wang et al., 2021). Comparison with the initial homogeneous composition (**Table 4.7**) demonstrated that both samples showed differences of Ti and Cu (~32 mass% in the as-cast sample and ~46 mass% in the LPBF sample (**Table 4.11**) due to the formation of corrosion products on the surface. This could affect structural integrity and biocompatibility (Liu et al., 2024), although the apparent lower Cu content could have been due to the TiO_2 layer, which shielded the Cu from EDX analysis. This indicated selective dissolution, potentially from galvanic coupling with Ti, which could affect structural integrity and biocompatibility (Liu et al., 2024). There was increased O, C, and PBS-derived elements (Cl, Na, Ca, K), while Ta and Zr remained unchanged, showing a combination of localised oxide formation and preferential dissolution, particularly in Cu-rich regions. The corrosion resistance of Ta and Zr was likely due to their stable passive films (Bocchetta et al., 2021).

The corrosion rates of the Ti-6Ta-1.5Zr-0.2Ru-5Cu (mass%) alloy varied with manufacturing technique: the as-cast sample exhibited $3.27 \times 10^{-3} \pm 7.62 \times 10^{-5}$ mm/year, while the LPBF-manufactured sample demonstrated a lower rate of $2.32 \times 10^{-3} \pm 6.21 \times 10^{-5}$ mm/year. These

results indicated improved corrosion resistance in the LPBF alloy, due to finer microstructure and the formation of a more stable passive film. Spotose (2023) reported a single as-cast value of 2.2×10^{-3} mm/year, which may not be fully representative. Wang et al. (2022) showed that increasing copper content in Ti–Cu alloys led to reduced corrosion resistance, with Ti–7Cu and Ti–10Cu having higher corrosion current densities than Ti–4Cu. Zadeh et al. (2024) investigated selective laser melted Ti–10Cu alloys with corrosion rates ranging from 0.0107 to 0.0251 mm/year, depending on scan strategy and remelting conditions. These values were higher than the present study, reaffirming that moderate Cu content and the addition of Ta, Zr, and Ru enhanced corrosion resistance by supporting the stability of the passive film and limiting ion release, as inferred from the lower corrosion rates.

Chapter 6. Conclusions and Recommendation

6.1 Conclusion

The atomised powder met the LPBF specifications by being spherical with a D_{50} of 58 µm. The ultrasonically atomised powder had a narrow particle size distribution, ranging from ~50 to ~200 µm. Sieving out the oversized and agglomerated splintered particles could be done to provide an ideal feedstock LPBF. The phases observed after atomisation were (αTi), (βTi) and Ti_2Cu.

The best LPBF Ti-6Ta-1.5Zr-0.2Ru-5Cu (mass%) alloy tracks produced were even, smooth and continuous, with the targeted alloy composition. The parameters for these tracks were: 157.5 W laser power, 600 mm/s scanning speed, 0.15 mm beam diameter, 0.263 J/mm linear energy and 1.750 J/mm² planar energy density. The surface of the best track did not have visible pores. The phases on the surface of the best track were (αTi), (βTi) and Ti_2Cu.

The LPBF-manufactured Ti-6Ta-1.5Zr-0.2Ru-5Cu (mass%) bulk samples had low overall porosity ~4% (**Figure 4.23**). The reduced density and porosity were attributed to: (1) incomplete melting of the powders, (2) poor bonding and (3) overlapping between adjacent tracks. The sample achieved the highest densification of 96.4% with porosity of 3.6% agreeing with micrographs (**Figures 4.20 and 4.21**).

The LPBF-manufactured alloy had finer (βTi) grains with (αTi) precipitated along grain boundaries and as Widmanstätten needles within the grains. In contrast, the as-cast sample had coarser (βTi) grains with coarse (αTi) on the grain boundaries and fine (αTi) within the grains. The LPBF-manufactured sample had lower Cu and higher Ta compositions than the as-cast sample, while both samples showed similar Ti, Zr and Ru compositions. The XRD patterns of both samples identified (αTi), (βTi) and Ti_2Cu. The LPBF-manufactured sample had similar hardness to as-cast sample, with greater variation.

The LPBF-manufactured samples had greater antibacterial activity than the as-cast samples of the same composition which was attributed to increased Cu ion release, which was enhanced by the fine microstructure and surface porosity.

The as-cast Ti-6Ta-1.5Zr-0.2Ru-5Cu (mass%) alloy showed lower tendency to initiate corrosion, while the LPBF alloy showed better long-term corrosion resistance due to its finer

microstructure and more stable passive oxide layer. The LPBF-manufactured had enhanced passivation and a lower corrosion rate. Both manufacturing techniques had lower corrosion rate than 0.13 mm/y the acceptable maximum corrosion rate for biomedical implants.

6.2 Recommendation for future work

- Future antibacterial testing experiments should include the Ti-6Ta-1.5Zr-0.2Ru alloy to calculate the antibacterial rate and compare its performance with alloys containing copper and those without copper.
- SEM analyses were insufficient to confirm the phases in the microstructure. To accurately determine the crystal structure on the alloy surfaces, Transmission Electron Microscopy or EBSD is recommended.
- Ti-6Ta-1.5Zr-0.2Ru-5Cu (mass%) manufactured using laser powder bed fusion, demonstrated potential for dental applications. To further optimise its properties, heat treatments should be conducted to enhance corrosion resistance, relieve residual stress and reduce hardness variability,

References

Abou Shahba, R.M., Ghannem, W.A., El-Shenawy, A.E.S., Ahmed, A.S. and Tantawy, S.M., 2011. Corrosion and inhibition of Ti-6Al-4V alloy in NaCl solution. *International Journal of Electrochemical Science*, *6*(11), pp. 5499-5509.

Ahangar, P., Cooke, M.E., Weber, M.H. and Rosenzweig, D.H., 2019. Current biomedical applications of 3D printing and additive manufacturing. *Applied Sciences*, *9*(8), pp. 1-23.

Akbarpour, M.R., Mirabad, H.M., Hemmati, A. and Kim, H.S., 2022. Processing and microstructure of Ti-Cu binary alloys: A comprehensive review. *Progress in Materials Science*, *127*, pp. 100933-100964.

Al-Bermani, S.S., Blackmore, M.L., Zhang, W. and Todd, I., 2010. The origin of microstructural diversity, texture, and mechanical properties in electron beam melted Ti-6Al-4V. *Metallurgical and Materials Transactions A*, *41*, pp. 3422-3434.

Ali, H., Ghadbeigi, H. and Mumtaz, K., 2018. Effect of scanning strategies on residual stress and mechanical properties of Selective Laser Melted Ti6Al4V. *Materials Science and Engineering: A*, *712*, pp. 175-187.

Allardyce, C.S. and Dyson, P.J., 2001. Ruthenium in medicine: current clinical uses and future prospects. *Platinum Metals Review*, *45*(2), pp. 62-69.

Al-Maharma, A.Y., Patil, S.P. and Markert, B., 2020. Effects of porosity on the mechanical properties of additively manufactured components: a critical review. *Materials Research Express*, *7*(12), pp. 122001-122028.

AMAZEMET, 2022. A novel approach for the production of metal powders with tailored chemical composition: AMAZEMET's rePowder, *Powder Metallurgy Review*, Winter 2022.

Anderson, I.E., White, E.M. and Dehoff, R., 2018. Feedstock powder processing research needs for additive manufacturing development. *Current Opinion in Solid State and Materials Science*, *22*(1), pp. 8-15.

Anil, S., Anand, P.S., Alghamdi, H. and Jansen, J.A., 2011. Dental implant surface enhancement and osseointegration. In: F. Khurshid, ed. *Implant Dentistry – A Rapidly Evolving Practice*. Rijeka: InTechOpen, pp. 83–108.ASTM, 2021. *ISO/ASTM 52900:2021 – Additive manufacturing – General principles – Fundamentals and vocabulary*. ASTM International/ISO.ASTM, A., 2017.

B962-17-Standard Test Methods for Density of Compacted or Sintered Powder Metallurgy (PM) Products Using Archimedes' Principle. *American Society for Testing and Materials (ASTM): West Conshohocken, PA, USA*.

ASTM, ASTM E384-17: Standard Test Method for Microindentation Hardness of Materials, 2021. (Online). Available: https://www.astm.org/e0384-17.html. (Accessed 14 August 2024).

Baker, J., Sitthisak, S., Sengupta, M., Johnson, M., Jayaswal, R.K. and Morrissey, J.A., 2010. Copper stress induces a global stress response in Staphylococcus aureus and represses sae and agr expression and biofilm formation. *Applied and Environmental Microbiology*, *76*(1), pp. 150-160.

Balamurugan, A., Rajeswari, S., Balossier, G., Rebelo, A.H.S. and Ferreira, J.M.F., 2008. Corrosion aspects of metallic implants—An overview. *Materials and Corrosion*, *59*(11), pp. 855-869.

Bałasz, B., Bielecki, M., Gulbiński, W. and Słoboda, Ł., 2023. Comparison of ultrasonic and other atomization methods in metal powder production. *Journal of Achievements in Materials and Manufacturing Engineering*, *116*(1), pp. 1-14.

Balazic, M., Kopac, J., Jackson, M.J. and Ahmed, W., 2007. Titanium and titanium alloy applications in medicine. *International Journal of Nano and Biomaterials*, *1*(1), pp. 3-34.

Bannon, B.P. and Mild, E.E., 1983 Titanium Alloys for Biomaterial Application: An Overview. *Titanium Alloys in Surgical Implants*; ASTM: Philadelphia, PA, USA, pp. 7–15.

Bazaka, O., Bazaka, K., Kingshott, P., Crawford, R.J. and Ivanova, E.P., 2021. *Metallic Implants for Biomedical Applications*. Elsevier.

Beaman, J.J., Bourell, D.L., Seepersad, C.C. and Kovar, D., 2020. Additive manufacturing review: Early past to current practice. *Journal of Manufacturing Science and Engineering*, *142*(11), pp. 110812- 110832.

Bhaskaran, T.A., Krishnan, R.V. and Raghavan, K.S., 1985. The decomposition of hexagonal martensite in a titanium-copper alloy. *Scripta Metallurgica*, *19*(3), pp. 319-322.

Bhola, R., Bhola, S.M., Mishra, B. and Olson, D.L., 2011. Corrosion in titanium dental implants/prostheses–a review. *Trends in Biomaterials and Artificial Organs*, *25*(1), pp.34-46.

Biamino, S., Penna, A., Ackelid, U., Sabbadini, S., Tassa, O., Fino, P., Pavese, M., Gennaro, P. and Badini, C., 2011. Electron beam melting of Ti–48Al–2Cr–2Nb alloy: Microstructure and mechanical properties investigation. *Intermetallics*, *19*(6), pp. 776-781.

Biesiekierski, A., Ping, D.H., Yamabe-Mitarai, Y. and Wen, C., 2014. Impact of ruthenium on microstructure and corrosion behaviour of β-type Ti–Nb–Ru alloys for biomedical applications. *Materials and Design*, *59*, pp. 303-309.

Blakey-Milner, B., Gradl, P., Snedden, G., Brooks, M., Pitot, J., Lopez, E., Leary, M.F., Berto, A. and Du Plessis, A. (2021). Metal additive manufacturing in aerospace: A review. *Materials and Design*, *209*, pp. 110008-110048.

Bocchetta, P., Chen, L.Y., Tardelli, J.D.C., Reis, A.C.D., Almeraya-Calderón, F. and Leo, P., 2021.Passive layers and corrosion resistance of biomedical Ti-6Al-4V and βTi alloys. *Coatings, 11(5),* pp. 487-519

Bolzoni, L. and Yang, F., 2019. Development of Cu-bearing powder metallurgy Ti alloys for biomedical applications. *Journal of the Mechanical Behavior of Biomedical Materials*, *97*, pp. 41-48.

Bose, S., Roy, M. and Bandyopadhyay, A., 2012. Recent advances in bone tissue engineering scaffolds. *Trends in Biotechnology*, *30*(10), pp. 546-554.

Bumke, L., Wolff, N., Chluba, C., Dankwort, T., Kienle, L. and Quandt, E., 2021. Coherent precipitates as a condition for ultra-low fatigue in Cu-rich Ti53. 7Ni24. 7Cu21. 6 shape memory alloys. *Shape Memory and Superelasticity*, *7*(4), pp. 526-540.

Callister Jr, W.D. and Rethwisch, D.G., 2020. *Materials Science and Engineering: an Introduction*. John Wiley and Sons.

Campbell, J., 2015. *Complete Casting Handbook: Metal Casting Processes, Metallurgy, Techniques and Design*. Butterworth-Heinemann.

Canale, P. and Servant, C., 2022. Thermodynamic assessment of the Cu–Ti system taking into account the new stable phase $CuTi_3$. *International Journal of Materials Research*, *93*(4), pp. 273-276.

Cao, S., Zou, Y., Lim, C.V.S. and Wu, X., 2021. Review of laser powder bed fusion (LPBF) fabricated Ti-6Al-4V: process, post-process treatment, microstructure, and property. *Light: Advanced Manufacturing*, *2*(3), pp. 313-332.

Carrozza, A., Mazzucato, F., Aversa, A., Lombardi, M., Bondioli, F., Biamino, S., Valente, A. and Fino, P., 2021. Single scans of Ti-6Al-4V by directed energy deposition: a cost and time effective methodology to assess the proper process window. *Metals and Materials International*, *27(3*), pp. 3590–3602

Cerezo, P.M., Aguilera, J.A., Garcia-Gonzalez, A. and Lopez-Crespo, P., 2024. Microhardness and Microstructure Analysis of the LPBF Additively Manufactured 18Ni300. *Materials*, *17*(3), pp. 661-674.

Challa, V.S.A., Mali, S. and Misra, R.D.K., 2013. Reduced toxicity and superior cellular response of preosteoblasts to Ti-6Al-7Nb alloy and comparison with Ti-6Al-4V. *Journal of Biomedical Materials Research Part A*, *101*(7), pp. 2083-2089.

Chandrasekaran, M. and Xia, Z.S., 2005. Effect of alloying time and composition on the mechanical properties of Ti alloy. *Materials Science and Engineering A*, *394*(1-2), pp. 220-228.

Chang, Y.H., Chao, C.Y., Chang, Y.T. and Du, J.K., 2020. Effect of Phase Distribution on the Antibacterial Property and Cytotoxicity of Ti-5Al-2.5 Cu Alloy after Heat Treatment at Various Temperatures. *Metals*, *10*(7), pp. 858-871.

Chen, G., Zhao, S.Y., Tan, P., Wang, J., Xiang, C.S. and Tang, H.P., 2018. A comparative study of Ti-6Al-4V powders for additive manufacturing by gas atomisation, plasma rotating electrode process and plasma atomisation. *Powder Technology*, *333*, pp. 38-46.

Chen, J.R. and Tsai, W.T., 2011. In situ corrosion monitoring of Ti–6Al–4V alloy in H2SO4/HCl mixed solution using electrochemical AFM. *Electrochimica Acta*, *56*(4), pp. 1746-1751.

Chen, M., Wang, X., Hou, X., Qiu, J., Zhang, E. and Hu, J., 2023. Enhanced mechanical, bio-corrosion, and antibacterial properties of Ti-Cu alloy by forming a gradient nanostructured surface layer. *Surface and Coatings Technology*, *465*, pp. 129609-129622.

Choubey, A., Basu, B. and Balasubramaniam, R., 2004. Tribological behaviour of Ti-based alloys in simulated body fluid solution at fretting contacts. *Materials Science and Engineering A*, *379*(1-2), pp.234-239.

Chun, H.J., Cheong, S.Y., Han, J.H., Heo, S.J., Chung, J.P., Rhyu, I.C., Choi, Y.C., Baik, H.K., Ku, Y. and Kim, M.H., 2002. Evaluation of design parameters of osseointegrated dental implants using finite element analysis. *Journal of Oral Rehabilitation*, *29*(6), pp. 565-574.

Cobbinah, P.V., Nzeukou, R.A., Onawale, O.T. and Matizamhuka, W.R., 2020. Laser powder bed fusion of potential superalloys: a review. *Metals*, *11*(1), pp. 58-95.

Cordeiro, J.M. and Barão, V.A., 2017. Is there scientific evidence favoring the substitution of commercially pure titanium with titanium alloys for the manufacture of dental implants? *Materials Science and Engineering C*, *71*, pp. 1201-1215.

Cordeiro, J.M., Beline, T., Ribeiro, A.L.R., Rangel, E.C., da Cruz, N.C., Landers, R., Faverani, L.P., Vaz, L.G., Fais, L.M., Vicente, F.B. and Grandini, C.R., 2017. Development of binary and ternary titanium alloys for dental implants. *Dental Materials*, *33*(11), pp. 1244-1257.

Dai, D., Gu, D., Ge, Q., Li, Y., Shi, X., Sun, Y. and Li, S., 2020. Mesoscopic study of thermal behaviour, fluid dynamics and surface morphology during selective laser melting of Ti-based composites. *Computational Materials Science*, *177*, pp. 109598-109609.

Dawes, J., Bowerman, R. and Trepleton, R., 2015. Introduction to the additive manufacturing powder metallurgy supply chain. *Johnson Matthey Technology Review*, *59*(3), pp. 243-256.

DebRoy, T., Wei, H.L., Zuback, J.S., Mukherjee, T., Elmer, J.W., Milewski, J.O., Beese, A.M., Wilson-Heid, A.D., De, A. and Zhang, W., 2018. Additive manufacturing of metallic components–process, structure and properties. *Progress in Materials Science*, *92*, pp. 112-224.

Delgado-Ruiz, R. and Romanos, G., 2018. Potential causes of titanium particle and ion release in implant dentistry: a systematic review. *International Journal of Molecular Sciences*, *19*(11), pp. 3585-3569.

DelRio, F.W., Khan, R.M., Heiden, M.J., Kotula, P.G., Renner, P.A., Karasz, E.K. and Melia, M.A., 2023. Porosity, roughness, and passive film morphology influence the corrosion behavior of 316L stainless steel manufactured by laser powder bed fusion. *Journal of Manufacturing Processes*, *102*, pp. 654-662.

Diep, J.K., 2020. Additive manufacturing applications in the medical industry. *Department of Materials Science and Engineering, University of Washington, Seattle, WA 98195, USA,* pp 1-4.

Dini, C., Costa, R.C., Sukotjo, C., Takoudis, C.G., Mathew, M.T. and Barão, V.A., 2020. Progression of bio-tribocorrosion in implant dentistry. *Frontiers in Mechanical Engineering*, *6*, pp. 1-14.

Donachie, M.J., 2000. *Titanium: A Technical Guide*. Materials Park, Ohio: ASM International.

Dyal Ukabhai, K., Curle, U.A., Masia, N.D.E., Smit, M., Mwamba, I.A., Norgren, S., Öhman-Mägi, C., Hashe, N.G. and Cornish, L.A., 2022. Formation of Ti_2Cu in Ti-Cu alloys. *Journal of Phase Equilibria and Diffusion*, *43*(3), pp. 332-344.

Dziadon, A. and Konieczny, M., 2004. Structural transformations at the Cu-Ti interface during synthesis of copper-intermetallics layered composite. *Kovové Materiály.*, 42, pp. 42-50.

Dzogbewu, T.C. and du Preez, W.B., 2021. Additive manufacturing of titanium-based implants with metal-based antimicrobial agents. *Metals*, *11*(3), pp. 453-465.

Eisenbarth, E., Velten, D., Müller, M., Thull, R. and Breme, J., 2004. Biocompatibility of β-stabilizing elements of titanium alloys. *Biomaterials*, *25*(26), pp. 5705-5713.

Elias, C.N., Lima, J.H.C., Valiev, R. and Meyers, M.A., 2008. Biomedical applications of titanium and its alloys. *Journal of Materials*, *60*, pp. 46-49.

EPMA, 2019. Introduction to Additive Manufacturing Technology, a Guide for Designers and Engineers. European Powder Metallurgy Association, pp. 28-34.

Filip, R., Kubiak, K., Ziaja, W. and Sieniawski, J., 2003. The effect of microstructure on the mechanical properties of two-phase titanium alloys. *Journal of Materials Processing Technology*, *133*(1-2), pp. 84-89.

Fiorindo, F., 2012. *Additive manufacturing opportunities: mass customisation in the biomedical industry*. Master's dissertation, University of Venice.

Fowler, L., 2019. *Development of titanium-copper alloys for dental applications* (Doctoral thesis, Acta Universitatis Upsaliensis).

Fowler, L., Engqvist, H. and Öhman-Mägi, C., 2019. Effect of copper ion concentration on bacteria and cells. *Materials*, *12*(22), pp. 3798-3811.

Froes, F. and Qian, M. eds., 2018. *Titanium in Medical and Dental Applications*. Woodhead Publishing, Cambridge. ISBN: 978-0-08-102202-7.

Fultz, B. (2020). *Diffusionless Transformations*. In: *Phase Transitions in Materials*, pp. 482–510. Cambridge University Press.

Gao, P., Wang, Z. and Zeng, X., 2019. Effect of process parameters on morphology, sectional characteristics and crack sensitivity of Ti-40Al-9V-0.5 Y alloy single tracks produced by selective laser melting. *International Journal of Lightweight Materials and Manufacture*, *2*(4), pp. 355-361.

Gaviria, L., Salcido, J.P., Guda, T. and Ong, J.L., 2014. Current trends in dental implants. *Journal of the Korean Association of Oral and Maxillofacial Surgeons*, *40*(2), pp. 50-60.

Gebhardt, A., 2007. Rapid Prototyping – Rapid Tooling – Rapid Manufacturing. *Carl Hanser, München*.

Geetha, M., Singh, A.K., Asokamani, R. and Gogia, A.K., 2009. Ti based biomaterials, the ultimate choice for orthopaedic implants–a review. *Progress in Materials Science*, *54*(3), pp. 397-425.

Geng, J.P., Xu, W., Tan, K.B.C. and Liu, G.R., 2004. Finite element analysis of an osseointegrated stepped screw dental implant. *Journal of Oral Implantology*, *30*(4), pp. 223-233.

Gibson, I., Rosen, D.W., Stucker, B. and Khorasani, M., 2021. *Additive Manufacturing Technologies*. 3rd ed. Cham, Switzerland: Springer.

Goettgens, V.S., Kaserer, L., Braun, J., Letofsky-Papst, I., Mitsche, S. and Leichtfried, G., 2023. Microstructure of a modulated Ti-6Al-4V–Cu alloy fabricated via in situ alloying in laser powder bed fusion. *Materialia*, *28*, pp. 101731-101740.

Gong, H., Rafi, K., Gu, H., Starr, T. and Stucker, B., 2014. Analysis of defect generation in Ti–6Al–4V parts made using powder bed fusion additive manufacturing processes. *Additive Manufacturing*, *1*, pp. 87-98.

Gonnabattula, A., Thanumoorthy, R.S., Bontha, S., Balan, A.S.S., Kumar, V.A. and Kanjarla, A.K., 2024. Process parameter optimization for laser directed energy deposition (LDED) of Ti6Al4V using single-track experiments with small laser spot size. *Optics and Laser Technology*, *175*, pp. 110861-110873.

Goodman, S.B., Yao, Z., Keeney, M. and Yang, F., 2013. The future of biologic coatings for orthopaedic implants. *Biomaterials*, *34*(13), pp. 3174-3183.

Grass, G., Rensing, C. and Solioz, M., 2011. Metallic copper as an antimicrobial surface. *Applied and Environmental Microbiology*, *77*(5), pp. 1541-1547.

Greer, L., 2016. Control of grain size in solidification**.** In: *Solidification and Casting*. Boca Raton: CRC Press, Taylor & Francis Group, pp. 199–247.

Gu, D.D., Meiners, W., Wissenbach, K. and Poprawe, R., 2012. Laser additive manufacturing of metallic components: materials, processes and mechanisms. *International Materials Reviews*, *57*(3), pp. 133-164.

Gubbi, P. and Wojtisek, T., 2018. The role of titanium in implant dentistry. In *Titanium in medical and dental applications* (pp. 505-529). Woodhead Publishing.

Guo, Y., Lina, J.I.A., Kong, B., Wang, N.A. and Zhang, H., 2018. Single track and single layer formation in selective laser melting of niobium solid solution alloy. *Chinese Journal of Aeronautics*,*31*(4), pp. 860-866.

Gupta, A., Khatirkar, R.K., Kumar, A. and Parihar, M.S., 2018. Investigations on the effect of heating temperature and cooling rate on evolution of microstructure in an α + β titanium alloy. *Journal of Materials Research*, *33*(8), pp. 946-957.

Haase, F., Siemers, C. and Rösler, J., 2023. Laser powder bed fusion (LPBF) of commercially pure titanium and alloy development for the LPBF process. *Frontiers in Bioengineering and Biotechnology*, *11*, pp.1260925-1260945.

Hadebe, N.D.E., 2022. Influence of copper on the corrosion and mechanical properties of Grade 4 titanium for biomedical applications. MSc dissertation, University of the Witwatersrand.

Hall, E.O. The deformation and ageing of mild steel: III discussion of results. *Proceedings of the Physical Society, Section B* 64.9 (1951): 747-753.

Han, C.H., Johansson, C.B., Wennerberg, A. and Albrektsson, T., 1998. Quantitative and qualitative investigations of surface enlarged titanium and titanium alloy implants. *Clinical Oral Implants Research*, *9*(1), pp. 1-10.

Han, H.S., 2009. *Design of new root-form endosseous dental implant and evaluation of fatigue strength using finite element analysis*. MSc dissertation. The University of Iowa.

Hao, Y.L., Li, S.J., Sun, S.Y. and Yang, R., 2006. Effect of Zr and Sn on Young's modulus and superelasticity of Ti–Nb-based alloys. *Materials Science and Engineering A*, *441*(1-2), pp. 112-118.

Hayama, A.O., Andrade, P.N., Cremasco, A., Contieri, R.J., Afonso, C.R. and Caram, R., 2014. Effects of composition and heat treatment on the mechanical behavior of Ti–Cu alloys. *Materials and Design*, *55*, pp.1006-1013.

Heinemann, F., Hasan, I., Bourauel, C., Biffar, R. and Mundt, T., 2015. Bone stability around dental implants: Treatment related factors. *Annals of Anatomy-Anatomischer Anzeiger*, *199*, pp. 3-8.

Herzog, D., Seyda, V., Wycisk, E. and Emmelmann, C., 2016. Additive manufacturing of metals. *Acta Materialia*, *117*, pp. 371-392.

Hong, I.T. and Koo, C.H., 2005. Antibacterial properties, corrosion resistance and mechanical properties of Cu-modified SUS 304 stainless steel. *Materials Science and Engineering: A*, *393*(1-2), pp. 213-222.

Hosseini, S., Hudak, R., Penhaker, M. and Majernik, J., 2012. Fatigue of Ti-6Al-4V. In: *Biomedical Engineering-Technical Applications in Medicine,* pp. 75-92. New York: Springer

Hu, H., Zhang, W., Qiao, Y.Q., Jiang, X.Y., Liu, X. and Ding, C., 2012. Antibacterial activity and increased bone marrow stem cell functions of Zn-incorporated TiO_2 coatings on titanium. *Acta Biomaterialia*, *8*(2), pp. 904-915.

Inagaki, I., Takechi, T., Shirai, Y. and Ariyasu, N., 2014. Application and features of titanium for the aerospace industry. *Nippon Steel and Sumitomo Metal Technical Report*, *106*(106), pp. 22-27.

Insights10 (2024) *South Africa Dental Implant Market Analysis*. Available at: https://www.insights10.com/report/south-africa-dental-implant-market-analysis/ (Accessed: 25 October 2024).

Jacobs, J.J., Gilbert, J.L. and Urban, R.M., 1998. Current concepts review-corrosion of metal orthopaedic implants. *Journal of Bone and Joint Surgery, 80*(2), pp.268-82.

Jamhari, F.I., Foudzi, F.M., Buhairi, M.A., Sulong, A.B., Radzuan, N.A.M., Muhamad, N., Mohamed, I.F., Jamadon, N.H. and Tan, K.S., 2023. Influence of heat treatment parameters on microstructure and mechanical performance of titanium alloy in LPBF: A brief review. *Journal of Materials Research and Technology*, *24*, pp. 4091-4110.

Javed, F., Ahmed, H.B., Crespi, R. and Romanos, G.E., 2013. Role of primary stability for successful osseointegration of dental implants: Factors of influence and evaluation. *Interventional Medicine and Applied Science*, *5*(4), pp. 162-167.

Jelliti, S., Richard, C., Retraint, D., Roland, T., Chemkhi, M. and Demangel, C., 2013. Effect of surface nanocrystallization on the corrosion behavior of Ti–6Al–4V titanium alloy. *Surface and Coatings Technology*, *224*, pp. 82-87.

Jensen, L.K., Koch, J., Aalbæk, B., Moodley, A., Bjarnsholt, T., Kragh, K.N., Petersen, A. and Jensen, H.E., 2017. Early implant-associated osteomyelitis results in a peri-implanted bacterial reservoir. *Acta Pathologica, Microbiologica, et Immunologica Scandinavica*, *25*(1), pp. 38-45.

Ji, H., Zhao, M.C., Xie, B., Zhao, Y.C., Yin, D., Gao, C., Shuai, C. and Atrens, A., 2021. Corrosion and antibacterial performance of novel selective-laser-melted (SLMed) Ti-xCu biomedical alloys. *Journal of Alloys and Compounds*, *864*, pp. 158415-158425.

Jin, X., Gao, L., Liu, E., Yu, F., Shu, X. and Wang, H., 2015. Microstructure, corrosion and tribological and antibacterial properties of Ti–Cu coated stainless steel. *Journal of the Mechanical Behavior of Biomedical Materials*, *50*, pp. 23-32.

Joshi, V.A., 2006. *Titanium Alloys: An Atlas of Structures and Fracture Features*. Boca Raton, Florida: CRC Press..

Kan, J.Y., Rungcharassaeng, K., Kim, J., Lozada, J.L. and Goodacre, C.J., 2002. Factors affecting the survival of implants placed in grafted maxillary sinuses: a clinical report. *The Journal of Prosthetic Dentistry*, *87*(5), pp. 485-489.

Kaoushik, V.M., Nichul, U., Chavan, V. and Hiwarkar, V., 2023. Development of microstructure and high hardness of Ti6Al4V alloy fabricated using laser beam powder bed fusion: A novel sub-transus heat treatment approach. *Journal of Alloys and Compounds*, *937*, pp.168387-168399.

Khan, H.M., Karabulut, Y., Kitay, O., Kaynak, Y. and Jawahir, I.S., 2020. Influence of the post-processing operations on surface integrity of metal components produced by laser powder bed fusion additive manufacturing: a review. *Machining Science and Technology*, *25*(1), pp. 118-176.

Kikuchi, M., Takada, Y., Kiyosue, S., Yoda, M., Woldu, M., Cai, Z., Okuno, O. and Okabe, T., 2003. Mechanical properties and microstructures of cast Ti–Cu alloys. *Dental Materials*, *19*(3), pp. 174-181.

Klotz, U.E., Liu, C., Uggowitzer, P.J. and Löffler, J.F., 2007. Experimental investigation of the Cu–Ti–Zr system at 800 C. *Intermetallics*, *15*(12), pp. 1666-1671.

Kocks, U.F. and Mecking, H., 2003. Physics and phenomenology of strain hardening: the FCC case. *Progress in Materials Science*, *48*(3), pp. 171-273.

Kok, Y., Tan, X., Tor, S.B. and Chua, C.K., 2015. Fabrication and microstructural characterisation of additive manufactured Ti-6Al-4V parts by electron beam melting: *Virtual and Physical Prototyping*, *10*(1), pp. 13-21.

Kustron, P., Korzeniowski, M., Sajbura, A., Piwowarczyk, T., Kaczynski, P. and Sokolowski, P., 2023. Development of High-Power Ultrasonic System Dedicated to Metal Powder Atomization. *Applied Sciences*, *13*(15), pp. 8984-9001.

Le Guéhennec, L., Soueidan, A., Layrolle, P. and Amouriq, Y., 2007. Surface treatments of titanium dental implants for rapid osseointegration. *Dental Materials*, *23*(7), pp. 844-854.

Leaper, D., McBain, A.J., Kramer, A., Assadian, O., Sanchez, J.L.A., Lumio, J. and Kiernan, M., 2010. Healthcare associated infection: novel strategies and antimicrobial implants to prevent surgical site infection. *The Annals of The Royal College of Surgeons of England*, *92*(6), pp. 453-458.

Lee, C.M., Ju, C.P. and Chern Lin, J.H., 2002. Structure–property relationship of cast Ti–Nb alloys. *Journal of Oral Rehabilitation*, *29*(4), pp. 314-322.

Lee, J.H., Frias, V., Lee, K.W. and Wright, R.F., 2005. Effect of implant size and shape on implant success rates: a literature review. *The Journal of Prosthetic Dentistry*, *94*(4), pp. 377-381.

Leyens, C. and Peters, M. eds., 2006. *Titanium and Titanium Alloys: Fundamentals and Applications*. Wiley-VCH in Weinheim, Germany.

Li, H.F., Qiu, K.J., Zhou, F.Y., Li, L. and Zheng, Y.F., 2016. Design and development of novel antibacterial Ti-Ni-Cu shape memory alloys for biomedical application. *Scientific Reports*, *6*(1), pp. 1-11.

Li, J.P., de Wijn, J.R., Van Blitterswijk, C.A. and de Groot, K., 2006. Porous Ti6Al4V scaffold directly fabricating by rapid prototyping: preparation and *in vitro* experiment. *Biomaterials*, *27*(8), pp. 1223-1235.

Li, Y., Yang, C., Zhao, H., Qu, S., Li, X. and Li, Y., 2014. New developments of Ti-based alloys for biomedical applications. *Materials*, *7*(3), pp. 1709-1800.

Lierke, E.G. and Griesshammer, G., 1967. The formation of metal powders by ultrasonic atomisation of molten metals. *Ultrasonics*, *5*(4), pp. 224-228.

Liu, H., Wang, H., Ren, L., Qiu, D. and Yang, K., 2023. Antibacterial copper-bearing titanium alloy prepared by laser powder bed fusion for superior mechanical performance. *Journal of Materials Science and Technology*, *132*, pp. 100-109.

Liu, H., Zhang, X., Shi, L., Hong, Y., Yao, H., Ren, L. and Yang, K., 2024. Effect of Cu content on the properties of laser powder bed fused biomedical titanium alloys. *Journal of Materials Research and Technology*, *30*, pp. 8992-8998.

Liu, H., Zhang, X., Shi, L., Hong, Y., Yao, H., Ren, L., and Yang, K., 2024. Effect of Cu content on the properties of laser powder bed fused biomedical titanium alloys. *Journal of Materials Research and Technology*, *22*, pp. 123–135.

Liu, J., Li, F., Liu, C., Wang, H., Ren, B., Yang, K. and Zhang, E., 2014a. Effect of Cu content on the antibacterial activity of titanium–copper sintered alloys. *Materials Science and Engineering C*, *35*, pp. 392-400.

Liu, J., Yang, Q., Yin, J. and Yang, H., 2020. Effects of alloying elements and annealing treatment on the microstructure and mechanical properties of Nb-Ta-Ti alloys fabricated by partial diffusion for biomedical applications. *Materials Science and Engineering C*, *110*, pp. 110542-110555.

Liu, J., Zhang, X., Wang, H., Li, F., Li, M., Yang, K. and Zhang, E., 2014b. The antibacterial properties and biocompatibility of a Ti–Cu sintered alloy for biomedical application. *Biomedical Materials*, *9*(2), pp. 025013-025025.

Liu, R., Memarzadeh, K., Chang, B., Zhang, Y., Ma, Z., Allaker, R.P., Ren, L. and Yang, K., 2016. Antibacterial effect of copper-bearing titanium alloy (Ti-Cu) against Streptococcus mutans and Porphyromonas gingivalis. *Scientific Reports*, *6*(1), pp. 29985-29995.

Liu, R., Tang, Y., Zeng, L., Zhao, Y., Ma, Z., Sun, Z., Xiang, L., Ren, L. and Yang, K., 2018. In vitro and in vivo studies of anti-bacterial copper-bearing titanium alloy for dental application. *Dental Materials*, *34*(8), pp. 1112-1126.

Liu, S. and Shin, Y.C., 2019. Additive manufacturing of Ti6Al4V alloy: A review. *Materials and Design*, *164*, pp. 107552-107575.

Liu, Y., Li, J., Xu, K., Cheng, T., Zhao, D., Li, W., Teng, Q. and Wei, Q., 2022. An optimised scanning strategy to mitigate excessive heat accumulation caused by short scanning lines in laser powder bed fusion process. *Additive Manufacturing*, *60*, pp. 103256-103268.

Liu, Y., Yang, Y., Mai, S., Wang, D. and Song, C., 2015. Investigation into spatter behaviour during selective laser melting of AISI 316L stainless steel powder. *Materials and Design*, *87*, pp. 797-806.

Liu, Z., Zhao, D., Wang, P., Yan, M., Yang, C., Chen, Z., Lu, J. and Lu, Z., 2022. Additive manufacturing of metals: Microstructure evolution and multistage control. *Journal of Materials Science and Technology*, *100*, pp. 224-236.

Luan, J.H., Jiao, Z.B., Chen, G. and Liu, C.T., 2014. Improved ductility and oxidation resistance of cast Ti–6Al–4V alloys by micro alloying. *Journal of Alloys and Compounds*, *602*, pp. 235-240.

Luan, J.H., Jiao, Z.B., Liu, W.H., Lu, Z.P., Zhao, W.X. and Liu, C.T., 2017. Compositional and microstructural optimization and mechanical-property enhancement of cast Ti alloys based on Ti-6Al-4V alloy. *Materials Science and Engineering A*, *704*, pp. 91-101.

Lütjering, G. and Williams, J.C., 2007. Titanium, Springer Science and Business Media. *Berlin Heidelberg*.

Lütjering, G., Williams, J.C. and Gysler, A., 2000. Microstructure and mechanical properties of titanium alloys. *Microstructure and Properties of Materials, 2,* pp. 1-77.

Malinov, S., Sha, W. and Guo, Z., 2000. Application of artificial neural network for prediction of time–temperature–transformation diagrams in titanium alloys. *Materials Science and Engineering A*, *283*(1-2), pp. 1-10.

Manriquez-Frayre, J.A., Bourell, D.L., 1991. Selective laser sintering of Cu-Pb/Sn solder powders. In: *International Solid Freeform Fabrication Symposium. Austin*, pp. 236-244.

Mantovani, D., 2000. Shape memory alloys: Properties and biomedical applications. *JOM*, *52*, pp. 36-44.

Mareci, D., Chelariu, R., Gordin, D.M., Ungureanu, G. and Gloriant, T., 2009. Comparative corrosion study of Ti–Ta alloys for dental applications. *Acta Biomaterialia*, *5*(9), pp. 3625-3639.

Marin, E. and Lanzutti, A., 2023. Biomedical applications of titanium alloys: a comprehensive review. *Materials*, *17*(1), pp. 114-156.

Masia, N.D.E., Smit, M., Mwamba, I.A., Fowler, L., Chown, L.H., Norgren, S., Öhman-Mägi, C., Hashe, N. and Cornish, L.A., 2021. Corrosion performance of Ti-Cu alloys targeted for biomedical applications. *Suid-Afrikaans Tydskrif vir Natuurwetenskap en Tegnologie/South African Journal of Science and Technology*, *40*(1), pp. 244-250.

Matsuno, H., Yokoyama, A., Watari, F., Uo, M. and Kawasaki, T., 2001. Biocompatibility and osteogenesis of refractory metal implants, titanium, hafnium, niobium, tantalum and rhenium. *Biomaterials*, *22*(11), pp. 1253-1262.

Mazumder, S., Pantawane, M.V., Joshi, S.S. and Dahotre, N.B., 2022. Electrochemical and thermal-induced degradation of additively manufactured titanium alloys: a review. *Critical Reviews in Solid State and Materials Sciences*, *47*(6), pp. 915-954.

Meng, Q.K., Huo, Y.F., Ma, W., Sui, Y.W., Zhang, J.Y., Guo, S. and Zhao, X.Q., 2018. Design and fabrication of a low modulus β-type Ti–Nb–Zr alloy by controlling martensitic transformation. *Rare Metals*, *37*, pp. 789-794.

Mijiritsky, E., Mazor, Z., Lorean, A. and Levin, L., 2013. Implant diameter and length influence on survival: interim results during the first 2 years of function of implants by a single manufacturer. *Implant Dentistry*, *22*(4), pp. 394-398.

Mitra, D., Kang, E.T. and Neoh, K.G., 2019. Antimicrobial copper-based materials and coatings: potential multifaceted biomedical applications. *ACS applied materials and interfaces*, *12*(19), pp. 21159-21182.

Mohammed, M.T., Khan, Z.A. and Siddiquee, A.N., 2014. Beta titanium alloys: the lowest elastic modulus for biomedical applications: a review. *International Journal of Chemical, Nuclear, Metallurgical and Materials Engineering*, *8*(8), pp. 726-731.

Möller, H., Motsweni, V., Żrodowski, Ł., Choma, T., Powder characterisation of Pt84-Al11-Cr3-Ru2 superalloy manufactured by ultrasonic atomisation, Proceedings of the 8th International PGM Conference, 2 – 3 November 2022, Sun City, South Africa (2022).

Mombelli, A., Hashim, D. and Cionca, N., 2018. What is the impact of titanium particles and biocorrosion on implant survival and complications? A critical review. *Clinical Oral Implants Research*, *29*, pp. 37-53.

Morais, L.S., Serra, G.G., Muller, C.A., Andrade, L.R., Palermo, E.F., Elias, C.N. and Meyers, M., 2007. Titanium alloy mini-implants for orthodontic anchorage: immediate loading and metal ion release. *Acta Biomaterialia*, *3*(3), pp. 331-339.

Moulyashree, M. and Mahantesha, S., 2023. Configurations of implant threads: A Review. *Journal of Dental Sciences*, *5*, pp. 86-90.

Mu, M., Liu, S., DeFlorio, W., Hao, L., Wang, X., Salazar, K.S., Taylor, M., Castillo, A., Cisneros-Zevallos, L., Oh, J.K. and Min, Y., 2023. Influence of surface roughness, nanostructure, and wetting on bacterial adhesion. *Langmuir*, *39*(15), pp. 5426-5439.

Mumtaz, K.A. and Hopkinson, N., 2010. Selective laser melting of thin wall parts using pulse shaping. *Journal of Materials Processing Technology*, *210*(2), pp. 279-287.

Murr, L.E., Gaytan, S.M., Ramirez, D.A., Martinez, E., Hernandez, J., Amato, K.N., Shindo, P.W., Medina, F.R. and Wicker, R.B., 2012. Metal fabrication by additive manufacturing using laser and electron beam melting technologies. *Journal of Materials Science and Technology*, *28*(1), pp. 1-14.

Murray, J.L., 1983. The Au-Ti (gold-titanium) system. *Bulletin of Alloy Phase Diagrams*, *4*(3), pp. 278-283.

Nabavi, S.F., Dalir, H. and Farshidianfar, A., 2024. A comprehensive review of recent advances in laser powder bed fusion characteristics modeling: metallurgical and defects. *The International Journal of Advanced Manufacturing Technology*, *132*(5), pp.2233-2269.

Nagay, B.E., Cordeiro, J.M. and Barao, V.A., 2022. Insight into corrosion of dental implants: from biochemical mechanisms to designing corrosion-resistant materials. *Current Oral Health Reports*, *9*(2), pp. 7-21.

Ni, J., Ling, H., Zhang, S., Wang, Z., Peng, Z., Benyshek, C., Zan, R., Miri, A.K., Li, Z., Zhang, X. and Lee, J., 2019. Three-dimensional printing of metals for biomedical applications. *Materials Today Biomedical*, *3*, pp. 1-18.

Niinomi, M., 1998. Mechanical properties of biomedical titanium alloys. *Materials Science and Engineering A*, *243*(1-2), pp. 231-236.

Niinomi, M., 2003. Recent research and development in titanium alloys for biomedical applications and healthcare goods. *Science and Technology of Advanced Materials*, *4*(5), pp. 445-456.

Niinomi, M., Nakai, M. and Hieda, J., 2012. Development of new metallic alloys for biomedical applications. *Acta Biomaterialia*, *8*(11), pp. 3888-3903.

Niu, H.J. and Chang, I.T.H., 1999. Instability of scan tracks of selective laser sintering of high speed steel powder. *Scripta Materialia*, *41*(11), pp. 1229-1234.

Nkosi, N. and Sacks, N., 2024. Process parameter development of a Ti6Al4V-5wt% Cr3C2 metal matrix composite fabricated by Laser Powder Bed Fusion. *Procedia CIRP*, *124*, pp.104-109.

Norman, J., Madurawe, R.D., Moore, C.M., Khan, M.A. and Khairuzzaman, A., 2017. A new chapter in pharmaceutical manufacturing: 3D-printed drug products. *Advanced Drug Delivery Reviews*, *108*, pp. 39-50.

Oliveira, V., Chaves, R.R., Bertazzoli, R. and Caram, R., 1998. Preparation and characterisation of Ti-Al-Nb alloys for orthopaedic implants. *Brazilian Journal of Chemical Engineering*, *15*, pp. 326-333.

Olmedo, D.G., Tasat, D.R., Duffó, G., Guglielmotti, M.B. and Cabrini, R.L., 2009. The issue of corrosion in dental implants: a review. *Acta Odontológica Latinoamericana*, *22*(1), pp. 3-9.

Ookubo, N., Nakamura, S., Yamamoto, M. and Miyakusu, K., 1998. Antimicrobial activity and basic properties of Antimicrobial stainless steels "NSSAM series". *Nisshin Steel Technical Report (Japan)*, *77*, pp. 69-81.

Osório, W.R., Cremasco, A., Andrade, P.N., Garcia, A. and Caram, R., 2010. Electrochemical behavior of centrifuged cast and heat treated Ti–Cu alloys for medical applications. *Electrochimica Acta*, *55*(3), pp. 759-770.

Özer, G. and Yilmaz, M.S., 2023. Corrosion Behaviour of Additive Manufactured Metals. In *Springer Handbook of Additive Manufacturing* (pp. 751-776). Cham: Springer International Publishing.

Palmquist, A., Lindberg, F., Emanuelsson, L., Brånemark, R., Engqvist, H. and Thomsen, P., 2009. Morphological studies on machined implants of commercially pure titanium and titanium alloy (Ti6Al4V) in the rabbit. *Journal of Biomedical Materials Research Part B: Applied Biomaterials*, *91*(1), pp. 309-319.

Pesode, P. and Barve, S., 2023. Additive manufacturing of metallic biomaterials: sustainability aspect, opportunity, and challenges. *Journal of Industrial and Production Engineering*, *40*(6), pp. 464-505.

Peters, M., and Leyens, C., 2003. Structure and properties of titanium and titanium alloys. *Titanium and Titanium Alloys: Fundamentals and Applications*, pp. 1-36.

Poole, K., 2017. At the nexus of antibiotics and metals: the impact of Cu and Zn on antibiotic activity and resistance. *Trends in Microbiology*, *25*(10), pp. 820-832.

Poondla, N., Srivatsan, T.S., Patnaik, A. and Petraroli, M., 2009. A study of the microstructure and hardness of two titanium alloys: Commercially pure and Ti–6Al–4V. *Journal of Alloys and Compounds*, *486*(1-2), pp. 162-167.

Qi, H., Zhou, X., Li, J., Hu, Y. and Xu, L., 2021. Performance testing and rapid solidification behavior of stainless steel powders prepared by gas atomization. *Materials*, *14*(18), pp. 5188-5188.

Qi, P., Li, B., Wang, T., Zhou, L. and Nie, Z., 2021. Microstructure and properties of a novel ternary Ti–6Zr–xFe alloy for biomedical applications. *Journal of Alloys and Compounds*, *854*, pp. 157119-157127.

Qiao, Q., 2023. *Investigation of Corrosion, Mechanical and Antibacterial Properties of Cu/Ag-Bearing Ti-Based Coatings Fabricated by Laser Surface Alloying* (Doctoral theis, University of Macau).

Rajendrachari, S. ed., 2023. *Practical Implementations of Additive Manufacturing Technologies*. Springer Nature.

Ralston, K.D. and Birbilis, N., 2010. Effect of grain size on corrosion: a review. *Corrosion, 66*(7), pp. 075005-075019

Rashid, M., Narayan, R.L., Zhang, D.L. and Han, W.Z., 2022. A comparative study of microstructures and mechanical behaviour of laser metal deposited and electron beam melted Ti-6Al-4V. *Journal of Materials Engineering and Performance*, *31*, pp. 542-551.

Rathbone, C.R., Cross, J.D., Brown, K.V., Murray, C.K. and Wenke, J.C., 2011. Effect of various concentrations of antibiotics on osteogenic cell viability and activity. *Journal of Orthopaedic Research*, *29*(7), pp. 1070-1074.

Rayleigh, L., 1878. On the instability of jets. *Proceedings of the London Mathematical Society*, *1*(1), pp. 4-13.

Rehme, O. and Emmelmann, C., 2005, June. Reproducibility for properties of selective laser melting products. In: *Proceedings of the Third International WLT-Conference on Lasers in Manufacturing* pp. 227-232.

Ren, L., Ma, Z., Li, M., Zhang, Y., Liu, W., Liao, Z. and Yang, K., 2014. Antibacterial properties of Ti–6Al–4V–xCu alloys. *Journal of Materials Science and Technology*, *30*(7), pp. 699-705.

Rescaglio, A., Schockmel, J., Vandewalle, N. and Lumay, G., 2017. Combined effect of moisture and electrostatic charges on powder flow. In: *EPJ Web of Conferences*, *140*, pp. 13009-13013. EDP Sciences.

Ryan, K.R., Down, M.P. and Banks, C.E., 2021. Future of additive manufacturing: Overview of 4D and 3D printed smart and advanced materials and their applications. *Chemical Engineering Journal*, *403*, pp. 126162-126175.

Saboori, A., Gallo, D., Biamino, S., Fino, P. and Lombardi, M., 2017. An overview of additive manufacturing of titanium components by directed energy deposition: microstructure and mechanical properties. *Applied Sciences*, *7*(9), pp. 883-906.

Saha, S. and Roy, S., 2022. Metallic dental implants wear mechanisms, materials, and manufacturing processes: a literature review. *Materials*, *16*(1), pp. 161-174.

Saini, M., Singh, Y., Arora, P., Arora, V. and Jain, K., 2015. Implant biomaterials: A comprehensive review. *World Journal of Clinical Cases, WJCC*, *3*(1), p. 52-57.

Sames, W.J., List, F.A., Pannala, S., Dehoff, R.R. and Babu, S.S., 2016. The metallurgy and processing science of metal additive manufacturing. *International Materials Reviews*, *61*(5), pp. 315-360.

Schutz, R.W., 1996. Ruthenium enhanced titanium alloys. *Platinum Metals Review*, *40*(2), pp. 54-61.

Searson, L.J., Gough, M. and Hemmings, K., 2019. *Implantology in General Dental Practice* (Vol. 4). Quintessence Publishing Company Limited.

Seebach, E. and Kubatzky, K.F., 2019. Chronic implant-related bone infections—can immune modulation be a therapeutic strategy? *Frontiers in Immunology*, *10*, pp. 1724-1732.

Seth, S. and Kalra, P., 2013. Effect of dental implant parameters on stress distribution at bone-implant interface. *International Journal of Science and Research*, *2*(6), pp. 121-124.

Sieniawski, J., Ziaja, W., Kubiak, K. and Motyka, M., 2013. Microstructure and mechanical properties of high strength two-phase titanium alloys. In: *Titanium Alloys - Advances in Properties Control*, pp. 69-80. Rijeka: InTech.

Simson, D. and Subbu, S.K., 2022. Effect of process parameters on surface integrity of LPBF Ti6Al4V. *Procedia CIRP*, *108*, pp. 716-721.

Sing, S.L., An, J., Yeong, W.Y. and Wiria, F.E., 2016. Laser and electron-beam powder-bed additive manufacturing of metallic implants: A review on processes, materials and designs. *Journal of Orthopaedic Research*, *34*(3), pp. 369-385.

Singla, A.K., Banerjee, M., Sharma, A., Singh, J., Bansal, A., Gupta, M.K., Khanna, N., Shahi, A.S. and Goyal, D.K., 2021. Selective laser melting of Ti6Al4V alloy: Process parameters, defects and post-treatments. *Journal of Manufacturing Processes*, *64*, pp.161-187.

Song, Y.Q., Li, S.C. and Du, G.H., 2009. Study on Formation Mechanism of Ti/Cu Solid Phase Interface Diffusion Solution Layer. *Rare Metal Materials and Engineering*, *38,* pp. 1188-1192.

Soro, N., Attar, H., Brodie, E., Veidt, M., Molotnikov, A. and Dargusch, M.S., 2019. Evaluation of the mechanical compatibility of additively manufactured porous Ti–25Ta alloy for load-bearing implant applications. *Journal of the Mechanical Behavior of Biomedical Materials*, *97*, pp. 149-158.

South Africa - Population Ages 65 And Above (% Of Total) - 2024 Data 2025 Forecast 1960-2022 Historical; https://tradingeconomics.com/south-africa/population-ages-65-and-above-percent-of-total-wb data.html#:~:text=Population%20ages%2065%20and%20above%20(%25%20of%20total%20population)%20in,compiled%20from%20officially%20recognized%20sources (Accessed:12 March 2024)

Souza, J.C., Ponthiaux, P., Henriques, M., Oliveira, R., Teughels, W., Celis, J.P. and Rocha, L.A., 2013. Corrosion behaviour of titanium in the presence of Streptococcus mutans. *Journal of Dentistry*, *41*(6), pp. 528-534.

Souza, S.A., Afonso, C.R.M., Ferrandini, P.L., Coelho, A.A. and Caram, R., 2009. Effect of cooling rate on Ti–Cu eutectoid alloy microstructure. *Materials Science and Engineering: C*, *29*(3), pp.1023-1028.

Spotose, L. Identifying Ti-Cu-based alloys for biomedical applications, MSc dissertation, University of the Witwatersrand, (2023).

Stamm, K., 1964. *Untersuchungen zum Mechanismus der Ultraschallvernebelung an Flüssigkeitsoberflächen im Hinblick auf technische Anwendungen* (Doctoral dissertation, Gerd Wasmund, Germany).

Stanford, C.M., 2008. Surface modifications of dental implants. *Australian Dental Journal*, *53*, pp. S26-S33.

Staroveski, T., Brezak, D. and Udiljak, T., 2015. Drill wear monitoring in cortical bone drilling. *Medical Engineering and Physics*, *37*(6), pp. 560-566.

Stenlund, P., Omar, O., Brohede, U., Norgren, S., Norlindh, B., Johansson, A., Lausmaa, J., Thomsen, P. and Palmquist, A., 2015. Bone response to a novel Ti–Ta–Nb–Zr alloy. *Acta Biomaterialia*, *20*, pp. 165-175.

Stenport, V.F. and Johansson, C.B., 2008. Evaluations of bone tissue integration to pure and alloyed titanium implants. *Clinical Implant Dentistry and Related Research*, *10*(3), pp. 191-199.

Sullivan, R.M., 2001. Implant dentistry and the concept of osseointegration: a historical perspective. *Journal of the California Dental Association*, *29*(11), pp. 737-744.

Sun, P., Fang, Z.Z., Zhang, Y. and Xia, Y., 2017. Review of the methods for production of spherical Ti and Ti alloy powder. *Journal of Materials*, *69*, pp. 1853-1860.

Sun, Y., Moroz, A. and Alrbaey, K., 2014. Sliding wear characteristics and corrosion behaviour of selective laser melted 316L stainless steel. *Journal of Materials Engineering and Performance*, *23*, pp. 518-526.

Svetlizky, D., Zheng, B., Steinberg, D.M., Schoenung, J.M., Lavernia, E.J. and Eliaz, N., 2022. The influence of laser directed energy deposition (DED) processing parameters for Al5083 studied by central composite design. *Journal of Materials Research and Technology*, *17*, pp. 3157-3171.

Tammas-Williams, S., Withers, P.J., Todd, I. and Prangnell, P.B., 2017. The influence of porosity on fatigue crack initiation in additively manufactured titanium components. *Scientific Reports*, *7*(1), pp. 7308-7321.

Tan, X.P., Tan, Y.J., Chow, C.S.L., Tor, S.B. and Yeong, W.Y., 2017. Metallic powder-bed based 3D printing of cellular scaffolds for orthopaedic implants: A state-of-the-art review on manufacturing, topological design, mechanical properties and biocompatibility. *Materials Science and Engineering C*, *76*, pp. 1328-1343.

Thakur, A., Kumar, A., Kaya, S., Marzouki, R., Zhang, F. and Guo, L., 2022. Recent advancements in surface modification, characterization and functionalization for enhancing the biocompatibility and corrosion resistance of biomedical implants. *Coatings*, *12*(10), pp. 1459-1508.

Thampy, V., Fong, A.Y., Calta, N.P., Wang, J., Martin, A.A., Depond, P.J., Kiss, A.M., Guss, G., Xing, Q., Ott, R.T. and van Buuren, A., 2020. Subsurface cooling rates and microstructural response during laser based metal additive manufacturing. *Scientific Reports*, *10*(1), pp. 1981-1990.

Thomas, M., Malot, T., Aubry, P., Colin, C., Vilaro, T. and Bertrand, P., 2016. The prospects for additive manufacturing of bulk TiAl alloy. *Materials at High Temperatures*, *33*(4-5), pp. 571-577.

Tofail, S.A., Koumoulos, E.P., Bandyopadhyay, A., Bose, S., O'Donoghue, L. and Charitidis, C., 2018. Additive manufacturing: scientific and technological challenges, market uptake and opportunities. *Materials Today*, *21*(1), pp. 22-37.

Tolochko, N.K., Mozzharov, S.E., Yadroitsev, I.A., Laoui, T., Froyen, L., Titov, V.I. and Ignatiev, M.B., 2004. Balling processes during selective laser treatment of powders. *Rapid Prototyping Journal*, *10*(2), pp. 78-87.

United Nations (2015), *2030 Agenda for Sustainable Development*. Available at: https://sdgs.un.org/2030agenda (Accessed: 13 January 2025).

Van der Schueren, B. and Kruth, J.P., 1995. Powder deposition in selective metal powder sintering. *Rapid Prototyping Journal*, *1*(3), pp. 23-31.

Veiga, C., Davim, J.P. and Loureiro, A.J.R., 2012. Properties and applications of titanium alloys: a brief review. *Reviews and Advanced Material Science*, *32*(2), pp. 133-148.

Velasco-Ortega, E., Flichy-Fernández, A., Punset, M., Jiménez-Guerra, A., Manero, J.M. and Gil, J., 2014. Fracture and fatigue of titanium narrow dental implants: New trends in order to improve the mechanical response. *Materials*, *12*(22), pp. 3728-3740.

Vilardell, A.M., Yadroitsev, I., Yadroitsava, I., Albu, M., Takata, N., Kobashi, M., Krakhmalev, P., Kouprianoff, D., Kothleitner, G. and Du Plessis, A., 2020. Manufacturing and characterization of in-situ alloyed Ti6Al4V (ELI)-3 at.% Cu by laser powder bed fusion. *Additive Manufacturing*, *36*, pp.101436-101450.

Vock, S., Klöden, B., Kirchner, A., Weißgärber, T. and Kieback, B., 2019. Powders for powder bed fusion: a review. *Progress in Additive Manufacturing*, *4*, pp. 383-397.

Wang, J., Zhang, S., Sun, Z., Wang, H., Ren, L. and Yang, K., 2019. Optimization of mechanical property, antibacterial property and corrosion resistance of Ti-Cu alloy for dental implant. *Journal of Materials Science and Technology*, *35*(10), pp. 2336-2344.

Wang, Q., Han, C., Choma, T., Wei, Q., Yan, C., Song, B. and Shi, Y., 2017. Effect of Nb content on microstructure, property and in vitro apatite-forming capability of Ti-Nb alloys fabricated via selective laser melting. *Materials and Design*, *126*, pp.268-277.

Wang, Q., Zhang, K. and Niu, W., 2021. Microstructural characteristic and mechanical properties of titanium-copper alloys in-situ fabricated by selective laser melting. *Journal of Alloys and Compounds*, *885*, pp. 161032-161043.

Wang, Z., Fu, B., Wang, Y., Dong, T., Li, J., Li, G., Zhao, X., Liu, J. and Zhang, G., 2022. Effect of Cu content on the precipitation behaviors, mechanical and corrosion properties of as-cast Ti-Cu alloys. *Materials*, *15*(5), pp. 1696-1712.

Wei, H., Wei, Y.H., Hou, L.F. and Dang, N., 2016. Correlation of ageing precipitates with the corrosion behaviour of Cu-4 wt.% Ti alloys in 3.5 wt.% NaCl solution. *Corrosion Science*, *111*, pp. 382-390.

Wei, Q., Wang, L., Fu, Y., Qin, J., Lu, W. and Zhang, D., 2011. Influence of oxygen content on microstructure and mechanical properties of Ti–Nb–Ta–Zr alloy. *Materials and Design*, *32*(5), pp. 2934-2939.

Welsch, G., Boyer, R. and Collings, E.W. (eds.) (1993) *Materials Properties Handbook: Titanium Alloys*. Materials Park, Ohio, USA: ASM International.

Williams, D., 2003. Revisiting the definition of biocompatibility. *Medical Device Technology*, *14*(8), pp. 10-13.

Williams, D.F., 2008. On the mechanisms of biocompatibility. *Biomaterials*, *29*(20), pp. 2941-2953.

World Bank. (2021) Challenges facing people with disabilities in Sub-Saharan Africa – in 5 charts. [online] Available at: https://www.worldbank.org/en/topic/poverty/brief/challenges-facing-people-with-disabilities-in-sub-saharan-africa-in-5-charts (Accessed 20 November 2024).

World Health Organization (WHO) (1982). *Copper*. [online] Available at: https://apps.who.int/food-additives-contaminants-jecfa-database/Home/Chemical/2824#:~:text=The%20level%20of%20copper%20in,mg%2Fday%20for%20infants (Accessed 6 January 2025).

Wunner, F.M., Florczak, S., Mieszczanek, P., Bas, O., De-Juan-Pardo, E.M. and Hutmacher, D.W., 2017. *Comprehensive Biomaterials II*. 2nd ed. Amsterdam: Elsevier.

Wysocki, B., Maj, P., Krawczyńska, A., Rożniatowski, K., Zdunek, J., Kurzydłowski, K.J. and Święszkowski, W., 2017. Microstructure and mechanical properties investigation of CP titanium processed by selective laser melting (SLM). *Journal of Materials Processing Technology*, *241*, pp.13-23.

Xie, Y., Lu, M., Cui, S., Yu, H., Wang, L., Ke, H. and Zhang, E., 2022. Construction of a rough surface with submicron Ti_2Cu particle on Ti-Cu alloy and its effect on the antibacterial properties and cell biocompatibility. *Metals*, *12*(6), pp .1008-1021.

Xin, C., Wang, N., Chen, Y., He, B., Zhao, Q., Chen, L., Tang, Y., Luo, B., Zhao, Y. and Yang, X., 2022. Biological corrosion behaviour and antibacterial properties of Ti-Cu alloy with different Ti_2Cu morphologies for dental applications. *Materials and Design*, *215*, pp. 110540-110551.

Xu, J., Lu, Y., Pan, X., Zhan, D., Wang, Q. and Zhang, N., 2023. Antibacterial performance of a porous Cu-bearing titanium alloy by laser additive manufacturing. *Frontiers in Bioengineering and Biotechnology*, *11*, pp. 1226745-1226775.

Xu, J.L., Tao, S.C., Bao, L.Z., Luo, J.M. and Zheng, Y.F., 2019. Effects of Mo contents on the microstructure, properties and cytocompatibility of the microwave sintered porous Ti-Mo alloys. *Materials Science and Engineering C*, 97, pp. 156-165.

Yadroitsev, I., Krakhmalev, P., Yadroitsava, I., Johansson, S. and Smurov, I., 2013. Energy input effect on morphology and microstructure of selective laser melting single track from metallic powder. *Journal of Materials Processing Technology*, *213*(4), pp. 606-613.

Yadroitsev, I., Yadroitsava, I., Du Plessis, A. and MacDonald, E. eds., 2021. *Fundamentals of Laser Powder Bed Fusion of Metals*. Amsterdam, The Netherlands: Elsevier.

Yamamoto, A., Honma, R. and Sumita, M., 1998. Cytotoxicity evaluation of 43 metal salts using murine fibroblasts and osteoblastic cells. *Journal of Biomedical Materials Research: An Official Journal of The Society for Biomaterials, The Japanese Society for Biomaterials, and the Australian Society for Biomaterials*, *39*(2), pp. 331-340.

Yan, M. and Yu, P., 2015. An Overview of Densification, Microstructure and Mechanical Property of Additively Manufactured Ti-6Al-4V—Comparison among Selective Laser Melting, Electron Beam Melting, Laser Metal Deposition and Selective Laser Sintering, and with Conventional Powder. Sintering Techniques of Materials**.** InTech.

Yang, Y., Guo, X. and Dong, Z., 2021. Effect of Nb on microstructure and mechanical properties of Ti-xNb-4Zr–8Sn alloys. *Materials Science and Engineering A*, *825*, p. 141741-141751.

Yueling, G.U.O., Lina, J.I.A., Bin, K.O.N.G., Na, W.A.N.G. and Zhang, H., 2018. Single track and single layer formation in selective laser melting of niobium solid solution alloy. *Chinese Journal of Aeronautics*, *31*(4), pp. 860-866.

Zadeh, J.M., Yeganeh, M., Zaree, S.R.A. and Khorasanian, M., 2024. Microstructure and corrosion behavior of Ti-10Cu fabricated by selective laser melting. *Materials Today Communications*, 39, pp. 109103-109119.

Zadeh, M.K., Yeganeh, M., Shoushtari, M.T., Ramezanalizadeh, H. and Seidi, F., 2022. Microstructure, corrosion behaviour, and biocompatibility of Ti-6Al-4 V alloy fabricated by LPBF and EBM techniques. *Materials Today Communications*, *31*, pp. 103502-103514.

Zadpoor, A.A., 2017. Design for additive bio-manufacturing: From patient-specific medical devices to rationally designed meta-biomaterials. *International Journal of Molecular Sciences*, *18*(8), pp. 1607-1625.

Zhan, Z., Zhang, Q., Wang, S., Liu, X., Zhang, H., Sun, Z., Ge, Y. and Du, N., 2024. Comparison on the electrochemical corrosion behavior of Ti6Al4V alloys fabricated by laser powder bed fusion and casting. *Materials*, *17*(13), pp. 3322-3334.

Zhang, E., Li, F., Wang, H., Liu, J., Wang, C., Li, M. and Yang, K., 2013. A new antibacterial titanium–copper sintered alloy: preparation and antibacterial property. *Materials Science and Engineering C*, *33*(7), pp. 4280-4287.

Zhang, E., Ren, J., Li, S., Yang, L., Qin, G., 2016a. Optimisation of mechanical properties, biocorrosion properties and antibacterial properties of as-cast Ti–Cu alloys. *Biomedical Materials. 11*, pp. 1-13.

Zhang, E., Wang, X., Chen, M. and Hou, B., 2016b. Effect of the existing form of Cu element on the mechanical properties, bio-corrosion and antibacterial properties of Ti-Cu alloys for biomedical application. *Materials Science and Engineering C*, *69*, pp. 1210-1221.

Zhang, E., Zheng, L., Liu, J., Bai, B. and Liu, C., 2015. Influence of Cu content on the cell biocompatibility of Ti–Cu sintered alloys. *Materials Science and Engineering C*, *46*, pp. 148-157.

Zhang, L.C., Klemm, D., Eckert, J., Hao, Y.L. and Sercombe, T.B., 2011. Manufactured by selective laser melting and mechanical behaviour of a biomedical Ti–24Nb–4Zr–8Sn alloy. *Scripta Materialia*, *65*(1), pp. 21-24.

Zhang, X., Wu, H., Geng, Z., Huang, X., Hang, R., Ma, Y., Yao, X. and Tang, B., 2014. Microstructure and cytotoxicity evaluation of duplex-treated silver-containing antibacterial TiO_2 coatings. *Materials Science and Engineering C*, *45*, pp. 402-410.

Zhao, Z., Dong, C., Kong, D., Wang, L., Ni, X., Zhang, L., Wu, W., Zhu, L. and Li, X., 2021. Influence of pore defects on the mechanical property and corrosion behavior of SLM 18Ni300 maraging steel. *Materials Characterization*, *182*, pp. 111514-111528.

Zhu, G., Wang, G. and Li, J.J., 2021. Advances in implant surface modifications to improve osseointegration. *Materials Advances*, *2*(21), pp. 6901-6927.

Zhu, L., Ye, X., Tang, G., Zhao, N., Gong, Y., Zhao, Y., Zhao, J. and Zhang, X., 2006. Corrosion test, cell behavior test, and in vivo study of gradient TiO2 layers produced by compound electrochemical oxidation. *Journal of Biomedical Materials Research Part A: An Official Journal of The Society for Biomaterials, The Japanese Society for Biomaterials, and The Australian Society for Biomaterials and the Korean Society for Biomaterials*, *78*(3), pp.515-522.

Ziaja, W., Sieniawski, J., Kubiak, K. and Motyka, M., 2001. Fatigue and microstructure of two-phase titanium alloys. *Inżynieria Materiałowa*, *22*(5), pp. 981-984.

Żrodowski, Ł., Wróblewski, R., Choma, T., Morończyk, B., Ostrysz, M., Leonowicz, M., Łacisz, W., Błyskun, P., Wróbel, J.S., Cieślak, G. and Wysocki, B., 2021. Novel cold crucible ultrasonic atomisation powder production method for 3D printing. *Materials*, *14*(10), pp. 2541-2552.

Zwicker, U., 1980. Mechanical properties and tissue reactions of a titanium alloy for implant materials. *Titanium 1980: Science and Technology*. AIME, pp. 505–514.

Appendices

Appendix 1: List of Publications from the MSc

1. Spotose L., **Phala N.S.**, Polese C. and L.A. Cornish. Development and characterisation of antibacterial titanium-based alloys with copper for biomedical applications. 57th Congress of the Microscopy Society of Southern Africa,5-8 December 2022. Gold Reef City Johannesburg, South Africa.
2. **Phala, N.S**., Polese, C., Choma, T., Möller, H., Żrodowski, Ł. and Cornish, L., 2023. Atomisation of Ti-6Ta-1.5Zr-0.2Ru-5Cu (wt%) for additive manufacturing for biomedical applications. In *MATEC Web of Conferences*, Vol. 388. EDP Sciences
3. **Phala, N.S**, Polese, C., Ciftci, J., Choma, T. and Cornish, L.A., 2024. Laser powder bed fusion of Ti-6Ta-1.5 Zr-0.2 Ru-5Cu (mass%)–process parameter evaluation using single tracks analysis. In *MATEC Web of Conferences,* Vol. 406. EDP Sciences.
4. **Phala N.S.**, Polese C., Ciftci J., Choma T. and Cornish L.A. Characterisation of Ti-6Ta-1.5Zr-0.2Ru-5Cu printed by laser powder bed fusion. 58th Congress of the Microscopy Society of Southern Africa, 2-5 December 2024. University of Free State (Bloemfontein), South Africa.

Appendix 2: Sample preparation

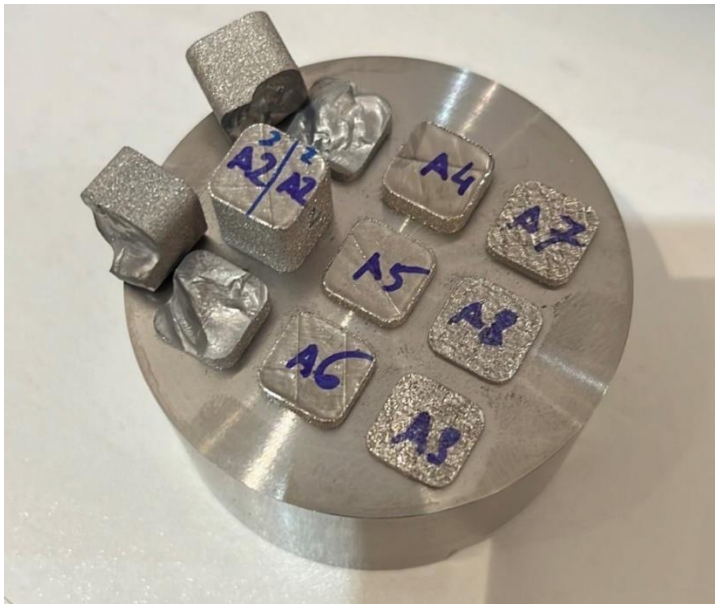

Figure A2.1. Fracture behaviour of the A1, A2, and A3 samples from the AconityMIDI system. The A1 and A3 samples cracked upon removal from the build plate and handling on the desk, while the A2 sample cracked during the Wire Electrical Discharge Machining (WEDM) cutting process. The image shows the high density of the material in the A2 sample.



Figure A2.2. Platform after process with selected parameters -angle view.



Figure A2.3. Platform after process with selected parameters - top view.



Figure A2.4. Homogeneous bars prior to atomisation.

Appendix 3: XRD DATA

1. βTi

00-044-1288 Jun 14, 2021 9:35 AM (669011)

Status Primary **Quality Mark:** Calculated **Environment:** Ambient **Temp:** 298.0 K (Assigned by ICDD editor)
Phase: β **Chemical Formula:** Ti **Empirical Formula:** Ti **Weight %:** Ti100.00 **Atomic %:** Ti100.00
Compound Name: Titanium **Alternate Name:** β-Ti **Entry Date:** 09/01/1994

Radiation: CuKα1 (1.5406 Å) **d-Spacing:** Calculated **Intensity:** Calculated **I/Ic:** 8.68

Crystal System: Cubic **SPGR:** Im-3m (229)
Author's Unit Cell [a: 3.3065 Å **Volume:** 36.15 Å³ **Z:** 2.00 **MolVol:** 18.07] **Calculated Density:** 4.401 g/cm³
SS/FOM: F(9) = 66.0(0.0152, 9)

Space Group: Im-3m (229) **Molecular Wt:** 47.90 g/mol
Crystal Data [a: 3.306 Å **b:** 3.306 Å **c:** 3.306 Å **α:** 90.00° **β:** 90.00° **γ:** 90.00° **XtlCell Vol:** 36.15 Å³
XtlCell Z: 2.00 **a/b:** 1.000 **c/b:** 1.000]
Reduced Cell [a: 2.864 Å **b:** 2.864 Å **c:** 2.864 Å **α:** 109.47° **β:** 109.47° **γ:** 109.47° **RedCell Vol:** 18.07 Å³
]

Crystal (Symmetry Allowed): Centrosymmetric

Subfiles: Explosive, Hydrogen Storage Material, Inorganic, Metal & Alloy **Pearson Symbol:** cI2.00
Prototype Structure [Formula Order]: W **Prototype Structure [Alpha Order]:** W
LPF Prototype Structure [Formula Order]: W,cI2,229 **LPF Prototype Structure [Alpha Order]:** W,cI2,229

Cross-Ref PDF #'s: 04-003-5566 (Primary)

References:

Type	DOI	Reference
Primary Reference		Calvert, L., Lakes Entrance, Victoria, Australia. Private Communication 1993.
Unit Cell		Eppelsheimer, D., Perman, R. Nature (London) 1950, 166, 960.

Database Comments: General Comments: High temperature phase, stable above 1153 K.

d-spacings (6) - Ti - 00-044-1288 (Stick, Fixed Slit Intensity) - Co Kα1 1.78896 Å

2θ (°)	d (Å)	I	h	k	l	*	2θ (°)	d (Å)	I	h	k	l	*	2θ (°)	d (Å)	I	h	k	l	*
44.998	**2.3375**	100	1	1	0		83.024	**1.3496**	17	2	1	1		117.660	1.0454	5	3	1	0	
65.512	**1.6532**	12	2	0	0		99.855	1.1689	4	2	2	0		139.179	0.9544	1	2	2	2	

2. αTi

00-044-1294 Feb 25, 2021 9:44 AM (669011)

Status Primary **Quality Mark:** Star **Environment:** Ambient **Temp:** 298.0 K (Assigned by ICDD editor) **Phase:** α
Chemical Formula: Ti **Empirical Formula:** Ti **Weight %:** Ti100.00 **Atomic %:** Ti100.00
Compound Name: Titanium **Mineral Name:** Titanium, syn **CAS Number:** 7440-32-6 **Entry Date:** 09/01/1994

Radiation: CuKα1 (1.5406 Å) **Filter:** Graph Mono **Internal Standard:** Si **d-Spacing:** Diffractometer **Cutoff:** 15.00 Å
Intensity: Diffractometer - Peak **I/Ic:** 0.9

Crystal System: Hexagonal **SPGR:** P63/mmc (194)
Author's Unit Cell [a: 2.9505(1) Å **c:** 4.6826(3) Å **Volume:** 35.30 Å³ **Z:** 2.00 **MolVol:** 17.65 **c/a:** 1.587]
Calculated Density: 4.506 g/cm³ **Color:** Gray **SS/FOM:** F(17) = 387.5(0.0026, 17)

Space Group: P63/mmc (194) **Molecular Wt:** 47.90 g/mol
Crystal Data [a: 2.951 Å **b:** 2.951 Å **c:** 4.683 Å **α:** 90.00° **β:** 90.00° **γ:** 120.00° **XtlCell Vol:** 35.30 Å³
XtlCell Z: 2.00 **c/a:** 1.587 **a/b:** 1.000 **c/b:** 1.587]
Reduced Cell [a: 2.950 Å **b:** 2.951 Å **c:** 4.683 Å **α:** 90.00° **β:** 90.00° **γ:** 120.00° **RedCell Vol:** 35.30 Å³]

Atomic parameters are cross-referenced from PDF entry 04-011-9045 **AC Space Group:** P63/mmc (194)
AC Unit Cell [a: 2.943(2) Å **b:** 2.943(2) Å **c:** 4.698(3) Å **α:** 90° **β:** 90° **γ:** 120°]
Space Group Symmetry Operators:

Seq	Operator	Seq	Operator	Seq	Operator	Seq	Operator	Seq	Operator
1	x,y,z	6	x-y,x,-z	11	-x+y,y,z	16	-y,x-y,-z+1/2	21	-x,-x+y,z+1/2
2	-x,-y,-z	7	-y,-x,z	12	x-y,-y,-z	17	x-y,x,z+1/2	22	x,x-y,-z+1/2
3	-y,x-y,z	8	y,x,-z	13	-x,-y,z+1/2	18	-x+y,-x,-z+1/2	23	x-y,-y,z+1/2
4	y,-x+y,-z	9	x,x-y,z	14	x,y,-z+1/2	19	y,x,z+1/2	24	-x+y,y,-z+1/2
5	-x+y,-x,z	10	-x,-x+y,-z	15	y,-x+y,z+1/2	20	-y,-x,-z+1/2		

Atomic Coordinates:

Atom	Num	Wyckoff	Symmetry	x	y	z	SOF	IDP	AET
Ti	1	2c	-6m2	0.33333	0.66666	0.25	1.0		

Crystal (Symmetry Allowed): Centrosymmetric

Subfiles: Common Phase, Explosive, Forensic, Hydrogen Storage Material, Inorganic, Metal & Alloy, Mineral Related (Mineral, Synthetic)
Pearson Symbol: hP2.00 **Prototype Structure [Formula Order]:** Mg **Prototype Structure [Alpha Order]:** Mg
LPF Prototype Structure [Formula Order]: Mg,hP2,194 **LPF Prototype Structure [Alpha Order]:** Mg,hP2,194

Cross-Ref PDF #'s: 00-005-0682 (Alternate), 04-001-8963 (Primary), 04-002-2539 (Alternate), 04-002-5384 (Alternate), 04-003-2226 (Alternate), 04-003-5531 (Alternate), 04-003-5533 (Alternate), 04-003-5550 (Alternate), 04-003-5575 (Alternate), 04-003-5577 (Alternate), 04-003-7293 (Alternate), 04-004-3071 (Alternate), 04-004-4447 (Alternate), 04-004-7631 (Alternate), 04-004-8480 (Alternate), 04-004-8487 (Alternate), 04-004-9042 (Alternate), 04-004-9158 (Alternate), 04-005-7594 (Alternate), 04-005-7641 (Alternate), 04-006-2824 (Alternate), 04-006-6380 (Alternate), 04-007-9313 (Alternate), 04-007-9759 (Alternate), 04-008-1385 (Alternate), 04-011-9045 (Alternate)

References:

Type	DOI	Reference
Primary Reference		Saller, R., McCarthy, G., North Dakota State University, Fargo, North Dakota, USA. ICDD Grant-in-Aid 1993.
Crystal Structure		Crystal Structure Source: LPF.
Structure		Acta Geol. Sin. (Engl. Ed.) 2013, 87, 1275.

Database Comments: Additional Patterns: Validated by calculated pattern. To replace 00-005-0682. General Comments: Average relative standard deviation in intensity of the ten strongest reflections for three specimen mounts = 6.7%. Component of pyrotechnic boom powders. Sample Source or Locality: Sample was obtained from A.D. Mackay Inc. Unit Cell Data Source: Powder Diffraction.

d-spacings (16) - Ti - 00-044-1294 (Stick, Fixed Slit Intensity) - Co Kα1 1.78896 Å

2θ (°)	d (Å)	I	h	k	l	*	2θ (°)	d (Å)	I	h	k	l	*	2θ (°)	d (Å)	I	h	k	l	*
40.986	**2.55500**	25	1	0	0		88.874	1.27760	1	2	0	0		129.579	0.98865	2	2	0	3	
44.927	**2.34100**	30	0	0	2		91.561	1.24810	9	1	1	2		135.692	0.96578	1	2	1	0	
47.005	**2.24300**	100	1	0	1		93.071	1.23240	6	2	0	1		142.039	0.94591	4	2	1	1	
62.420	1.72620	13	1	0	2		99.646	1.17070	1	0	0	4		154.546	0.91701	3	1	1	4	
74.645	1.47530	11	1	1	0		105.798	1.12150	1	2	0	2								
84.371	1.33200	11	1	0	3		114.373	1.06430	1	1	0	4								

© 2021 International Centre for Diffraction Data. All rights reserved.

3. Ti_2Cu

04-003-1382 Oct 26, 2020 12:08 PM (669011)

Status Primary **Quality Mark:** Indexed **Environment:** Ambient **Temp:** 298.0 K (Assigned by ICDD editor)
Chemical Formula: Cu Ti2 **Empirical Formula:** Cu Ti2 **Weight %:** Cu39.89 Ti60.11 **Atomic %:** Cu33.33 Ti66.67
Compound Name: Copper Titanium **Entry Date:** 09/01/2005 **Modification Date:** 09/01/2011
Modifications: Reflections

Radiation: CuKα1 (1.5406 Å) **d-Spacing:** Calculated **Intensity:** Calculated - Peak **I/Ic:** 7.5 **I/Ic - CW ND:** 0.41

Crystal System: Tetragonal **SPGR:** I4/mmm (139)
Author's Unit Cell [a: 2.9438 Å **c:** 10.7861 Å **Volume:** 93.47 Å³ **Z:** 2.00 **MolVol:** 46.73 **c/a:** 3.664]
Calculated Density: 5.659 g/cm³ **Structural Density:** 5.66 g/cm³ **SS/FOM:** F(30) = 999.9(0.0001, 31)
R-factor: 0.05

Space Group: I4/mmm (139) **Molecular Wt:** 159.28 g/mol
Crystal Data [a: 2.944 Å **b:** 2.944 Å **c:** 10.786 Å **α:** 90.00° **β:** 90.00° **γ:** 90.00° **XtlCell Vol:** 93.47 Å³
XtlCell Z: 2.00 **c/a:** 3.664 **a/b:** 1.000 **c/b:** 3.664]
Reduced Cell [a: 2.944 Å **b:** 2.944 Å **c:** 5.781 Å **α:** 104.75° **β:** 104.75° **γ:** 90.00° **RedCell Vol:** 46.74 Å³]

AC Space Group: I4/mmm (139)
AC Unit Cell [a: 2.9438 Å **b:** 2.9438 Å **c:** 10.7861 Å **α:** 90° **β:** 90° **γ:** 90°]
Space Group Symmetry Operators:

Seq	Operator	Seq	Operator	Seq	Operator	Seq	Operator	Seq	Operator	Seq	Operator
1	x,y,z	4	x,y,-z	7	x,-y,z	10	y,-x,-z	13	y,x,z	16	y,x,-z
2	-x,-y,-z	5	-x,y,z	8	-x,y,-z	11	y,-x,z	14	-y,-x,-z		
3	-x,-y,z	6	x,-y,-z	9	-y,x,z	12	-y,x,-z	15	-y,-x,z		

Atomic Coordinates:

Atom	Num	Wyckoff	Symmetry	x	y	z	SOF	IDP	AET
Ti	1	4e	4mm	0.0	0.0	0.339	1.0		14-b
Cu	2	2a	4/mmm	0.0	0.0	0.0	1.0		14-b

Crystal (Symmetry Allowed): Centrosymmetric

Subfiles: Inorganic, Metal & Alloy **Pearson Symbol:** tI6.00 **Prototype Structure [Formula Order]:** Zr2 Cu
Prototype Structure [Alpha Order]: Cu Zr2 **LPF Prototype Structure [Formula Order]:** Cu Zr2,tI6,139
LPF Prototype Structure [Alpha Order]: Cu Zr2,tI6,139 **ANX:** NO2

Cross-Ref PDF #'s: 00-015-0717 (Primary), 00-018-0458 (Deleted), 01-078-9518 (Alternate), 04-001-2220 (Alternate), 04-001-3025 (Alternate), 04-002-0043 (Alternate), 04-003-2231 (Alternate), 04-003-6095 (Alternate), 04-003-6103 (Alternate), 04-003-6220 (Alternate)
Former PDF Numbers: 01-072-0441

References:

Type	DOI	Reference
Primary Reference		Calculated from LPF using POWD-12++.
Structure		Mueller M.H., Knott H.W. "The Crystal Structures of Ti2Cu, Ti2Ni, Ti4Ni2O, and Ti4Cu2O". Trans. Met. Soc. AIME 1963, 227, 674.

Database Comments: ANX: NO2. LPF Collection Code: 452044. Sample Preparation: STARTING MATERIALS:Cu,Ti. Compound Preparation: arc-melted. Sample annealed at 973 K for 5 d in evacuated Vycor tube. Minor Warning: No e.s.d reported/abstracted on the cell dimension. Unit Cell Data Source: Powder Diffraction.

d-spacings (34) - Cu Ti2 - 04-003-1382 (Stick, Fixed Slit Intensity) - Co Kα1 1.78896 Å

2θ (°)	d (Å)	I	h	k	l	*	2θ (°)	d (Å)	I	h	k	l	*
19.094	5.393050	44	0	0	2		92.697	**1.236240**	150	2	1	3	
36.717	2.839930	14	1	0	1		103.519	1.138860	50	2	0	6	
38.746	2.696520	1	0	0	4		104.454	1.131620	3	1	1	8	
46.246	**2.277710**	1000	1	0	3		105.493	1.123770	3	2	1	5	
50.899	**2.081580**	366	1	1	0		107.382	1.110000	43	1	0	9	
54.853	1.941950	11	1	1	2		112.052	1.078610	1	0	0	10	
59.679	1.797680	100	0	0	6		118.504	1.040790	17	2	2	0	
61.869	1.740030	14	1	0	5		122.157	1.021930	1	2	2	2	
65.756	1.647740	1	1	1	4		126.671	1.000930	1	2	1	7	
74.847	1.471900	87	2	0	0		128.235	0.994207	2	2	0	8	
78.090	1.419960	3	2	0	2		132.503	0.977231	1	3	0	1	
82.211	1.360540	116	1	1	6		134.210	0.970974	1	2	2	4	
83.124	1.348260	2	0	0	8		138.137	0.957678	1	1	1	10	
86.389	1.306810	1	2	1	1		141.782	0.946643	24	3	0	3	
87.632	1.291960	1	2	0	4		147.836	0.930911	24m	1	0	11	

© 2020 International Centre for Diffraction Data. All rights reserved.

2θ (°)	d (Å)	I	h	k	l	*	2θ (°)	d (Å)	I	h	k	l	*
147.836	0.930911	24m	3	1	0		166.502	0.900722	21	2	2	6	
154.361	0.917345	1	3	1	2		168.706	0.898842	5	0	0	12	

© 2020 International Centre for Diffraction Data. All rights reserved.

4.Ti_3Cu

04-007-0841 Oct 26, 2020 12:11 PM (669011)

Status Primary **Quality Mark:** Indexed **Environment:** Ambient **Temp:** 298.0 K (Assigned by ICDD editor)
Chemical Formula: Cu Ti3 **Empirical Formula:** Cu Ti3 **Weight %:** Cu30.67 Ti69.33 **Atomic %:** Cu25.00 Ti75.00
Compound Name: Copper Titanium **Entry Date:** 09/01/2005 **Modification Date:** 09/01/2011
Modifications: Reflections

Radiation: CuKα1 (1.5406 Å) **d-Spacing:** Calculated **Intensity:** Calculated - Peak **I/Ic:** 7.37 **I/Ic - CW ND:** 0.25

Crystal System: Tetragonal **SPGR:** P4/mmm (123)
Author's Unit Cell [a: 4.158 Å **c:** 3.594 Å **Volume:** 62.14 Å³ **Z:** 1.00 **MolVol:** 62.14 **c/a:** 0.864]
Calculated Density: 5.536 g/cm³ **Measured Density:** 5.41 g/cm³ **Structural Density:** 5.54 g/cm³
SS/FOM: F(30) = 71.6(0.0113, 37)

Space Group: P4/mmm (123) **Molecular Wt:** 207.15 g/mol
Crystal Data [a: 4.158 Å **b:** 4.158 Å **c:** 3.594 Å **α:** 90.00° **β:** 90.00° **γ:** 90.00° **XtlCell Vol:** 62.14 Å³
XtlCell Z: 1.00 **c/a:** 0.864 **a/b:** 1.000 **c/b:** 0.864]
Reduced Cell [a: 3.594 Å **b:** 4.158 Å **c:** 4.158 Å **α:** 90.00° **β:** 90.00° **γ:** 90.00° **RedCell Vol:** 62.14 Å³]

AC Space Group: P4/mmm (123)
AC Unit Cell [a: 4.158 Å **b:** 4.158 Å **c:** 3.594 Å **α:** 90° **β:** 90° **γ:** 90°]
Space Group Symmetry Operators:

Seq	Operator	Seq	Operator	Seq	Operator	Seq	Operator	Seq	Operator	Seq	Operator
1	x,y,z	4	x,y,-z	7	x,-y,z	10	y,-x,-z	13	y,x,z	16	y,x,-z
2	-x,-y,-z	5	-x,y,z	8	-x,y,-z	11	y,-x,z	14	-y,-x,-z		
3	-x,-y,z	6	x,-y,-z	9	-y,x,z	12	-y,x,-z	15	-y,-x,z		

Atomic Coordinates:

Atom	Num	Wyckoff	Symmetry	x	y	z	SOF	IDP	AET
Cu	1	1a	4/mmm	0.0	0.0	0.0	1.0		12-b
Ti	2	1c	4/mmm	0.5	0.5	0.0	1.0		12-b
Ti	3	2e	mmm.	0.0	0.5	0.5	1.0		12-b

Crystal (Symmetry Allowed): Centrosymmetric

Subfiles: Inorganic, Metal & Alloy **Pearson Symbol:** tP4.00 **Prototype Structure [Formula Order]:** Ti3 Cu
Prototype Structure [Alpha Order]: Cu Ti3 **LPF Prototype Structure [Formula Order]:** Cu Ti3,tP4,123
LPF Prototype Structure [Alpha Order]: Cu Ti3,tP4,123 **ANX:** NO3

Cross-Ref PDF #'s: 00-025-1144 (Primary) **Former PDF Numbers:** 01-071-7898

References:

Type	DOI	Reference
Primary Reference		Calculated from LPF using POWD-12++.
Structure		Karlsson N. "AN X-RAY STUDY OF THE PHASES IN THE COPPER-TITANIUM SYSTEM". J. Inst. Met. 1951, 79, 391.

Database Comments: ANX: NO3. LPF Collection Code: 1250535. Sample Preparation: STARTING MATERIALS:Cu,Ti. Compound Preparation: melted in induction furnace. CRUCIBLE: zirconia. ATMOSPHERE: vacuum. Sample annealed in sealed evacuated silica tube below 1173 K, water-quenched. Minor Warning: No e.s.d reported/abstracted on the cell dimension. No R factor reported/abstracted.

d-spacings (41) - Cu Ti3 - 04-007-0841 (Stick, Fixed Slit Intensity) - Co Kα1 1.78896 Å

2θ (°)	d (Å)	I	h	k	l	*	2θ (°)	d (Å)	I	h	k	l	*
24.845	4.158000	15	1	0	0		92.834	**1.234830**	150	3	1	1	
28.823	3.594000	5	0	0	1		96.601	1.198000	1	0	0	3	
35.424	2.940150	6	1	1	0		101.726	1.153220	1	3	2	0	
38.412	2.719050	10	1	0	1		101.977	1.151170	1	1	0	3	
46.290	**2.275670**	1000	1	1	1		103.649	1.137840	51	2	2	2	
50.966	**2.079000**	356	2	0	0		107.461	1.109440	45	1	1	3	
57.505	1.859510	3	2	1	0		109.093	1.098080	1m	3	0	2	
59.704	1.797000	102m	0	0	2		109.093	1.098080	1m	3	2	1	
59.704	1.797000	102m	2	0	1		114.904	1.061140	1	3	1	2	
65.585	1.651550	4m	1	0	2		118.743	1.039500	17	4	0	0	
65.585	1.651550	4m	2	1	1		124.991	1.008460	1	4	1	0	
71.376	1.533290	1	1	1	2		125.292	1.007090	1	2	1	3	
74.956	1.470080	86	2	2	0		127.212	0.998571	1	4	0	1	
80.387	1.386000	1	3	0	0		131.759	0.980050	1	3	3	0	
82.285	1.359530	118m	2	0	2		134.213	0.970963	1m	3	2	2	
82.285	1.359530	118m	2	2	1		134.213	0.970963	1m	4	1	1	
85.730	1.314880	1	3	1	0		142.174	0.945526	24	3	3	1	
87.611	1.292210	1m	2	1	2		148.333	0.929757	23	4	2	0	
87.611	1.292210	1m	3	0	1		161.434	0.906350	1	3	0	3	

© 2020 International Centre for Diffraction Data. All rights reserved.

2θ (°)	d (Å)	I	h	k	l	*	2θ (°)	d (Å)	I	h	k	l	*
167.534	0.899799	22m	4	0	2		169.156	0.898500	6	0	0	4	
167.534	0.899799	22m	4	2	1								

© 2020 International Centre for Diffraction Data. All rights reserved.

Appendix 4: Copies of publications from the MSc

DEVELOPMENT AND CHARACTERISATION OF ANTIBACTERIAL TITANIUM-BASED ALLOYS WITH COPPER FOR BIOMEDICAL APPLICATIONS

L Spotose[1,2], N.S. Phala[1,2], C. Polese[1,3] and L.A. Cornish[1,2]

[1]School of Chemical and Metallurgical Engineering, University of the Witwatersrand, , [2]DSI-NRF CoE in Strong Materials, hosted by the University of the Witwatersrand, and DSI Collaborative Programme in Additive Manufacturing, [3]School of Mechanical, Aeronautical and Industrial Engineering, University of the Witwatersrand

Titanium and its alloys are used biomedically, including dental implants, due to their favourable combination of properties: low density, high strength, corrosion resistance, excellent biocompatibility and good osseointegration[1]. The widely used Ti-6Al-4V alloy has concerns as Al been associated with Alzheimer diseases and phosphorus deficiency in the blood and bone, while V appeared to be cytotoxic and show carcinogenic properties[1].Hence the development of new alloys with non–toxic elements is necessary.

The aim of this study is to develop a Ti-based alloy that is not toxic and has improved corrosion resistance as the human body has different electrolytes which contain corrosive species. The addition of 5 mass% copper promotes good antibacterial properties as well as balanced mechanical properties in Ti-Cu based alloys[2]. Small ruthenium additions enhance corrosion resistance without changing the microstructure of the alloy[3].

The titanium alloys were selected using Thermo-Calc and four alloys were chosen as their (α+β) phase proportions were similar to Ti-6Al-4V, which was used as a reference alloy[3]. The alloys were: Ti-6Ta-1.5Zr, Ti-6Ta-1.5Zr-5Cu, Ti-6Ta-1.5Zr-0.2Ru and Ti-6Ta-1.5Zr-5Cu-0.2Ru (mass%). High purity powders were mixed in the required ratios and cast in a button arc furnace. The samples were submerged in phosphate buffered solution to test their corrosion resistance. Open circuit potential was measured for up to 17 hours and potentiodynamic polarisation was carried out at 37°C.

The corrosion rates of all the alloys were: Ti-6Ta-1.5Zr (0.00021 mm/y), Ti-6Ta-1.5Zr-5Cu (0.00014 mm/y), Ti-6Ta-1.5Zr-0.2Ru (0.00030 mm/y) and Ti-6Ta-1.5Zr-0.2Ru-5Cu (0.00022 mm/y). Ti-6Ta-1.5Zr-0.2Ru had the highest corrosion rate as compared to other alloys and all were below the recommended rates[4] in biomedical applications which is 0.13 mm/y. Fig. 1 shows the microstructure of the Ti-6Ta-1.5Zr-0.2Ru before the corrosion test and Fig. 2 shows the microstructure of Ti-6Ta-1.5Zr-0.2Ru afterwards. There was corrosion damage, as well as some scratches from handling. Table 1 shows the EDX results of Ti-6Ta-1.5Zr-5Cu (mass%) before and after the corrosion tests, the EDX was done on an area of 20x20 μm^2 on five different places and the average was taken to represent the bulk composition. The EDX results shows that there were minor losses of Ta and Zr, but higher losses of Cu (almost 50%), which shows that some of the Cu was lost. However, this is beneficial since the antimicrobial action occurs when copper is in the surrounding solution[5].

References:
1. Jingjing, Z., et al. (2020), Calphad.
2. Liu, J., et al. (2014), Mat. Sci. Eng. C, 35, 392.
3. Spotose, L. and Cornish, L.A. (2021) African Inclusive Microscopy Network's Student Symposium.
4. Bhola, R., et al. (2011), Trends Biomater Artif. Organs, 25(1) 34
5. Li, M., et al. (2016), Adv. Healthc. Mater., 5(5), 557.

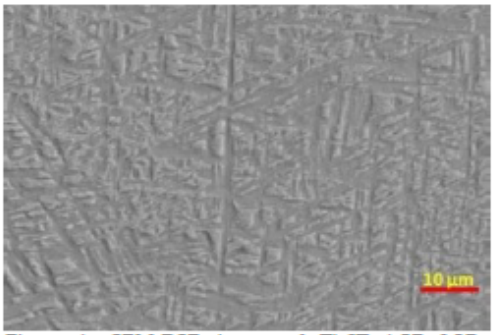

Figure 1. SEM-BSE image of Ti-6Ta-1.5Zr-0.2Ru (mass%) before corrosion, showing (βTi) (light contrast) and (αTi) (dark contrast).

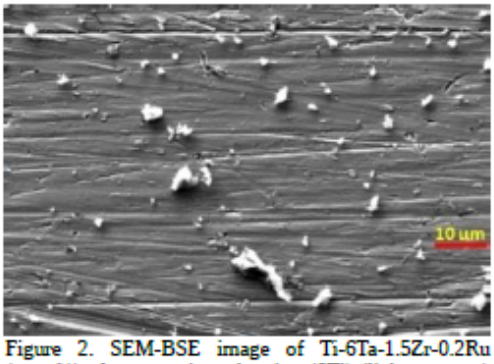

Figure 2. SEM-BSE image of Ti-6Ta-1.5Zr-0.2Ru (mass%) after corrosion, showing (βTi) (light contrast) and (αTi) (dark contrast).

Table 1. Overall EDX analyses of Ti-6Ta-1.5Zr-5Cu (mass%) before and after corrosion.

	EDX analysis (mass%)			
	Ti	Ta	Zr	Cu
Before corrosion	86.0±1.2	5.9±0.5	3.1±0.5	4.9±0.7
After corrosion	90.0±0.3	5.0±0.5	2.1±0.6	2.3 ±0.1

Corresponding author: 820850@students.wits.ac.za

Development and Characterisation of Antibacterial Titanium-based Alloys with Copper for Additive Manufacturing for Biomedical Applications

L. Spotose[1,2,3], **N.S. Phala**[1,2,3], C. Polese[1,2,3,4] and L.A. Cornish[1,2,3]

1 .School of Chemical and Metallurgical Engineering, University of the Witwatersrand, 2. DSI-NRF CoE in Strong Materials, hosted by the University of the Witwatersrand, 3. DSI Collaborative Programme in Additive Manufacturing, 4. School of Mechanical, Aeronautical and Industrial Engineering, University of the Witwatersrand

INTRODUCTION

- Titanium and its alloys are used in biomedical applications due to low density, and low Young's modulus close to that of the bone, excellent biocompatibility and good osseointegration [1].
- The current used α+β titanium alloy Ti-6Al-4V is toxic the living tissues.
- The addition of 5 mass% copper promotes good antibacterial properties as well as balanced mechanical properties in Ti-Cu based alloys [2].
- Ta and Zr are non-toxic β stabilisers.
- Small ruthenium additions enhance corrosion resistance without changing the microstructure of the alloy [3] .
- In biomedical corrosion resistance is important for the dental implants as the human mouth has different electrolytes which contain corrosive species.

AIM

- The aim of this study is to develop a Ti-based alloy that is not toxic and has improved corrosion resistance.

OBJECTIVES

- To as-cast the titanium alloys.
- To run corrosion tests.
- To study the microstructures of the corroded surfaces.

METHODOLOGIES [6]

- Four types of titanium (α+β) alloys were selected using Thermo-Calc which were similar to Ti-6Al-4V, which was used as a reference [4].
- The alloys were: Ti-6Ta-1.5Zr, Ti-6Ta-1.5Zr-5Cu, Ti-6Ta-1.5Zr-0.2Ru and Ti-6Ta-1.5Zr-5Cu-0.2Ru (mass%).
- High purity powders were mixed in the required ratios and cast in a button arc furnace.
- The samples were submerged in phosphate buffered solution to test their corrosion resistance.
- Open circuit potential was measured for up to 17 hours and potentiodynamic polarisation was carried out at 37°C.

RESULTS AND DISCUSSION

- Table 1 shows the corrosion rates of the alloys which were all below the recommended corrosion rates of the biomedical alloys which is 0.13 mm/y [4].
- In Figures 1(b) the light contrast represent the β phase while the dark contrast represent the α phase.
- From the microstructures there is a evident of corrosion taking place and there are scratches that resulted from handling.
- Table 2 shows EDX results of Ti-6Ta-1.5Zr-5Cu before and after the corrosion tests. The analyses were done on five different areas of 20 x 20 μm^2 and the averages were taken for the bulk composition.
- EDX showed minor losses of Ta and Zr, and higher losses of Cu (almost 50%), which shows that some of the Cu was corroded.
- This higher loss of Cu is beneficial since the antimicrobial action occurs when copper is in the surrounding solution [5].

Alloy	Corrosion rate (mm/y)
Ti-6Ta-1.5Zr	0.00021
Ti-6Ta-1.5Zr-5Cu	0.00014
Ti-6Ta-1.5Zr-0.2Ru	0.00030
Ti-6Ta-1.5Zr-0.2Ru-5Cu	0.00022

Table 1. Corrosion rates of all the alloys

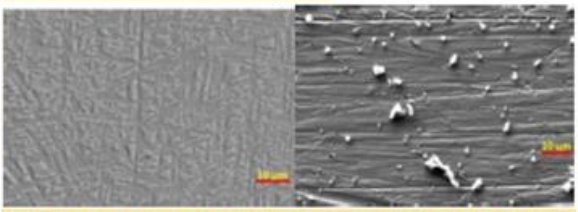

Figure 1. (a) Ti-6Ta-1.5Zr-0.2Ru: SEM-SEI before corrosion and (b) SEM BSE: after corrosion.

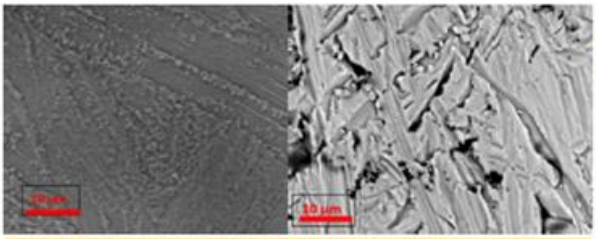

Figure 2(a) SEM-BSI: Ti-6Ta-1.5Zr before corrosion and (b) SEM-SEI:after corrosion.

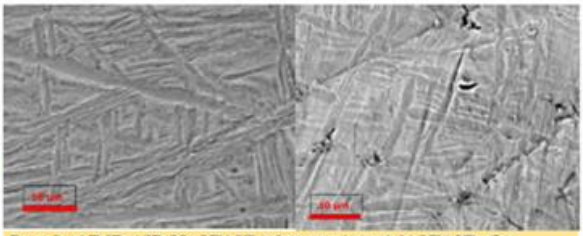

Figure 3. (a) Ti-6Ta-1.5Zr-5Cu:SEM-SEI before corrosion and (b) SEM-SEI: after corrosion.

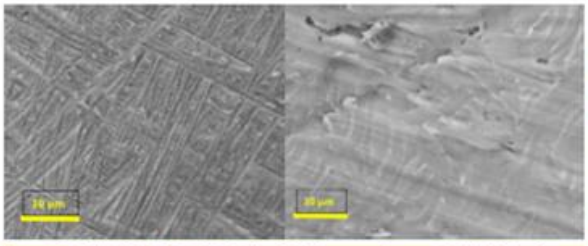

Figure 4. (a) SEM-SEI: Ti-6Ta-1.5Zr-0.2Ru-5Cu before corrosion and (b) SEM-SEI: after corrosion.

CONCLUSIONS

- Ti-6Ta-1.5Zr-5Cu was the best alloy because it had the lowest corrosion rate and the loss of Cu (Table 2) should allow for good antimicrobial properties.
- From corrosion tests, all the corrosion rates were within the WHO limits.

FUTURE WORK

- High purity powder will be characterised for additive manufacturing
- Ti-6Ta-1.5Zr-0.2Ru-5Cu will be manufactured using additive manufacturing and its corrosion rate will be compared to the as-cast sample.

	EDX analysis (mass%)			
	Ti	Ta	Zr	Cu
Before corrosion	86.0±1.2	5.9±0.5	3.1±0.5	4.9±0.7
After corrosion	90.0±0.3	5.0±0.5	2.1±0.6	2.3 ±0.1

Table 2. Overall EDX analyses of Ti-6Ta-1.5Zr-5Cu (mass%) before and after corrosion.

REFERENCES

1. Leyens C. & Peters M.: Titanium and Titanium Alloys. Wiley-VCH, ISBN 3-527-30534-3 (2003) 1-58.
2. Liu, J., Li, F., Liu, C., Wang, H., Ren, B., Yang, K. and Zhang, E., 2014. Effect of Cu content on the antibacterial activity of titanium–copper sintered alloys. Materials Science and Engineering: C, 35, pp.392-400.
3. Schutz, R.W. 1996. Ruthenium enhanced titanium alloys. Platinum Metals Review 40 (2), 54-61.
4. Bhola, RW., Bhola, S.M., Mishra, B. and Olson, D.L., 2011. Corrosion in titanium dental implants/prostheses–a review. Trends Biomater. Artif. Organs, 25(1), pp.34-46.
5. Spotose, L., 2022. Identifying a Ti-Cu based alloys for biomedical applications, MSc Dissertation, submitted to the University of the Witwatersrand.
6. Liu, R., Memarzadeh, K., Chang, B., Zhang, Y., Ma, Z., Allaker, R.P., Ren, L. and Yang, K., 2016. Antibacterial effect of copper-bearing titanium alloy (Ti-Cu) against Streptococcus mutans and Porphyromonas gingivalis. Scientific reports, 6(1), pp.1-10.

- Academic participation in the Conference with paper taken up in the proceedings of the conference: Extended abstract and full paper required.

ATOMISATION OF Ti-6Ta-1.5Zr-0.2Ru-5Cu (wt%) FOR ADDITIVE MANUFACTURING FOR BIOMEDICAL APPLICATIONS

N.S. Phala[1], C. Polese[2], T. Choma[3], Ł Żrodowski[4] H. Möller[5] and L.A. Cornish[6]

[1]School of Chemical and Metallurgical Engineering and DSI-NRF CoE-SM, University of the Witwatersrand, South Africa, 820850@students.wits.ac.za
[2]School of Mechanical, Aeronautical and Industrial Engineering, South Africa, claudia.polese@wits.ac.za
[3]AMAZEMET Warsaw University of Technology, Warsaw, Poland, tomasz.choma@amazemet.com
[4]AMAZEMET Warsaw University of Technology, Warsaw, Poland, lukasz.zrodowsk @amazemet.com
[5]Advanced Materials Division, Mintek, South Africa. HeinM@mintek.co.za
[6]School of Chemical and Metallurgical Engineering, University of the Witwatersrand and DSI-NRF CoE-SM, South Africa, lesley.cornish@wits.ac.za

ABSTRACT

The use of titanium alloys is growing fast as more people are living longer, and need bio-medical implants, some of which are complex, especially in dental applications. This encourages the use of additive manufacturing (AM), which is being increasingly applied to shape titanium alloys. Laser Powder Bed Fusion (L-PBF) requires the starting powders to be spherical and with 10-100 µm particle size. For a previously identified alloy, Ti-6Ta-1.5Zr-0.2Ru-5Cu (wt%), the powder was atomised by ultrasound then analysed by Malvern Mastersizer, XRD and SEM-EDX to ascertain that it met the requirements for L-PBF.

*NS Phala

INTRODUCTION

Titanium and its alloys are used in biomedical applications, due to their favourable combination of properties: low density, high strength, corrosion resistance, excellent biocompatibility and good osseointegration[1]. These materials are difficult to manufacture by conventional casting as they react with oxygen, so additive manufacturing can be used successfully to produce complex, high accuracy geometric parts cost-effectively. Laser Powder Bed Fusion (L-PBF) is used to produce titanium alloys with good mechanical

properties and low surface roughnes[2], and the feedstock powders should be spherical with 10-100 µm particle size. Atomisation produces spherical powders for easy flowability and spreadability. Adding at least 5 wt% copper gives good antibacterial activity as it forms Ti_2Cu which is responsible for anti-microbial properties[1], and the Ti-6Ta-1.5Zr-0.2Ru-5Cu (wt%) alloy had been identified as being suitable, with a small Ru addition for better corrosion resistance[3].

METHODOLOGY AND RESULTS

The Ti-6Ta-1.5Zr-0.2Ru-5Cu (wt%) elemental powders were mixed manually, then compacted. They were atomised ultrasonically using a rePowder system, at 40 kHz frequency[4]. Initially, the powder had irregular shapes and a D_{50} between 45-60 µm.. After atomisation, the powder was analysed by a Malvern Mastersizer and had a D_{50} of 58 µm for particle size. SEM showed that the powder was spherical after atomisation, Figure 1. X-ray diffraction was used to determine the phases and (αTi) and Ti_2Cu were found, as expected[3].

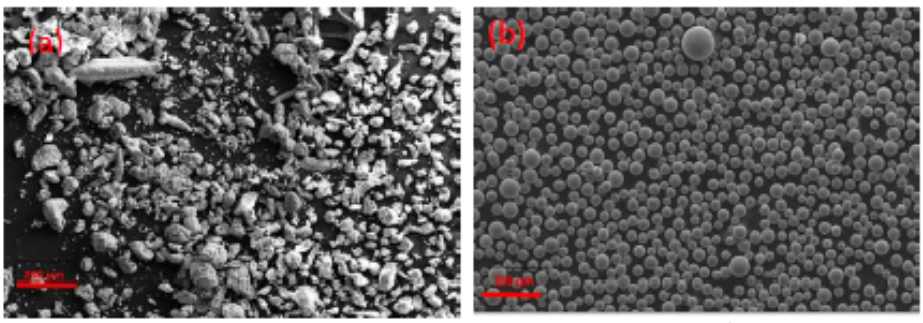

Fig 1. SEM-SE images of Ti-6Ta-1.5Zr-0.2Ru-5Cu (wt%) mixed elemental powder: a) before atomisation and b) after atomisation.

CONCLUSIONS

The powder met the L-PBF specifications being spherical and within the 10-100 µm particle size range with a 58 µm D_{50}. The (αTi) and Ti_2Cu phases were found by XRD.

REFERENCES

[1] Zhang, E., et al. 2013. A new antibacterial titanium–copper sintered alloy. *Materials Science and Engineering C*, 33(7), pp. 4280-4287.
[2] Ni, J., et al. 2019. Three-dimensional printing of metals for biomedical applications. *Materials Today Bio.*, 3, pp. 1-18.
[3] Spotose, L. Identifying Ti-Cu-based alloys for biomedical applications, MSc dissertation, University of the Witwatersrand, 2023.
[4] Żrodowski, L, et al. 2021. Novel cold crucible ultrasonic atomization powder production method for 3D printing. *Materials,* 14(10), pp 2541-2555.

Atomisation of Ti-6Ta-1.5Zr-0.2Ru-5Cu (wt%) for additive manufacturing for biomedical applications

Ngwakoana Phala[1*], *Claudia* Polese[2], *Tomasz* Choma[3], *Hein* Möller[4], *Łukasz* Żrodowski[3] and *Lesley* Cornish[1]
[1]School of Chemical and Metallurgical Engineering and DSI-NRF CoE in Strong Materials, University of the Witwatersrand, South Africa
[2]School of Mechanical, Aeronautical and Industrial Engineering, University of the Witwatersrand, South Africa
[3]AMAZEMET, Warsaw, Poland
[4]Advanced Materials Division, Mintek, South Africa

Abstract. The use of titanium alloys is growing fast as people have longer life expectancies and small, customised, biomedical implants, especially in dental applications, encourage the use of additive manufacturing (AM) to shape them. The Ti-6Ta-1.5Zr-0.2Ru-5Cu (wt%) alloy has been identified as a potential alloy for biomedical applications. Since laser powder bed fusion (L-PBF) requires starting powders to be spherical and within a 10-100 µm size range, the Ti-6Ta-1.5Zr-0.2Ru-5Cu (wt%) powder was ultrasonically atomised and then analysed by a Malvern Mastersizer, XRD and SEM-EDX to ascertain that it met the requirements of L-PBF.

1 Introduction

Titanium alloys are used in biomedical applications, including dental uses, due to their high strength, low Young's modulus, excellent corrosion resistance and biocompatibility, and their ability to bond with bone (i.e. osseointegration) [1]. The Ti-6Al-4V alloy and commercially pure titanium (CP-Ti) have been used in aerospace for engine components [2]. Both these materials started to replace stainless steels and cobalt-based alloys in many biomedical applications since the 1970s [3] and are considered compatible due to their excellent combination of tensile and fatigue performance as well as biocompatibility [4]. However, there are some concerns about Ti-6Al-4V since the alloying elements, aluminium and vanadium, are considered toxic [5], whereas CP-Ti does not have sufficient strength for load bearing implant applications [6].

Using Ti-6Al-4V as the (α+β) reference, recent studies were done to replace Al and V with non-toxic elements for α+β stabilising, with zirconium and tantalum being proposed as the potential non-toxic alloying elements [7]. Copper was chosen because Cu additions to Ti alloys promote antibacterial properties [8, 9]. According to Liu et al. [9], the Cu content must

* Correspondant author: 820850@students.wits.ac.za

© The Authors, published by EDP Sciences. This is an open access article distributed under the terms of the Creative Commons Attribution License 4.0 (https://creativecommons.org/licenses/by/4.0/).

be at least 5 wt% to obtain stable antibacterial activity and balanced mechanical properties. The Ti-6Ta-1.5Zr-0.2Ru-5Cu (wt%) alloy was developed as a new potential (α+β) Ti alloy for dental applications [10]. Tantalum was chosen to replace V as a β stabiliser and Zr as a solution-hardening element, with Zr also contributing to the formation of a protective passive film to give good corrosion resistance [7]. Ruthenium was added to enhance corrosion resistance without changing the microstructure and is also non-toxic to living tissues [11].

Additive manufacturing (AM) was developed four decades ago and more recently has become useful and cost effective for fabricating small, geometrically complex objects [12]. The AM process involves fabrication of an object by depositing materials layer-by-layer following a three-dimensional model generated using computer-aided drawing. Hence, AM offers the added advantage of fabricating fully compatible and accurate biomedical components [13]. Conventional methods (such as casting and powder metallurgy) require multiple steps which limit the time for modification of the final product, and it is difficult to produce complex shapes.

AM includes different technologies; for this work, the laser powder-based fusion (L-PBF) method was selected because it can be used to manufacture almost all metal alloys and has a low direct cost [14]. L-PBF requires the starting powder to be spherical and within a typical size range of 15-45 µm for easy flowability and spreadability [15], although AMAZEMET stated that the powder could be in the size range of 10-100 µm [16]. The rePowder ultrasound atomisation system (AMAZEMET) was used to atomise the powder in small batches [16], using common laboratory conditions and can generate high purity spherical powders.

Ultrasound atomisation is a liquid to solid process, where the material can either be melted in a crucible if the material is non-reactive and has a low melting point (e.g., Sn, Zn, Mg, Pb and Al alloys), and can be poured into the vibrating element or melted directly into the sonotrode if the material is highly reactive or has a high melting point (e.g., alloys based on Fe, Ti and Pt) [16]. The main principle of ultrasound atomisation depends on the amplitude and the surface wettability of the material [16]. Increasing the amplitude makes the liquid droplets smaller, and their size also depends on the frequency used and the properties of the liquid itself. These droplets are ejected from the melt within the thin film of liquid on the sonotrode surface [16]. The Particle Size Distribution (PSD) of ultrasound atomisation is narrow which means that up to 80% of the manufactured powder can be used [16]. The main factor that influences the PSD of the resulting powder is the frequency used. For L-PBF, a 40 kHz frequency is suitable for powder with a D_{50} (average particle size) of 45-60 µm. The atomisation is carried under inert gas using an electric arc or focused plasma [17].

2 Experimental procedure

Pure elemental powders of: Ti <45 µm, Ta < -60+100 mesh, Zr = APS 2-3 µm, Ru <45 µm and Cu <45 µm particle sizes were mixed in the ratio for Ti-6Ta-1.5Zr-0.2Ru-5Cu (wt%) for a total mass of 100 g. The powders were blended in a WAB T2C Turbula mixer to obtain a good mixture, followed by compaction with an Instron 1175 testing machine with the maximum load of 70 kN and cross-head speed of 20 mm/min. Ultrasonic atomisation was done using a rePower system [16], with a molybdenum alloy sonotrode at 40 kHz, with fixed 155A current and 100-130% amplitude of the sonotrode at 180-280W, and 7 L/min argon gas flow, with the blower set at 13-17% maximum power. The whole process was carried out in an argon atmosphere. Powder produced was collected in an air lock container which was sealed in argon for safe handling. Fig 1. shows the rePower system used [16]. A Malvern

Mastersizer was used for particle analysis and the average of the three runs was recorded before and after the atomisation. The powder was characterised by scanning electron microscopy-energy dispersive X-ray spectroscopy (SEM-EDX) to determine the morphology and elemental compositions before and after atomisation. X-ray diffraction (XRD) with Co radiation was used to determine the phases in the powder before and after atomisation. The atomised powder was mounted in epoxy hot mounting resin and ground on 1200 grit grinding paper and polished to ~1µm and the cross sections of the particles were characterised by SEM-EDX.



Fig 1. Fully equipped rePower system [16].

3 Results and discussion

SEM back scattered electron images of elemental powders show irregular shapes, Fig. 2. In Fig. 2(b), the order of contrasts from lightest to darkest (based on atomic number) was Ta, Ru, Zr, Cu and Ti.

Fig. *3* shows X-ray mapping results of the blended powder, which indicates the sizes and morphologies of the different elemental powders. The titanium powder particles are larger compared to Ta and Cu, which tended to be concentrated together. The Ru and Zr powder particles were barely discernible due to their low proportions.

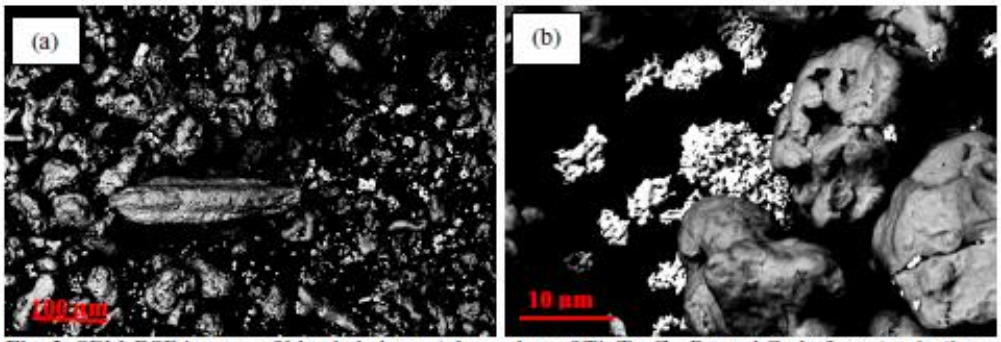

Fig. 2. SEM-BSE images of blended elemental powders of Ti, Ta, Zr, Ru and Cu before atomisation: (a) lower and (b) higher magnification.

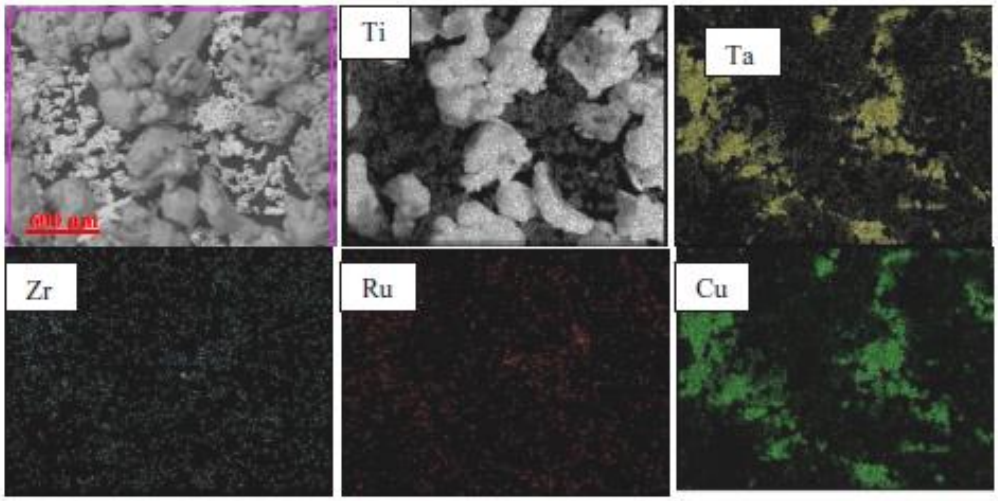

Fig. 3. Elemental EDX maps of the elemental blended powder of Ti, Ta, Zr, Ru and Cu before atomisation.

SEM-SE images of powders after atomisation are given in Fig. 4, showing that the powder was spherical and within the size range required for L-PBF [17], although there was a large irregular particle (indicated by the arrow) in Fig. 4 (b).

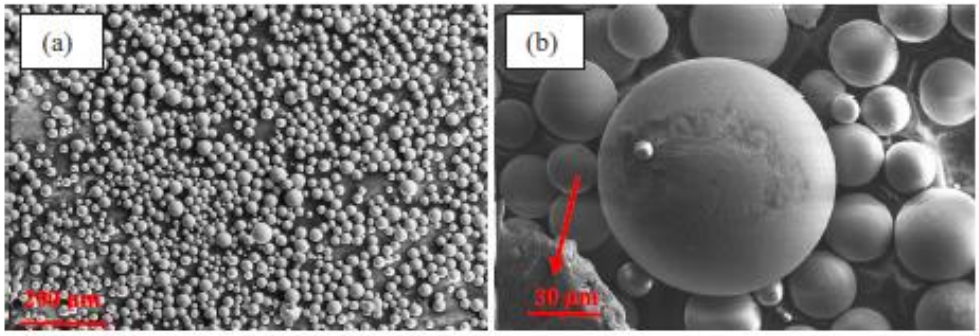

Fig. 4. SEM-SE images of Ti-6Ta-1.5Zr-0.2Ru-5Cu (wt%) powder after atomisation: (a) lower and (b) higher magnification, showing large spherical particles and an irregular particle.

The EDX mapping results of powder particles after atomisation are given in Fig. 5. Alloying occurred during atomisation and the distribution of elements was homogeneous.

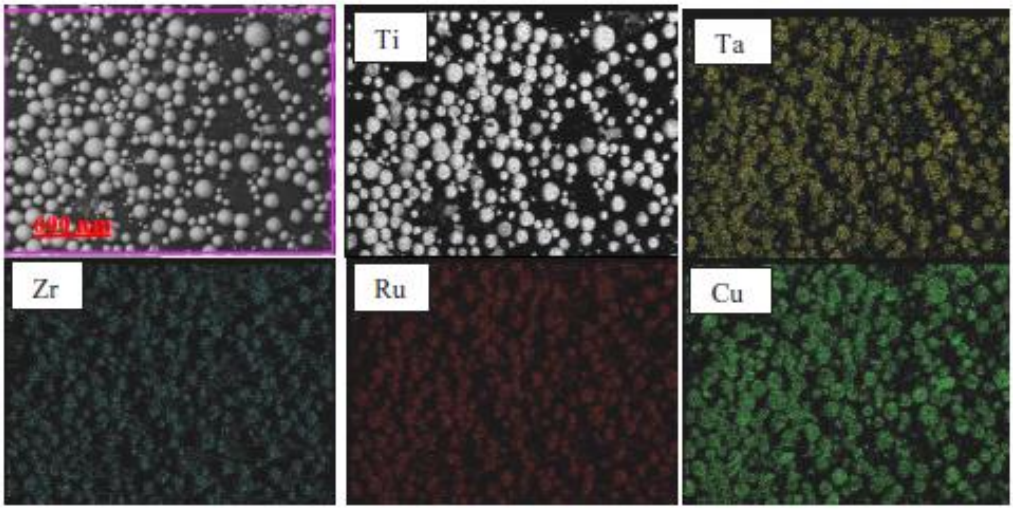

Fig. 5. EDX mapping of the atomised Ti-6Ta-1.5Zr-0.2Ru-5Cu (wt%) atomised powder.

Fig. 6 shows SEM images of the cross-sections of the atomised powder at lower and higher magnification showing minor internal porosity, an irregular particle with regions of different compositions (Fig. 6(a)) and dendrites (Fig. 6(b)). Fig. 7 shows the mapping of the cross-sections of the powder. Table 1 shows that the contents were close to the targeted composition, except for Zr which was lower than expected, probably because prior to atomisation, the Zr had been weighed together with the liquid in which it was stored to prevent oxidation. The EDX results of the cross-sections of the irregular powders showed that some particles did not have Zr and Ru. Ruthenium could have been lost because it was the heaviest element and was also in a small proportion.

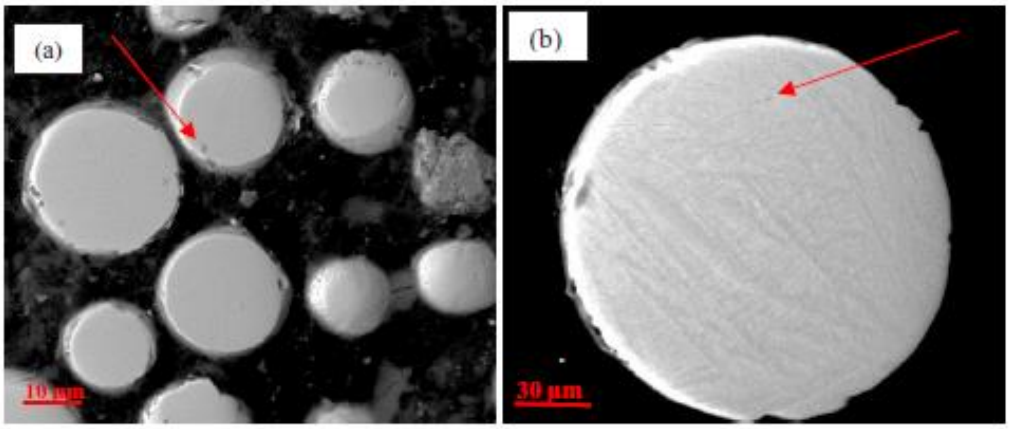

Fig. 6 . SEM-BSE images of cross-sections of Ti-6Ta-1.5Zr-0.2Ru-5Cu (wt%) powder, arrow showing internal porosity.

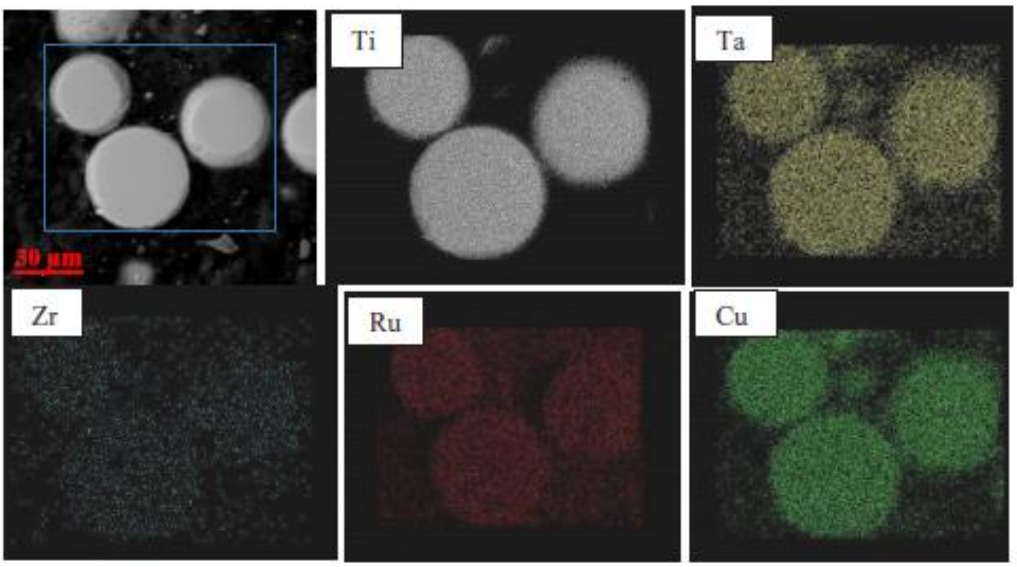

Fig. 7. EDX mapping of cross-sections of a few Ti-6Ta-1.5Zr-0.2Ru-5Cu (wt%) atomised powder particles.

The area shown by the squares in Fig. 8 are examples of the scans on ten different particle cross-sections and the average results are recorded in Table 1. The larger particles had compositions closer to the target than the smaller and irregular particles.

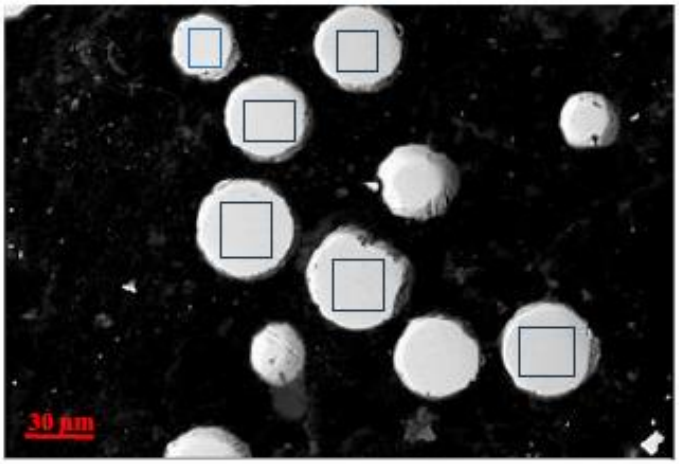

Fig. 8. SEM-BSE image indicating the areas of the EDX analyses within cross-sectioned atomised powder particles.

Table 1. Targeted composition and EDX results for area scans of cross-sections of atomised Ti-6Ta-1.5Zr-0.2Ru-5Cu (wt%) powder particles.

	Ti	Ta	Zr	Ru	Cu
Targeted	87.3	6	1.5	0.2	5
Larger spherical particles	88.0 ± 0.4	6.9 ± 0.4	0.1 ± 0.6	0.2 ± 0.1	4.8 ± 0.2
Smaller irregular particles	87.2 ± 0.5	5.2 ± 0.6	0.0 ± 0.0	0.0 ± 0.0	7.6 ± 0.8

Particle size distributions of the blended elemental powder before atomisation are shown in Fig. 9, and Fig. 10 for the alloy powder after atomisation. Fig. 9 has a small peak at ~9 µm with the largest peak at ~50 µm, and another small peak around ~250 µm. Fig. 10 shows that there were no particles below 10 µm and a second peak at ~800 µm after atomisation. EDX of these particles showed that all the targeted elements were present in the large, spherical particles. Fig. 11 shows a large particle formed by agglomeration of smaller particles, which had not been atomised correctly, and this was also observed by Möller et al. [18] who attributed the phenomenon to splintering of the feedstock material before melting. It is likely that the splintered particles, having high surface areas, would combine to form the larger particles and reduce the surface area and energy, even if not atomised properly. Möller et al. [18] also observed composite particles that formed by spattering of liquid that was ejected from the arc and landed on another particle, and in this work is shown as agglomerated small particles of different compositions in Fig. 6(a). This could also explain why some of the irregularly shaped particles had only Ti, Ta, and Cu (Table 1). Fig. 11 shows this, and that some of the spherical particles were included in the agglomeration.

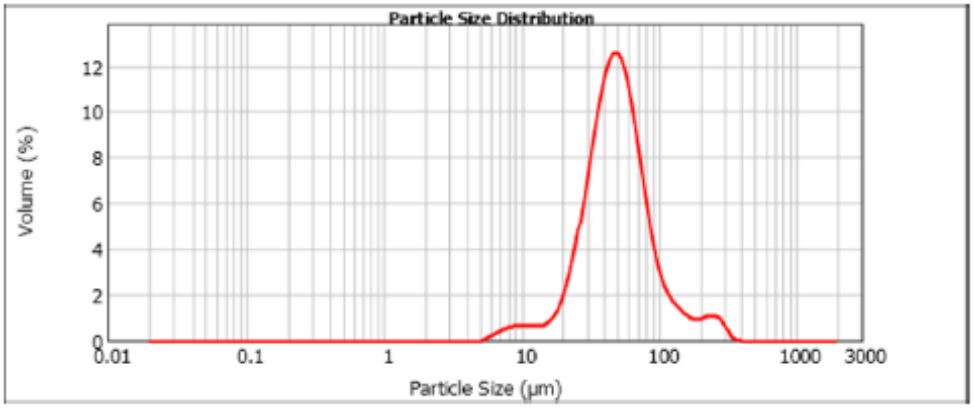

Fig. 9. Particle size distribution of blended elemental powders of Ti, Ta, Zr, Ru and Cu before atomisation.

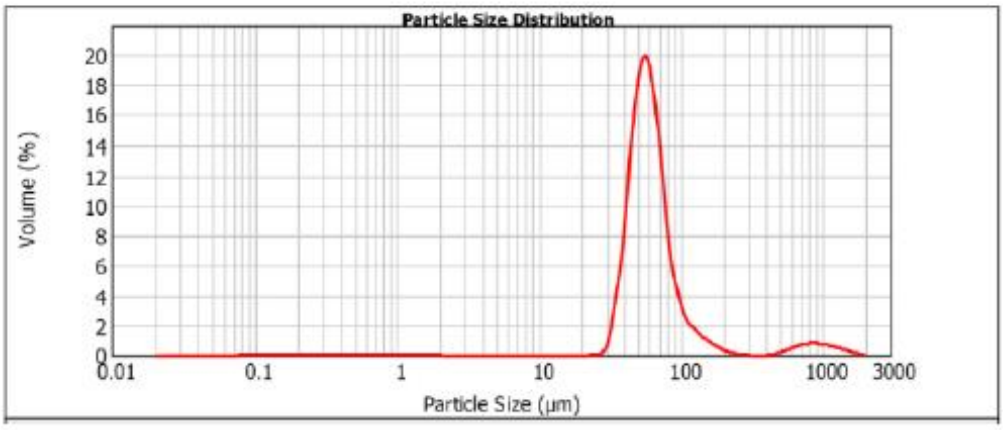

Fig. 10. Particle size distribution of Ti-6Ta-1.5Zr-0.2Ru-5Cu (wt%) powder after atomisation.

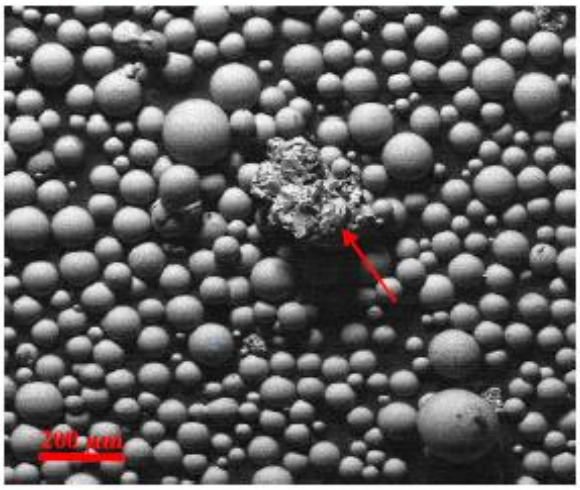

Fig. 11. SEM-SE image showing an agglomeration of splintered particles.

Table 2 shows the summary of the particle size distributions (PSD) before and after atomisation. For both, the D_{50} was within 45-60 µm, where D_{50} is defined as the average particle size of the powder. The PSD of the powder after atomisation could have been narrower if a #200 µm sieve had been used.

Table 2. Average particle size distributions of blended powder and after atomisation.

	D_{10}	D_{50}	D_{90}
Blended elemental powder	25.1	48.6	100.6
After atomisation	40.7	58.3	106.9

X-ray diffraction (XRD) also showed that alloying occurred during the atomisation. Fig. 12 shows XRD results of the blended elemental powders of Ti, Ta, Zr, Ru and Cu before

atomisation, with major peaks of Ti and a Ta peak. Conversely, Fig. 13, after atomisation, has some different peaks, with Ti_2Cu that gives the antibacterial properties of the alloys [8], which is beneficial for biomedical applications. The Zr and Ru would not be expected to have been detected, since their amounts were below the 4 vol.% detection limit for XRD, although Cu should have been detected, albeit with low peaks. Since the backgrounds were high (small particles), possibly the Cu peaks were lost in the background.

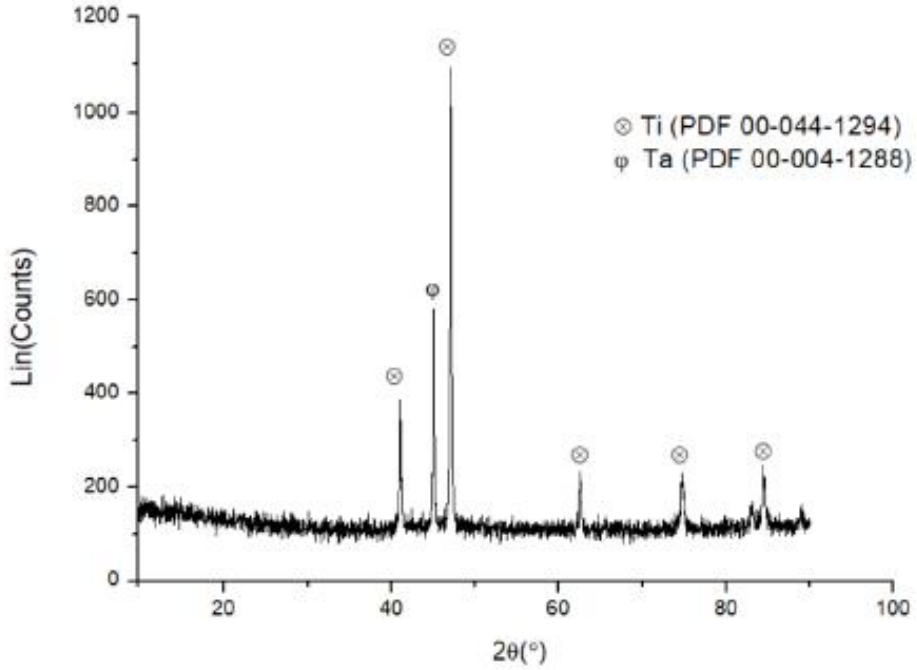

Fig. 12. XRD pattern for blended elemental powder before atomisation.

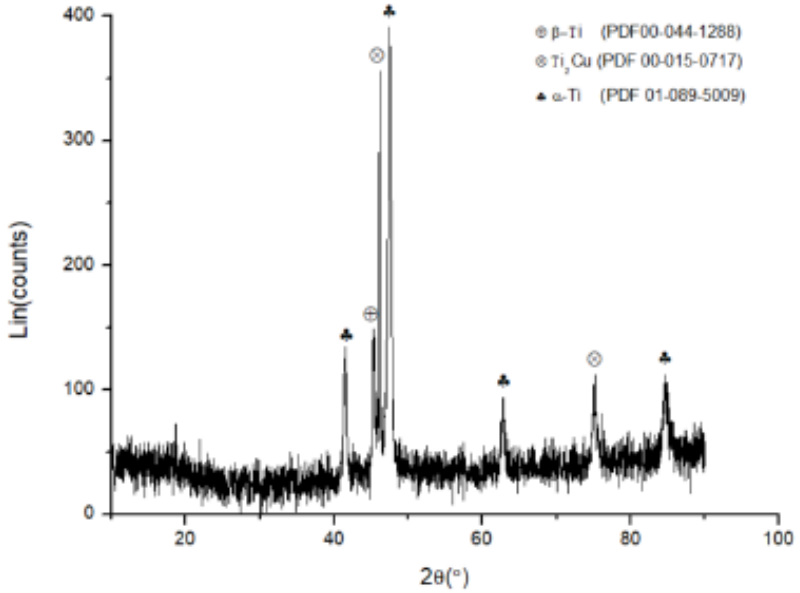

Fig. 13. XRD pattern for Ti-6Ta-1.5Zr-0.2Ru-5Cu (wt%) powder after atomisation.

4 Conclusions

- The powder met the L-PBF specifications of being spherical and with a D_{50} of 58 µm.
- The ultrasonically atomised powder had a narrow particle size distribution. Sieving out the oversized, agglomerated splintered particles would make it an ideal feedstock for Additive Manufacturing technologies.
- The (αTi), (βTi) and Ti_2Cu phases were found by XRD after atomisation.

The authors would like to acknowledge Libo Spotose for developing this alloy, NRF, CoE-SM and the Collaborative Programme on Additive Manufacturing (CPAM) (Contract CSIR-NLC-CPAM-21-MOA-WITS-01) for financial support, Mintek for blending and compaction of the elemental powders, Warsaw University of Technology and AMAZEMET for atomisation of the powder, Letta Ntuli for XRD measurements, and Zaynab Cader for SEM operation.

References

1. C. Leyens and M. Peters. Titanium and Titanium Alloys, Weinheim: Wiley-vch. (2003).
2. I. Inagaki, T. Takechi, Y. Shirai, N. Ariyasu. Application and features of titanium for the aerospace industry. Nippon Steel & Sumitomo Metal Technical Report, Number 106,. pp. 22-27, (2014).
3. D. Mantovani. Shape memory alloys: Properties and biomedical applications. JOM, **52**, pp. 36-44, (2000).

4. J.L. Xu, S.C. Tao, L.Z. Bao, J.M Luo, Y.F. Zheng. Effects of Mo contents on the microstructure, properties and cytocompatibility of the microwave sintered porous Ti-Mo alloys. Mat. Sci. Eng.: C, **97**. pp. 156-165, (2019).
5. V.S.A. Challa, S. Mali, R.D.K. Misra. Reduced toxicity and superior cellular response of preosteoblasts to Ti-6Al-7Nb alloy and comparison with Ti-6Al-4V. J. Biomed. Mat. Res. Part A, **101**, 7, pp. 2083-2089, (2013).
6. N. Soro, H. Attar, E. Brodie, M. Veidt, A. Molotnikov, M.S. Dargusch. Evaluation of the mechanical compatibility of additively manufactured porous Ti–25Ta alloy for load-bearing implant applications. J. Mech. Behav. Biomedi. Mat., **97**, pp. 149-158, (2019).
7. P. Stenlund, O. Omar, U. Brohede, S. Norgren, B. Norlindh, A. Johansson, J. Lausmaa, P. Thomsen, A. Palmquist, Bone response to a novel Ti-Ta-Nb-Zr alloy. Acta Biomat., **20**, pp. 165-175, (2015).
8. E. Zhang, F. Li, H. Wang, J. Liu, C. Wang, M. Li, K. Yang. A new antibacterial titanium–copper sintered alloy: preparation and antibacterial property. Mat. Sci. Eng. C, **33**, 7, pp. 4280-4287, (2013).
9. J. Liu, F. Li, C. Liu, H. Wang, B. Ren, K. Yang, E. Zhang. Effect of Cu content on the antibacterial activity of titanium–copper sintered alloys. Mat. Sci.Eng. C, **35**, pp. 392-400, (2014).
10. L. Spotose. Identifying Ti-Cu-based alloys for biomedical applications, MSc dissertation, University of the Witwatersrand, (2023).
11. C.S. Allardyce, P.J. Dyson. Ruthenium in medicine: current clinical uses and future prospects. Plat. Met. Rev., **45**, 1, pp. 62-69, (2001).
12. P. Ahangar, M.E. Cooke, M.H. Weber, D.H. Rosenzweig. Current biomedical applications of 3D printing and additive manufacturing. Appl. Sci., **9**, 8, pp. 1-23, (2019).
13. A.A Zadpoor. Design for additive bio-manufacturing: From patient-specific medical devices to rationally designed meta-biomaterials. Int. J. Molec. Sci., **18**, 8, pp. 1607-1625, (2017).
14. J. Ni, H. Ling, S. Zhang, Z. Wang, Z. Peng, C. Benyshek, R. Zan, A.K Miri, Z. Li, X. Zhang, J. Lee. Three-dimensional printing of metals for biomedical applications. Mat. Today Bio, **3**, pp. 1-18, (2019).
15. I. Yadroitsev, I. Yadroitsava, A. Du Plessis, E. MacDonald. Fundamentals of Laser Powder Bed Fusion of Metals, pp. 245-276. Amsterdam, The Netherlands: Elsevier, (2021).
16. A novel approach for the production of metal powders with tailored chemical composition: AMEZEMET's rePowder, Powder Metallurgy Review, Winter 2022.
17. L. Żrodowski, R. Wróblewski, T. Choma, B. Morończyk, M. Ostrysz, M. Leonowicz, W. Łacisz, P. Błyskun, J.S. Wróbel, G. Cieślak, B. Wysocki. Novel cold crucible ultrasonic atomization powder production method for 3D printing. Mater., **14**, 10, pp. 2541-2552, (2021).
18. H. Möller, V. Motsweni, L. Zrodowski, T. Choma, Powder characterisation of Pt84-Al11-Cr3-Ru2 superalloy manufactured by ultrasonic atomisation, in Proceedings of the 8th International PGM Conference, 2 – 3 November 2022, Sun City, South Africa (2022).

LASER POWDER BED FUSION OF TI-6TA-1.5ZR-0.2RU-5CU (wt%)-PROCESS PARAMETER OPTIMISATION USING SINGLE TRACKS ANALYSIS

N.S. Phala[1], C. Polese[2], J Ciftci[3,4], T. Choma[3,4]and L.A. Cornish[5]

[1]School of Chemical and Metallurgical Engineering and DSI-NRF CoE-SM, University of the Witwatersrand, South Africa, 820850@students.wits.ac.za
[2]School of Mechanical, Aeronautical and Industrial Engineering, South Africa, Claudia.polese@wits.ac.za
[3] Warsaw University of Technology, Faculty of Materials Science and Engineering, Wołoska 141, 02-507 Warsaw, Poland
Jakub.Ciftci.dokt@pw.edu.pl, Tomasz.Choma.dokt@pw.edu.pl
[4] AMAZEMET Sp. z o. o. [Ltd.], Al. Jana Pawła II 27, 00-867 Warsaw, Poland Jakub.Ciftci@amazemet.com, Tomasz.Choma@amazemet.com
[5]School of Chemical and Metallurgical Engineering, University of the Witwatersrand and DSI-NRF CoE-SM, South Africa, Lesley.cornish@wits.ac.za

ABSTRACT

Printing of single tracks from atomised powder was done to determine the optimal parameters for Laser Powder Bed Fusion of Ti-6Ta-1.5Zr-0.2Ru-5Cu (wt%) varying: laser power, scanning speed, beam diameter, linear and planer energy density. The single tracks were characterised by SEM and showed variations of microstructural homogeneity. The best tracks were produced at 157.5 W laser power, 600 mm/s scanning speed, 0.15 mm beam diameter, 0.263 J/mm linear energy and 1.750 J/mm^2 planer energy density.

*NS Phala

INTRODUCTION

Titanium alloys are used in dental implants because of their excellent properties which include biocompatibility, osseointegration and good mechanical properties [1]. The original Ti-6Ta-1.5Zr-0.2Ru-5Cu (wt%) alloy was cast [2] and had Ti_2Cu precipitates which are responsible for anti-bacterial properties [1]. Spherical atomised powder had been produced within 10-100 µm particle size and had (αTi), (βTi) and Ti_2Cu phases [3]. This powder was used to fabricate the Ti-alloy with the same composition using Laser Powder Bed Fusion (L-PBF). The first stage was to produce single tracks to optimise the printing parameters.

METHODOLOGY AND RESULTS

Single tracks of atomised powder of Ti-6Ta-1.5Zr-0.2Ru-5Cu (wt%)[3] were printed using an Aconity MIDI system [4] with different parameters: laser power, P: 120-280 W, scanning speed, V_s: 200-1200 mm/s, beam diameter, D: 0.8-0.36 mm, linear energy, E_v: (0.120-0.7880 J/mm) and planer energy density, U: 0.600-9.844 J/mm^2. The single tracks were characterised by SEM. Balling effect phenomenon and stable melt track obtained with optimised parameters are presented in Figure 1.

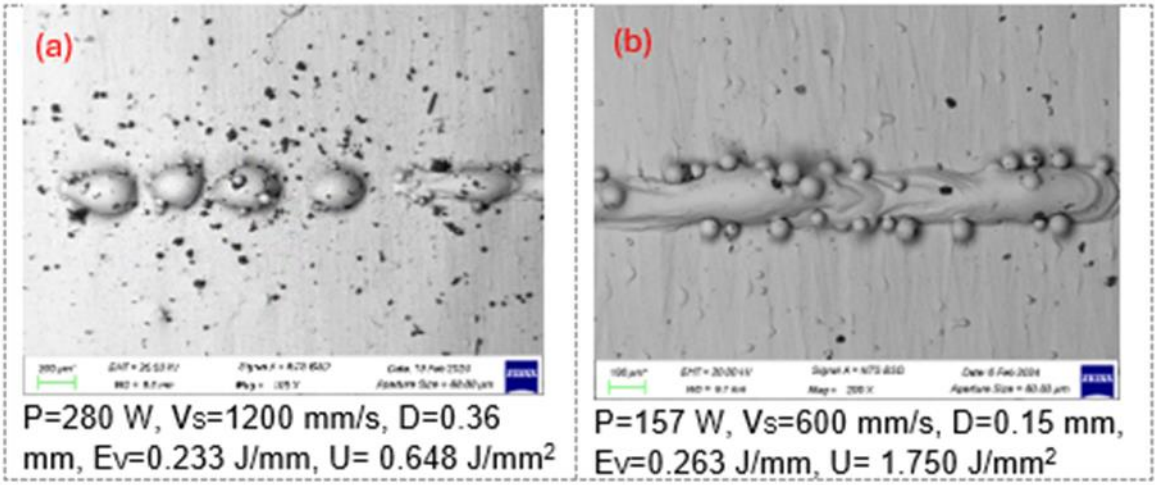

P=280 W, V_s=1200 mm/s, D=0.36 mm, E_v=0.233 J/mm, U= 0.648 J/mm^2

P=157 W, V_s=600 mm/s, D=0.15 mm, E_v=0.263 J/mm, U= 1.750 J/mm^2

Figure 1: SEM images of selected single tracks fabricated using L-PBF.

CONCLUSIONS

- The optimised parameters were 157.5 W laser power, 600 mm/s scanning speed, 0.15 mm beam diameter, 0.263 J/mm linear energy and 1.750 J/mm^2 planer energy density.
- These parameters produced a homogeneous microstructure.

REFERENCES

1. **Zhang, E., et al.** 2013. A new antibacterial titanium–copper sintered alloy. *Materials Science and Engineering C, 33(7),* pp. 4280-4287.
2. **Spotose, L.** Identifying Ti-Cu-based alloys for biomedical applications, MSc dissertation, University of the Witwatersrand, 2023.
3. **Phala, NS., et al**. 2023. Atomisation of Ti-6Ta-1.5 Zr-0.2 Ru-5Cu (wt%) for additive manufacturing for biomedical applications. *MATEC Web of Conferences*. Vol. 388. EDP Sciences.
4. **Żrodowski, Ł, et al.,** 2003 How to control the crystallization of metallic glasses during laser powder bed fusion? Towards part-specific 3D printing of in situ composites *Additive Manufacturing* 76, pp 103775-1037790.

MATEC Web of Conferences **406**, 07009 (2024) https://doi.org/10.1051/matecconf/202440607009
2024 RAPDASA-RobMech-PRASA-AMI Conference

Laser powder bed fusion of Ti-6Ta-1.5Zr-0.2Ru-5Cu (mass%) – process parameter evaluation using single tracks analysis

Ngwakoana Phala[1*], *Claudia* Polese[2], *Jakub* Ciftci[3,4], *Tomasz* Choma[3,4], and *Lesley* Cornish[1]

[1]School of Chemical and Metallurgical Engineering and DSI-NRF CoE in Strong Materials, University of the Witwatersrand, Johannesburg, South Africa
[2]School of Mechanical, Aeronautical and Industrial Engineering, University of the Witwatersrand, Johannesburg, South Africa
[3]Warsaw University of Technology, Faculty of Materials Science and Engineering, Wołoska 141, 02-507 Warsaw, Poland
[4]AMAZEMET Sp. z o. o. [Ltd.], Al. Jana Pawła II 27, 00-867 Warsaw, Poland

Abstract. Printing of single tracks from atomised powder was carried out to determine the potential parameters for Laser Powder Bed Fusion of Ti-6Ta-1.5Zr-0.2Ru-5Cu (mass%). Parameters that were varied included laser power, scanning speed, beam diameter, linear and planar energy density. The single tracks were characterised by SEM and SEM-EDX, showing variations in microstructural homogeneity. Promising tracks were produced using laser power of 157.5 W, scanning speed of 600 mm/s, beam diameter of 0.15 mm, 0.263 J/mm linear energy and 1.750 J/mm^2 planar energy density. XRD for one of these tracks indicated (αTi) and (βTi) solid solutions as well as the Ti_2Cu phase.

1 Introduction

Laser Powder Bed Fusion (LPBF) is an additive manufacturing (AM) technique that involves applying thin layers of powder to a build plate and using a laser energy source, fuses the powder based on the designed geometry [1]. Powders are heated and fused layer-by-layer according to the design created in computer-aided design (CAD) software to produce near-net-shapes [2]. This can be done to build Ti-based alloy components with complicated

* Corresponding author: 820850@students.wits.ac.za

© The Authors, published by EDP Sciences. This is an open access article distributed under the terms of the Creative Commons Attribution License 4.0 (https://creativecommons.org/licenses/by/4.0/).

geometries and excellent mechanical properties [2], which is beneficial for increased design flexibility for complex geometries, shorter production times and less material waste [3].

LPBF is now being used to produce near full density (99.5%) parts with mechanical properties like those fabricated using conventional methods although they are still weaker when exposed to cyclic loading [1]. Medical devices are a significant portion of the AM market, and the request for healthcare components is increasing for therapeutic delivery, surgical planning, implant design and tissue engineering applications [4]. AM can be used to customise medical devices and prostheses to the unique anatomy of each patient [5].

Titanium alloys are used in dental implants because of their excellent properties, including biocompatibility, osseointegration and good mechanical properties [6]. Ti-6Ta-1.5Zr-0.2Ru-5Cu (mass%) was developed as a potential α+β alloy for biomedical implants [7]. The addition of 5 mass% copper promotes good antibacterial properties thanks to the formation of Ti_2Cu precipitates [6], as well as balanced mechanical properties. A 0.2 mass% ruthenium addition enhanced corrosion resistance without changing the microstructure [7]. In dental implants, corrosion resistance is important as mouths have various electrolytes with some corrosive species. The as-cast Ti-6Ta-1.5Zr-0.2Ru-5Cu (mass%) alloy [7] had the required Ti_2Cu precipitates, Fig. 1. Spherical atomised powder of the same composition had been produced with particle sizes within a 10-100 μm range for compatibility with the LPBF process [8].

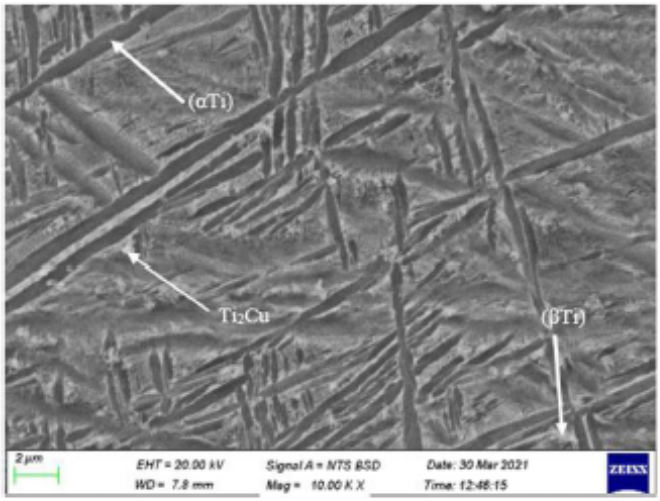

Fig. 1. SEM-BSE image of as-cast Ti-6Ta-1.5Zr-0.2Ru-5Cu (mass%) showing inside one grain with (αTi) needles (dark), (βTi) matrix (medium) and Ti_2Cu (light) [7].

To achieve the desired properties, optimisation of LPBF process parameters is necessary to produce high-quality, defect-free components [9]. Thus, it is important to understand the relationship between the processing parameters, geometry and the resulting microstructure [10]. Preliminary methods that are mostly used are expensive and require more material and energy, as aviation standards mention that the first 2.5 mm of the part from the base plate should be discarded as the process has not reached thermal stability [11]. A more recent single track approach is instead cost-effective as it requires less material and

energy to preliminarily evaluate the effects of different combinations of LPBF process parameters on the geometric characteristics of the obtained deposit and the changes in microstructure [12]. While these single tracks might primarily indicate weldability, as the interaction with the base plate limits their ability to provide insights into the final properties of the components, they can help identify a suitable process window to build complex 3D shapes.

In LPBF, the influence of laser power and scan speed on AM components is important [12]. Linear energy density (LED), defined as the ratio of laser power to scan speed, significantly impacts the melt pool's characteristics, including its shape and thermal dynamics, which in turn affect the microstructure, grain size, porosity and mechanical properties of the final part [13]. Additionally, factors such as the base plate size and powder characteristics influence cooling rates, ultimately determining microstructure and mechanical properties. Utilising a finer laser spot size can create a localised concentration of heat, yielding more energy for a given laser power and scan speed. Moreover, planar energy density (PED), which is the energy input per unit area, along with the thermal properties of the powder, offers a deeper understanding of the melting and fusing processes [12]. Controlling PED is crucial for achieving the desired dimensional and morphological characteristics of the melt pool, ensuring good adhesion between the base substrate and the fused tracks [12].

This study investigates LPBF of a newly developed Ti-6Ta-1.5Zr-0.2Ru-5Cu (mass%) alloy, aiming to identify potential process parameters through single tracks analysis. Single tracks printing experiments were performed with varying laser power, scanning speed and beam diameter. The analysis of the surface of the LPBF single tracks involved their morphology and microstructural characterisation, in comparison to the as-cast alloy, using SEM, EDX and XRD. The final goal is to fabricate defect-free components for biomedical implants using a newly developed Ti-Cu alloy with improved antibacterial properties, contributing to the expansion of the LPBF process in the field.

2 Experimental procedure

Single tracks of atomised powder of Ti-6Ta-1.5Zr-0.2Ru-5Cu (mass%) [8] were printed using an AconityMIDI system with different parameters, Table 1. The particle size used was 30-60 µm. The single tracks were LPBF printed on squares made of 20 layers of this alloy on a 1 mm thick disc of Ti-6Al-4V used as the substrate, see Figure 2. This was done to prevent melting of the substrate and prevent the influence of its chemical composition on the single tracks. Subgroups of five single tracks, each with a different parameter combination, as reported in A LPBF sample was prepared using standard metallographic preparation and polished using colloidal silica.

Table *2*, were printed on eight supporting squares. Fig. *2* shows also the directions of argon gas for oxidation prevention, melting and recoating (the blade that is used to coat a layer of powder during LPBF).

Table 1. Printing range parameters for the single tracks.

Laser power	Scanning speed	Beam diameter	Linear energy density	Planar energy density
120-280 W	200-1200 mm/s	0.08-0.36 mm	0.120-0.7880 J/mm	0.600-9.844 J/mm^2

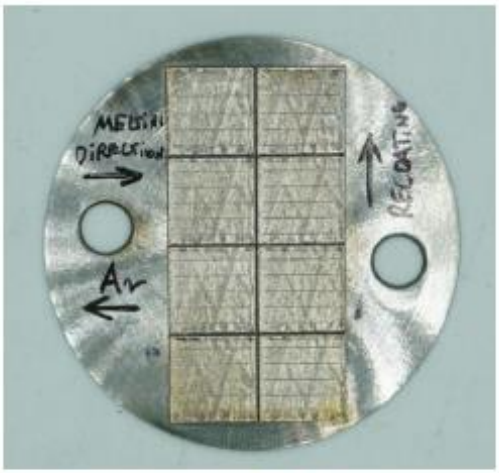

Fig. 2. Photograph of the Ti-6Al-4V substrate disc with 8 LPBF squares supporting 5 horizontal single tracks each, showing directions of argon gas flow, melting and recoating.

Micrographs of the tracks from different processing parameters were compared using scanning electron microscopy (SEM) (Zeiss Sigma Field Emission Scanning Electron Microscope (FEG-SEM500)) to check if they were printed evenly. The compositions were analysed using energy dispersive X-ray spectroscopy (EDX) on the SEM to ascertain whether they were homogeneous and of the targeted composition. The squares with the single tracks were removed from the disk using electrical discharge machining (EDM). An X-ray diffraction (XRD) D2 Phaser (Bruker XRD) with Co-Kα radiation (λ=1.78899 Å) was operated at 50 kV and 20 mA with a nickel filter, scanning for 10-130° degrees for 17 minutes to identify the phases. A LPBF sample was prepared using standard metallographic preparation and polished using colloidal silica.

Table 2. Printing parameters for the single tracks.

Number	Laser power (W)	Scanning speed (mm/s)	Beam diameter (mm)	Linear energy density (J/mm)	Planar energy density (J/mm^2)
1.	171	600	0,08	0,285	3,563
	171	400	0,08	0,428	5,344
	171	600	0,15	0,285	1,900
	171	400	0,15	0,428	2,850
	171	200	0,15	0,855	5,700
2.	157.5	1200	0,08	0,131	1,641
	157.5	1000	0,08	0,158	1,969
	157.5	800	0,08	0,197	2,461
	157.5	600	0,08	0,263	3,281
	157.5	400	0,08	0,394	4,922
3.	157.5	1200	0,15	0,131	0,875
	157.5	1000	0,15	0,158	1,050
	157.5	800	0,15	0,197	1,313
	157.5	600	0,15	0,263	1,750
	157.5	400	0,15	0,394	2,625
4.	157.5	600	0,22	0,263	1,193
	157.5	600	0,15	0,263	1,750
	157.5	600	0,08	0,263	3,281
	120	1000	0,15	0,120	0,800
	120	1000	0,08	0,120	1,500
5.	315	1200	0,08	0,263	3,281
	315	1000	0,08	0,315	3,938
	315	800	0,08	0,394	4,922
	315	600	0,08	0,525	6,563
	315	400	0,08	0,788	9,844
6.	315	1200	0,15	0,263	1,750
	315	1000	0,15	0,315	2,100
	315	800	0,15	0,394	2,625
	315	600	0,15	0,525	3,500
	315	400	0,15	0,788	5,250
7.	157.5	600	0,36	0,263	0,729
	157.5	600	0,29	0,263	0,905
	157.5	600	0,22	0,263	1,193
	157.5	600	0,15	0,263	1,750
	1575	600	0,08	0,263	3,281
8.	280	1200	0,36	0,233	0,648
	280	1200	0,29	0,233	0,805
	280	1200	0,22	0,233	1,061
	280	1200	0,15	0,233	1,556
	280	1200	0,08	0,233	2,917

3 Results and discussion

Figure 3 shows the morphology of the single tracks of Ti-6Ta-1.5Zr-0.2Ru-5Cu (mass%) for constant laser power and beam diameter, with varying scanning speeds. The un-melted spherical particles in Figure 3a had a particle size of 51.4±1.9 µm which was within the 45-60 µm average particle size of the atomised powder [8]. The un-melted spherical powders were randomly distributed and were present in all the samples; some samples had more un-melted spherical particles, Figure 3a, and others had fewer, Figure 3c. Figure 3d shows that at higher scanning velocities, the tracks were unstable along the printing direction, and "balling" occurred as shown by the circle. Balling is a surface defect that occurs because of severe instability of the molten pool induced by the high melt viscosity under a relatively low energy density [12], decreasing surface quality and densification [13]. Gao et al. [16] demonstrated that large Marangoni convection and liquid capillary instability in the molten pool were the primary causes of balling at high scanning speed. Balling, shown in Figure 3d, is caused by insufficient contact of the melt with the solid substrate and occurs at high scanning speeds due to the limited energy input [17]. The dark particles in Figure 3d were contaminations from separating different squares of tracks using EDM.

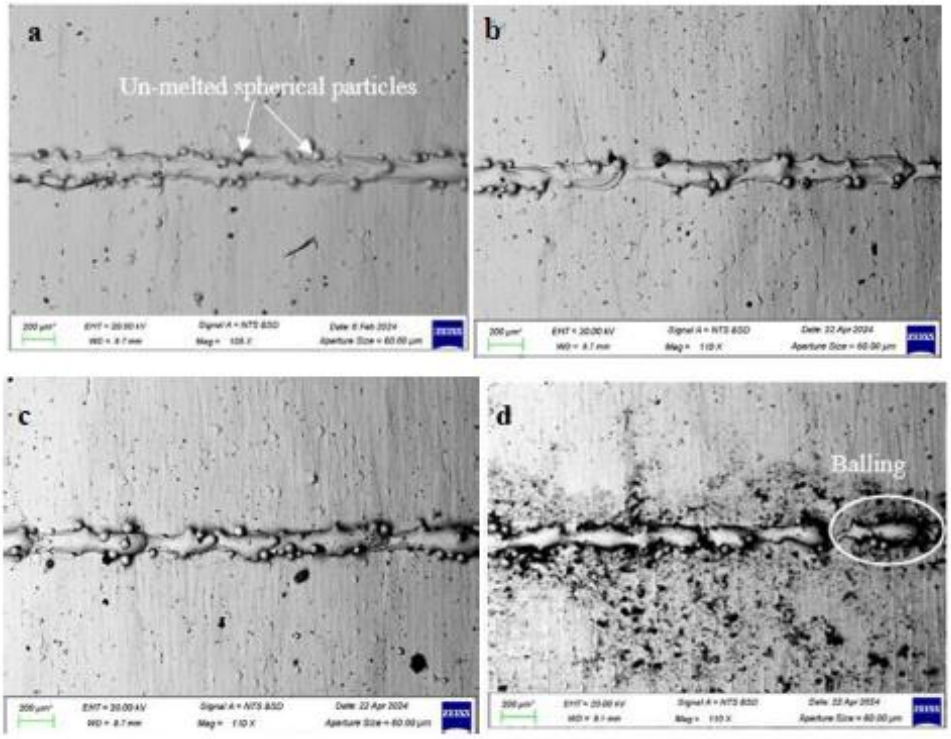

Fig. 3. SEM-BSE images show the morphology of the single tracks at constant laser power: 157.5 W, beam diameter: 0.15 mm and scanning speeds of (a) 600 mm/s, (b) 800 mm/s, (c) 1000 mm/s and (d) 1200 mm/s, the white circle showing the balling.

Fig. *4* shows that increasing the laser powder and reducing the beam diameter reduced "balling" at higher scanning speeds. High voltage and lower scanning speed results in higher

LED which causes porosity [12]. However, Fig. *4*d shows that high scanning speed results in balling. Guo et al. [18] studied single-track fabrication of niobium and titanium alloys finding that when laser energy density increased, the track width and substrate penetration also increased. This was found in this work because when the LED increased, the tracks were more even.

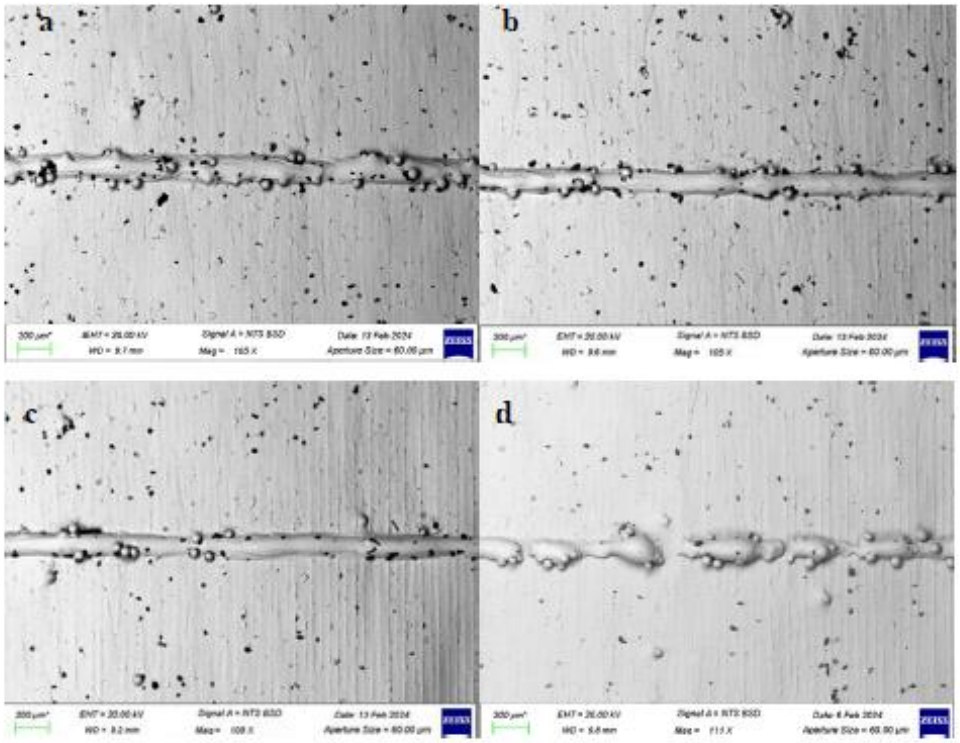

Fig. 4. SEM-BSE images showing the morphology of single tracks at 315 W laser power, 0.08 mm beam diameter and scanning speeds of: (a) 600 mm/s, (b) 800 mm/s, (c) 1000 mm/s and (d) 1200 mm/s.

Fig. *5* shows that "balling" at higher voltage and higher scanning speed increased with increasing beam diameter. High beam diameter resulted in lower PED which caused rougher surfaces and lower hardness [19], and Fig. *5*c and 5d show that lower PED caused balling.

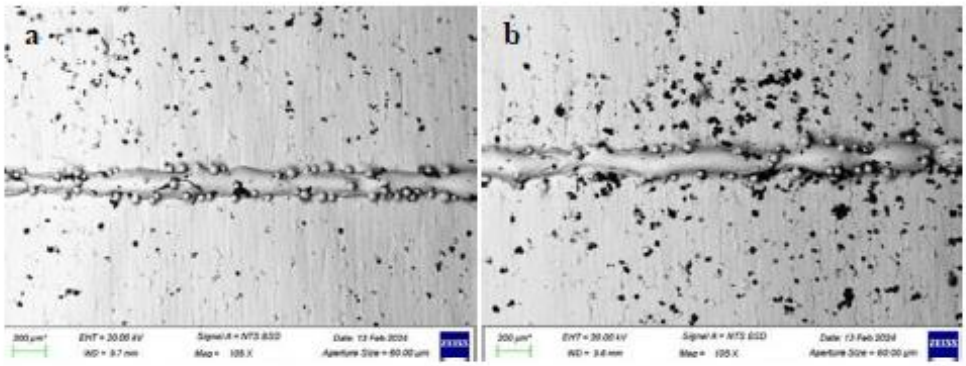

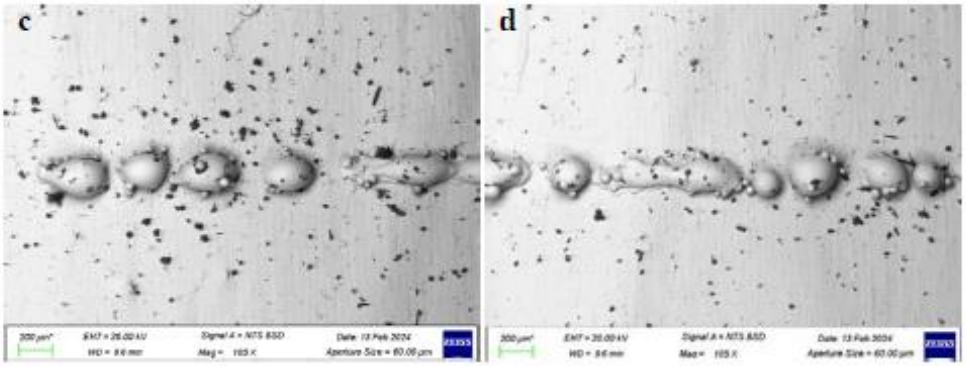

Fig. 5. SEM-BSE images showing the morphology of the single tracks at 280 W constant laser power and 1200 mm/s scanning speed for beam diameter: (a) 0.15 mm, (b) 0.22 mm, (c) 0.29 mm and (d) 0.3 mm.

Fig. *3*a identified the best single track which was even, continuous with a smooth surface. Although the tracks in Fig. *4*a-c also appear good, they were done with high LED which can cause porosity [12], even though no porosity was observed on any single track surface (and the surfaces were not sectioned). "Balling" is undesirable in LPBF because it can lead to inhomogeneity in the next powder layer or to collisions with the recoater/roller that deposits the powder layer [19]. The best single track was printed using 157.5 W laser power, 600 mm/s scanning speed, 0.15 mm beam diameter, 0.263 J/mm linear energy and 1.750 J/mm^2 planer energy density, so these were identified as potential parameters.

Fig. *6* shows a higher magnification image of the best single track within the analysed combinations showing nucleation sites with the dendrites growing out from them.

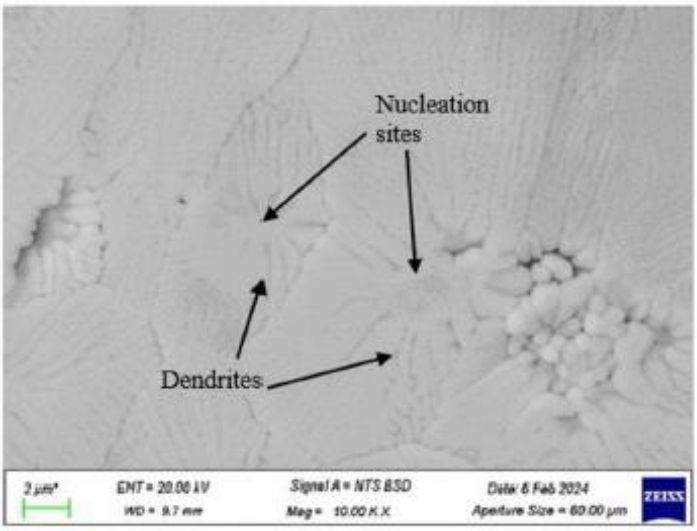

Fig. 6. SEM-BSE image showing the best single track of Ti-6Ta-1.5Zr-0.2Ru-5Cu (mass%) at higher magnification.

Fig. 7 shows the microstructure of the LPBF sample. The previous as-cast sample [7], Figure 1, had (βTi) needles, while the LPBF microstructure showed (αTi) formed along the grain boundaries with small precipitates in the (βTi) matrix. The difference in the microstructures was due to the different solidification rates.

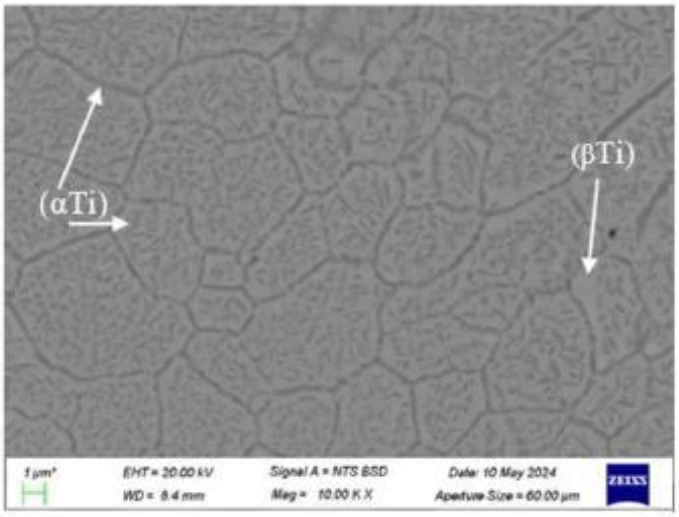

Fig. 7. SEM-BSE image of LPBF Ti-6Ta-1.5Zr-0.2Ru-5Cu (mass%), showing inside (αTi) along grain boundaries and dendrites within (βTi).

The expected composition was obtained for the spherical particle and the best single track, as shown in Table 3. The EDX results were the same for Ta and Ru, The LPBF sample had slightly higher Cu and lower Ti and Zr than the as-cast sample [7]. The dark spot was mostly contamination,
Table 4.

Table 3. EDX results from as-cast [7], surface of the best single track and the spherical particle of Ti-6Ta-1.5Zr-0.2Ru-5Cu (mass%).

Alloy	EDX (mass%)				
	Ti	Ta	Zr	Ru	Cu
As-cast [7]	86.0±1.6	7.4±0.9	2.0±0.8	0.4±0.6	4.5±1.5
Best single track	83.8±1.5	7.4±0.3	1.7±0.1	0.4±0.1	6.7±1.8
Spherical Particles	81.6±1.5	7.4±0.2	1.9±1.5	0.2±0.1	8.9±0.1

Table 4. EDX result of dark spot on Ti-6Ta-1.5Zr-0.2Ru-5Cu (mass%) best single track.

Alloy	C	O	Si	Cl	K	Ti	Fe

Dark spot	42.6±5.6	34±9.4	0.7±0.1	0.6±0.4	3,2±1.4	18±2.8	0.9±0.1

Fig. *8* shows the XRD pattern of the best single track of Ti-6Ta-1.5Zr-0.2Ru-5Cu (mass%) identifying (αTi), (βTi) and the Ti_2Cu phase which is beneficial for enhancing the antibacterial properties of the alloys [6]. Although Canale and Servant [21] identified Ti_3Cu on solidification and Fowler [22] identified it in a 5 mass% Cu sample, the XRD peaks are so similar to Ti_2Cu that they are indistinguishable at low amounts and Ti_3Cu is not stable [23]. Tantalum, zirconium and ruthenium were not detected, because they were dissolved in the (αTi) and (βTi) solid solutions.

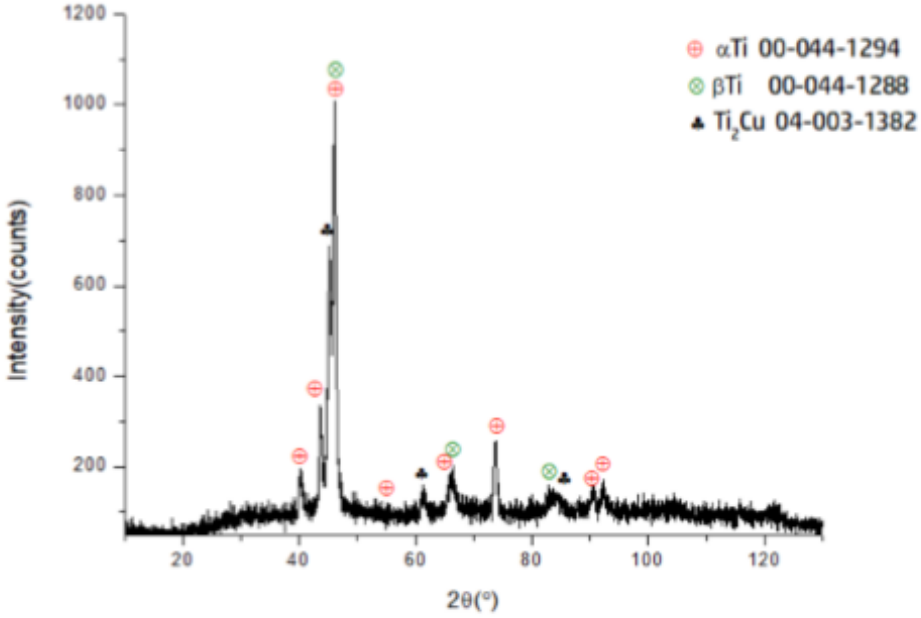

Fig. 8. XRD pattern of the best single track of Ti-6Ta-1.5Zr-0.2Ru-5Cu (mass%).

4. Conclusions

The best LPBF Ti-6Ta-1.5Zr-0.2Ru-5Cu alloy (mass%) tracks produced during this preliminary study were even, smooth and continuous, with the targeted alloy composition. The parameters for these tracks were 157.5 W laser power, 600 mm/s scanning speed, 0.15 mm beam diameter, 0.263 J/mm linear energy and 1.750 J/mm² planar energy density. Their surface microstructure consisted of a matrix of βTi, with αTi located at the grain boundaries and precipitated within the grains. These LPBF tracks exhibited smaller grains compared to the as-cast sample. X-ray diffraction (XRD) analysis of the surface of these LPBF tracks identified the presence of αTi, βTi, and Ti_2Cu phases.

The authors would like to acknowledge National Research Foundation, DSI-NRF CoE in Strong Materials (Grant UID 41292) and the Collaborative Programme on Additive Manufacturing (CPAM) (Contract CSIR-NLC-CPAM-21-MOA-WITS-01) for financial support, Warsaw University of Technology and AMAZEMET for printing single tracks, Letta Ntuli for XRD analysis, and Collen Makola for SEM analysis.

References

1. W.E. King, A.T. Anderson, R.M. Ferencz, N.E. Hodge, C. Kamath, S.A. Khairallah, and A.M. Rubenchik. Laser powder bed fusion additive manufacturing of metals; physics, computational, and materials challenges. App Phy Rev, **2**(4), pp 1-27, (2015).
2. H.L. Wei, Y. Cao, W.H. Liao, and T.T Liu 2020. Mechanisms on inter-track void formation and phase transformation during laser powder bed fusion of Ti-6Al-4V. *Add Man*, **34**, pp.101221-101237, (2020).
3. K. Raut, A.K Ball, and A. Basak, A. Impact of track length, track shape, and track location on thermal distortion in laser powder bed fusion of IN625: Single laser vs. three lasers. J of Eng Res, pp 1-16, (2023).
4. T. Nakano and T. Ishimoto. Powder-based additive manufacturing for development of tailor-made implants for orthopedic applications. *KONA Powder and Particle Journal*, **32**, pp.75-84, (2015).
5. A. Nouri, A.R. Shirvan, Y. Li, and C. Wen, C. Additive manufacturing of metallic and polymeric load-bearing biomaterials using laser powder bed fusion: A review. J of Mat Sci & Tech, **94**, pp.196-215, (2021).
6. E. Zhang, F. Li, H. Wang, J. Liu, C. Wang, M. Li, K. Yang. A new antibacterial titanium–copper sintered alloy: preparation and antibacterial property. Mat. Sci. Eng. C, **33** (7), pp. 4280-4287, (2013).
7. L. Spotose. Identifying Ti-Cu-based alloys for biomedical applications, MSc dissertation, University of the Witwatersrand, (2023).
8. N.S. Phala, C. Polese, T. Choma, H. Möller, Ł. Żrodowski, and L.A.Cornish. Atomisation of Ti-6Ta-1.5 Zr-0.2 Ru-5Cu (wt%) for additive manufacturing for biomedical applications. In *MATEC Web of Conferences* (Vol. 388, p. 08003). EDP Sciences, (2023).
9. A. Carrozza, F. Mazzucato, A. Aversa, M. Lombardi, F Bondioli, S. Biamino, A. Valente, and P. Fino. Single scans of Ti-6Al-4V by directed energy deposition: a cost and time effective methodology to assess the proper process window. Met and Mat Int, pp.1-13, (2021).
10. D. Svetlizky, B. Zheng, D.M. Steinberg, J.M. Schoenung,E.J. Lavernia, and N. Eliaz. The influence of laser directed energy deposition (DED) processing parameters for Al5083 studied by central composite design. J of Mat Res and Tech, **17**, pp.3157-3171, (2022).

11. B. Blakey-Milner, P. Gradl, G. Snedden, M. Brooks, J. Pitot, E. Lopez, M.F. Leary,. Berto and A. Du Plessis . Metal additive manufacturing in aerospace: A review. *Mat & Des*, *209*, pp.110008-110048, (2021).

12. A. Gonnabattula, R.S. Thanumoorthy, S. Bontha, A.A.S. Balan, V.A. Kumar, and A.K. Kanjarla. Process parameter optimization for laser directed energy deposition (LDED) of Ti6Al4V using single-track experiments with small laser spot size. Optics & Laser Tech, **175**, pp.110861-110873, (2024).

13. D.D. Gu, W. Meiners, K. Wissenbach, and R. Poprawe. Laser additive manufacturing of metallic components: materials, processes and mechanisms. Int Mat Rev, **57**(3), pp.133-164, (2012).

14. D. Dai, D. Gu, Q. Ge, Y. Li, X. Shi, Y. Sun, and S. Li, S., 2020. Mesoscopic study of thermal behaviour, fluid dynamics and surface morphology during selective laser melting of Ti-based composites. Comp Mat Sci, **177**, pp.109598-109609, (2020).

15. J Sun, M. Guo, K. Shi, and D. Gu. Influence of powder morphology on laser absorption behaviour and printability of nanoparticle-coated 90W-Ni-Fe powder during laser powder bed fusion. Mat Sci in Add Man, **1**(2), pp.11-24, (2022).

16. P. Gao, Z. Wang, and X. Zeng. Effect of process parameters on morphology, sectional characteristics and crack sensitivity of Ti-40Al-9V-0.5 Y alloy single tracks produced by selective laser melting. Int J of Light Mat and Man, **2**(4), pp.355-361, (2019).

17. J. Robinson, M. Stanford, and A. Arjunan. Stable formation of powder bed laser fused 99.9% silver. Mat Today Com, **24**, pp.101195-101208, (2020).

18. Y. Guo, J.I.A. Lina, B Kong, N.A. Wang, and H. Zhang. Single track and single layer formation in selective laser melting of niobium solid solution alloy. Chin J of Aer, **31**(4), pp.860-866, (2018).

19. Y. Liu, J. Li, K. Xu, T. Cheng, D. Zhao, W. Li, Q. Teng, and Q. Wei, Q., 2022. An optimized scanning strategy to mitigate excessive heat accumulation caused by short scanning lines in laser powder bed fusion process. Add Man, **60**, pp.103256-103268, (2022).

20. I. Yadroitsev, and I. Yadroitsava. A step-by-step guide to the L-PBF process. In Fundamentals of laser powder bed fusion of *metals* (pp. 39-77). Elsevier, (2021).

21. P. Canale and C. Servant. Thermodynamic assessment of the Cu–Ti system taking into account the new stable phase $CuTi_3$. Inter J of Mat Res, **93**(4), pp.273-276, (2022).

22. L. Fowler. Development of titanium-copper alloys for dental applications (Doctoral dissertation, Acta Universitatis Uppsaliensis), (2019).

23. K. Dyal Ukabhai, U.A Curle, N.D.E. Masia, M. Smit, I.A. Mwamba, S. Norgren, C. Öhman-Mägi, N.G. Hashe, and L.A. Cornish. Formation of Ti_2Cu in Ti-Cu alloys, J. Phase Equil and Dif, **43**, pp. 332-344, (2022).

CHARACTERISATION OF Ti-6Ta-1.5Zr-0.2Ru-5Cu PRINTED BY LASER POWDER BED FUSION

N.S. Phala[1,2], C. Polese[2,3], J. Ciftci[4], T. Choma[4] and L.A. Cornish[1,2]

[1]School of Chemical and Metallurgical Engineering, University of the Witwatersrand, [2]DSI-NRF Centre of Excellence in Strong Materials, hosted by the University of the Witwatersrand, [3]School of Mechanical, Industrial and Aeronautical Engineering, University of the Witwatersrand, Johannesburg, [4]Warsaw University of Technology, Warsaw

Titanium alloys are used in biomedical applications for their strength, corrosion resistance, and biocompatibility[1]. Additive manufacturing, particularly laser powder bed fusion (LPBF), enables the production of complex, customised implants[2]. This study evaluated the effectiveness of 3D printing the Ti-6Ta-1.5Zr-0.2Ru-5Cu (mass%) alloy, which had been designed[3] and ultrasonically atomised[4], and printed as single tracks to determine the optimal conditions[5].

Ti-6Ta-1.5Zr-0.2Ru-5Cu (mass%) squares (10 x 10 x 1.2 mm) were manufactured using an AconityMIDI system. Manufacturing parameters were: 157.5 W laser power, 600 mm/s scanning speed, 0.15 mm beam diameter, 0.03 mm layer thickness, 0.05 mm hatching, and 0.2625 J/mm linear energy density, with 5 mm stripes and 0.1 mm overlap under argon flow. Remelting of the previous solidified layer was done with 280 W laser power, 3000 mm/s speed, and 0.08 mm beam diameter. Both LPBF and bulk composition (arc-melted bars prior to atomisation) samples were prepared by standard metallography, polished with colloidal silica, and characterised by SEM (Zeiss Sigma Field Emission Scanning Electron Microscope (FEG-SEM500)).

Fig. 1. shows the bulk sample with (αTi) needles in a eutectoid-like mixture of (αTi) and (βTi). Fig. 2. shows an LPBF square, with (αTi) along the (βTi) grain boundaries and as small precipitates in the matrix. The bulk sample had (αTi) needles as the primary phase, whereas the LPBF squares had primary (βTi), with (αTi) precipitated along the grain boundaries and as coarse Widmanstätten needles. Both samples had darker contrasts in the (αTi) phase, which were partially detached (αTi). However, Thermo-Calc[3] identified the phases as primary (βTi) with three phases at low temperatures: mainly (αTi) with small amounts of (βTi) and Ti_2Cu, although the latter was not identified here.

The LPBF sample had the targeted Zr composition, with lower Ti and Cu, and higher Ta and Ru. Conversely, the bulk sample had the targeted Ta composition, with lower Ti and Zr, and higher Ru and Cu, Table 1. The driving force for the difference in microstructure of the bulk and LPBF is the cooling rate, irrespective of the ~3 mass% difference in Ta and Cu, as shown in Table 1. LPBF had much higher cooling rates resulting in smaller grains, while the bulk had slower cooling rates and larger grains.

References:

1. Leyens, C. and Peters, M. (2003) Titanium and Titanium Alloys: Fundamentals and Applications. Cologne, WILEY-VCH Verlag GmbH & Co. KGaA, Weinheim.
2. Ni, J., et al. (2019) Mater Today Bio, 3, 1-18.
3. Spotose, L. (2023) MSc, University of the Witwatersrand
4. Phala, N.S. et al. (2023) MATEC Web of Conferences. 388, 08003
5. Phala, N.S. et al. (2024) MATEC Web of Conferences (submitted)

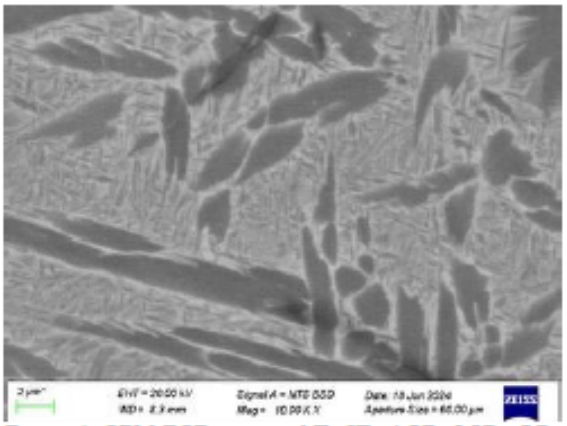

Figure 1. SEM-BSE image of Ti-6Ta-1.5Zr-0.2Ru-5Cu (mass%) bulk sample: (αTi) needles (dark) and (aTi) + (βTi) matrix (light and dark).

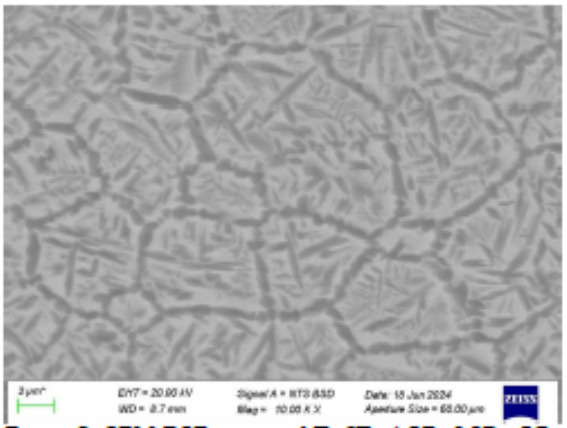

Figure 2. SEM-BSE image of Ti-6Ta-1.5Zr-0.2Ru-5Cu (mass%) LPBF square: (βTi) (light) and (αTi) (dark).

Table 1. EDX results of a bulk sample and LPBF squares of Ti-6Ta-1.5Zr-0.2Ru-5Cu (mass%).

Alloy	Ti	Ta	Zr	Ru	Cu
Bulk: Areal	84.4±0.4	6.4±0.2	1.4±0.2	0.4±0.2	7.4±0.3
LPBF: Areal	84.5±0.7	8.9±0.5	1.5±0.1	0.3±0.1	4.8±0.2

Corresponding author: 820850@students.wits.ac.za

CHARACTERISATION OF Ti-6Ta-1.5Zr-0.2Ru-5Cu PRINTED BY LASER POWDER BED FUSION (LPBF)

N.S. Phala[1,2], C. Polese[2,3], J. Ciftci[4], T. Choma[4] and L.A. Cornish[1,2]

[1]School of Chemical and Metallurgical Engineering, University of the Witwatersrand, [2]DSI-NRF Centre of Excellence in Strong Materials, hosted by the University of the Witwatersrand, [3]School of Mechanical, Industrial and Aeronautical Engineering, University of the Witwatersrand, Johannesburg, [4]Warsaw University of Technology, Warsaw

INTRODUCTION

- Ti-6Ta-1.5Zr-0.2Ru-5Cu (mass%) was designed as a potential α+β alloy[1] with Ta for strength, Zr for solution hardening and corrosion resistance, Ru for corrosion resistance[2] and Cu for antibacterial properties[3].
- The alloy was manufactured by LPBF using ultrasonically atomised powder[4].
- The single-track method was used to identify potential printing parameters[5].

AIM and OBJECTIVE

Aim

- To evaluate the effectiveness of 3D printing Ti-6Ta-1.5Zr-0.2Ru-5Cu (mass%) alloy using LPBF.

Objectives

- To assess the suitability of the selected LPBF parameters for fabricating alloy squares by microstructure and phase analysis.
- To compare properties of LPBF manufactured and as-cast samples.

EXPERIMENTAL PROCEDURE

LPBF sample manufactured using an AconityMIDI system.

Manufacturing parameters
- 157.5 W laser power,
- 600 mm/s scanning speed,
- 0.15 mm beam diameter,
- 0.03 mm layer thickness,
- 0.05 mm hatching,
- 0.2625 J/mm linear energy density.

As-cast sample prepared by arc-melting mixed elemental powders before atomisation.

LPBF and as-cast samples prepared by standard metallography and polished with colloidal silica.

LPBF and as-cast samples characterised by SEM-EDX and XRD.

Vickers hardness tests done on LPBF and as-cast samples.

RESULTS AND DISCUSSION

- Fig. 1. LPBF square had finer primary (βTi) grains with (αTi) precipitated along grain boundaries and as Widmanstätten needles.
- Fig. 2. As-cast sample had coarser (βTi) grains with coarse (αTi) on the grain boundaries and fine (αTi) within the grains. The darker parts of the needles had slightly more Ti, slightly less Cu and slightly less Ta, showing that there was variation in (αTi).
- The coarser needles inside the grains in the LPBF sample were caused by the reheating when depositing the next layer, even though the LPBF sample cooled quicker.
- The LPBF sample had lower Cu and higher Ta compositions than as-cast sample, while both samples showed similar Ti, Zr and Ru compositions (Table 1).
- Fig. 3. shows the hardness profiles across the samples. The LPBF sample had more variation, although the average hardnesses were similar.
- Fig. 4. XRD identified Ti_2Cu, needed for antibacterial properties[3], while Ta, Zr, and Ru dissolved in (αTi) and (βTi) solid solutions.

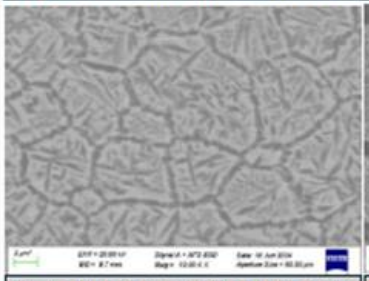

Fig. 1. SEM-BSE image of Ti-6Ta-1.5Zr-0.2Ru-5Cu (mass%) LPBF showing equiaxed (βTi) (light) grains with (αTi) (dark) along (βTi) grain boundaries and within the grains.

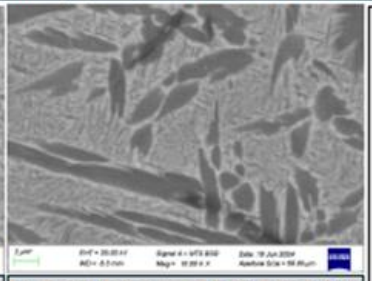

Fig. 2. SEM-BSE image of Ti-6Ta-1.5Zr-0.2Ru-5Cu (mass%) as-cast: (βTi) (light) with (αTi) (dark) precipitated on grain boundaries and within the grains.

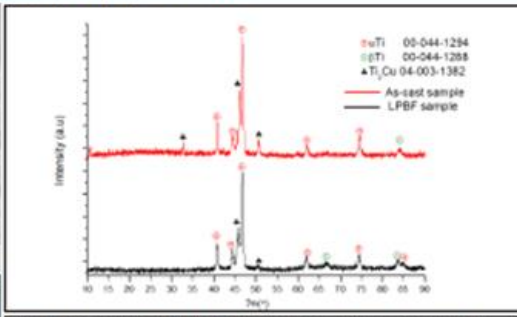

Fig. 4. XRD patterns of LPBF and as-cast samples showing (αTi), (βTi) and Ti_2Cu phases.

Table 1. EDX results of LPBF squares and as-cast sample of Ti-6Ta-1.5Zr-0.2Ru-5Cu (mass%).

Alloy	EDX (mass %)				
	Ti	Ta	Zr	Ru	Cu
LPBF: Areal	84.5±0.8	8.9±0.6	1.5±0.1	0.3±0.2	4.8±0.3
As-cast: Areal	84.4±0.5	6.4±0.2	1.4±0.2	0.4±0.2	7.4±0.3

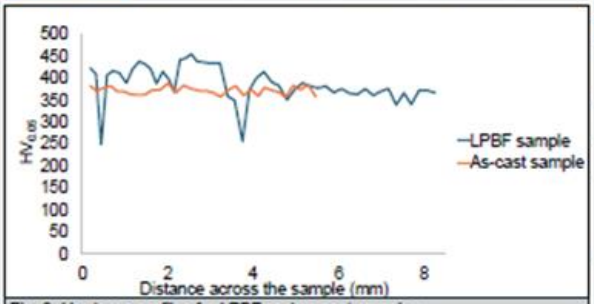

Fig. 3. Hardness profiles for LPBF and as-cast samples.

CONCLUSIONS AND FUTURE WORK

- Both samples had (αTi), (βTi) and Ti_2Cu.
- LPBF sample was assumed to have had higher cooling rates with smaller grains.
- LPBF sample had more variable hardness than arc-melted, although both were similar.
- Future work will include corrosion tests.

REFERENCES

1. Spotose, L. Identifying Ti-Cu-based alloys for biomedical applications, MSc dissertation, University of the Witwatersrand, (2023).
2. Schutz, R.W., 1996. Ruthenium enhanced titanium alloys. *Platinum Metals Review*, 40(2), pp. 54-61.
3. Zhang, X. and Lee, J., 2019. Three-dimensional printing of metals for biomedical applications. *Materials Today Biomedical*, 3, pp. 1-18
4. Phala, N.S., Polese, C., Choma, T., Möller, H., Zrodowski, Ł. and Cornish, L.A., 2023. Atomisation of Ti-6Ta-1.5 Zr-0.2 Ru-5Cu (wt%) for additive manufacturing for biomedical applications. In *MATEC Web of Conferences* (Vol. 388, p. 08003). EDP Sciences.
5. Phala, N.S., Polese, C., Ciftci, J., Choma, T. and Cornish, L.A., 2024. Laser Powder Bed Fusion of Ti-6Ta-1.5Zr-0.2Ru-5Cu (mass%) - Process parameter evaluation using single tracks analysis. In *MATEC Web of Conferences* (submitted).